COPPE
Instituto Alberto Luiz Coimbra de Pós-Graduação e Pesquisa de Engenharia
UFRJ

ANALYSIS OF MECHANICAL ENERGY HARVESTERS USING A NONLINEAR DYNAMICS PERSPECTIVE

Luã Guedes Costa

Tese de Doutorado apresentada ao Programa de Pós-graduação em Engenharia Mecânica, COPPE, da Universidade Federal do Rio de Janeiro, como parte dos requisitos necessários à obtenção do título de Doutor em Engenharia Mecânica.

Orientador: Marcelo Amorim Savi

Rio de Janeiro
Maio de 2024

ANALYSIS OF MECHANICAL ENERGY HARVESTERS USING A NONLINEAR DYNAMICS PERSPECTIVE

Luã Guedes Costa

TESE SUBMETIDA AO CORPO DOCENTE DO INSTITUTO ALBERTO LUIZ COIMBRA DE PÓS-GRADUAÇÃO E PESQUISA DE ENGENHARIA DA UNIVERSIDADE FEDERAL DO RIO DE JANEIRO COMO PARTE DOS REQUISITOS NECESSÁRIOS PARA A OBTENÇÃO DO GRAU DE DOUTOR EM CIÊNCIAS EM ENGENHARIA MECÂNICA.

Orientador: Marcelo Amorim Savi

Aprovada por: Prof. Marcelo Amorim Savi
Prof. Thiago Gamboa Ritto
Prof. Argimiro Resende Secchi
Prof. Luciana Loureiro da Silva Monteiro
Prof. Americo Barbosa da Cunha Junior
Prof. Luiz Bevilacqua

RIO DE JANEIRO, RJ – BRASIL
MAIO DE 2024

Guedes Costa, Luã

Analysis of Mechanical Energy Harvesters Using a Nonlinear Dynamics Perspective/Luã Guedes Costa. – Rio de Janeiro: UFRJ/COPPE, 2024.

XLVI, 199 p.: il.; 29, 7cm.

Orientador: Marcelo Amorim Savi

Tese (doutorado) – UFRJ/COPPE/Programa de Engenharia Mecânica, 2024.

Referências Bibliográficas: p. 149 – 176.

1. Energy Harvesting. 2. Nonlinear Dynamics. 3. Smart Materials. 4. Hybrid Systems. 5. Compact Systems. 6. Multidirectional Systems. 7. Electromechanical Systems. 8. Pendulum Structures. 9. Multistability. 10. Chaos. 11. Hyperchaos. I. Amorim Savi, Marcelo. II. Universidade Federal do Rio de Janeiro, COPPE, Programa de Engenharia Mecânica. III. Título.

À minha família, com amor e gratidão.

Agradecimentos

Desde criança eu fui muito curioso com as coisas. Eu sempre queria saber o porquê. Lembro até hoje, eu com mais ou menos 6 - 7 anos de idade, lendo sobre átomos e elétrons, sobre núcleo da terra e galáxias, desmontando vários eletrônicos e separando cada componente tentando adivinhar o que cada um fazia. Um dia ganhei um telescópio desses simples, que vendem em supermercado. Eu fiquei 2 meses futucando aquilo, até que um dia eu consegui ver Saturno, muito muito de longe, mas vi, com os anéis e tudo. Chamei meus pais correndo e eles ficaram super felizes. Apesar disso tudo, eu nunca pensei que chegaria tão longe. Olhando para trás, era óbvio que era o caminho que eu deveria seguir, mas durante o trajeto não foi tão óbvio assim pra mim. Por isso, gostaria de aproveitar este espaço para destacar a importância de algumas pessoas que me ajudaram ao longo desta trajetória.

Primeiramente, agradeço aos meus pais, João e Suely, que sempre me deram suporte, amor, incentivo e carinho, e por sempre priorizarem a minha educação. Agradeço também por todos os sacrifícios que fizeram por mim. Sem tudo isso, eu nunca teria chegado a esse momento. Amo muito vocês!

Ao meus amigos de longa data, em especial o Antonio, a Louise, o Rodrigo, o Giovanni, o Breno, o Pedro, e o João Pedro, por todos os momentos incriveis que passamos. Principalmente nesses últimos 4 anos, que indiretamente me ajudaram muito ao longo da realização dessa tese.

À minha namorada Rafaela, que pegou o início meio e fim de todo esse processo. Provavelmente foi a pessoa que mais ouviu eu falando (e muitas vezes reclamando) sobre provas, artigos, tese, congressos... Muito obrigado pelo amor, pelo carinho, pelo incentivo, pelo companheirismo, pela paciência, pela confiança, e por ser muito incrível nesses quase 4 anos. Obrigado por embarcar nessa aventura entre Rio e São Paulo comigo!!

Um agradecimento especial à minha segunda mãe, tia Joane, que de perto ou de longe, sempre esteve comigo e contribuiu muito pra formar a pessoa que sou hoje.

À minha avó Leda, e meu avô Antonio (in memorian) que foram sempre sinônimo de alegria e boas memórias! E também a todos os familiares que sempre torceram por mim.

Aos colegas do Mecanon e afiliados, que foram muito importantes durante o pro-

cesso de desenvolvimento desse trabalho. Em especial ao Vanderson e o Daniel pelos sempre engraçados papos da tarde, e ao Arthur pelas discussões super construtivas que tivemos ao longo desses anos. Ademais, a todos os já citados e a todos os demais colegas, muito obrigado pelo espírito de cooperação e equipe compartilhados durante esse tempo.

Um agradecimento especial à Prof. Luciana, minha orientadora do mestrado e iniciação científica, que foi essencial para que eu começasse a trilhar esse caminho.

Essa tese foi inteiramente feita ao som de todos os estilos de metal possíveis. Por isso, fica um agradecimento ao deus metal e a todos os artistas que me deram todos os gases possíveis com suas músicas!!

E por último, é difícil até achar palavras, mas não poderia deixar de agradecer ao meu mestre, professor, orientador e amigo Marcelo Savi pela grande generosidade, pelos conselhos profissionais e pessoais, pela orientação impecável, pela confiança e incentivo, pelo direcionamento, por abrir portas, e pela pessoa incrível que é! Foi um grande privilégio, durante os últimos 5 anos, poder realizar parte do mestrado e esse doutorado sendo seu orientado! Que a força das não linearidades esteja com você!

Agradeço ao CNPq e a FAPERJ pelo apoio financeiro e à UFRJ pela estrutura.

Resumo da Tese apresentada à COPPE/UFRJ como parte dos requisitos necessários para a obtenção do grau de Doutor em Ciências (D.Sc.)

ANALYSIS OF MECHANICAL ENERGY HARVESTERS USING A NONLINEAR DYNAMICS PERSPECTIVE

Luã Guedes Costa

Maio/2024

Orientador: Marcelo Amorim Savi

Programa: Engenharia Mecânica

A natureza manifesta energia mecânica em diversas formas, incluindo vibração, som, ondas, vento e biomecânica, que podem ser aproveitadas para alimentar sistemas eletrônicos. A colheita de energia utilizando materiais inteligentes aliada a fenômenos mecânicos não lineares tem ganhado atenção pela sua alta densidade de potência, design simples, escalabilidade e melhoria de desempenho. Apesar de muitas soluções propostas, desafios de implementação persistem. Características não lineares desencadeiam dinâmicas complexas, afetando diretamente a performance. Portanto, uma análise adequada requer uma caracterização profunda do coletor guiada pela perspectiva da dinâmica não linear. Este trabalho propõe um arcabouço de análise não linear para sistema de colheita de energia, permitindo abordar dois desafios recentes: coletores com restrição de espaço e colheita de energia de fontes multidirecionais, ambos mantendo alta performance. Para os sistemas com restrição de espaço propõe-se um novo dispositivo compacto com dois pares de transdutores piezoelétricos e de interações magnéticas, revelando características multiestáveis sem precedentes. A análise de diferentes configurações associa dinâmicas de alto deslocamento de período-3, período-1 e caóticas com alto desempenho. Comparativos com o dispositivo clássico biestável destacam melhorias consideráveis de performance. A colheita de energia multidirecional considera o uso de pêndulos, propondo um coletor que combina transdutores piezoelétricos e eletromagnéticos. A análise de três configurações demonstra que a multitransdução híbrida é crucial para uma conversão de energética eficaz. Uma análise paramétrica mapeia a dinâmica e o desempenho do sistema, revelando comportamentos complexos e irregulares caracterizados por combinações de oscilação e rotação, associados à maiores larguras de banda de operação.

Abstract of Thesis presented to COPPE/UFRJ as a partial fulfillment of the requirements for the degree of Doctor of Science (D.Sc.)

ANALYSIS OF MECHANICAL ENERGY HARVESTERS USING A NONLINEAR DYNAMICS PERSPECTIVE

Luã Guedes Costa

May/2024

Advisor: Marcelo Amorim Savi

Department: Mechanical Engineering

Nature manifests mechanical energy in various forms including vibration, sound, waves, wind, and biomechanics, which can be harnessed to power electronic systems. Energy harvesting using smart materials allied with mechanical nonlinear phenomena has gained attention for its high power density, simple design, scalability, and improved performance. Despite many proposed solutions, implementation challenges remain. Nonlinear characteristics trigger complex dynamics, directly affecting performance. Thus, a proper analysis requires the harvester's deep characterization guided by a nonlinear dynamics perspective. This work proposes a nonlinear dynamics framework of analysis for energy harvesting systems, addressing two recent challenges: harvesters in confined spaces, and energy harvesting from multidirectional sources, both while maintaining optimal performance. To deal with confined spaces, a novel compact structure is proposed with two pairs of magnetic interactions and piezoelectric transducers, revealing unprecedented multistable features. Analysis of different configurations successfully associates high-displacement period-3, period-1, and chaotic dynamics with higher performances. Comparisons with the classical bistable harvester highlight considerable performance enhancements. The multidirectional energy harvesting considers the use of pendulum structures, proposing a device that combines piezoelectric and electromagnetic transducers. Analysis of three configurations demonstrates that hybrid multitransduction is crucial for effective energy conversion. A parametric analysis maps the system dynamics and performance, revealing complex and irregular behaviors characterized by a combination of oscillation and rotational motion, leading to wider bandwidth systems.

Contents

List of Figures

List of Tables

List of Symbols

A	Area occupied by a power-motion attractor within a basin of attraction, p. 85
A_b	Mechanical base excitation amplitude, p. 50, 101
A_{red}	The area within a PCD where the harvester under study outperforms the reference harvester, p. 90
C_{pi}	CMEH internal capacitances of the piezoelectric elements ($i = 1, 2$), p. 49
C_{pz}	Internal capacitance of the MHEH piezoelectric transducer, p. 98
D	Dissipation function, p. 50, 101
D_x	Dissipation function associated with the MHEH x direction, p. 101
D_z	Dissipation function associated with the MHEH z direction, p. 101
D_{ϕ_e}	Dissipation function associated with the interaction of the MHEH pendulum with the surrounding media, p. 101
D_{ϕ_i}	Dissipation function associated with the magnetic forces within the electromagnetic transucer, p. 101
D_{em}	Dissipation function associated with the resistance of the electromagnetic circuit, p. 101
D_{pz}	Dissipation function associated with the resistance of the piezoelectric circuit, p. 101
I	Electrical current of the electromagnetic transducer, p. 100
I_{pz}	Electric current induced by the piezoelectric coupling, p. 98

L	Reference length, p. 51
L_m	Internal inductance of the MHEH electromagnetic transducer, p. 98
L_p	Pendulum length, p. 98
N	Half of the number of equilibrium positions of a system, excluding zero, p. 44
N	Number of time steps, p. 28, 182
N_c	Turns of a coil, p. 12
N_p	Number of discrete points in time, p. 25
N_x	Sample points for the x axis of a 2D diagram, p. 34
N_y	Sample points for the y axis of a 2D diagram, p. 34
N_{attr}	Number of motion-power attractors combined into "OT" classification, p. 85
N_{div}	Number of time steps per period of excitation, T, p. 116
N_{div}	Number of time steps per period, T, of excitation, p. 179
N_{per}	Number of periods, T, of excitation, p. 179
P_i	Square of p_i, p. 46
P_p	Transformation, p. 25
P_r	Performance metric of the reference harvester, p. 38
P_s	Performance metric of the harvester under study, p. 38
P_{avg}	CMEH average output power, p. 53
P_{avg}	MHEH overall average output power, p. 103
$P_{\text{avg}}^{\text{den}}$	CMEH average output power density, p. 53
P_{inst_i}	CMEH instantaneous output power ($i = 1, 2$), p. 52
P_{inst_j}	Instantaneous electrical power of the MHEH transducers ($j = pz, em$), p. 103
P_{inst}	MHEH instantaneous output power, p. 103

R_i CMEH equivalent electrical resistances ($i = 1, 2$), p. 49

R_{iem} Internal resistance of the electromagnetic transducer, p. 98

R_{ij} Internal resistance of the MHEH transducers ($j = pz, em$), p. 98

R_j Equivalent resistances of the HMEH circuits ($j = pz, em$), p. 98

R_{lem} Load resistance connected to the electromagnetic transducer, p. 98

R_{li} CMEH external load resistances ($i = 1, 2$), p. 49

R_{lj} Load resistances connected to the MHEH transducers ($j = pz, em$), p. 98

R_{pi} CMEH internal electrical resistances of the piezoelectric elements ($i = 1, 2$), p. 49

$Re(\square)$ Real part of a variable, p. 32

S Generic surface, p. 11

S_p Set of points in the state space, p. 25

T Kinetic energy, p. 50, 98

T Temperature, p. 8

T_C Curie temperature, p. 8

T_p Kinetic energy of the MHEH pendulum, p. 98

T_s Kinetic energy of the MHEH structure, p. 98

U Potential energy, p. 34, 50

U_m Magnetic potential energy, p. 50

U_p MHEH pendulum potential energy, p. 99

U_s CMEH structure potential energy, p. 50

U_s MHEH structure potential energy, p. 99

U_t Evolution operator, p. 30

V	Reference voltage, p. 51
W	Total energy of the MHEH electrical domain, p. 100
W_C	Electric energy in the capacitance, p. 100
W_L	Magnetic energy in the inductance, p. 100
W_e	Electric energy of the piezoelectric element, p. 100
W_e	Piezoelectric energy, p. 50
W_m	Magnetic energy of the electromagnetic transducer, p. 100
W_{em}	Electromagnetic energy, p. 100
W_{pz}	Piezoelectric energy, p. 100
X	Square of x, p. 46
$\bar{Z}$	CMEH equilibrium positions, p. 54
$\square^E$	Variable assessed under constant electric field, p. 10
$\square^H$	Variable assessed under constant magnetic field, p. 16
$\square^T$	Transpose operator, p. 10
$\square^\sigma$	Variable assessed under constant stress, p. 10
$\square^{\mathrm{RMS}}$	Index representing the root mean square of a variable, p. 53, 103
$\square_0$	Index symbolizing initial state/condition, p. 26
$\square_t$	Discrete time index, p. 27
$\square_x$	Subscript related to the MHEH x direction, p. 97
$\square_z$	Subscript related to the MHEH z direction, p. 97
$\square_{\max}$	Subscript represent the max value of a variable, p. 36
$\square_{\min}$	Subscript represent the minimum value of a variable, p. 36
$\square_{\mathrm{norm}}$	Subscript that represents the ratio of a characteristic at each point in a single sample diagram, to the maximum value of the characteristic across all points in the same sample diagram, $\square/\square_{\max}$, p. 43

$\square_{em}$	Subscript related to the MHEH electromagnetic transducer, p. 97
$\square_{pz}$	Subscript related to the MHEH piezoelectric transducer, p. 97
$\square_{p}$	Subscript related to the MHEH pendulum, p. 97
$\Delta P(\%)$	Performance percentage difference metric, p. 38
$\Delta \bar{P}_{\text{avg}}(\%)$	Normalized average output power percentage difference, p. 89
Γ_i	Generic polynomial variables, p. 177
Ω	Normalized base excitation frequency, p. 53
Ω_s	CMEH ratio of linearized natural frequencies, p. 52
Ω_s	Ratio of MHEH structure natural frequencies, p. 102
Φ_B	Magnetic flux, p. 11
Σ_p	Poincaré Section, p. 25
α_i	CMEH normalized 1$^{\text{st}}$ restitution coefficient ($i = 1, 2$), p. 52
$\bar{P}_{\text{avg}}$	CMEH normalized average output power, p. 53
$\bar{P}_{\text{avg}}$	HMEH normalized overall average output power, p. 104
$\bar{P}_{\text{avg}}^{(\text{max})}$	CMEH maximum normalized average output power, p. 69
$\bar{P}_{\text{avg}}^{\text{den}}$	CMEH normalized average output power density, p. 53
$\bar{P}_{\text{inst}_i}$	CMEH normalized instantaneous output power ($i = 1, 2$), p. 53
$\bar{P}_{\text{norm}}$	Ratio of the average output power at each point in the OPD, to the maximum average output power in the same OPD, p. 92
$\bar{P}_{\text{norm}}^{(\text{em})}$	Ratio of the MHEH electromagnetic transducer average output power at each point in the OPD, to the maximum average output power in the same OPD, p. 126
$\bar{P}_{\text{norm}}^{(\text{overall})}$	Ratio of the overall MHEH average output power at each point in the OPD, to the maximum average output power in the same OPD, p. 126

$\bar{P}_{\text{norm}}^{(\text{pz})}$ Ratio of the MHEH piezoelectric transducer average output power at each point in the OPD, to the maximum average output power in the same OPD, p. 126

$\bar{P}_j$ HMEH normalized transducer average output powers ($j = pz, em$), p. 104

$\bar{U}$ Normalized potential energy, p. 52

$\bar{\square}$ Important normalized variables, p. 52

$\bar{z}$ CMEH normalized z relative displacement, p. 52

$\bar{z}_{\text{rel}}$ Relative position between the first and the second DoFs of the compact multistable energy harvester, p. 70

β_i CMEH normalized 2$^{\text{nd}}$ restitution coefficient ($i = 1, 2$), p. 52

$\boldsymbol{\mu}$ Linear magnetic permeability tensor, p. 16

$\boldsymbol{\sigma}$ Stress field, p. 10

$\boldsymbol{\varepsilon}$ Dielectric tensor, p. 10

$\boldsymbol{\varsigma}$ Set of points in the Poincaré map, p. 25

$\boldsymbol{\lambda}$ Lyapunov exponents spectrum, p. 28

χ_i CMEH normalized piezoelectric coupling coefficient in the mechanical ODE ($i = 1, 2$), p. 52

χ_j Normalized transducer couplings in the MHEH mechanical ODE ($j = pz, em$), p. 102

$\delta\mathbf{x}$ Small perturbation vector of the system, p. 26

$\delta\mathbf{x}(t)$ Function that describes the evolution of the perturbation with respect to time, p. 28

$\delta\mathbf{x}_0$ Initial perturbation vector, p. 28

δ_0 Magnitude of the initial small perturbation of the system, p. 26

$\dot{\square}$ Derivative with respect to time t, $d\square/dt$, p. 24

$\dot{\bar{\square}}$ Derivative with respect to normalized time τ, $d\bar{\square}/d\tau$, p. 52

ℓ	Normalized pendulum length, p. 102
η	Ratio between electromechanical couplings, p. 108
$\exists$	Mathematical symbol for "there exists", p. 32
$\forall$	Mathematical symbol for "for all", p. 32
γ	Normalized amplitude of excitation, p. 53
$\hat{\theta}_t$	Cylindrical time coordinate, p. 26
$\in$	Mathematical symbols for "in/belongs to", p. 24
κ_i	CMEH normalized piezoelectric coupling coefficient in the electrical ODE ($i = 1, 2$), p. 52
κ_j	Normalized transducer couplings in the MHEH electrical ODE ($j = pz, em$), p. 102
λ	Lyapunov Exponent, p. 28
$\mathbb{C}$	Set of complex numbers, p. 32
$\mathbb{R}$	Set of real numbers, p. 24
$\mathbf{D}$	Electric displacement field, p. 10
$\mathbf{E}$	Electric field, p. 10
$\mathbf{H}$	Magnetic field tensor, p. 16
$\mathbf{S}$	Strain field, p. 10
$\mathbf{d}$	Piezoelectric constant tensor, p. 10
$\mathbf{d}_m$	Piezomagnetic constant tensor, p. 16
$\mathbf{s}$	Linear elastic compliance tensor, p. 10
$\mathbf{x}_p$	Point that composes a Poincaré map, p. 25
$\mathbf{0}$	Vector filled with zeros, p. 32
$\mathbf{A}$	Generic second order tensor, p. 27
$\mathbf{B}$	Magnetic induction field, p. 11
$\mathbf{I}$	Identity matrix, p. 32

$\mathbf{J}$	Jacobian Matrix, p. 27
$\mathbf{J}_D$	Displacement current tensor, p. 12
$\mathbf{P}$	Polarization field density tensor, p. 12
$\mathbf{P}_S$	Polarization field generated by surface electrostatic charges, p. 13
$\mathbf{Q}$	Vector associated with the MHEH generalized coordinates, p. 101
$\bar{\mathbf{q}}$	CMEH set of normalized generalized coordinates, p. 52
$\hat{\mathbf{e}}_x$	Unitary vector in the Cartesian x direction, p. 25
$\hat{\mathbf{e}}_y$	Unitary vector in the Cartesian y direction, p. 25
$\hat{\mathbf{e}}_z$	Unitary vector in the Cartesian z direction, p. 25
$\hat{\mathbf{e}}_d$	Arbitrary orthogonal direction in the state space, p. 26
$\mathbf{a}$	Generic vector, p. 27
$\mathbf{f}(\mathbf{x})$	Generic dynamical system, p. 24
$\mathbf{r_b}$	Multidirectional base excitation, p. 98
$\mathbf{r}_p$	Absolute pendulum position of the MHEH, p. 98
$\mathbf{r}_s$	Absolute structure position of the MHEH, p. 98
$\mathbf{u}$	Set of CMEH generalized coordinates, p. 50
$\mathbf{x}$	Generic state variable vector, p. 24
$\mathbf{x}_0$	Set of initial conditions, p. 30
$\mathcal{I}$	Reference electrical current, p. 101
$\mathscr{L}$	Lagrangian for an electromechanical system, p. 50, 101
$\mathcal{O}_{\text{method}}$	Order of the error of the method of integration, p. 36
$\mathcal{S}$	Attractor subspace of the phase space of a dynamical system, p. 30
$\mathcal{b}$	Base of reference, p. 28

$\mathfrak{a}_i$	Polynomial coefficients of the magnetic/equivalent restitution force ($i = 1, \cdots, N+1$), p. 44
μ	Base excitation angle, p. 98
μ_j	j^{th} eigenvalue of a n-dimensional system, p. 32
∇	Nabla operator, p. 11
ω	Mechanical base excitation frequency, p. 50, 101
ω_0	Reference frequency, p. 193
ω_i	CMEH linearized natural frequency ($i = 1, 2$), p. 53
ω_j	MHEH structure natural frequencies ($j = x, z, \phi$), p. 102
∂S	Contour of S, p. 11
ϕ	Pendulum angle, p. 98
$\prod$	Product operator, p. 28
ψ	Magnetic flux linkage, p. 12, 100
ψ_i	CMEH magnetic flux linkages ($i = 1, 2$), p. 50
ρ	Ratio of corresponding equivalent masses of both harvesters, p. 52, 102
$\sum$	Sum operator, p. 44
τ_p	Time for the return of $\mathbf{x}_p$ to Σ_p, p. 25
τ	Normalized time, p. 51
τ_0	Normalized initial time, p. 53
τ_f	Normalized final time, p. 53
τ_{trans}	Normalized time at which the transient state is considered to end, p. 116
θ_i	CMEH piezoelectric coupling coefficients ($i = 1, 2$), p. 49
θ_j	MHEH coupling coefficients ($j = pz, em$), p. 97
ε	Material permittivity, p. 12
ε_0	Vacuum permittivity, p. 12

φ_i CMEH normalized electrical conductance ($i = 1, 2$), p. 52

φ_j Normalized equivalent resistances of the MHEH transducer circuits ($j = pz, em$), p. 102

ζ_i CMEH normalized mechanical damping coefficient ($i = 1, 2$), p. 52

ζ_j MHEH normalized damping coefficients ($j = x, z, \phi$), p. 102

a First generic parameter for depicting the construction method of the diagrams, p. 40

a_i CMEH first restitution force polynomial coefficient ($i = 1, 2$), p. 50

b Second generic parameter for depicting the construction method of the diagrams, p. 40

b_i CMEH second restitution force polynomial coefficient ($i = 1, 2$), p. 50

c Third generic parameter for depicting the construction method of the diagrams, p. 40

c_i CMEH damping coefficients ($i = 1, 2$), p. 49

c_j MHEH damping coefficients ($j = x, z, em, p$), p. 97

$d\Omega$ Frequency step, p. 105

$d\mathbf{A}$ Infinitesimal area vector of the surface S, p. 11

$d\mathbf{l}$ Infinitesimal vector of dS, p. 11

dt Time increment, p. 27

e Exponential function, p. 28

e_j Elementary symmetric polynomial, p. 46

f_j MHEH Restitution forces ($j = x, z, pz$), p. 99

f_r Equivalent restitution force, p. 44

f_{m_i} Magnetic restitution force ($i = 1, 2$), p. 50

g Gravity acceleration, p. 98

k_i CMEH equivalent structural stiffnesses ($i = 1, 2$), p. 49

k_j MHEH equivalent stiffnesses ($j = x, z, pz$), p. 97

m_i CMEH equivalent masses ($i = 1, 2$), p. 49

m_j MHEH Equivalent masses ($j = s, p$), p. 97

n Dimension of the dynamical system, p. 24

n_{DoF} Number of degrees-of-freedom, p. 53

p_i Equilibrium points of a single-DoF multistable system ($i = 1, \cdots, N$), p. 46

p_{tol} Numerical tolerance for classification of periodic attractors, p. 36

q Electrical charge of the electromagnetic transducer, p. 100

r_b Excitation function, p. 98

t Time, p. 11

t_0 Initial time, p. 26

t_f Final time, p. 34, 182

t_{trans} Time at which the transient state is considered to end, p. 35

t_i Discrete points in the time continuum ($i = 1, \cdots, N_p$), p. 25

u_i Single CMEH generalized coordinate within $\mathbf{u}$ set ($i = 1, 4$), p. 50

v Electric voltage, p. 11

v Voltage of the MHEH piezoelectric transducer, p. 100

v_i CMEH voltages ($i = 1, 2$), p. 49

v_m Magnet's velocity, p. 11

v_{em} Resulting voltage induced by the MHEH electromagnetic transducer motion, p. 98

x Generic position coordinate, p. 44

x MHEH structure relative displacement in the x direction, p. 98

x_1 Generic state variable, p. 31

x_2 Generic state variable, p. 31

x_b Base excitation in x direction, p. 98

x_p Pendulum position in x direction, p. 98

x_s MHEH structure relative displacement in the x direction, p. 98

$x_{\max}$ Maximum value of the state variable between t_{trans} and t_f, p. 36

$x_{\min}$ Minimum value of the state variable between t_{trans} and t_f, p. 36

z MHEH structure relative displacement in the z direction, p. 98

z_b Base excitation in z direction, p. 98

z_b Mechanical base excitation displacement in z Cartesian direction, p. 50

z_i CMEH relative displacement in the z Cartesian direction ($i = 1, 2$), p. 50

z_p Pendulum position in z direction, p. 98

z_{st} MHEH structure static displacement due to gravity, p. 98

G Generic characteristic used to exemplify the construction of certain OPDs, p. 43

T Period of excitation, p. 25, 36

q HMEH Electrical charge of the electromagnetic transducer, p. 100

List of Abbreviations

1T	Periodic attractor that repeats its characteristics every 1 period, T, of excitation, p. 36
2T	Periodic attractor that repeats its characteristics every 2 periods, T, of excitation, p. 36
3T	Periodic attractor that repeats its characteristics every 3 periods, T, of excitation, p. 36
4T	Periodic attractor that repeats its characteristics every 4 periods, T, of excitation, p. 36
5T	Periodic attractor that repeats its characteristics every 5 periods, T, of excitation, p. 36
6T	Periodic attractor that repeats its characteristics every 6 periods, T, of excitation, p. 36
9T	Periodic attractor that repeats its characteristics every 9 periods, T, of excitation, p. 85
AC	Alternate Current, p. 2
API	Application Programming Interface, p. 182
CBEH	Classical Bistable Energy Harvester, p. 89
CH	Chaotic attractor, p. 36
CMEH	Compact Multistable Energy Harvester, p. 48, 89
CPEH	Classical Piezoelectric Energy Harvester, p. 96
CPU	Computer Processing Unit, p. 182
CS	Contact-Sliding Triboelectric Mode, p. 13
DPD	Dynamical Pattern Diagram, p. 39

DRD	Dynamical Response Diagram, p. 34
DoF	Degree(s)-of-freedom, p. 19
FTL	Freestanding Triboelectric-Layer Mode, p. 13
HC	Hyperchaotic attractor, p. 36
IM	Irregular Mixed, p. 131
IO	Irregular Oscillation, p. 131
IR	Irregular Rotation, p. 131
IoT	Internet of Things, p. 1
LASMP	Light-Activated Shape Memory Polymer, p. 22
LED	Lyapunov Exponent Diagram, p. 30
MEMS	Micro-Electromechanical Systems, p. 1
MHEH	Multidirectional Hybrid Energy Harvester, p. 97
MPEH	Multidirectional Piezoelectric Energy Harvester, p. 96
MP	Classification that includes all the attractors with periodicity greater than 5T, p. 36
OCD	Occurrence Diagram, p. 40
OPDs	Overall Performance Diagrams / Output Power Diagrams, p. 38
OT	Other motion-power attractors that presents $A < 1\%$ combined, p. 85
PCD	Performance Comparison Diagram, p. 38
PS	Specific region within the OPD chosen to highlight some phase subspaces, p. 84
PVC	Polyvinyl Chloride, p. 14
PVDF	Polyvinylidene Fluoride, p. 8
PZT	Lead Zirconate Titanate, p. 8
RM	Regular Mixed, p. 131

RO	Regular Oscillation, p. 131
RR	Regular Rotation, p. 131
SEP	Stable Equilibrium Points, p. 31
SE	Single-Electrode Triboelectric Mode, p. 13
SMA	Shape Memory Alloy, p. 22
TEH	Triboelectric Energy Harvester, p. 13
UAVs	Unmaned Aerial Vehicles, p. 2
VCS	Vertical Contact-Separation Triboelectric Mode, p. 13

Chapter 1

Introduction

The rapid development of society in recent years has caused an increase in global energy demand. Induced by modern science tools and elements of Industry 4.0, such as wireless electronic devices and smart systems, energy-related issues are linked to bottlenecks that need to be overcome. Moreover, the need for environmentally friendly power supplies due to climate changes and the reduction of e-waste [7, 8] are motivating the development of new paradigms. This scenario results in the need for new strategies and creative solutions that can be viable for long-term applications. In this regard, the constant evolution of semiconductor technology keeps significantly reducing the power consumption of electronic systems in general, especially wireless devices [9]. This trend is driving interest in harvesting environmental wasted energy such as vibration, sound, wind, sea waves, and biomechanical motion as an alternative power supply to traditional batteries [10] and for small-medium size systems, as these sources of mechanical energy can be enough to power from small electronic devices to small-scale urban areas [11, 12].

While the practice of energy conversion has prehistoric origins, the initial works involving mechanical energy harvesting within this recent scope trace back to the decade of 1990, when authors described a simple dynamical model demonstrating the feasibility of such devices and explored their potential applications with different types of transduction mechanisms [13, 14]. Since then, researchers have shown the versatility of such systems by investigating a wide range of interesting applications in the fields of the Internet of Things (IoT), Micro-electromechanical Systems (MEMS), data collection, and small power grids. Among them, as depicted in Figure 1.1, notable instances include:

- **Civil infrastructure applications:** Energy harvesting from bridge vibrations [15, 16], powering charging stations for electric cars in smart roads [17], extracting energy from loads on pavements in general (roads and sidewalks) [18, 19], contributing to sustainable interior space design by harvesting energy

from pressure of human walking [20, 21], enabling smart monitoring of footbridges [22], AC power lines [23, 24], and sanitation systems pipelines [25, 26].

- **Biology and biomedic applications:** used to power biomedical devices within the body by exploiting the natural contraction and relaxation motions of the heart, lung, and diaphragm [27–30], real-time arterial pulse monitoring through the epidermis [31], facilitating self-powered deep brain stimulation used for neural prosthetics and brain-computer interfacing [32], and wildlife monitoring [33–36].

- **Self-charging wearables:** Energy harvesters employed to power wearable or portable devices through biomechanical human motion, such as jaw movements [37], finger bending [38], knee articulation dynamics [39], impact of shoes on the ground [40, 41], arm swinging [42, 43], and overall full body motion [44–47].

- **Vehicle and transportation applications:** Harvesting energy from vehicle vibrations [48] and rotational energy of wheels [49], thereby powering sensors or small circuits. Applied to monitor suspension systems [50, 51] and tires [52]. Deployment in powering sensors in freight trains [53] and railroad tracks [54], aiming to store otherwise dissipated into the environment.

- **Offshore applications:** Mainly associated with marine buoys to environmental monitoring and communications [55–58]. Additionally, some works address energy harvesting from flow-induced vibration energy in the oil and gas industry, aiming to reduce the cost of maintaining and replacing batteries of sensors around well regions [59], although these do not precisely align towards the environmental-friendly paradigm.

- **Aerospace applications:** Harvesting energy from flow-induced vibrations in structural aerospace vehicles like unmanned aerial vehicles (UAVs) [60] and drones [61]. Also, employed for structural health monitoring in larger aerospace vehicles [62, 63].

While numerous potential applications exist, several challenges still persist in terms of practical implementation and dissemination of this technology, as various factors can influence the performance of such systems.

In this work, two of these challenges are addressed with enhancement in performance as the primary goal. The first challenge is related to the implementation of these systems into confined and compact spaces, given that many applications are compact and limited in size. The second challenge relates to the energy harvester's ability to harness energy from multidirectional sources since numerous solutions up to the present time have been designed to operate solely in one specific direction.

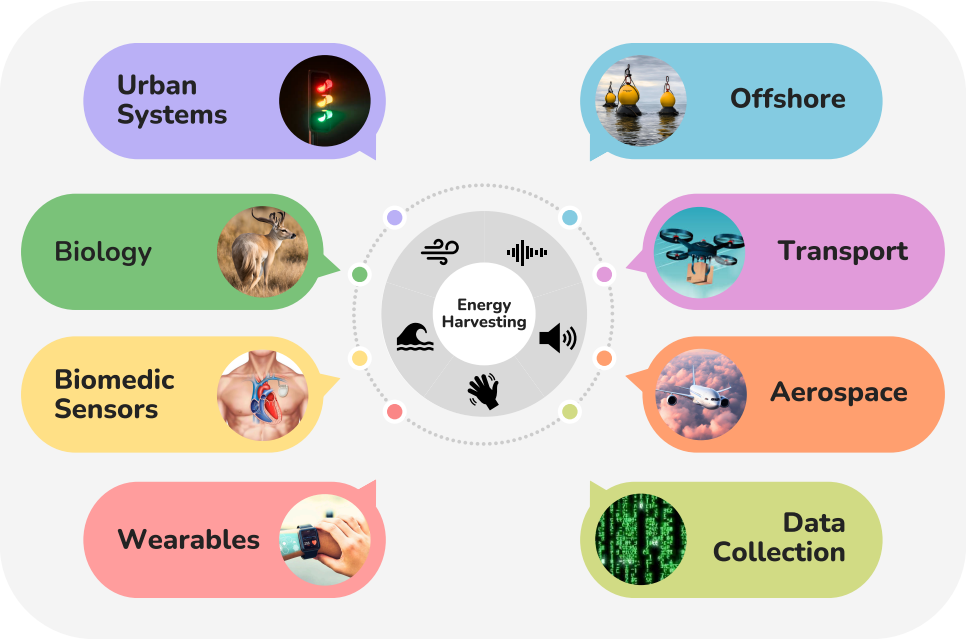

Figure 1.1: Energy harvesting applications.

Both problems are tackled through the integration or refinement of mechanical nonlinear modulation techniques applied to conventional energy harvester structures, as numerous nonlinear features are known to drastically increase energy harvesting performance [64]. Among the most noteworthy contributions of this doctoral thesis, the following stand out:

First, the proposal of a framework of analysis for energy harvesters, guided by a nonlinear dynamics perspective, where classical tools are revised and new tools, based on the combination of classical techniques, are introduced. The framework is built aiming to achieve a deep understanding of the energy harvesters' characteristics and unique traits. These characteristics, such as dynamical patterns and performance, are mapped and quantified through an in-depth parametric analysis providing valuable insights for the design decision-making of energy harvesting systems. This facilitates the understanding of whether the energy harvester is suitable for a specific application and whether it warrants further investigation. This framework formalizes the methodology previously employed in analyzing bistable harvesters in a prior study [65], and it is used to handle all the analyses showcased in this work.

Second, the concept of a novel compact two-degrees-of-freedom nonlinear energy harvester structure with multistable behavior, building upon improvements made to previous harvesters detailed in existing literature [1, 2, 66, 67]. This new harvester is characterized by a compact inner-outer beam arrangement. Each beam is associated with a set of magnets and a piezoelectric element, resulting in the presence

of two magnetic interactions and two piezoelectric elements within the system. The interaction of the structure with these magnetic forces gives rise to unprecedented multistable characteristics. A reduced-order model of the harvester is established and the nonlinear dynamics framework is employed to analyze this system. Essential characteristics are mapped and, subsequently, a comprehensive comparison with the classical bistable harvester is conducted, showcasing performance improvements across virtually all relevant conditions. Additionally, the performance comparison between distinct configurations of the multistable harvester is performed, determining the best and the worst configurations in terms of energy conversion.

Third, the development of a hybrid pendulum-based energy harvester designed with multidirectional energy conversion capabilities. This new harvester is a modified version of the classical cantilever-based piezoelectric energy harvester [68] with an attached pendulum in its free end. Specifically, a piezoelectric transducer is attached to a cantilever structure to convert energy from flexural oscillations, while an electromagnetic converter is attached to the pendulum to harness the rotational energy. The design is developed in such a way that the system can perform multidirectional energy harvesting, mitigating the energy-absorbing effects of the pendulum. First, a lumped model is established to capture the essential characteristics of the system. Subsequently, an analysis is presented assessing the viability of employing pendulum structures to attain multidirectional capabilities. The analysis revealed that this kind of system must have an associated transduction mechanism to harness rotational energy, as without it, the pendulum works as an energy absorber. Moreover, an in-depth analysis using the nonlinear dynamics framework is showcased, characterizing the global dynamics of the system and identifying the optimal and suboptimal structural parameters in terms of energy conversion. Finally, the dynamical responses and patterns associated with high performance are identified. The analysis revealed that these responses are often characterized by a blend of irregular complex behaviors, coupled with a mix of oscillatory and rotational patterns of motion, resulting in wider bandwidth systems.

These contributions are related to the following publications in international journals:

- COSTA, L. G., MONTEIRO, L. L. S., PACHECO, P. M. C. L., et al. "A parametric analysis of the nonlinear dynamics of bistable vibration-based piezoelectric energy harvesters", *Journal of Intelligent Material Systems and Structures*, v. 32, n. 7, pp. 699–723, 2021. doi:10.1177/1045389X20963188. Available at: <https://doi.org/10.1177/1045389X20963188>.

- COSTA, L. G., SAVI, M. A. "Nonlinear dynamics of a compact and multistable mechanical energy harvester", *International Journal of Mechan-*

ical Sciences, v. 262, pp. 108731, 2024. ISSN: 0020-7403. doi: 10.1016/j.ijmecsci.2023.108731. Available at: <https://www.sciencedirect.com/science/article/pii/S0020740323006331>.

- COSTA, L. G., MONTEIRO, L. L. S., SAVI, M. A. "Multistability investigation for improved performance in a compact nonlinear energy harvester", *Journal of the Brazilian Society of Mechanical Sciences and Engineering*, v. 46, n. 4, pp. 212, mar. 2024. ISSN: 1806-3691. doi: 10.1007/s40430-024-04766-5. Available at: <https://doi.org/10.1007/s40430-024-04766-5>.

- COSTA, L. G., SAVI, M. A. "Pendulum-based hybrid system for multidirectional energy harvesting". *Nonlinear Dynamics*, 2024, doi: 10.1007/s11071-024-10040-z, accepted for publication.

- COSTA, L. G., SAVI, M. A. "Complex nonlinear dynamics of a multidirectional energy harvester with hybrid transduction", *Smart Materials and Structures*, in review.

In addition, there are 8 more national and international conference publications that included preliminary results for the final version of this document.

1.1 Layout of the Thesis

This thesis is organized into seven main chapters and one appendix chapter. This first chapter introduces the work, emphasizing its motivations, objectives, contributions and overall organization.

Chapter 2 provides a historical overview of the evolution of mechanical energy harvesters, supported by the theoretical foundations behind the main transduction mechanisms, and the most common nonlinear modulations used to enhance performance in this field.

Chapter 3 formalizes the nonlinear dynamics framework applied throughout the entirety of this thesis. Brief explanations of classical nonlinear dynamics theories are presented, along with a depiction of the methodologies developed to deeply analyze nonlinear mechanical energy harvesters.

Chapter 4 provides a brief generalization of the modeling of nonlinear symmetric multistable systems utilizing polynomials.

Chapter 5 introduces the design concepts behind the proposed compact multistable energy harvester. A reduced-order model is, then, presented to describe the main characteristics of the structure. An initial analysis is conducted to characterize the stability of the system and identify parameters that can alter its stability

properties. Subsequently, a comprehensive overview analysis of the system is conducted aimed at understanding its main qualitative dynamical traits and identifying the conditions in which the harvester achieves the best performances. Furthermore, a comparison between the proposed system and the classic bistable harvester is performed, highlighting its potential to be employed in compact spaces.

Chapter 6 discusses the incorporation of pendulum structure into conventional energy harvester designs to achieve multidirectional capabilities. A generic archetype model is introduced to examine the fundamental characteristics of this type of harvester. The initial analysis encompasses three configurations to determine the feasibility of employing pendulum structures for multidirectional energy harvesting. Then, a general parametric analysis of the system is performed to determine the most and the least favorable combination of structural parameters in terms of energy harvesting capacity. Additionally, the dynamical responses and patterns associated with high performance are identified. These responses are often characterized by a blend of irregular complex behaviors, coupled with a mix of oscillatory and rotational patterns of motion, resulting in wider bandwidths.

Chapter 7 summarizes the outcomes of this work, draws conclusions from the preceding chapters, and offers recommendations for potential future research within the thematic scope of this thesis.

Lastly, Appendix A presents the theory behind elementary symmetric polynomials used to generalize the modeling of multistable systems, Appendix B presents the main algorithms utilized in this work and some of their limitations, and Appendix C presents the procedure to normalize the dynamical systems proposed in this work.

Chapter 2

Literature Review

This chapter is dedicated to performing a brief historical review of the development of mechanical energy harvesters and the mechanisms of energy conversion used in these systems.

2.1 Transduction Mechanisms

A transducer is a device, component, or material that converts one form of energy into another. In the context of engineering and physics, a transducer is commonly used to convert a physical quantity, such as mechanical displacement, pressure, temperature, or light intensity, into an electrical signal, or vice-versa. This conversion allows for measurement, detection, or transmission of the physical quantity in a more convenient or usable form. In other words, they are the core mechanisms used in energy harvesting systems that directly or indirectly couple the mechanical physical domain to the electrical physical domain.

There are many types of transduction mechanisms used in mechanical energy harvesting systems including piezoelectricity, electromagnetic induction, triboelectricity, magnetostriction, flexoelectricity, piezomagnetism, and magnetoelectricity. The following subsections are devoted to describing the working mechanism of the most common ones found in the literature. Towards the end, Table 2.1 is presented outlining the strengths and weaknesses of each main mechanism, demonstrating that the choice of which to use depends on the specific application.

2.1.1 Piezoelectricity

Piezoelectricity is a naturally occurring phenomenon observed in certain crystals. It involves the electromechanical relationship between mechanical deformation and electrical voltage. The effect was discovered around 1880 by the brothers Jacques and Pierre Curie, who experimentally demonstrated that an electrical voltage would

emerge on the surface of specific crystalline materials when subjected to mechanical deformation. In the subsequent years, it was revealed that the reverse of this effect also took place [69]. These phenomena were called the direct and inverse piezoelectric effects, respectively, and are illustrated in Figures 2.1 and 2.2.

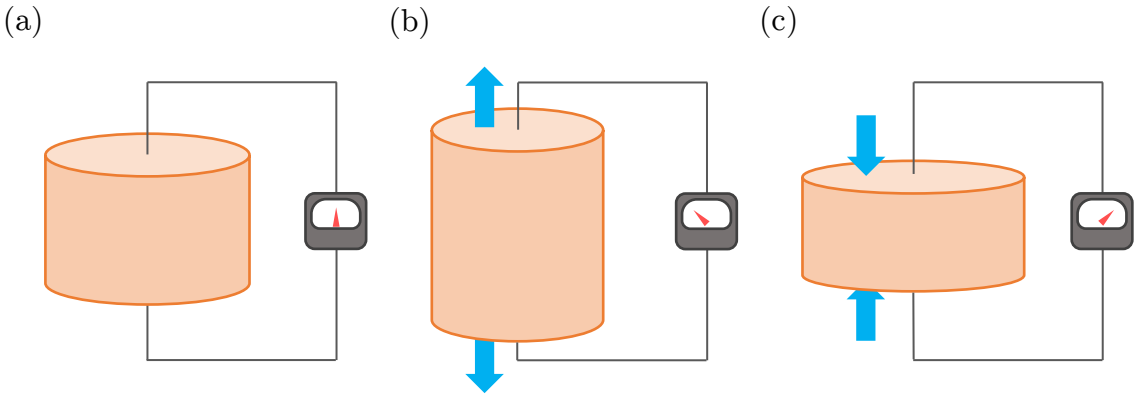

Figure 2.1: Direct piezoelectric effect. Material (a) at rest, (b) subjected to a mechanical tensile stress, (c) subjected to a mechanical compression stress.

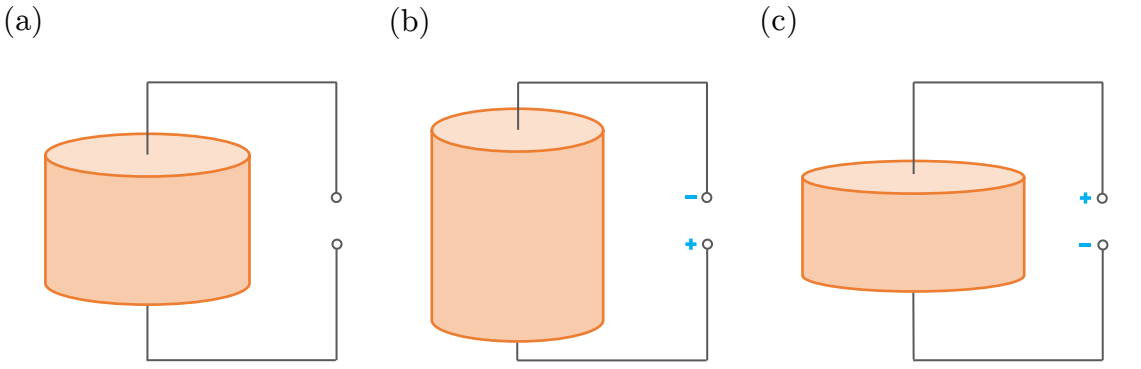

Figure 2.2: Inverse piezoelectric effect. Material (a) at rest, (b) subjected to an electrical voltage, (c) subjected to an electrical voltage of opposite polarity.

Despite piezoelectricity having been observed in natural crystalline materials such as tourmaline, quartz, Rochelle salt, and topaz, its effects were relatively weak. It was only in the mid-20th century that synthetic piezoelectric materials emerged, enabling practical applications due to their high degree of electromechanical coupling [70]. Some of these materials are illustrated in Figure 2.3, and for a more complete list of piezoelectric materials refer to [71].

The typical manufacturing process of synthetic piezoelectric ceramics begins with a mixture of base materials in powder form. The materials are heated to a temperature range of $T = 1200°\text{C}$ to $T = 1500°\text{C}$ (above the Curie temperature, T_C) and shaped into the desired geometry. In this form, the material doesn't yet exhibit

Figure 2.3: Natural piezoelectrics: Quartz, human bone, and topaz. Synthetic: PZT (*Lead Zirconate Titanate*) and PVDF (*Polyvinylidene Fluoride*), respectively.

strong piezoelectric characteristics due to the misaligned orientation of its electric dipoles. The piezoelectric effect is associated with the quantity of electric dipoles present in the material and their alignment. Therefore, through the process known as Poling, the electric dipoles of the raw material are reoriented to remain relatively aligned, resulting in a strong electromechanical coupling [72].

The Poling process involves applying a strong electric field to the material, as depicted in Figure 2.4. Firstly, the material is heated to temperatures above the Curie temperature, followed by the application of a strong electric field to the material, causing the alignment of its electric dipoles in the direction of the field. Subsequently, the temperature is rapidly reduced, and the electric field is removed, maintaining the alignment of the material's electric dipoles.

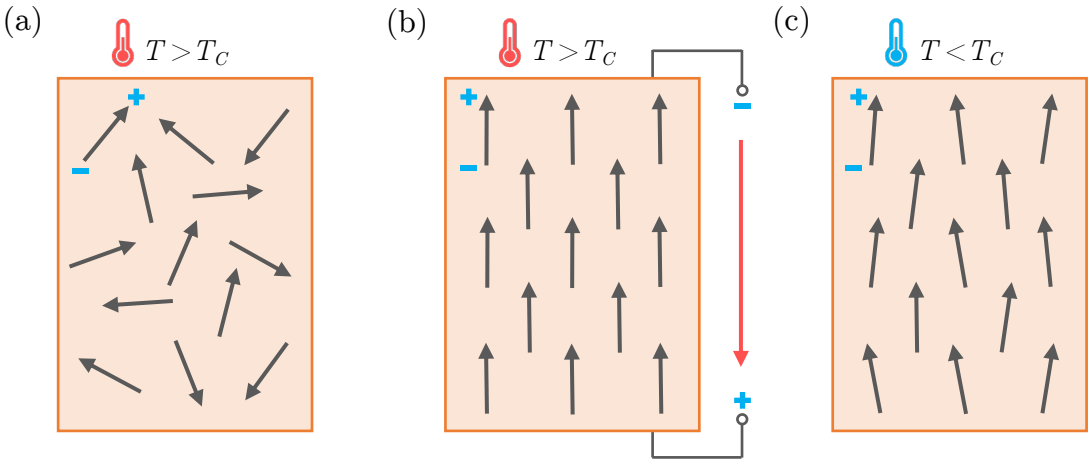

Figure 2.4: Polarization process in synthetic piezoelectrics. (a) Heating the material above the Curie temperature, T_C; (b) Application of a strong electric field; (c) Rapid cooling of the material and removal of the electric field.

In microstructural terms, the piezoelectric effect arises from atomic misalignment, resulting in polarization among the atoms. Figure 2.5 illustrates this behavior for a crystallographic structure of PZT (Lead Zirconate Titanate), one of the main materials utilized in energy harvesting applications.

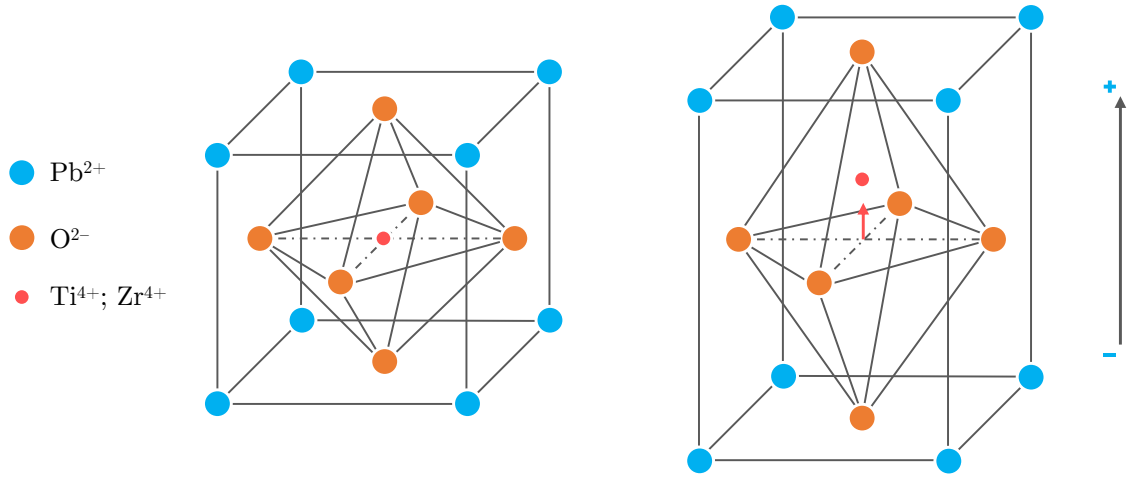

Figure 2.5: PZT unit cell at rest, and subjected to an electric field or strain, respectively, resulting in the atomic misalignment, which produces a polarization among the atoms.

For high-efficiency energy harvesting purposes, the direct piezoelectric effect of synthetic materials is exploited, and through the application of the principles of thermodynamics and the continuum hypothesis, the behavior of linear piezoelectric materials is explained by Equations 2.1 and 2.2 [73].

$$\mathbf{S} = \mathbf{s}^E \, \boldsymbol{\sigma} + \mathbf{d}^T \, \mathbf{E} \tag{2.1}$$

$$\mathbf{D} = \mathbf{d} \, \boldsymbol{\sigma} + \boldsymbol{\varepsilon}^\sigma \, \mathbf{E}. \tag{2.2}$$

The stress ($\boldsymbol{\sigma}$), the strain ($\mathbf{S}$), the electric field ($\mathbf{E}$), and the electric displacement ($\mathbf{D}$) constitute the field variables, while the elastic compliance tensor ($\mathbf{s}$), piezoelectric constant tensor ($\mathbf{d}$), and dielectric tensor ($\boldsymbol{\varepsilon}$) represent pertinent coefficients. Superscripts $\square^E$ and $\square^\sigma$ indicate their assessment under constant electric field and constant stress conditions, respectively, while $\square^T$ denotes the transpose operation.

In fact, four standard forms exist for the constitutive equations of linear piezoelectric materials. Of these, the formulation encapsulated in Equations 2.1 and 2.2 stands out as the preferred paradigm for piezoelectric constitutive equations in bounded media and, correspondingly, for the context of energy harvesting. This choice is motivated by the ability to eliminate specific stress components depending on the geometry, as well as particular electric field components dependent on electrode placement.

2.1.2 Electromagnetic Induction

In 1831, Michael Faraday conducted a series of experiments and observed that when a wire and a magnet move relative to each other, the change in the magnetic

flux results in a current being induced to the wire, thus generating a voltage [74]. This is known as Faraday's law of induction. Figure 2.6 illustrates this behavior: when the velocity, v_m, of the magnet, is zero, no voltage is produced. On the other hand, when $v_m > 0$, a proportional voltage is produced.

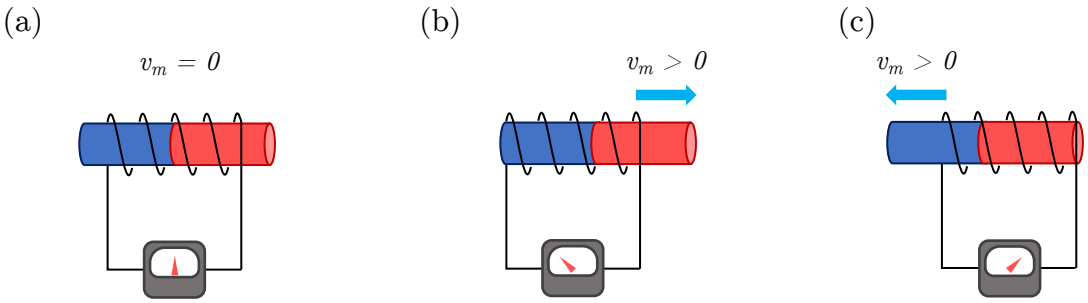

Figure 2.6: Electromagnetic induction. (a) A stationary magnet near a coil or wire does not change the magnetic flux through the coil, resulting in no induced current. (b) and (c) A moving magnet near a coil or wire changes the magnetic flux through the coil, inducing a current. The signal of the current/voltage is associated with the direction of the magnet's movement.

Later, in 1865, this behavior was fully analytically explained by James Clerk Maxwell [75], which states that:

$$v(t) = \oint_{\partial S} \mathbf{E} \cdot d\mathbf{l} = -\int_S \frac{\partial \mathbf{B}}{\partial t} \cdot d\mathbf{A} = -\frac{d\Phi_B(t)}{dt}, \tag{2.3}$$

where $v(t)$ is the voltage produced, $\mathbf{E}$ is the electric field, $\mathbf{B}$ is the magnetic induction, Φ_B is the magnetic flux, S is a surface bounded by the closed contour ∂S, $d\mathbf{l}$ is an infinitesimal vector of the contour ∂S, and $d\mathbf{A}$ is an infinitesimal vector element of the surface S. A negative sign arises due to Lenz's law, which ensures energy conservation. It is also possible to represent Faraday's law in differential form by applying Stoke's theorem, as shown by Equation 2.4.

$$\nabla \times \mathbf{E} = -\frac{\partial \mathbf{B}}{\partial t} \tag{2.4}$$

By extension, one can define the magnetic flux linkage, $\psi(t)$, as the change in magnetic flux in a coil of N_c turns as $\psi(t) = N_c \Phi_B$. This means that Faraday's law

can also be represented in terms of the flux linkage as depicted by Equation 2.5.[1]

$$v(t) = -\frac{d\psi(t)}{dt} = -N_c \frac{d\Phi_B(t)}{dt} \tag{2.5}$$

2.1.3 Triboelectric Effect

The triboelectric effect is the phenomenon wherein electric charges accumulate as a result of the contact and subsequent friction between two different materials, that is, a coupling effect of contact electrification and electrostatic induction caused by the potential difference of two materials [77].

Despite triboelectrification being a common phenomenon observed in nature, the actual mechanisms behind its effect within the microstructure domain are still not very clear. The phenomenon involving the establishment of chemical bonds at the interfaces of distinct contacting materials, accompanied by the migration of charges driven by disparate electron affinities, is commonly acknowledged. The transferred charges between two materials can be molecules, ions, and electrons. Upon disengagement, certain bonded atoms exhibit a propensity to retain the acquired electrons, while others tend to relinquish them. This can lead to opposite charges on the surfaces of the respective materials that were in contact. The resulting opposing charges on the contacting surfaces give rise to a triboelectric potential, which, in turn, can cause electrons in the underlying material to move in order to balance out the created difference in electric potential [78, 79]. This process is illustrated in Figure 2.7.

Regarding the macroscopic domain, the theoretical basis of the triboelectric effect is constituted by Maxwell's displacement current [80], $\mathbf{J}_D$, which is defined by Equation 2.6.

$$\mathbf{J}_D = \frac{\partial \mathbf{D}}{\partial t} = \varepsilon_0 \frac{\partial \mathbf{E}}{\partial t} + \frac{\partial \mathbf{P}}{\partial t} \tag{2.6}$$

where $\mathbf{E}$ is the electric field, $\mathbf{D}$ is the electric displacement field, $\mathbf{P}$ is the polarization field density, ε_0 is the vacuum permittivity.

In the context of a conventional isotropic media, the relationship $\mathbf{P} = (\varepsilon - \varepsilon_0)\,\mathbf{E}$ governs, yielding $\mathbf{D} = \varepsilon \mathbf{E}$, with ε representing the permittivity of the dielectric material. Consequently, the displacement current becomes $\mathbf{J}_D = \varepsilon\,(\partial \mathbf{E}/\partial t)$.

In contrast, in media characterized by the existence of surface polarization charges (typical of piezoelectric and triboelectric materials), the impact of polarization density originating from surface electrostatic charges on the displacement current cannot be ignored [81]. As such, the expression takes the form represented

[1] In the case of inductance, the definition of magnetic flux and magnetic flux linkage can be treated as equivalent for convenience in engineering disciplines. However, this is not true, especially for memristors, which are the fundamental nonlinear circuit elements [76].

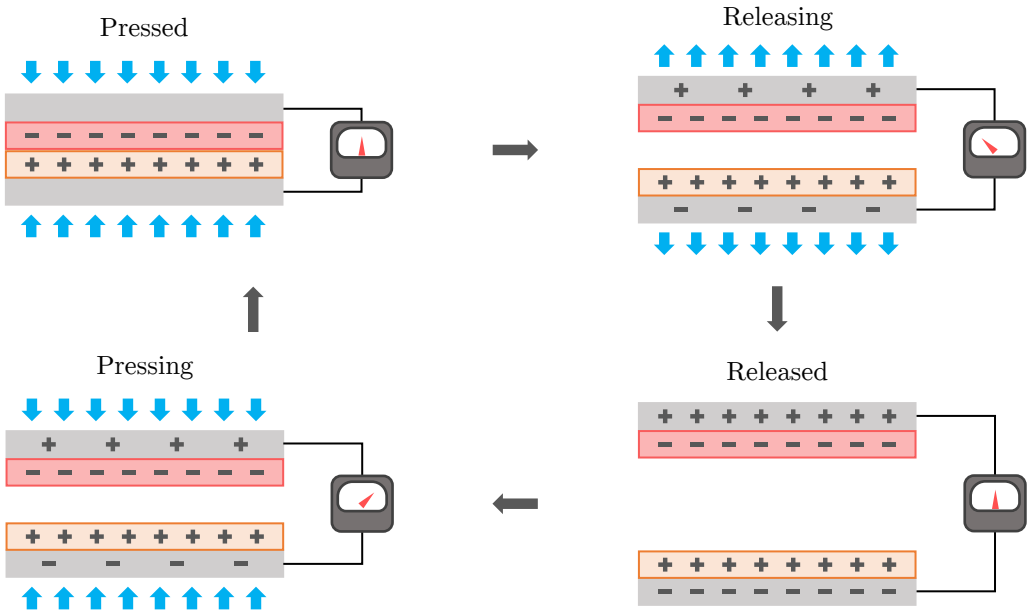

Figure 2.7: Triboelectric effect in a vertical contact-separation triboelectric energy harvester. Electrodes are represented in gray, while the tribopositive and triboneg-ative distinct materials are represented in orange and red, respectively.

in Equation 2.7

$$\mathbf{J}_D = \frac{\partial \mathbf{D}}{\partial t} = \varepsilon \frac{\partial \mathbf{E}}{\partial t} + \frac{\partial \mathbf{P}_S}{\partial t}. \tag{2.7}$$

Here, the first term signifies the current induced by the dynamic electric field, while the second term represents the current arising from the polarization field generated by surface electrostatic charges, denoted as $\mathbf{P}_S$. Notably, the latter term constitutes the foundation premise of triboelectric energy harvesters (TEHs). In essence, TEHs embody the practical implementation of displacement current within the domain of energy conversion and sensing.

Based on this concept, four operational modes have been developed to align with different applications, as visually presented in Figure 2.8. The vertical contact-separation mode (VCS) involves inducing current through the vertical motion of both layers. In the contact-sliding mode (CS), current induction arises from the lateral friction occurring between the two material layers. The single electrode mode (SE) triggers current by intermittently engaging a single material with an electrode. Meanwhile, the freestanding triboelectric-layer mode (FTL) operates with a solitary layer, intermittently contacting various electrodes laterally. Notably, the VCS and FTL modes predominantly find application in rotational contexts, whereas the CS and SE modes find utility in other scenarios. It is noteworthy that these modes can be synergistically used within a singular application context [82].

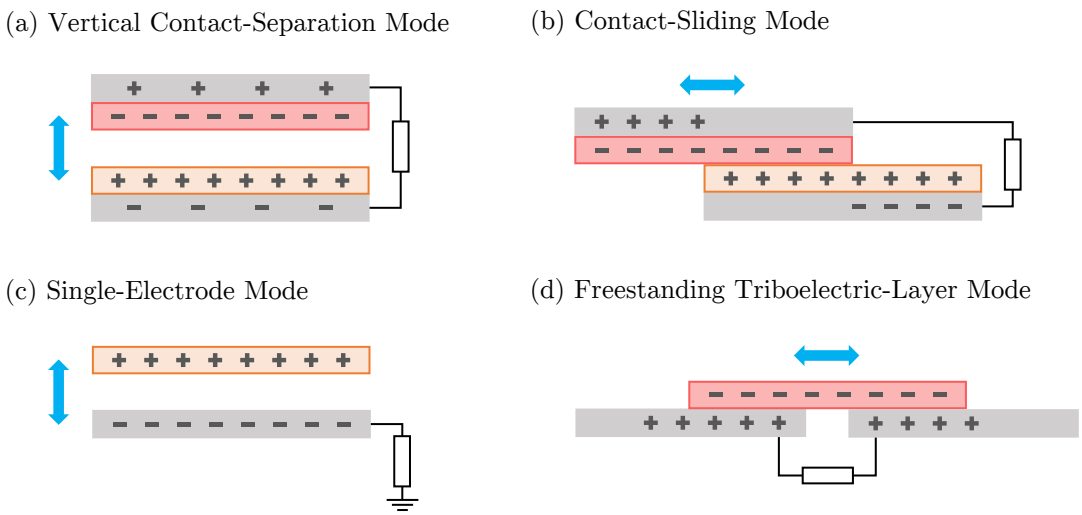

Figure 2.8: Triboelectric modes. (a) Vertical Contact-Separation Mode (VCS), (b) Contact-Sliding mode (CS), (c) Single-Electrode mode (SE), and (d) Freestanding Triboelectric-Layer mode (FTL).

TEHs encompass a broad spectrum of materials, spanning from organic sources such as silk, wool, and cotton, to engineered synthetics like peptide, polyamide, polyester, polydimethylsiloxane, polyvinylchloride, and polytetrafluoroethylene. Additionally, TEHs incorporate commonly employed metals like aluminum, copper, and iron, as well as semiconductors including SiO2, TiO2, and silicon [83]. Also, liquid metals, such as mercury (Hg) can be used as a tribopositive layer [84]. A subset of these materials is visually depicted in Figure 2.9, while a more complete compilation can be found in [82] for reference.

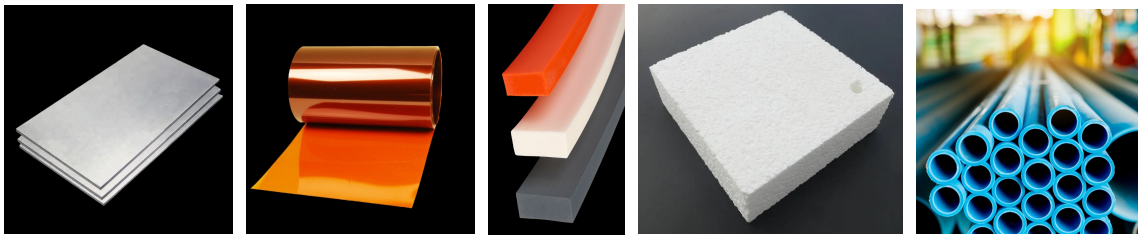

Figure 2.9: Some common materials that can be employed for triboelectric energy harvesting. From left to right: Aluminium, Kapton (*Polyimide*), different types of Rubber, Polystyrene, and PVC (*Polyvinyl Chloride*).

2.1.4 Magnetostriction

The magnetostrictive effect is a phenomenon exhibited by specific materials in which a change in length occurs when they are exposed to a magnetic field. The

first observation of this phenomenon was documented in 1842 by James Prescott Joule during his experimentation with the effects of a magnetic field on a piece of iron [85]. Subsequently, Emilio Villari discovered the reciprocal effect, wherein applying stress to a magnetostrictive material subjected to a magnetic field alters its magnetization. This phenomenon is now recognized as the inverse magnetostrictive effect, magnetoelastic effect, or Villari effect.

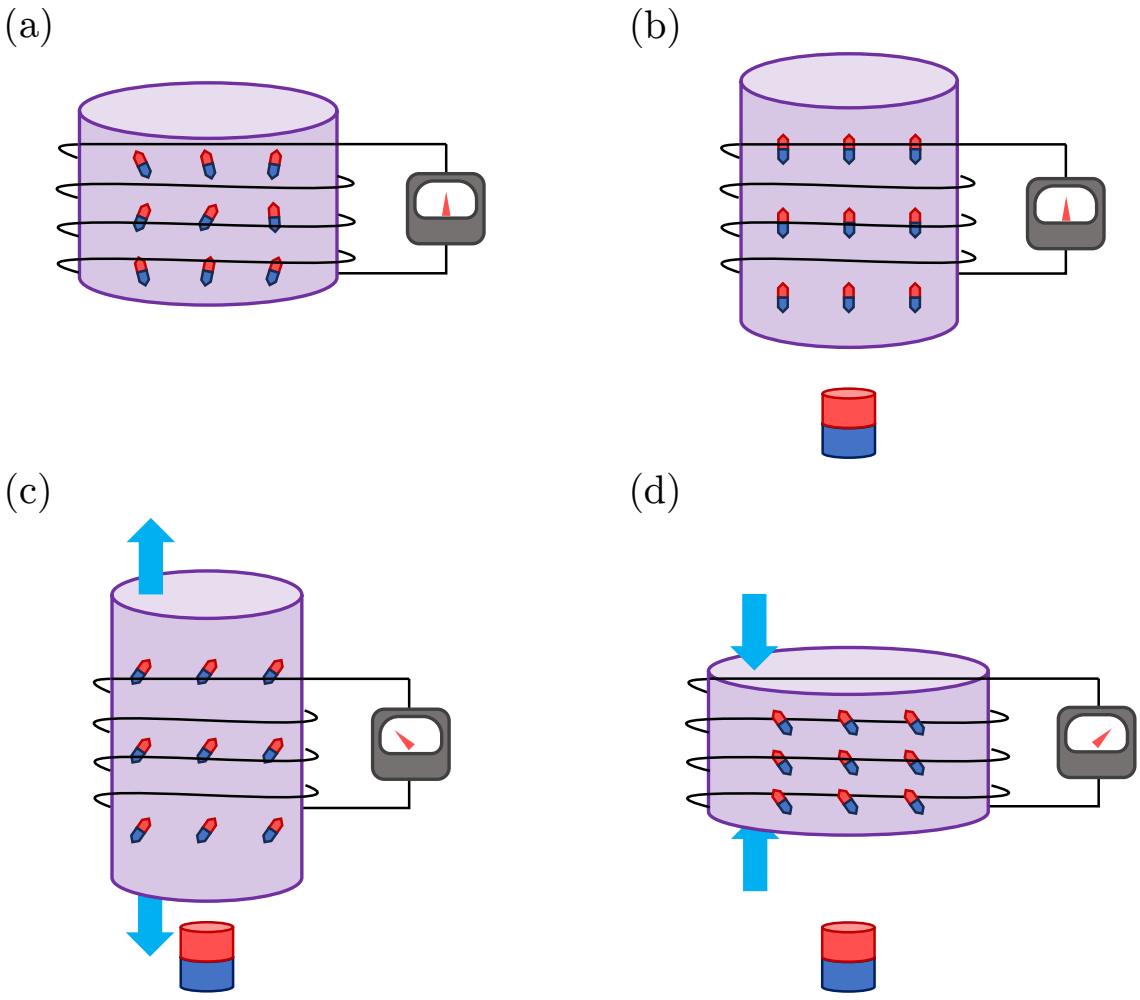

Figure 2.10: Villari effect in a magnetostrictive material. (a) Initially, the magnetic domains within the material are randomly oriented. (b) When a magnetic field is introduced, the magnetic domains align, causing slight deformation. (c) Applying tensile stress deforms the material and reorients the magnetic domains, inducing a current in the external circuit. (d) Applying compressive stress also deforms the material and reorients the magnetic domains, inducing a current with opposite polarity in the external circuit.

Figure 2.10 visually portrays the Villari effect, depicting the arrangement of magnetic domains within the magnetostrictive material. When the material is at

rest, its magnetic domains exhibit arbitrary orientations. Upon the placement of a magnet in proximity to the magnetostrictive material, these domains align with the biased magnetic field's direction, leading to a minor deformation. The application of compressive or tensile stress on the material prompts a rotation of its magnetic domains, consequently inducing alterations in the surrounding magnetic field. Following Maxwell's equations, this transformation induces a current within the coil surrounding the material, which can be harnessed for energy-harvesting purposes.

Through the application of the fundamental principles of thermodynamics and considering the continuum hypothesis, Equations 2.8 and 2.9 serve as models for characterizing the behavior of linear magnetostrictive materials [86].

$$\mathbf{S} = \mathbf{s}^H \ \boldsymbol{\sigma} + \mathbf{d}_m^T \ \mathbf{H} \tag{2.8}$$

$$\mathbf{B} = \mathbf{d}_m \ \boldsymbol{\sigma} + \boldsymbol{\mu}^\sigma \ \mathbf{H} \tag{2.9}$$

In these expressions, $\mathbf{H}$ and $\mathbf{B}$ correspond to the magnetic field and magnetic induction tensors, respectively, while $\mathbf{S}$ and $\boldsymbol{\sigma}$ stand for the strain and stress tensors. The parameter $\mathbf{s}$ denotes the pure linear elastic compliance matrix, $\boldsymbol{\mu}$ represents the linear magnetic permeability matrix, and $\mathbf{d}_m$ symbolizes the piezomagnetic constant matrix. $\square^H$ and $\square^\sigma$ denotes that the variable is measured at constant magnetic field and stress, respectively. $\square^T$ stands for the transpose [87, 88].

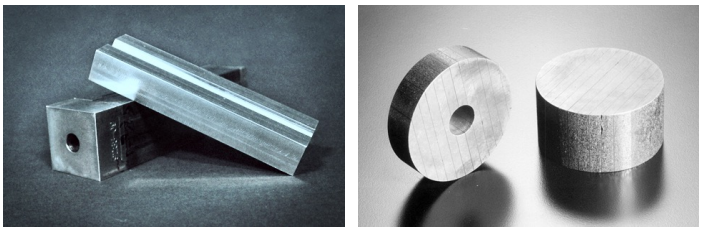

Figure 2.11: Synthetic magnetostrictive materials. Galfenol and Terfenol-D, respectively.

Similar to the scenario observed in piezoelectricity, only synthetic materials are feasible candidates for energy harvesting purposes. Figure 2.11 shows two prevalent magnetostrictive materials employed within the field of energy harvesting: Galfenol and Terfenol-D. Notably, these materials exhibit a noteworthy magneto-mechanical coupling coefficient, which renders them prominent choices for application in energy harvesting contexts.

Table 2.1: Advantages and disadvantages of the main transduction mechanisms found in the literature.

Transduction	Advantages	Disadvantages
Piezoelectricity [11, 77, 89–91]	• High power density • Easy to manufacture • 3D deposition in any shape • Compact • Lightweight • High durability • Environment friendly • Can be directly integrated into MEMs • Biocompatibles (some materials)	• Functional fatigue (depolarization) • Material fatigue • Energy converted limited to small electronics or small urban centers
Electromagnetic Induction [89, 92–95]	• Energy conversion in any scale • Energy converted is proportional to coil turns • Does not rely on any special material properties	• Low power density • Bulk structure due to magnets and coils • Heavyweight • May be interfered with by other electromagnetic waves
Solid Triboelectricity [89, 96–98]	• High power density • Compact • High efficiency • Low cost • Easy to manufacture • Lightweight • Environment friendly • Wide range of material choices	• Energy converted limited to small electronics • Limited knowledge of triboelectric physical mechanisms • Mechanical wear over time
Liquid Triboelectricity [84, 99]	• All the solid triboelectricity advantages • Shape adaptability • No mechanical wear • High electron mobility	• Energy converted limited to small electronics • Limited knowledge of triboelectric physical mechanisms
Magnetostriction [87, 100]	• High power density • No functional fatigue (no depolarization) • Large coupling coefficient • Energy converted is proportional to coil turns	• Material fatigue • Bulk structure due to magnets and coils • May be interfered with by other electromagnetic waves

2.2 Mechanical Energy Harvesters

Mechanical energy harvesters usually consist of three main parts: the main structure, the transducer, and the circuit. The transducer is typically attached to the main structure, which acts as an energy bridge between the surroundings and the transducer. The transducer then connects the main structure to the circuit. In this process, energy moves in two directions, but some energy is lost due to heat, damping and other factors. As a result, a portion of the initial mechanical energy is transformed into electrical energy by the system. This electrical energy is collected by the circuit at the end of this process, as depicted in Figure 2.12.

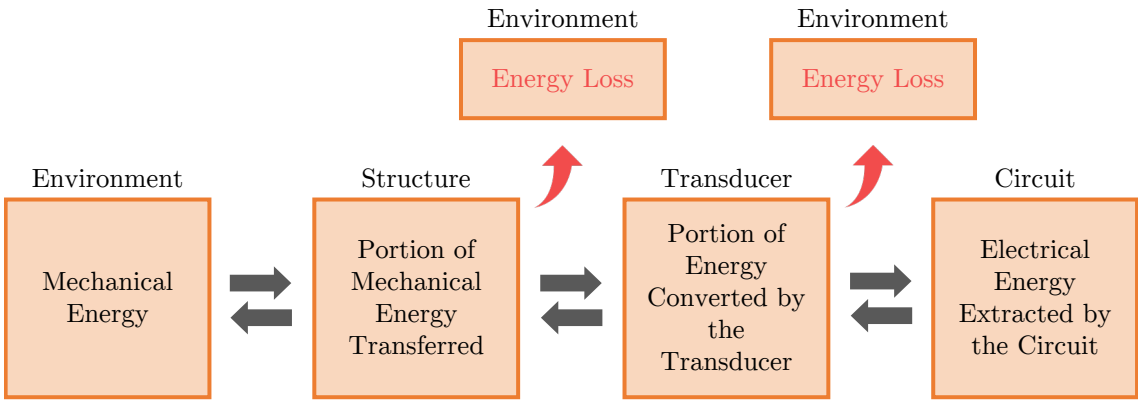

Figure 2.12: Energy flow in the mechanical energy harvesting process.

In terms of efficiency in real applications, the hybridization strategy of mechanical energy harvesters utilizing different types of transducers is a trend in literature. By combining different types of transducers, the hybridization approach can exploit the unique advantages of each transducer, resulting in a greater energy harvesting capacity. Depending on the combination of transducers, various applications can be realized. For instance, CHUNG *et al.* [101] utilized a Kresling origami structure that combined rotational triboelectric and piezoelectric/triboelectric nanoconverters in contact mode. This innovative approach allowed the structure to take advantage of the rotational movement, the generated strain and contact, resulting in a better energy harvesting performance. Similarly, ZHONG *et al.* [102] utilized both electromagnetic and triboelectric transducers to build a hybrid energy harvester based on rotation to scavenge biomechanical energy as a mobile power source. EGBE *et al.* [103] employed three different transduction mechanisms to enhance the conversion of wind energy to electrical energy through a rotational device to power sensors. Other researchers have also reported the use of various hybrid devices showing improved performance through the utilization of different conversion strategies [104–107]. By leveraging the benefits of multiple transducers, hybrid energy harvesters can pave the way for more efficient and practical energy harvesting solutions.

Despite the transducer mechanism, the host structure itself exerts a major influence on the performance of the energy harvester. The choice of a proper structural design configuration is an essential point. The designs found in the literature can be classified into two main types: resonators and non-resonators. Resonator-type energy harvesters are generally highly efficient when operating within a limited frequency range, whereas non-resonant energy harvesters typically achieve higher efficiency at higher excitation frequencies. This characteristic renders resonant energy harvesters particularly well-suited for applications involving low frequencies. Within the scope of this study, particular emphasis is placed on energy harvesters of the

resonator variety.

The archetypal resonant energy harvesting structure is based on design containing beams, especially cantilever beams [108]. Many efforts have been made to fully model and experimentally validate this type of design, making the cantilever arrangement one of the most common designs found in the literature [109–111]. Figure 2.13 illustrates some configurations of a cantilever-type piezoelectric energy harvester. The significant shortcoming of this design is the lack of efficiency when operating at frequencies that deviate significantly from its natural frequency. Under these conditions, the harvester deflection tends to decrease, resulting in low electrical output and limiting its application [112]. This drawback leads researchers to insert mechanical modulations in this design to enhance its performance.

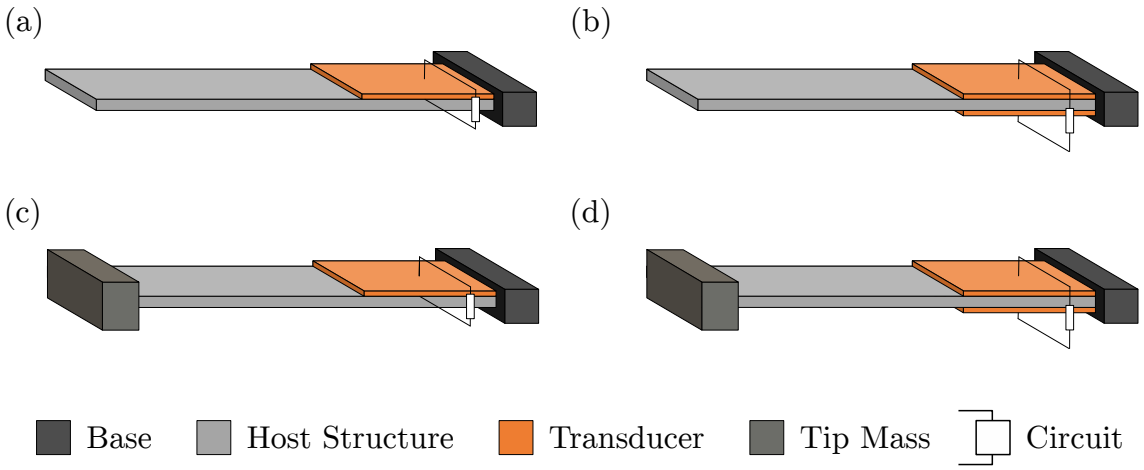

Figure 2.13: Piezoelectric mechanical energy harvester cantilever designs: (a) Simple unimorph design, (b) simple bimorph design, (c) unimorph design with a tip mass, and (d) bimorph design with a tip mass.

The evolution of the cantilever design has led to the incorporation of additional mechanical degrees-of-freedom (DoF) to operate in the parallel direction of the external input excitation, creating an additional efficient operating region [113]. This progression led to the design proposed by WU *et al.* [1], which consists of an outer beam and an inner beam, as shown in Figure 2.14a. This configuration brings the first two natural frequencies closer together, thereby creating a larger operating region for the harvester and rendering the 2-DoF cantilever-based system more compact.

The improvement of the cantilever system has also led to the incorporation of nonlinear characteristics. A variety of nonlinear modulations have been proposed, and new ones continue to be proposed to this day [114, 115]. In this regard, nonlinear energy harvesters are highly effective in delivering broadband performance, making them well-suited for general applications. Multistable energy harvesters, as

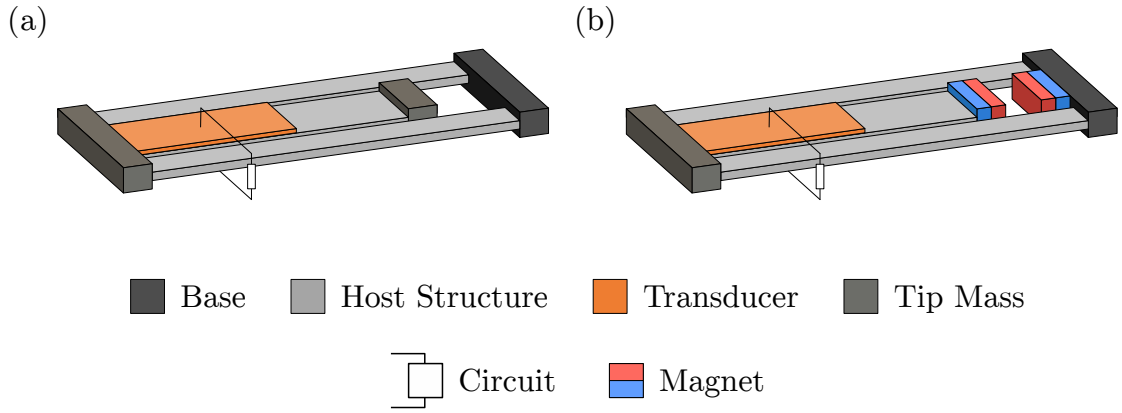

Figure 2.14: Representation of dual-beam cantilever-based energy harvester structures, which can be approximated as 2 DoF structures. (a) The compact structure proposed by WU *et al.* [1]. (b) The nonlinear bistable compact structure proposed later by WU *et al.* [2].

the name suggests, belong to a class of systems that exhibit multiple stable positions. This approach has proven to be effective as it increases the deflection of the system, enhancing its energy harvesting capabilities. Various techniques can be employed to achieve multistability, such as incorporating magnetic interactions [116], spring actuation [117], gravity effects [118], and inducing the mechanical buckling by axial forces [119] or magnetic induced buckling [120]. As far as this is concerned, researchers have extensively studied the potential of multistability in one-degree-of-freedom systems, exploring different configurations including bistable [65, 121], tristable [122, 123], tetrastable [124, 125], and pentastable [126, 127] systems. The problem of adding more stable positions is the creation of a potential energy barrier, which can reduce its performance depending on the level of the input excitation. Generally, the literature shows that increasing the number of stable positions can reduce this barrier.

The construction of multistable harvesters involves various aspects, such as the position and angle of the magnets, as well as potential asymmetries, which are crucial considerations. KUMAR *et al.* [128] revealed the potential benefits of employing a monostable asymmetric nonlinear system in specific cases, surpassing the symmetric bistable system. WANG *et al.* [129] demonstrated that the utilization of an asymmetric bistable potential negatively impacts energy harvesting capacity when the system dynamics originate from the vicinity of the deeper equilibrium point. However, if an initial condition is established near the shallower energy well, performance can be improved. CAO *et al.* [130] established that modifying the angle of the magnets responsible for inducing bistability can significantly alter the dynamics of the classical bistable energy harvester. Furthermore, NORENBERG *et al.* [131] demonstrated that adjusting the slope angles of magnets can effectively counteract

the adverse effects of a bistable asymmetric potential.

Another strategy is to exploit non-smoothness, for example, incorporating impacts into the system. This idea increases the system bandwidth but at the cost of reducing its maximum output power [132]. This approach is well-suited for scenarios where the ambient mechanical excitation exhibits a wide range of frequencies. The disadvantage is that the non-smoothness can cause mechanical wear over time, leading to structural damage in long-term applications [133]. In addition, flow/vortex-induced energy harvesters are also explored, where the input excitation is mainly (but not always) provided by fluids interacting with a bluff body with different geometries [134–137], including asymmetric designs [138], metasurfaces [139]. It is also possible to concurrently harness base excitation and wind excitation with this type of nonlinear modulation [140], and combine magnetic-induced multistability with this type of harvester [141–144].

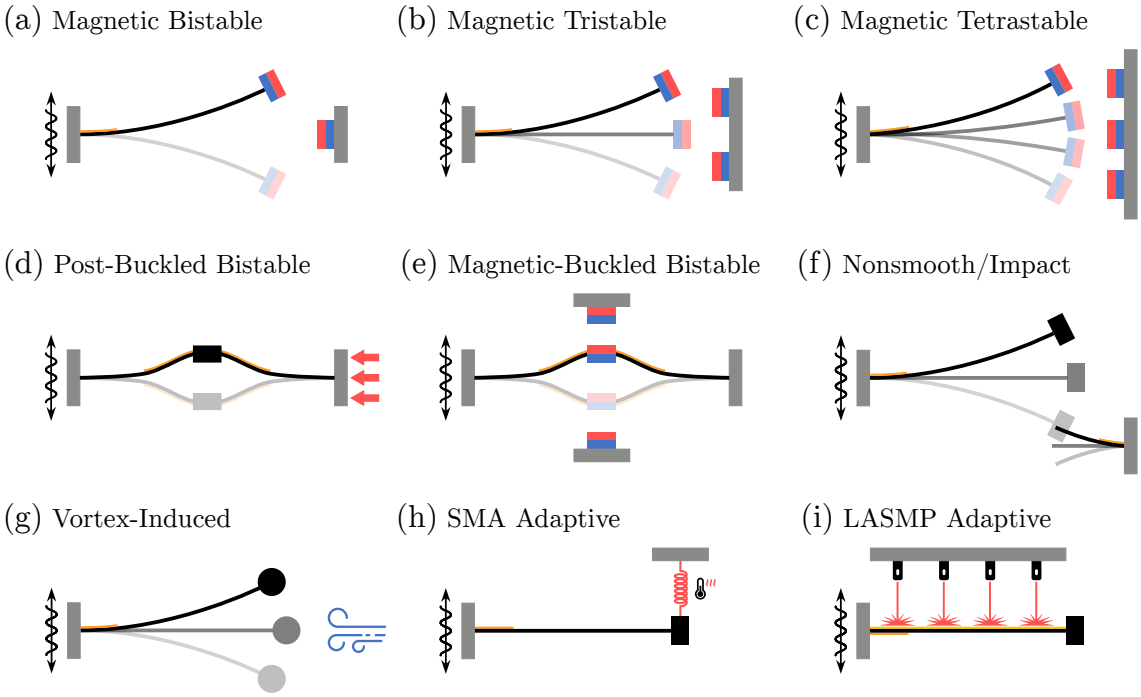

Figure 2.15: Some nonlinear modulations incorporated into the cantilever design. Letters (a), (b) and (c) are multistable devices induced by magnetic interactions. Letters (d) and (e) are buckled bistable systems induced by compressive forces and magnetic attraction, respectively. (f) A system with impact. (g) Vortex-induced energy harvester, which has vibration and wind as energy input. (h) and (i) are adaptive systems using synergistic usage of shape memory materials to change the natural frequency of the system: the first is a shape memory alloy spring that can change its natural stiffness by thermomechanical induced phase transformation, and the last is a light-activated shape memory polymer that can modify its stiffness by light-induced change of its molecular chains structures and connections.

New ideas for nonlinear modulations are still being developed. The synergis-

tic use of smart materials is one possibility and two interesting designs make use of shape memory materials to achieve adaptability in energy harvesting systems. ADEODATO *et al.* [145] employed a Nitinol Shape memory alloy (SMA) spring attached to the free end of the cantilever beam to alter the natural frequency of the energy harvesting system by controlling the temperature. YUAN *et al.* [146] proposed a strategy of using a light-activated shape memory polymer (LASMP) layer attached to the cantilever beam to control the natural frequency of the structure. In this case, the Young modulus of the LASMP can be adjusted according to the level of light exposure. Finally, a quasi-zero-stiffness energy harvester was presented by MARGIELEWICZ *et al.* [147], which is characterized by an almost flat potential energy function, countering the drawbacks of multistable classical systems. However, the disadvantage of this method is that the quasi-zero module is composed of three springs attached to the free end of the cantilever beam, making it difficult to set up and potentially not a compact solution. Furthermore, some mechanical modulations incorporated on cantilever-based energy harvesters described in this chapter are illustrated in Figure 2.15.

Novel designs have also been presented in the literature. CAETANO & SAVI [148] proposed a pizza-shaped system exploiting multiple degrees of freedom and obtaining a broadband device, where it was concluded that irregular structures are the most effective for enhancing energy harvesting capacity. Afterward, CAETANO & SAVI [149] proposed a star-shaped device coupled with inertial pendulum-like masses that provides either broadband characteristics or multidirectionality. YANG *et al.* [150] suggested an enhancement to the cantilever design by incorporating an arc-shaped segment that significantly improved its performance, and ZHOU *et al.* [151] developed a distributed parameter model of this new harvester. Subsequent works studied the incorporation of various types of multistability characteristics in this type of structure with static [152–154] and variable potential aspects [155]. Nonlinear frequency-up conversion mechanisms [156, 157] showed to be capable of converting a low-frequency external excitation motion into a higher frequency response. In addition, other interesting subjects related to mechanical energy harvesting are associated with nonlinear rotational harvesters [158], metastructures with both vibration suppression and energy harvesting characteristics [159].

The design feasibility is restricted as many of the mechanical energy harvester applications dispose of limited available space. The search for compact and efficient solutions remains a challenge. To address this, WU *et al.* [2] successfully combined the magnetically induced bistable concept with a dual beam compact structure they had previously designed in WU *et al.* [1] to create a bistable dual beam energy harvester with a compact design and good performance. Subsequently, UPADRASHTA & YANG [160] and KRISHNASAMY *et al.* [161] conducted finite element simula-

tions and experiments to validate and formalize a distributed parameter modeling of this design. This new nonlinear compact bistable harvester is illustrated in Figure 2.14b.

Another interesting concept that has been exploited in the literature is the capacity to harvest energy effectively in multiple directions. It has been shown that leveraging pendulum structures to achieve multidirectionality is an interesting and effective solution to achieve this goal. WU *et al.* [162] introduced a piezoelectric spring-pendulum design based on a binder clip structure capable of scavenging ultra-low frequency vibration across multiple directions. Several investigations presented electromagnetic energy harvesters based on pendulum structures used for simultaneous multidirectional vibration mitigation and energy harvesting [163, 164]. Furthermore, the integration of pendulum structures with cantilever-type energy harvesters as a form of nonlinear mechanical modulation has also been explored [165–167]. The advantages and disadvantages of this approach will be discussed in the following chapters. Pendulum structures, when coupled with magnetic interactions between the pendulum's tip mass and its surroundings, have demonstrated the potential for achieving both multidirectionality and multistability within the same system [168, 169]. Lastly, KUMAR *et al.* [170] proposed an electromagnetic energy harvesting concept based on a base-excited double pendulum, designed to harness energy from chaotic motion.

Chapter 3

Nonlinear Dynamics Framework

In Chapter 2, an overview of several solutions for mechanical energy harvesting is presented, with a notable emphasis on nonlinear structures. By examining the literature, it became clear the absence of standardized methods for analyzing and, more critically, comparing nonlinear energy harvesters. The prevalent presence of potentially misleading analyses, which tend to showcase only the favorable attributes of the studied harvester, further increases the challenge of conducting meaningful comparisons with analogous devices. In response to these concerns, this Chapter introduces an integrated set of theories and tools based upon a nonlinear dynamics perspective that forms a robust and comprehensive framework, characterized by classical approaches and newly proposed tools. This approach is designed to facilitate in-depth analyses of mechanical energy harvesters and enable proper comparisons among different configurations. The proposed methodology is adopted in all analyses within the scope of this thesis by utilizing the combination of classical nonlinear dynamics techniques and measures related to energy harvesting performance assessment. By doing so, it is possible to concurrently investigate different (positive and negative) facets of the configurations proposed in this work. A detailed description of all techniques utilized in the framework is elucidated in the next sections.

3.1 Classical Approaches in Nonlinear Analysis

This section presents a comprehensive review of the established nonlinear dynamics methodologies documented in the literature that are employed in this study. It also serves as a foundation for the introduction of the new integrated tools proposed in this work. First, it is important to define the basics of a dynamical system. A dynamical system can be represented by a system of first-order ordinary differential equations of the type

$$\dot{\mathbf{x}}(t) = \mathbf{f}(\mathbf{x}(t)), \quad \mathbf{x}(t) \in \mathbb{R}^n. \tag{3.1}$$

This system can be viewed as a frame-by-frame description of reality, where each frame represents the information of the state of the system at a given instant of time. The dynamics of the system are fully described when the difference between a previous instant of time and the next tends to zero. This system is then called a continuous dynamical system.

Alternatively, a discrete dynamical system can be viewed as a map, that is, a sequence of data of the form $\{\mathbf{x}(t_1), \mathbf{x}(t_2), \cdots, \mathbf{x}(t_{N_p})\}$ that describes some information of the system, where $\{t_1,\ t_2,\ ...,\ t_{N_p}\}$ are discrete N_p points in the time continuum. In this regard, a specific kind of map, known as a Poincaré map, can be defined.

3.1.1 Poincaré Map

A Poincaré map, named after Jules Henri Poincaré (1854 - 1912), can be defined as a subspace of the state space of a n-dimensional dynamical system. This subspace is defined as a section, Σ_p, placed in a transverse position, $\mathbf{x}_p$, to the vector field formed by the response of the system within the state space. For a three-dimensional system, the Poincaré section is a plane, whereas for a n-dimensional system with $n > 3$, the Poincaré section is a hyperplane of dimension $n-1$. Formally, the method to obtain the Poincaré map is to construct a transformation P_p such as

$$P_p : S_p \to \Sigma_p, \tag{3.2}$$

$$\mathbf{x}_p \mapsto \boldsymbol{\varsigma}(\mathbf{x}_p, \tau_p(\mathbf{x}_p)), \tag{3.3}$$

where U_p is the set of points in the state space, τ_p, is the time for the return of $\mathbf{x}_p$ to Σ_p, and $\boldsymbol{\varsigma}$ defines the set of points in the map [171]. This process is illustrated in Figure 3.1.

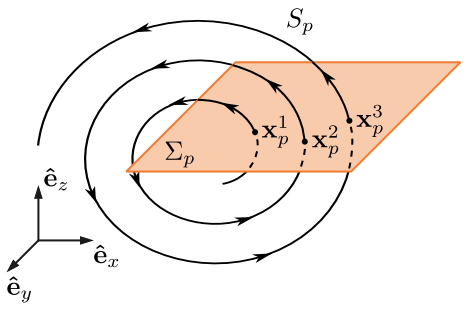

Figure 3.1: Poincaré Map of a three-dimensional orbit, where $\mathbf{x}_p^1$, $\mathbf{x}_p^2$, $\mathbf{x}_p^3$ are the set of points that compose the map.

In the context of a harmonically excited non-autonomous system, where the excitation exhibits a well-defined period denoted as T, the characterization of a periodic orbit becomes more explicit. In such a unique scenario, it becomes feasible

to strategically position the Poincaré section along the temporal dimension of the system, partitioning it into equally spaced intervals of duration T, as illustrated in Figure 3.2a. Consequently, the geometrical representation of the orbit can be accomplished using cylindrical coordinates, as depicted in Figure 3.2b.

By simply analyzing a reduced set of data, the Poincaré map allows the gathering of important information on continuous trajectories within the state space of a dynamical system. Therefore, a set of classifications can be done based on the shape of the Poincaré map as shown in Table 3.1. In this work, this method is widely used to study the periodicity of motion of the proposed energy harvesters.

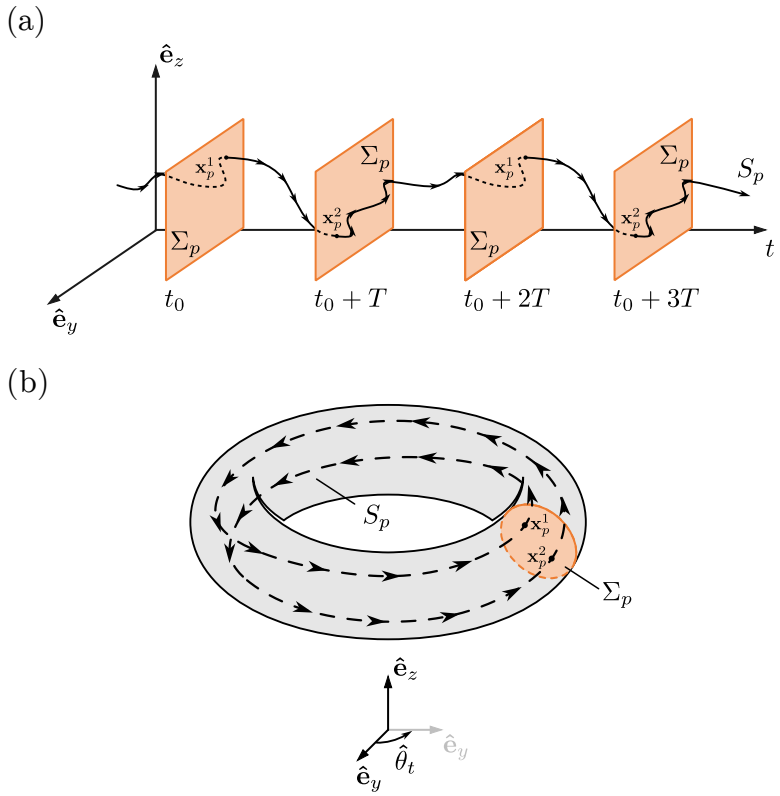

Figure 3.2: Poincaré section Σ_p of an orbit of a two-dimensional non-autonomous system with time-periodic terms. (a) $(\hat{\mathbf{e}}_y, \hat{\mathbf{e}}_z, t)$ space. (b) $(\hat{\mathbf{e}}_y, \hat{\mathbf{e}}_z, \hat{\theta}_t)$ space.

3.1.2 Lyapunov Exponents

The analysis of the motion of a system is closely related to the system's stability. The Lyapunov exponents, named after Aleksandr Mikhailovich Lyapunov (1857 - 1918), quantify stability by assessing the average growth rate of initially small deviations, that is, the estimation of the sensitivity to initial conditions by evaluating the local divergence of nearby orbits.

Consider a n-dimensional system and let $\delta\mathbf{x} = \delta_0\hat{\mathbf{e}}_d$ be the initial perturbation of a system in a single direction in its state space with respect to a reference solution

Table 3.1: Poincaré map interpretation based on different map shapes (adapted from MOON [4]).

Poincaré Map Shape	Possible Interpretations
A finite number of points	• Periodic or subharmonic oscillation
Closed curve	• Quasiperiodic (two incommensurate frequencies present)
Open curve	• Suggest modeling as a one-dimensional map (plot $x(t)$ versus $x(t+dt)$)
Fractal collection of points	• Strange attractor in three phase-space dimensions
Fuzzy collection of points	• Dynamical system with random or noisy input • Strange attractor, but the system has very small dissipation (need another method to verify) • Strange attractor in phase space with more than three dimensions • Quasiperiodic motion with three or more dominant incommensurate frequencies

of the system (fiducial trajectory), where δ_0 is the magnitude of the perturbation, and $\hat{\mathbf{e}}_d$ is an arbitrary orthogonal direction within the state space. Consider also a discrete system given by $\mathbf{x}_{t+1} = \mathbf{f}(\mathbf{x}_t)$. If the perturbation $\delta\mathbf{x}$ is applied to a specific system state variable, its evolution can be expressed as

$$\begin{aligned} \mathbf{x}_{t+1} + \delta\mathbf{x}_{t+1} &= \mathbf{f}(\mathbf{x}_t + \delta\mathbf{x}_t) \\ &\approx \mathbf{J}(\mathbf{x}_t) \cdot \delta\mathbf{x}_t + \mathbf{f}(\mathbf{x}_t). \end{aligned} \tag{3.4}$$

where $\mathbf{J} = (\partial f_i(\mathbf{x})/\partial x_j)\hat{\mathbf{e}}_i\hat{\mathbf{e}}_j$ is the Jacobian matrix of the system, meaning that the product $\mathbf{J}(\mathbf{x}_t) \cdot \delta\mathbf{x}_t$ is a linearization of the system in the vicinity of its solution. If the gradient of a vector is defined as $\boldsymbol{\nabla}\mathbf{a} = \nabla a_j = (\partial u_j/\partial x_i)\hat{\mathbf{e}}_i\hat{\mathbf{e}}_j = A_{ij} = \mathbf{A}$, then the Jacobian matrix can also be written as $\mathbf{J} = \nabla^T\mathbf{f}(\mathbf{x})$, where $\square^T$ is the transpose operator, $\mathbf{a}$ is a generic vector, and $\mathbf{A}$ is the resulting generic second order tensor.

Equation 3.4 leads to

$$\delta\mathbf{x}_{t+1} = \mathbf{J}(\mathbf{x}_t) \cdot \delta\mathbf{x}_t = \mathbf{J}(\mathbf{x}_t) \cdot \delta_0\hat{\mathbf{e}}_d. \tag{3.5}$$

This perturbation can be represented by the radius of a hypersphere of dimension n, centered at the initial state of the system. If the evolution of the perturbation

vector is monitored across N time steps, the perturbation vector becomes

$$\begin{aligned}\delta\mathbf{x}_{t+N} &\approx \mathbf{J}(\mathbf{x}_{t+N-1}) \cdot \mathbf{J}(\mathbf{x}_{t+N-2}) \cdot \ \cdots \ \cdot \mathbf{J}(\mathbf{x}_t) \cdot \delta\mathbf{x}_t \\ &= \left[\prod_{k=1}^{N} \mathbf{J}(\mathbf{x}_{t+N-k})\right] \cdot \delta\mathbf{x}_t \\ &= \mathbf{J}(\mathbf{x}_t)^N \cdot \delta\mathbf{x}_t \\ &= \mathbf{J}(\mathbf{x}_t)^N \cdot \delta_0 \hat{\mathbf{e}}_d.\end{aligned} \tag{3.6}$$

being $\prod$ the product operator. Equations 3.5 and 3.6 are satisfied by the exponential function written in Equation 3.7,

$$\|\delta\mathbf{x}_{t+N}\| = e^{\lambda N}\|\delta\mathbf{x}_t\|, \tag{3.7}$$

where λ is the largest average growing rate known as Lyapunov exponent [172]. Equation 3.7 can be generalized to any base, $\mathscr{b}$, of reference, leading to[1]:

$$\|\delta\mathbf{x}_{t+N}\| = \mathscr{b}^{\lambda N}\|\delta\mathbf{x}_t\|. \tag{3.8}$$

Considering Equation 3.8 and a continuous trajectory, the general definition for the largest Lyapunov exponents is established by Equation 3.9:

$$\lambda = \lim_{t\to\infty} \lim_{\|\delta\mathbf{x}_0\|\to 0} \frac{1}{t - t_0} \log_{\mathscr{b}} \left(\frac{\|\delta\mathbf{x}(t)\|}{\|\delta\mathbf{x}_0\|}\right), \tag{3.9}$$

where $\delta\mathbf{x}_0 = \delta\mathbf{x}(t_0) = \delta_0\hat{\mathbf{e}}_d$ is the initial perturbation vector, $\delta\mathbf{x}(t)$ is the function that describes the evolution of the perturbation with respect to time, and t_0 is the initial time. Oseledec's theorem [174, 175] states that this limit exists for almost all initial conditions in the same basin of attraction. If the perturbation is given in all orthogonal directions of the phase space, the Lyapunov exponents spectrum $\boldsymbol{\lambda} = \{\lambda_1, \lambda_2, \cdots, \lambda_n\}$ can be determined, where each exponent is related to the average growth rate in a given direction.

In geometric terms, by monitoring the perturbation of the system while t increases, the hypersphere evolves into a hyperellipsoid. This process is illustrated in Figure 3.3 for a system with dimension $n = 2$.

[1]The Lyapunov exponents measure the rate at which the system processes create or destroy information. Therefore, the base, $\mathscr{b}$, determines the unit of the exponent. For example, for $\mathscr{b} = 2$, the unit of λ is [bit/s]. Alternatively, if $\mathscr{b} = e$, the unit of λ is [nat/s] [173].

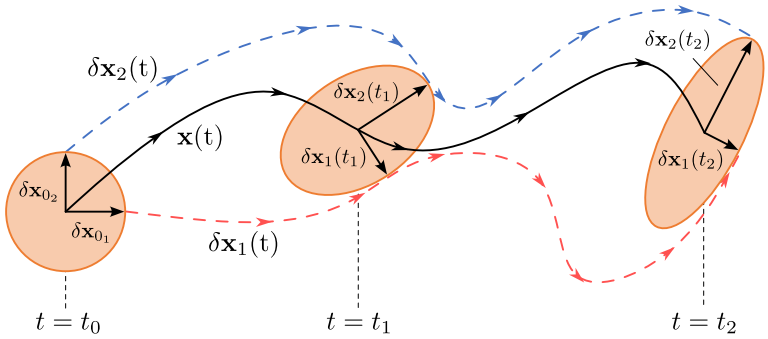

Figure 3.3: Evolution of the system, where $\mathbf{x}(t)$ is the reference solution (fiducial trajectory), and $\mathbf{x}_i(t)$ $(i = 1, 2)$ are the perturbed solutions.

Lyapunov exponents are invariants of the system's dynamics, which means that it is a measure that is independent of the initial conditions or a specific orbit in the same basin of attraction. They serve as robust indicators of the system's dynamical behavior, as they are the measure of the divergence (expansion) or convergence (contraction) of an orbit near a limit set. Therefore, once the largest exponent is known, it is possible to characterize the system's dynamics. If the largest exponent is greater than zero ($\lambda > 0$), it characterizes a divergence between the reference trajectory and the perturbed solution, meaning that the system is chaotic in nature. The greater the value of λ is, the less the capacity of predictability of the chaotic system for larger values of t. Additionally, if the system exhibits two or more positive exponents, that is, more than one divergent direction, then its behavior is classified as hyperchaotic.

Other values are dependent on the type of the system. For a non-autonomous system, if the largest Lyapunov exponent is negative ($\lambda < 0$) it presents a convergence between the reference orbit and the perturbed orbit, meaning that the system exhibits periodic behavior. If $\lambda = 0$, in this case, the system manifests quasiperiodic motion, that is, neither divergence nor convergence between orbits occurs. Alternatively, for autonomous systems, if the largest exponent is zero ($\lambda = 0$), it is said that the system presents periodic motion as there is an additional exponent that accounts for the time dimension, t. Additionally, for conservative systems, the sum of all Lyapunov exponents must be zero, while for non-conservative systems, the sum of all exponents must be negative. A list of behaviors based on the sign of the exponents is exhibited in Table 3.1.2.

Table 3.2: Characterization of system's behavior based on the values in the Lyapunov exponent spectrum of a $n-$dimensional system.

Behavior	$\boldsymbol{\lambda}$	
	Non-autonomous systems	Autonomous systems
Periodic	$\{-,-,\cdots,-\}$	$\{0,-,\cdots,-\}$
Quasi-periodic	$\{0,-,\cdots,-\}$	$\{0,0,\cdots,-\}$
Chaotic	$\{+,-,\cdots,-\}$	$\{+,0,\cdots,-\}$
Hyperchaotic	$\{+,+,\cdots,-,\cdots,-\}$	$\{+,+,\cdots,0,\cdots,-\}$

Furthermore, the results related to the Lyapunov exponents analysis in this thesis are presented in the form of a Lyapunov Exponent Diagram (LED). An example of an LED of the largest exponent, λ_1, of a generic system is shown in Figure 3.4, where positive exponents are represented by rainbow colors, while grayscale colors represent negative exponents. Further details regarding the methodology of exponent convergence for the construction of the LEDs are elucidated in Appendix B.4.

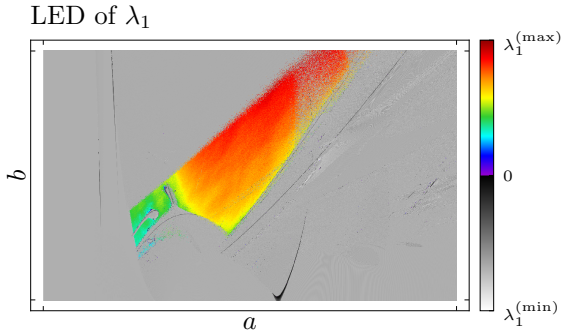

Figure 3.4: Example of a Lyapunov Exponent Diagram (LED) of the largest exponent (λ_1) of a generic system. a and b are generic system parameters. Rainbow colors represent positive exponents, while grayscale colors represent negative exponents.

3.1.3 Basins of Attraction

An attractor within the context of a dynamical system can be characterized as a specific subspace, denoted as $\mathcal{S}$, of its phase space such that for a variety of choices of initial conditions, the system will evolve towards $\mathcal{S}$. Formally, consider an evolution operator, denoted as U_t, that acts on initial conditions $\mathbf{x}_0 = \mathbf{x}(t_0)$ in $\mathbb{R}^n$ such that

$U_t\mathbf{x}_0 = \mathbf{x}(\mathbf{x}_0, t)$, where $\mathbf{x} \in \mathbb{R}^n$. Repeated applications of the U_t operator may take the state of the system to a subspace $\mathcal{S}$ of $\mathbb{R}^n$ known as attractor [176].

For continuous systems, equilibrium points, stable limit cycles, periodic closed, quasi-periodic, chaotic and hyperchaotic orbits can be cited as types of attractors. In this context, for every attractor, its basin of attraction encompasses the set of initial conditions that guide the system's long-term behavior towards the attractor itself [177].

In general, dynamical systems can exhibit more than one attractor in its state space, leading to the possibility of the coexistence of solutions based on the initial condition the system starts. In this context, there are regions within the state space where one single attractor is dominant, whereas in other regions a fractal zone can arise where various attractors are present. In the first case, a small perturbation in the initial conditions leads to the same attractor, while in the second case, any small perturbation of the initial conditions can lead to a different solution. Therefore, the analysis of the basin of attraction of a system is essential as it informs the predictability of a solution based on the initial conditions. Also, for a multistable system, it can predict how many stable equilibrium points the system has, and the chance of the system to rest at each stable condition based on its initial condition.

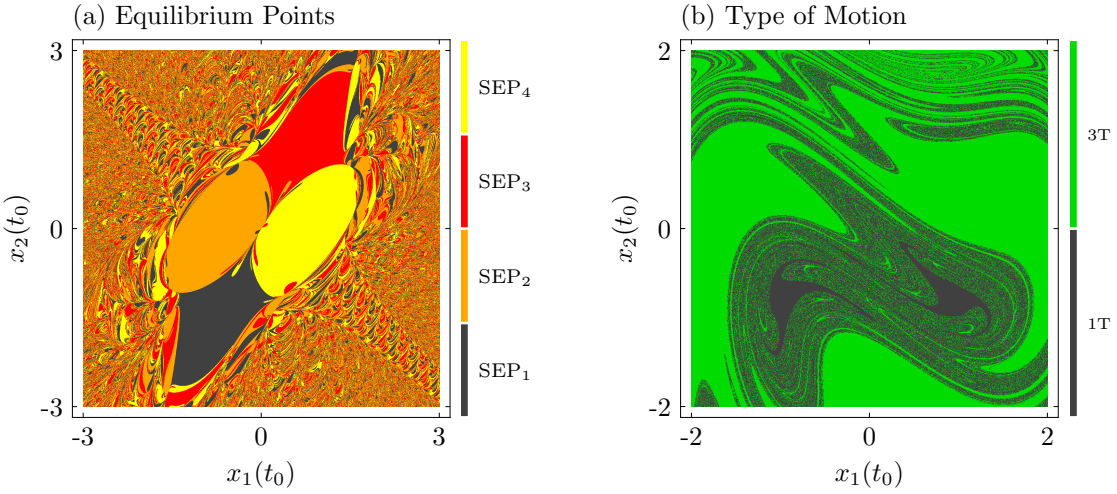

Figure 3.5: Examples of basins of attraction. (a) The attractors are equilibrium points. (b) The attractors are related to the type of motion of a system. x_1 and x_2 are generic state space variables and t_0 represents the initial time.

Figure 3.5 depicts two examples of basins of attraction, where $x_1(t_0) \times x_2(t_0)$ are the sets of initial conditions of an arbitrary system. Figure 3.5a shows the basins of attraction where the attractors are equilibrium positions (SEPs) the system converges after an adequate amount of simulation time. Alternatively, Figure 3.5b, shows basins where the attractors are related to the type of motion. Regarding mechanical systems, the type of basin presented in Figure 3.5a is usually associated

with the solutions of a non-forced system, where the basins are associated with the position the system rests after releasing it from a specific initial condition. Conversely, the type of basins presented in Figure 3.5b are associated with a forced mechanical system, where the attractors are the steady-state orbits associated with the dynamics of the system. In both cases, it is possible to observe areas within the state space where the solution is predictable (regions with a consistent single color) and areas that present fractal-like patterns that are associated with a higher degree of unpredictability.

In the scope of this thesis, the basins of attraction are used to investigate different characteristics of the compact multistable energy harvester in Chapter 5: The basins related to the non-forced system are widely used to analyze stability states of the system, while the basin related to the forced system is employed to study regions of multiple solutions in its excitation parameter domain.

3.1.4 Characterization of the Equilibria

In the context of multistable systems, a stability analysis is essential to fully characterize the system and its specific characteristics. Notably, for multistable energy harvesters, the stability of the system is an interesting point to investigate since it is directly related to the enhancement of the energy harvesting capacity. This subsection dedicates special attention to this subject by describing the combination of tools that are used in this work to characterize the stability of the compact multistable energy harvester in Chapter 5.

Linear Stability Theory

The equilibrium configurations of a system can be determined by identifying the solution of Equation 3.10.

$$\dot{\mathbf{x}} = \mathbf{f}(\mathbf{x}) = \mathbf{0}. \tag{3.10}$$

The nature of each equilibrium point can be determined through a linearization of the system around each point, evaluating the Jacobian matrix, $\mathbf{J} = \nabla^T \mathbf{f}(\mathbf{x})$.

The stability characteristics of each point are evaluated from the eigenvalues of the Jacobian matrix, μ_j $(j = 1, \cdots, n)$, by solving $\det(\mathbf{J} - \mu\mathbf{I}) = \mathbf{0}$. These points can be classified into three sets:

1. Stable if $\{\mu_j \in \mathbb{C} \mid Re(\mu_j) < 0, \forall j\}$;
2. Unstable if $\{\mu_j \in \mathbb{C} \mid Re(\mu_j) > 0, \exists j\}$;
3. Center if $\{\mu_j \in \mathbb{C} \mid Re(\mu_j) = 0, \exists j\}$.

Besides that, according to the Hartman-Grobman theorem, the stability of the linearized system at the vicinity of an equilibrium point corresponds to the nonlinear system as long as the point is hyperbolic, meaning that there is not an eigenvalue that vanishes the real part ($Re\,(\mu_j) \neq 0, \forall j$) [171]. Therefore, if there exists an eigenvalue with zero real part, that is, a center point, the stability of this point cannot be determined with this approach and other techniques as Lyapunov functions, for instance, must be used. For the multistable systems analyzed in this thesis all the points showcased hyperbolic traits, which enables the usage of the linear stability approach.

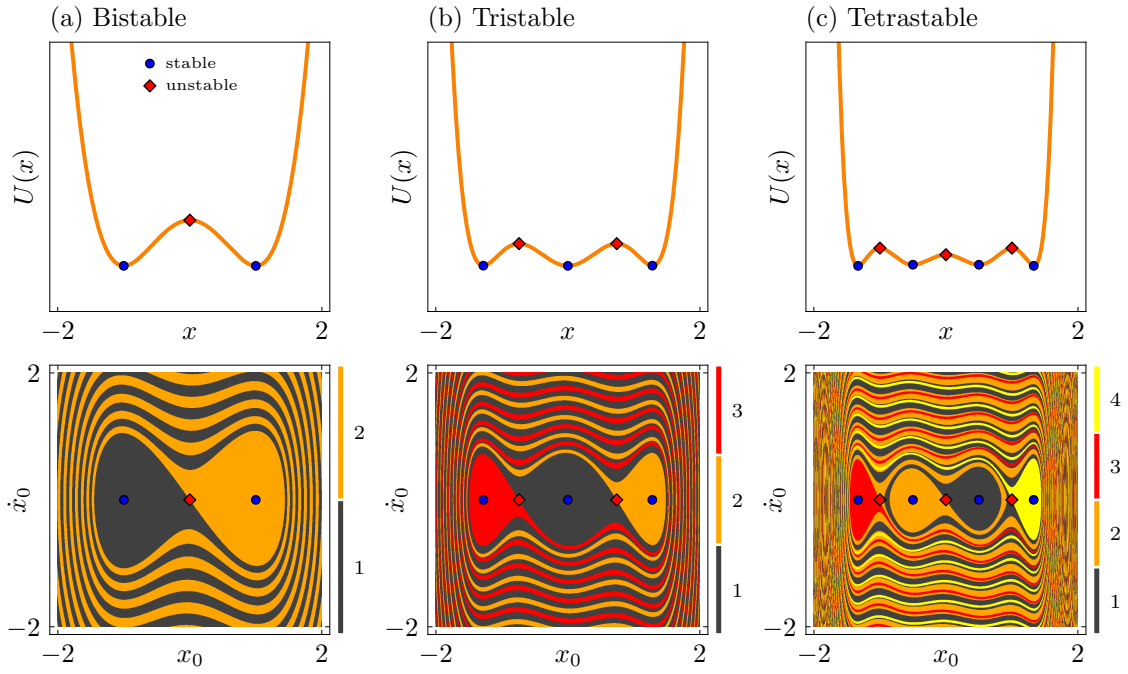

Figure 3.6: Stability evaluation of (a) a bistable, (b) a tristable, and (c) a tetrastable system. Each column represents the analysis of one system, with the top plot showing its potential energy and the bottom diagram illustrating its basins of attraction. Blue dots represent stable equilibria, while red diamonds render unstable equilibria. Different colors within the basins of attraction depict different stable equilibrium points to which the system converges after a reasonable period of evolution.

Evaluating the Stability

In order to fully characterize the system's stability, a combination of three approaches was used in this work:

- **Linear Stability Theory**: To identify and classify the type of equilibrium points of the system;

- **Basins of Attraction**: To identify the combination of initial conditions that leads the system towards an equilibrium position;
- **The Potential Energy Function**: To evaluate the energy thresholds required for transitions between stable equilibrium states.

The integration of these three approaches provides a comprehensive understanding of the system's stability characteristics. This knowledge is essential to better understand the dynamical behaviors of the system, being an essential step in the analysis of multistable energy harvesting systems. Figure 3.6 displays an example of the stability analysis for different types of multistability, where x and $\dot{x}$ are the state space variables, while $U(x)$ represents the potential energy. $\square_0$ is an index symbolizing the initial state. Blue circles illustrate stable equilibria, while red diamonds illustrate unstable equilibria. Different colors in the basins of attraction portray the stable equilibrium the system moves towards after a long time based on its initial condition.

3.2 Proposed Approaches in Nonlinear Energy Harvesting Analysis

This section proposes a new set of tools designed to complement the analysis of energy harvesting systems. The integration of these new proposed tools with the classical approaches can provide a deep and robust understanding of the dynamical and performance characteristics of an energy harvester.

3.2.1 Dynamical Response Diagrams (DRDs)

In order to analyze a dynamical system, it is important to characterize it with proper tools and robustness. So far two classical methods of nonlinear dynamics analysis have been presented in this regard: the Poincaré map and the Lyapunov exponents. Both are suitable to determine some aspects of the behavior of a system, but not all of them. In this section, we present an algorithm that seeks to better classify the dynamical behavior of systems by the combination of both techniques. The result of the algorithm is what we call a dynamical response diagram (DRD), in which is possible to classify automatically different types of periodic and aperiodic behaviors.

The DRDs can be used as a tool to map and quantify the dynamical attractors of the system resulting from a specific initial condition within a 2D parameter space of choice. The diagrams are built with a grid of $N_x \times N_y$ sample points, each of which is obtained from a time series integration from t_0 to t_f considering a suitable

integration time step. A time t_{trans} is chosen to determine when in the time series the transient regime is considered to be over (usually it is chosen as $t_{\text{trans}} > 0.7t_f$). Additionally, all the samples have the same initial conditions to standardize the analysis.

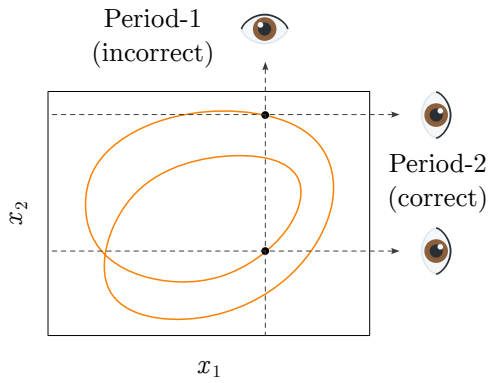

Figure 3.7: Relying on the monitoring of a single state variable of the Poincaré map points can lead to erroneous attractor classification due to the alignment of points.

From each sample, a behavior is classified. All classifications are based on the Lyapunov exponents spectrum and the verification of the steady state Poincaré map. Initially, the first two Lyapunov exponents, λ_1 and λ_2, are analyzed. The behavior

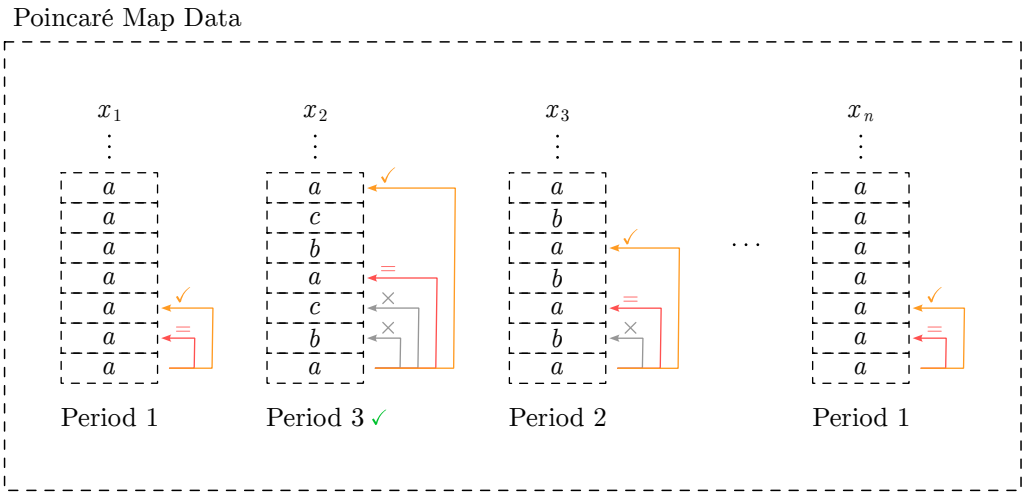

Figure 3.8: Procedure to classify periodic attractors. a, b and c are arbitrary numbers to represent the real data. $x_1, x_2, \cdots, x_n$ represent the n state variables within the state space of the system. Light gray arrows followed by a "×" represent that the two values compared are not equal. Alternatively, red arrows labeled as "=" represent positive equality in the comparison (i^th position). Finally, the orange arrows labeled with a ✓ represent the $2i^{th}$ position at which the value is equal to the i^{th} position. The greatest orange value is chosen as the final classification, and it is marked by the green checkmark.

is classified based on the values presented in Table 3.1.2 in which three of the four behaviors are analyzed (periodic, chaotic and hyperchaotic). If the classification

is chaotic or hyperchaotic, the classification procedure is over. Alternatively, if the classification is periodic, then the Poincaré map of the steady state time series sample is analyzed. A list of values with all the points of the Poincaré map is loaded, and the last point is used as the reference. Then, the previous points are analyzed one by one until it is found an equal at the i^{th} position. After that, if it finds another equal value in the $2i^{th}$ position, then it can be classified as a i-periodic candidate, if not, it continues to analyze previous points until these two conditions are met. The same procedure is done for all dimensions of the system, and the greatest periodic behavior found is used as the final classification. The comparison for all state variables is needed as limiting the observation to only one direction may yield misleading results of smaller periodicity due to the alignment of points in this direction, as shown in Figure 3.7. To avoid numerical errors, a tolerance of $p_{\text{tol}} = (x_{\max} - x_{\min})\mathcal{O}_{\text{method}}$ for each state variable must be placed when comparing the points, where $x_{\max}$ and $x_{\min}$ are the maximum and minimum values of the state variable between t_{trans} and t_f (steady state), and $\mathcal{O}_{\text{method}}$ is the order of error of the method of integration. The procedure depicting the comparison of the Poincaré map data is illustrated in Figure 3.8.

Figure 3.9 depicts an example of a DRD of a generic $a \times b$ parameter domain with phase spaces representing each corresponding color within the diagram. Different periodicities are classified by colors, considering that T represents the excitation period: dark gray (1T), yellow (2T), green (3T), orange (4T) and purple (5T). Light blue is employed to represent responses with a period equal or greater than 6T, which means multiple periods (MP). Red regions represent chaotic (CH) responses, while dark red regions represent hyperchaotic (HC) responses. These responses can be referred to as dynamical attractors since they represent either stable closed orbits or strange attractors[2]. Also, Poincaré Maps, represented by the black dots in the phase spaces (in the case of the dark gray attractor, the Poincaré map is represented in red) are displayed as a visual representation of the periodicity of each orbit. A discussion about the limitations of the DRDs is presented in Appendix B.4.

3.2.2 Output Power Diagrams (OPDs) and Performance Comparison Diagrams (PCDs)

One-dimensional diagrams, typically frequency diagrams, are frequently used in the literature to analyze the performance of energy harvesting systems [178–183]. While this method has its merits, with the growing number of proposed harvesters, each with its own unique features and increasing complexity, this simplistic approach

[2]In this section the expressions *attractors*, *responses* and *behaviors* are used interchangeably to refer to the same thing in the context of the dynamics of the system.

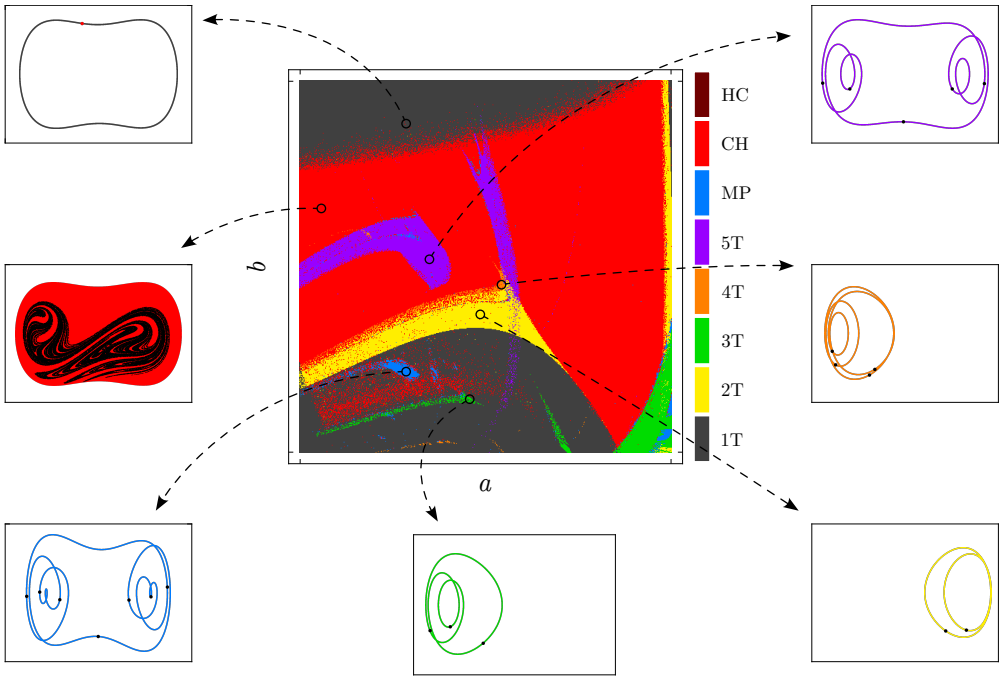

Figure 3.9: Example of a Dynamical Response Diagram (DRD). Each color represents a dynamical response (attractor), as described in the text. Black circles marked in the DRD represent selected cases to illustrate the system's response type. Each point is depicted within its respective phase space, colored accordingly, and accompanied by a Poincaré map of the specific attractor. In the case of 1T responses, the Poincaré map is denoted by a red dot in the phase space plot, whereas for the other attractors, it is represented by black dots.

is proving to be inadequate. This approach often restricts the scope of analysis to a limited number of scenarios. Typically the authors vary one of all key parameters (usually the amplitude or frequency of excitation) while keeping another key parameter constant. Also, they only consider a small set of values for that constant parameter. This practice can result in misleading conclusions as the entire excitation parameter space is not well evaluated. This limitation is particularly evident when comparing devices. Moreover, as computational power continues to increase, the generation, acquisition, and manipulation of larger datasets are becoming more feasible, even for entry-level personal computers. Consequently, the depth and sophistication of energy harvesting analysis, for both numerical and experimental analyses, must progress to align with these technological advancements.

For this reason, in this work, the performance of the energy harvesters is evaluated in terms of a wider perspective, contemplating a considerable region of a parameter space of choice (usually the excitation parameter space) and summarizing the results in an Average Output Power Diagram (OPD)[3].

[3]The OPD can also be referred as "Overall Performance Diagram" to specify that the OPD is evaluating an alternative type of performance metric different from the standard average output power.

The construction of each OPD relies on a similar procedure of the construction of the DRDs, using $N_x \times N_y$ sample points, each of which has the same initial conditions to standardize the analysis. However, instead of evaluating the attractors, the OPDs show the steady state average electrical output power (or any variable related to that) under excitation conditions. This type of two-dimensional performance diagram is not new to the literature, it has been shown with other names in other works [169, 184–188]. However, their application in a comparative scenario is new.

In this context, a comprehensive performance evaluation of two harvester configurations is conducted using a Performance Comparison Diagram (PCD). Each point on their respective Output Power Diagrams (OPDs) is compared using a percentage difference metric, denoted as $\Delta P(\%)$, as outlined in Equation 3.11. Here, P_r represents the performance metric of the reference harvester, while P_s denotes the performance metric of the harvester under study.

$$\Delta P(\%) = \frac{P_s - P_r}{P_r} \times 100. \tag{3.11}$$

Equation 3.11 is used to compute the percentage difference, which allows a classification based on three sets:

- $\Delta P(\%) > 0$: The harvester under study shows better performance;
- $\Delta P(\%) = 0$: Both harvesters present the same performance;
- $\Delta P(\%) < 0$: The harvester used as reference shows better performance.

Figure 3.10 showcases an example of a performance analysis done utilizing OPDs and a PCD. Specifically, Figure 3.10a shows an OPD for a generic reference harvester configuration, while Figure 3.10b displays an OPD for a generic harvester configuration under study. The diagrams present a section of a generic two-dimensional $a \times b$ parameter space. Within the OPDs, cold colors (purple, blue and light blue) indicate regions of lower performance, while warmer colors (orange, red and dark red) indicate regions of higher performance. Each OPD has its own colormap values, indicated by the accompanying colorbar next to it. Moreover, Figure 3.10c displays the PCD for the comparison of both harvesters, where red colors indicate regions in which the harvester under study outperforms the reference harvester configuration, while black color regions indicate that the reference harvester outperforms the harvester under study. Throughout the entirety of this work, the PCDs colorbars limits are truncated by 50% to better illustrate the difference between the two harvesters. In other words, the darker colors in each red or black colormap represent scenarios

in which one harvester outperforms the other by a factor of 50% or more. Theoretically, the limit of the red % is ∞, while the limit of the black values is -100%, as the comparison is done utilizing the reference harvester as basis, as determined in Equation 3.11.

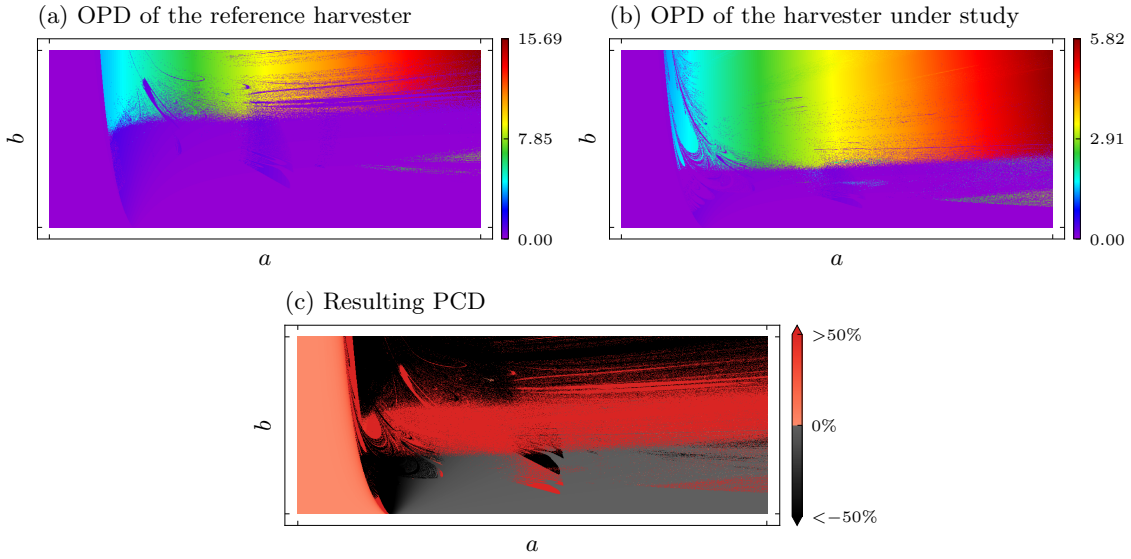

Figure 3.10: Diagrams used for performance analysis within the generic parameter space $a \times b$. (a) The Output Power Diagram (OPD) for a generic reference harvester configuration. (b) The OPD for a generic harvester configuration under study. (c) The Performance Comparison Diagram (PCD), showing the comparison of both harvesters. Accompanying colorbars in (a) and (b) show the output power levels of the associated OPD. The colorbar in (c) represents $\Delta P(\%)$. The regions in red represent where in the two-dimensional parameter space the harvester under study outperforms the reference harvester, while black regions show the opposite.

With these integrated tools, it is possible to map and quantify the performance of energy harvesters across a wide range of excitation conditions. Additionally, they enable robust comparisons between different energy harvester configurations.

3.2.3 Dynamical Pattern Diagrams (DPDs)

The Dynamical Pattern Diagram (DPD) is an extension of the Dynamical Responses Diagram (DRD) that accounts for the classification and mapping of specific dynamical patterns unique to a dynamical system. The type of the monitored trait will depend exclusively on the type and characteristics of the system at hand. The idea is to extend the standard classification of the DRD in some way. In the specific context of this work, the DPDs are utilized to monitor whether the pendulum structure of the second proposed harvester oscillates, rotates, or presents a mix of the two patterns. It also monitors if it is a regular pattern or an irregular pattern. An

in-depth discussion about the DPD, the specific conditions of classification, and classification patterns is presented in Chapter 6, Subsection 6.5.4, as it directly relates to the specific harvester analyzed in that Chapter.

3.2.4 Occurrence Diagrams (OCDs)

In general, nonlinear systems are characterized by their inherent complexity, where a small change in a parameter can lead to very different results, rendering the analysis of these systems a non-trivial task. To address that, it becomes advantageous to map specific characteristics within a parameter domain for a range of values of system parameters and evaluate the occurrence of that characteristic in each region of the parameter domain. The result of the analysis is summarized in an Occurrence Diagram (OCD), allowing for a more informed estimation of the likelihood of these target features emerging.

The procedure to construct an OCD involves the progressive analysis of different 2D diagram datasets. To illustrate this concept, consider a generic system characterized by three parameters: a, b and c. Within the parameter domain defined by $a \times b$, n distinct diagrams are generated, each representing a different value of the c parameter $(c_1, c_2, \cdots, c_n)$. Suppose our goal is to visually depict the prevalence of the *red characteristic* of the system and assess where, within the $a \times b$ parameter domain, this characteristic is most prominent for a range of values of c.

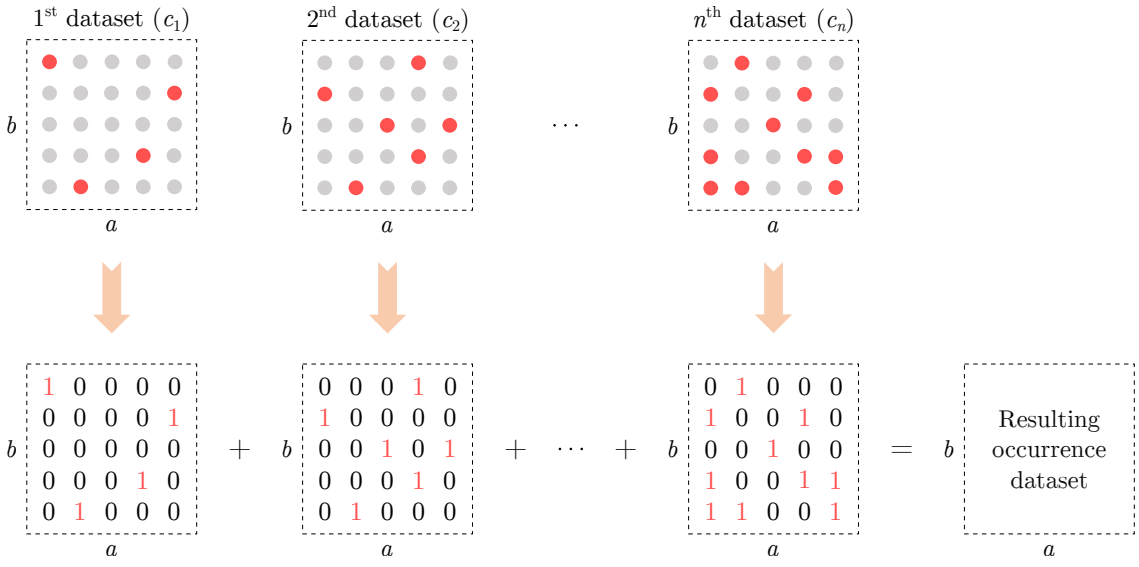

Figure 3.11: Procedure to construct the occurrence diagrams (OCDs). Red points are related to the points that have the wanted characteristic, while gray points do not have the wanted characteristic. For each red point, the location within the diagram is marked as 1, while for each gray point, the location is marked as 0. The resulting occurrence dataset is the sum of all datasets.

To achieve this, we start by marking all data points exhibiting the red characteristic with the number 1, and all the remaining data points that do not exhibit the characteristic with the number 0. By summing up the values of each point in their respective locations within the parameter domain, we produce a resulting dataset. This dataset indicates how frequently the red feature appears at each unique point within the parameter domain. This procedure is illustrated in Figure 3.11.

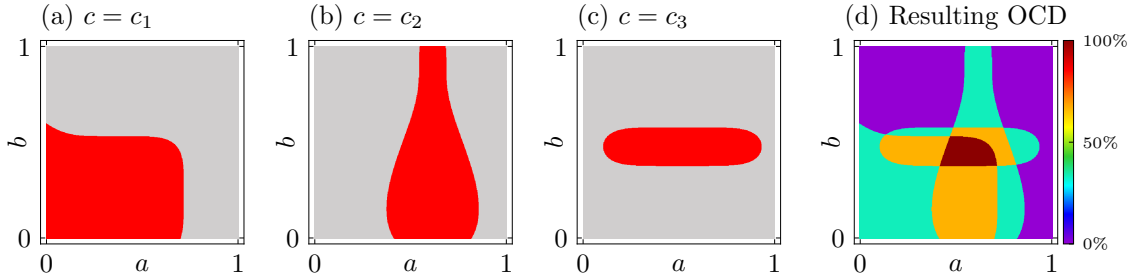

Figure 3.12: In the first row are displayed 3 pseudo-random diagrams used to construct the resulting OCD in the second row. The colorbar in the second row represents the likelihood of the red characteristic to emerge within the $a \times b$ parameter space, based on the diagrams provided to construct the resulting OCD.

Moreover, 400 pseudo-random data were generated to simulate a data collection, to provide a comprehensive view of how the number of analyzed sample diagrams influences the resulting OCD. In Figures 3.12a, 3.12b and 3.12c, 3 of these data collections are displayed in diagrams, which are used to construct the OCD. The resulting OCD, presented in Figure 3.12d, indicates that the area within the parameter space $a \times b$ that the red characteristic is mostly likely to emerge is predominantly centered at the intersection of the three red areas. This serves as a comprehensive illustration of the procedure outlined in Figure 3.11. By increasing the number of diagram samples to 400, as shown in Figure 3.13, the resulting OCD undergoes significant changes, displaying a notable shift in the region where the red characteristic is more likely to emerge. This result shows that the number of data available to construct the OCD provides more accuracy in the predictions.

Another potential scenario of analysis that can arise in the making of an OCD involves evaluating characteristics that can vary in value across different sample diagrams. For instance, in the context of energy harvesting, this situation can arise when assessing system performance, where performance metrics such as output power can exhibit significant variations in maximum and minimum values from one sample diagram to another. To account for these variations, a necessary normalization step must be performed before the summation of each dataset. This normalization takes the form of Equation 3.12, where G_{norm} is the normalized value of the generic characteristic, G, at each point in the single sample diagram, while

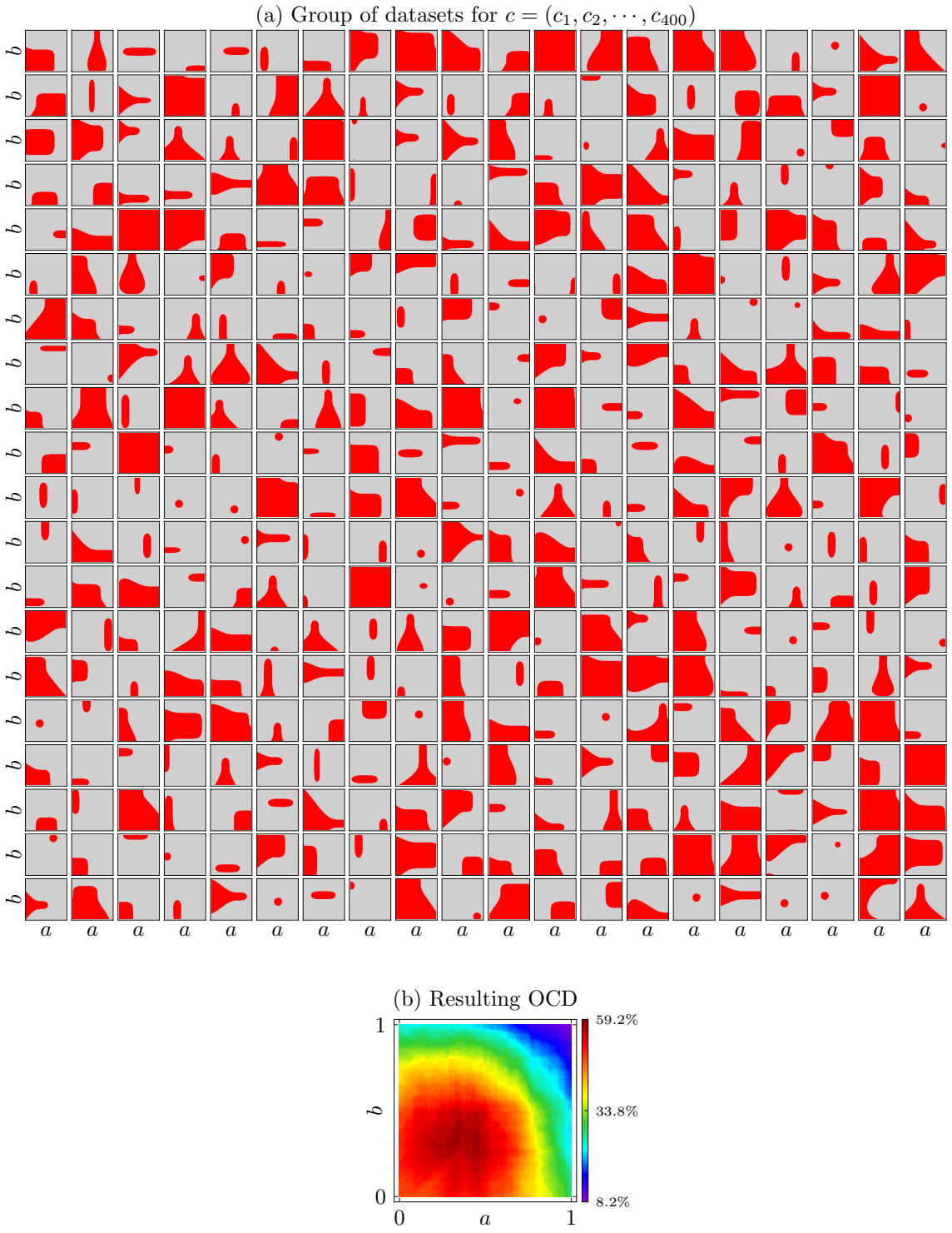

Figure 3.13: 400 pseudo-random diagrams are displayed and used to construct the resulting OCD displayed at the bottom. The colorbar represents the likelihood of the red characteristic to emerge within the $a \times b$ parameter space, based on the diagrams provided to construct the resulting OCD.

$G_{\max}$ denotes the maximum value of this characteristic across all points within the same diagram.

$$G_{\text{norm}} = \frac{G}{G_{\max}} \tag{3.12}$$

This normalization procedure results in all values within the sample diagrams being scaled to the range $[0, 1]$, providing a measure of the quality of the characteristic

Chapter 4

Modeling Multistability

As discussed in Chapter 2, multistability can be induced by a wide array of sources, including magnetic interactions, compressive forces, gravity, and more. In its simplest manifestation, the constitutive relationship governing these interactions with the structural elements can be reasonably approximated by a restitution polynomial function, $f_r(x) = -dU(x)/dx$, where $U(x)$ is the potential energy associated with the restitution force [5, 6, 122, 123, 189, 190]. To facilitate a deeper understanding, Table 4 provides a small compilation of common polynomial functions employed to represent distinct stability conditions within single-degree-of-freedom systems.

Table 4.1: Common polynomial functions used to represent different symmetric stability conditions in a single-degree-of-freedom system.

Stability	Restitution force, $f_r(x)$	Potential Energy, $U(x)$
Bistable	$\mathfrak{a}_1 x - \mathfrak{a}_2 x^3$	$-\frac{1}{2}\mathfrak{a}_1 x^2 + \frac{1}{4}\mathfrak{a}_2 x^4$
Tristable	$-\mathfrak{a}_1 x + \mathfrak{a}_2 x^3 - \mathfrak{a}_3 x^5$	$\frac{1}{2}\mathfrak{a}_1 x^2 - \frac{1}{4}\mathfrak{a}_2 x^4 + \frac{1}{6}\mathfrak{a}_3 x^6$
Tetrastable	$\mathfrak{a}_1 x - \mathfrak{a}_2 x^3 + \mathfrak{a}_3 x^5 - \mathfrak{a}_4 x^7$	$-\frac{1}{2}\mathfrak{a}_1 x^2 + \frac{1}{4}\mathfrak{a}_2 x^4 - \frac{1}{6}\mathfrak{a}_3 x^6 + \frac{1}{8}\mathfrak{a}_4 x^8$

To encompass the concept of a $(N+1)$-stable system in a more generalized context, one can formally express these relationships as Equations 4.1 and 4.2, as detailed below:

$$f_r(x) = \sum_{j=0}^{N} (-1)^{1+j+N} \mathfrak{a}_{j+1} x^{2j+1}, \tag{4.1}$$

$$U(x) = -\int_0^x f_r(x)\, dx = -\frac{1}{2} \sum_{j=0}^{N} (-1)^{1+j+N} \frac{1}{j+1} \mathfrak{a}_{j+1} x^{2(j+1)}. \tag{4.2}$$

Figure 4.1 depicts different symmetric stability conditions based on Equations 4.1 and 4.2.

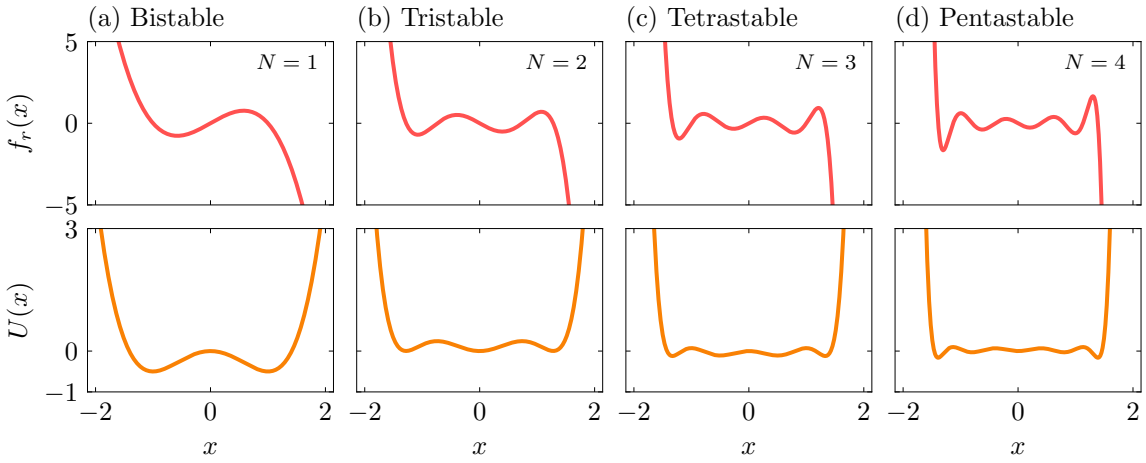

Figure 4.1: Restitution forces and potential energy functions for different symmetric stability conditions represented in each column.

Equations 4.1 and 4.2 provide a generalized representation of $f_r(x)$ and $U(x)$, both of which require the inclusion of constant coefficients as essential input parameters. This approach may be inconvenient in certain situations, especially when studying the qualitative characteristics of a system. In such cases, an alternative approach emerges, offering the flexibility to select equilibrium positions. To explore this option, consider the alternative formulations of restitution forces and potential energies, conveniently outlined in Table 4 [127]. Here, $p_i, i(1, \cdots, N)$ represent the

Table 4.2: Equivalent alternative form of polynomial functions used to represent different stability conditions in a single-degree-of-freedom system, where the equilibrium positions can be chosen by specifying the parameters $p_i, (i = 1, \cdots, N)$.

Stability	Restitution force, $f_r(x)$	Potential Energy, $U(x)$
Bistable	$-\frac{\mathfrak{a}_1 x}{p_1^2}\left(x^2 - p_1^2\right)$	$-\frac{1}{2}\mathfrak{a}_1 x^2 + \frac{1}{4}\frac{\mathfrak{a}_1}{p_1^2}x^4$
Tristable	$-\frac{\mathfrak{a}_1 x}{p_1^2 p_2^2}\left(x^2 - p_1^2\right)\left(x^2 - p_2^2\right)$	$\frac{1}{2}\mathfrak{a}_1 x^2 - \frac{1}{4}\frac{\mathfrak{a}_1\left(p_1^2 + p_2^2\right)}{p_1^2 p_2^2}x^4 + \frac{1}{6}\frac{\mathfrak{a}_1}{p_1^2 p_2^2}x^6$
Tetrastable	$-\frac{\mathfrak{a}_1 x}{p_1^2 p_2^2 p_3^2}\left(x^2 - p_1^2\right)\left(x^2 - p_2^2\right)\left(x^2 - p_3^2\right)$	$-\frac{1}{2}\mathfrak{a}_1 x^2 + \frac{1}{4}\frac{\mathfrak{a}_1\left(p_1^2 p_2^2 + p_1^2 p_3^2 + p_2^2 p_3^2\right)}{p_1^2 p_2^2 p_3^2}x^4$ $-\frac{1}{6}\frac{\mathfrak{a}_1\left(p_1^2 + p_2^2 + p_3^2\right)}{p_1^2 p_2^2 p_3^2}x^6 + \frac{1}{8}\frac{\mathfrak{a}_1}{p_1^2 p_2^2 p_3^2}x^8$

modulus of the symmetric equilibrium points of the system, excluding the point located at $x = 0$, which is always an equilibrium position. For N odd, $x = 0$ is

an unstable equilibrium (peak), while for N even, $x = 0$ is a stable equilibrium (well). Additionally, i odd values are stable equilibria (wells), while i even values are unstable equilibria (peaks). Note that now, all coefficients are dependent on $\mathfrak{a}_1$, which is the absolute stiffness of the system around $x = 0$, and of the location of equilibria. This way, it is easier to determine the coefficients $\mathfrak{a}_i$ based on the shape of the restitution force and potential energy curves and the location of the equilibria. Figure 4.2 shows a visual representation of N and p_i, $(i = 1, \cdots, N)$.

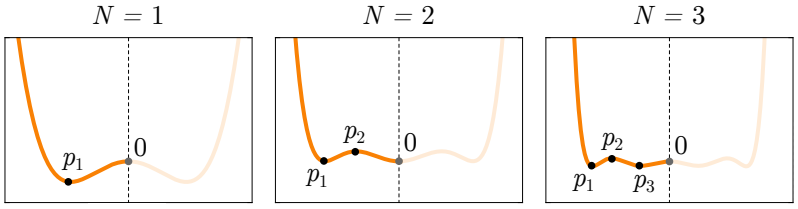

Figure 4.2: Illustrative representation of N and $p_i, (i = 1, \cdots, N)$.

The restitution force expressions presented in Table 4 can then be generalized to any symmetric multistable configuration in the form of Equation 4.3:

$$f_r(x) = -\frac{\mathfrak{a}_1 x}{\prod_{i=1}^{N} p_i^2} \prod_{i=1}^{N} \left(x^2 - p_i^2\right). \tag{4.3}$$

The determination of the potential energy function is less trivial. For that, consider the following transformations $X = x^2$ and $P_i = p_i^2$, yielding:

$$f_r(X) = -\frac{\mathfrak{a}_1 \sqrt{X}}{\prod_{i=1}^{N} P_i} \prod_{i=1}^{N} \left(X - P_i\right). \tag{4.4}$$

This facilitates the rewriting of Equation 4.4 in terms of elementary symmetric polynomials[1], e_j, as:

$$f_r(X) = -\frac{\mathfrak{a}_1 \sqrt{X}}{\prod_{i=1}^{N} P_i} \sum_{j=1}^{N} (-1)^j e_j \left(P1, \cdots, P_N\right) X^{N-j}. \tag{4.5}$$

Thus, as $dX = 2x dx \rightarrow dx = dX/2\sqrt{X}$, by integrating the force, the generalized potential function can be derived as shown by Equation 4.6,

$$\begin{aligned} U(X) &= -\int_0^X \frac{f_r(X)}{2\sqrt{X}}\, dX \\ &= \frac{1}{2} \frac{\mathfrak{a}_1}{\prod_{i=1}^{N} P_i} \sum_{j=0}^{N} \left[\frac{(-1)^j}{N-j+1} e_j \left(P_1, \cdots, P_N\right) X^{N-j+1} \right]. \end{aligned} \tag{4.6}$$

[1]For reference about elementary symmetric polynomials, please refer to Appendix A.

By substituting back $X = x^2$ and $P = p^2$, the generalized potential energy is written in its final form as in Equation 4.7:

$$U(x) = \frac{1}{2}\frac{\mathfrak{a}_1}{\prod_{i=1}^{N} p_i^2}\sum_{j=0}^{N}\left[\frac{(-1)^j}{N-j+1}e_j\left(p_1^2,\cdots,p_N^2\right)x^{2(N-j+1)}\right]. \tag{4.7}$$

A summary of these equations is established in Table 4, where the final equations that use coefficients $\mathfrak{a}_i$, $i = (1,\cdots,N+1)$ as input are referred to as *first form equations*, and the final equations that use equilibrium positions p_i, $i = (1,\cdots,N)$, as input are named *second form equations*.

Table 4.3: Summary of the different forms of the generalized polynomial equations used to represent symmetric multistability in single-degrees-of-freedom systems. The first-form equations are used when the coefficients are known, while the second-form equations are used when the equilibrium positions are known. $e_j(p_1^2,\cdots,p_N^2)$ is the representation of elementary symmetric polynomials as detailed in Appendix A.

Designation	Restitution force, $f_r(x)$	Potential Energy, $U(x)$
1st Form	$\sum_{j=0}^{N}(-1)^{1+j+N}\mathfrak{a}_{j+1}x^{2j+1}$	$-\frac{1}{2}\sum_{j=0}^{N}(-1)^{1+j+N}\frac{1}{j+1}\mathfrak{a}_{j+1}x^{2(j+1)}$
2nd Form	$-\frac{\mathfrak{a}_1 x}{\prod_{i=1}^{N} p_i^2}\prod_{i=1}^{N}\left(x^2-p_i^2\right)$	$\frac{1}{2}\frac{\mathfrak{a}_1}{\prod_{i=1}^{N} p_i^2}\sum_{j=0}^{N}\left[\frac{(-1)^j}{N-j+1}e_j\left(p_1^2,\cdots,p_N^2\right)x^{2(N-j+1)}\right]$

Chapter 5

The Compact Multistable Energy Harvester

This Chapter is devoted to exploring the design concept of the novel compact multistable energy harvester (CMEH), as well as detailing the underlying assumptions employed for its modeling.

Inspired by classical bistable energy harvesters and bistable dual-beam structures, and motivated by the trend of maximizing energy harvesting capabilities through compact designs, in this Chapter we propose a new nonlinear dual beam structure with two sets of magnets and transducers.

This goal is accomplished by building a classical bistable energy harvester but introducing new relevant degrees-of-freedom by cutting off the main beam, and adding an inner beam as done by [1, 2, 66, 67]. Furthermore, we have introduced a novel element into the harvester by incorporating an additional set of magnetic interactions and an extra piezoelectric transducer into the inner beam. Figure 5.1 presents the conceptual design of the novel device compared with the classical bistable cantilever beam. This novel design offers a more efficient use of space and potentially greater performance capabilities compared with the classical version. This design enables efficient utilization of previously unused space and results in unprecedented multistable characteristics, which can enhance the overall functionality of this type of harvester.

5.1 Reduced Order Modeling

The proposed energy harvester is modeled by considering a 2-DoF (2-degrees-of-freedom) multistable device assuming the first vibration mode as a reference, as shown in Figure 5.2. This prototype represents the main characteristics of the energy harvester, presenting 1-DoF for each beam. Therefore, by considering that subscript

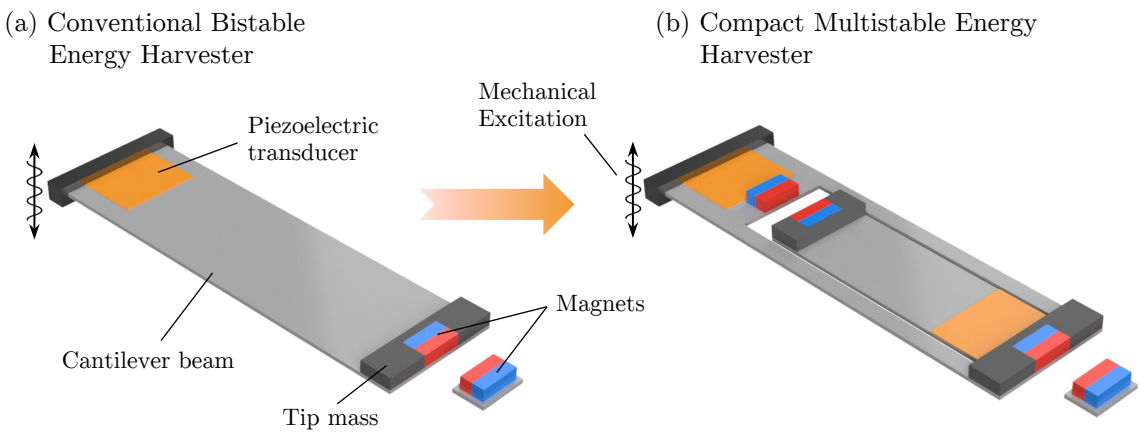

Figure 5.1: Conceptual representation of the novel energy harvester, illustrating its compact and space-efficient design, which is comparable in size to the traditional bistable energy harvester.

$i = 1, 2$ denotes the properties associated with each one of the two degrees-of-freedom, m_i represents the mass, k_i is the equivalent stiffness and c_i is the equivalent mechanical dissipation coefficient. Additionally, piezoelectric patches are attached to the structure and can be represented by the electromechanical coupling coefficient, θ_i, an internal capacitance C_{pi}, and an internal resistance, R_{pi}.

The electrical circuits are assumed to be simple resistive circuits that are connected to the piezoelectric elements, each with a load resistance, R_{li}. The output voltage of each circuit is represented by $v_i(t)$, and the equivalent electrical resistance, R_i, of each circuit is composed by the piezoelectric internal resistance and the load resistance connected in parallel, such that $R_i = R_{li}R_{pi}/\left(R_{li} + R_{pi}\right)$.

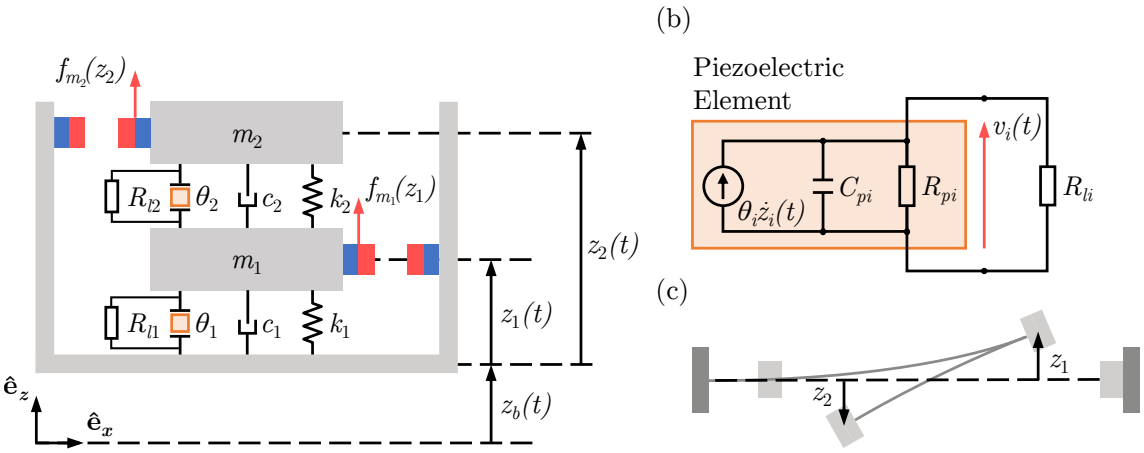

Figure 5.2: Lumped model representing (a) the compact multistable energy harvester structure, (b) the equivalent electrical circuit composed by the piezoelectric element attached to a resistance, and (c) the respective positive z_i directions for each DoF of the reduced order model related to the beam's structure.

The system is subjected to a base excitation of $z_b = A_b \sin(\omega t)$, where A_b and ω represent the excitation amplitude and frequency, respectively. Furthermore, the displacement of each mass is represented by $z_i(t)$ and the respective positive directions related to the real harvester's structure are presented in Figure 5.2c, that is, when $z_1(t)$ is positive, the motion of the outer beam is directed upward, while when $z_2(t)$ is positive, the motion of the inner beam presents a downward direction [161]. Also, the upper dot represents derivatives with respect to time, as $\dot{\square} = d\square/dt$, and the effects of gravity are neglected.

The Euler-Lagrange equations are defined from 2 mechanical coordinates, $z_1(t)$ and $z_2(t)$, and 2 electrical coordinates, $\psi_1(t)$ and $\psi_2(t)$, the magnetic flux linkages. Therefore, it is assumed that $\mathbf{u} = [z_1(t), z_2(t), \psi_1(t), \psi_2(t)]$, resulting in the following equation,

$$\frac{d}{dt}\left(\frac{\partial \mathcal{L}}{\partial \dot{u}_i}\right) - \frac{\partial \mathcal{L}}{\partial u_i} + \frac{\partial D}{\partial \dot{u}_i} = 0, \tag{5.1}$$

where the Lagrangian, $\mathcal{L} = T - U + W_e$, is given by the sum of the kinetic energy, T, the potential energy, U, and the total piezoelectric energy, W_e. Moreover, the total energy dissipation is defined from the function D.

Within the context of the proposed system, and considering the motion of the base magnet of the second degree-of-freedom negligible, one can apply the first form of the restitution force function, expressed by Equation 4.1, in each degree-of-freedom separately. For a set with two magnets, a maximum of two stable equilibria arises at each DoF [5, 6], implying that $N = 1$ should be used, resulting in Duffing-type restitution forces, and its respective potential energy functions of the form:

$$f_{m_i}(z_i) = -a_i z_i(t) - b_i z_i(t)^3, \quad i = 1, 2; \tag{5.2}$$

$$U_m(z_1, z_2) = \sum_{i=1}^{2} \frac{1}{2} a_i z_i(t)^2 + \frac{1}{4} b_i z_i(t)^4, \tag{5.3}$$

where the coefficients $\mathfrak{a}_{1_i} = a_i$ and $\mathfrak{a}_{2_i} = b_i$, for better readability ($i = 1, 2$). These coefficients can be estimated by a polynomial fitting to experimental or numerical data [186].

Considering these assumptions, the potential and kinetic energies can be written as Equations 5.4 and 5.5, respectively, where U_m is the magnetic potential and U_s is the potential energy of the structure.

$$\begin{aligned} U &= U_m + U_s \\ &= \frac{1}{2}\left(a_1 + k_1\right) z_1(t)^2 + \frac{1}{4} b_1 z_1(t)^4 + \frac{1}{2} a_2 z_2(t)^2 + \frac{1}{4} b_2 z_2(t)^4 \\ &\quad + \frac{1}{2} k_2 \left[z_2(t) - z_1(t)\right]^2, \end{aligned} \tag{5.4}$$

$$T = \sum_{i=1}^{2} \frac{1}{2} m_i \left[\dot{z}_i(t) + \dot{z}_b(t)\right]^2 . \tag{5.5}$$

The piezoelectric effect is considered by the definition of the total piezoelectric energy, W_e, as showed by PREUMONT [191], where the flux linkages are such that $\dot{\psi}_1(t) = v_1(t)$ and $\dot{\psi}_2(t) = v_2(t)$. Therefore:

$$W_e = \sum_{i=1}^{2} \left[\frac{1}{2} C_{p_i} \dot{\psi}_i(t)^2\right] + \theta_1 \dot{\psi}_1(t) z_1(t) + \theta_2 \dot{\psi}_2(t) \left[z_2(t) - z_1(t)\right]. \tag{5.6}$$

The total energy dissipation can be described by the sum of Rayleigh's dissipation function [192] and the electrical dissipation function as follows

$$D = \frac{1}{2} c_1 \dot{z}_1(t)^2 + \frac{1}{2} c_2 \left[\dot{z}_2(t) - \dot{z}_1(t)\right]^2 + \sum_{i=1}^{2} \left[\frac{\dot{\psi}_i(t)^2}{2R_i}\right]. \tag{5.7}$$

On this basis, by applying the Euler-Lagrange equations associated with the set $\mathbf{u}$ of generalized coordinates, the electromechanical equations of the system are determined:

$$\begin{aligned} m_1 \ddot{z}_1 + c_1 \dot{z}_1 - c_2 \left(\dot{z}_2 - \dot{z}_1\right) + \left(k_1 + a_1\right) z_1 + b_1 z_1^3 - k_2 \left(z_2 - z_1\right) \\ - \theta_1 v_1 + \theta_2 v_2 = -m_1 \ddot{z}_b; \end{aligned} \tag{5.8}$$

$$m_2 \ddot{z}_2 + c_2 \left(\dot{z}_2 - \dot{z}_1\right) + a_2 z_2 + b_2 z_2^3 + k_2 \left(z_2 - z_1\right) - \theta_2 v_2 = -m_2 \ddot{z}_b; \tag{5.9}$$

$$C_{p1} \dot{v}_1 + \frac{v_1}{R_1} + \theta_1 \dot{z}_1 = 0; \tag{5.10}$$

$$C_{p2} \dot{v}_2 + \frac{v_2}{R_2} + \theta_2 \left(\dot{z}_2 - \dot{z}_1\right) = 0. \tag{5.11}$$

The terms (t) that indicate time dependency are conveniently suppressed to improve readability.

A normalization approach, as detailed in Appendix C.1, is carried out by considering a reference length, L, and a reference voltage, V, resulting in the dimensionless electromechanical equations given by Equations 5.12 to 5.15, where the terms (τ)

that indicate normalized time dependency are also conveniently suppressed[1].

$$\begin{aligned}\ddot{\bar{z}}_1 + 2\zeta_1\dot{\bar{z}}_1 - 2\zeta_2\left(\dot{\bar{z}}_2 - \dot{\bar{z}}_1\right) + \left(1+\alpha_1\right)\bar{z}_1 + \beta_1\bar{z}_1^3 - \rho\Omega_s^2\left(\bar{z}_2 - \bar{z}_1\right) \\ - \chi_1\bar{v}_1 + \chi_2\bar{v}_2 = -\ddot{\bar{z}}_b;\end{aligned} \tag{5.12}$$

$$\rho\ddot{\bar{z}}_2 + 2\zeta_2\left(\dot{\bar{z}}_2 - \dot{\bar{z}}_1\right) + \alpha_2\bar{z}_2 + \beta_2\bar{z}_2^3 + \rho\Omega_s^2\left(\bar{z}_2 - \bar{z}_1\right) - \chi_2\bar{v}_2 = -\ddot{\bar{z}}_b; \tag{5.13}$$

$$\dot{\bar{v}}_1 + \varphi_1\bar{v}_1 + \kappa_1\dot{\bar{z}}_1 = 0; \tag{5.14}$$

$$\dot{\bar{v}}_2 + \varphi_2\bar{v}_2 + \kappa_2\left(\dot{\bar{z}}_2 - \dot{\bar{z}}_1\right) = 0. \tag{5.15}$$

The electromechanical system can be rewritten in its canonical form as follows:

$$\begin{aligned}\dot{\bar{\mathbf{q}}} &= \mathbf{f}(\bar{\mathbf{q}}) \\ &= \begin{bmatrix} \dot{\bar{z}}_1 \\ -2\zeta_1\dot{\bar{z}}_1 + 2\zeta_2\left(\dot{\bar{z}}_2 - \dot{\bar{z}}_1\right) - \left(1+\alpha_1\right)\bar{z}_1 - \beta_1\bar{z}_1^3 + \rho\Omega_s^2\left(\bar{z}_2 - \bar{z}_1\right) \\ \qquad + \chi_1\bar{v}_1 - \chi_2\bar{v}_2 - \ddot{\bar{z}}_b \\ \dot{\bar{z}}_2 \\ -\frac{1}{\rho}\left[2\zeta_2\left(\dot{\bar{z}}_2 - \dot{\bar{z}}_1\right) + \alpha_2\bar{z}_2 + \beta_2\bar{z}_2^3 - \chi_2\bar{v}_2\right] - \Omega_s^2\left(\bar{z}_2 - \bar{z}_1\right) - \ddot{\bar{z}}_b \\ -\varphi_1\bar{v}_1 - \kappa_1\dot{\bar{z}}_1 \\ -\varphi_2\bar{v}_2 - \kappa_2\left(\dot{\bar{z}}_2 - \dot{\bar{z}}_1\right) \end{bmatrix},\end{aligned} \tag{5.16}$$

with $\bar{\mathbf{q}} = [\bar{z}_1(\tau), \dot{\bar{z}}_1(\tau), \bar{z}_2(\tau), \dot{\bar{z}}_2(\tau), \bar{v}_1(\tau), \bar{v}_2(\tau)]$ and dimensionless parameters related to equations of motion are presented in Table 5.1. Also, a proper comprehension of the system behavior needs to consider the normalized form of the potential energy, expressed in Equation 5.17.

$$\bar{U} = \frac{1}{2}\left(1+\alpha_1\right)\bar{z}_1^2 + \frac{1}{4}\beta_1\bar{z}_1^4 + \frac{1}{2}\rho\Omega_s^2\left(\bar{z}_2 - \bar{z}_1\right)^2 + \frac{1}{2}\alpha_2\bar{z}_2^2 + \frac{1}{4}\beta_2\bar{z}_2^4. \tag{5.17}$$

5.1.1 Performance Metrics

The performance analysis of an energy harvester device is usually defined by the electrical output variables. In this regard, either instantaneous or average values can be monitored. The instantaneous electrical power in each resistive circuit is represented by Equation 5.18, where the subscript $\square_i$ $(i = 1, 2)$ represents each degree of freedom analyzed, and $\square^{\mathrm{RMS}}$ indicate the root mean square value.

$$P_{\mathrm{inst}_i}(t) = \frac{1}{R_i}v_i(t)^2, \tag{5.18}$$

[1]Note that upper dots in the normalized case are related to the derivatives with respect to the normalized time, as $\dot{\bar{\square}} = d\bar{\square}/d\tau$.

Table 5.1: System parameters and values used in the analyses. The values presented in this table are based on established literature sources [5, 6].

Parameter Description	Symbol	Definition	Value
Linearized natural frequency of the 1st mass	ω_1	$\sqrt{k_1/m_1}$	-
Linearized natural frequency of the 2nd mass	ω_2	$\sqrt{k_2/m_2}$	-
Normalized time	τ	$\omega_1 t$	-
Normalized displacement of the 1st mass	$\bar{z}_1(\tau)$	$z_1(t)/L$	-
Normalized displacement of the 2nd mass	$\bar{z}_2(\tau)$	$z_2(t)/L$	-
Normalized voltage of the 1st circuit	$\bar{v}_1(\tau)$	$v_1(t)/V$	-
Normalized voltage of the 2nd circuit	$\bar{v}_2(\tau)$	$v_2(t)/V$	-
Normalized base excitation frequency	Ω	ω/ω_1	$0.01 \rightarrow 10$
Normalized base excitation amplitude	γ	A_b/L	$0.01 \rightarrow 1$
Normalized base excitation displacement	$\bar{z}_b(\tau)$	$\gamma \sin(\Omega\tau)$	-
Ratio of masses	ρ	m_2/m_1	1
Normalized damping coef. of the 1st mechanical DoF	ζ_1	$c_1/(2\omega_1 m_1)$	0.025
Normalized damping coef. of the 2nd mechanical DoF	ζ_2	$c_2/(2\omega_1 m_1)$	0.025
Ratio of linearized natural frequencies	Ω_s	ω_2/ω_1	$0.25 \rightarrow 2.0$
Normalized 1st restitution coef. of the 1st mechanical DoF	α_1	$a_1/(\omega_1^2 m_1)$	$-2, 0, 1$
Normalized 1st restitution coef. of the 2nd mechanical DoF	α_2	$a_2/(\omega_1^2 m_1)$	$-1, 0, 1$
Normalized 2nd restitution coef. of the 1st mechanical DoF	β_1	$b_1 L^2/(\omega_1^2 m_1)$	1
Normalized 2nd restitution coef. of the 2nd mechanical DoF	β_2	$b_2 L^2/(\omega_1^2 m_1)$	1
Normalized 1st piezo coupling coef. in the mechanical ODE	χ_1	$\theta_1 V/(k_1 L)$	0.05
Normalized 2nd piezo coupling coef. in the mechanical ODE	χ_2	$\theta_2 V/(k_1 L)$	0.05
Normalized 1st piezo coupling coef. in the electrical ODE	κ_1	$\theta_1 L/(C_{p1} V)$	0.5
Normalized 2nd piezo coupling coef. in the electrical ODE	κ_2	$\theta_2 L/(C_{p2} V)$	0.5
Normalized electrical conductance of the 1st circuit	φ_1	$1/(C_{p1} R_1 \omega_1)$	0.05
Normalized electrical conductance of the 2nd circuit	φ_2	$1/(C_{p2} R_2 \omega_1)$	0.05
Normalized output power of the 1st electrical DoF	$\bar{P}_{\text{inst}_1}(\tau)$	$P_{\text{inst}_1}(t)/(C_{p1}\omega_1 V^2)$	-
Normalized output power of the 2nd electrical DoF	$\bar{P}_{\text{inst}_2}(\tau)$	$P_{\text{inst}_2}(t)/(C_{p2}\omega_1 V^2)$	-

The average output power can, then, be evaluated by the sum of the average output power of each circuit, as expressed in Equation 5.19.

$$P_{\text{avg}} = \sum_{i=1}^{2} P_{\text{avg}_i} = \sum_{i=1}^{2} \left[\frac{1}{t_f - t_0} \int_{t_0}^{t_f} P_{\text{inst}_i}(t)\, dt \right] = \sum_{i=1}^{2} \left[\frac{1}{R_i} \left(v_i^{\text{RMS}} \right)^2 \right]. \tag{5.19}$$

Furthermore, an average power density can be calculated by dividing the average power by the number of degrees-of-freedom of the system (n_{DoF}), resulting in Equation 5.20.

$$P_{\text{avg}}^{\text{den}} = \frac{P_{\text{avg}}}{n_{\text{DoF}}}. \tag{5.20}$$

Based on these concepts and according to Table 5.1, the normalized average electrical output power and the normalized average electrical output power density can be determined by Equations 5.21 and 5.22, respectively.

$$\bar{P}_{\text{avg}} = \sum_{i=1}^{2} \bar{P}_{\text{avg}_i} = \sum_{i=1}^{2} \left[\frac{1}{\tau_f - \tau_0} \int_{\tau_0}^{\tau_f} \bar{P}_{\text{inst}_i}(t)\, dt \right] = \sum_{i=1}^{2} \left[\varphi_i \left(\bar{v}_i^{\text{RMS}} \right)^2 \right], \tag{5.21}$$

$$\bar{P}_{\text{avg}}^{\text{den}} = \frac{\bar{P}_{\text{avg}}}{n_{\text{DoF}}}. \tag{5.22}$$

5.2 Stability Analysis

The magnetic interactions within the system and the elastic properties of the structure have shown to be an interesting point to be investigated since they are directly related to the possible stability states of the system, which, in turn, hold the potential to amplify its energy harvesting capabilities.

Following the definitions presented in Chapter 3, Section 3.1.4, the equilibrium configurations of the system can be determined by solving Equation 5.23.

$$\dot{\bar{\mathbf{q}}} = \mathbf{f}(\bar{\mathbf{q}}) = \mathbf{0}. \tag{5.23}$$

Yielding a solution containing a group of sets of the form $\bar{\mathbf{q}} = \{\bar{z}_1, \dot{\bar{z}}_1, \bar{z}_2, \dot{\bar{z}}_2, \bar{v}_1, \bar{v}_2\}_j = \left\{\bar{Z}_1, 0, \bar{Z}_2, 0, 0, 0\right\}_j$ that determines each equilibrium position, where j determines the specific set within the solution. The nature of each equilibrium point can be determined through a linearization around each point, evaluating the eigenvalues of the Jacobian matrix, $\mathbf{J}$, displayed in Equation 5.24

$$\begin{aligned}\mathbf{J} &= \nabla^{\mathrm{T}}\mathbf{f}(\bar{\mathbf{q}}) \\ &= \begin{bmatrix} 0 & 1 & 0 & 0 & 0 & 0 \\ -1-\alpha_1-\rho\Omega_s^2-3\beta_1\bar{z}_1^2 & -2\left(\zeta_1+\zeta_2\right) & \rho\Omega_s^2 & 2\zeta_2 & \chi_1 & -\chi_2 \\ 0 & 0 & 0 & 1 & 0 & 0 \\ \Omega_s^2 & \dfrac{2\zeta_2}{\rho} & -\dfrac{\alpha_2+\rho\Omega_s^2+3\beta_2\bar{z}_2^2}{\rho} & -\dfrac{2\zeta_2}{\rho} & 0 & \dfrac{\chi_2}{\rho} \\ 0 & -\kappa_1 & 0 & 0 & -\varphi_1 & 0 \\ 0 & \kappa_2 & 0 & -\kappa_2 & 0 & -\varphi_2 \end{bmatrix}\end{aligned} \tag{5.24}$$

Results show that for this system, all solutions are hyperbolic and, additionally to the definitions presented in Chapter 3, the unstable points can be split into two distinct groups: saddle-type unstable points and source-type unstable points. Saddle-type unstable points exhibit one positive eigenvalue, indicating the presence of a single unstable direction. On the other hand, source-type unstable points exhibit two positive eigenvalues, indicating the presence of two unstable directions. Furthermore, the stability analysis is further complemented by evaluating the normalized form of the potential energy function, as detailed in Equation 5.17, and the basins of attraction of the non-forced system, providing a comprehensive understanding of the system's stability characteristics.

5.2.1 The Influence of Ω and ρ

The analysis of the influence of Ω_s and ρ in the stability characteristics of the system is now in focus. For that, consider the fixed set of restitution parameters $(\alpha_1, \alpha_2, \beta_1, \beta_2) = (-2, -1, 1, 1)$, associated with localized bistability in each DoF,

as previously discussed in Chapter 4. The solution sets $\{\bar{z}_1, \dot{\bar{z}}_1, \bar{z}_2, \dot{\bar{z}}_2, \bar{v}_1, \bar{v}_2\}_j = \{\bar{Z}_1, 0, \bar{Z}_2, 0, 0, 0\}_j$ allow the visualization of stability characteristics through the subsets $\{\bar{z}_1, \bar{z}_2\}_j = \{\bar{Z}_1, \bar{Z}_2\}_j$, and their respective subspace $\bar{z}_1 \times \bar{z}_2$, as the other values are zero and do not change. Consequently, from this point forward, the term "basin of attraction" will be used as a shorthand for the expression "section of the basin of attraction", as the basins of attraction of the system have 6 dimensions, while the analysis is reduced to a section of the basin with 2 dimensions.

Figure 5.3 illustrates the stability for different values of Ω_s, with a fixed mass ratio of $\rho = 1$. The colorbar represents the potential energy levels, with darker colors representing lower energies and lighter colors representing higher energies. Figure

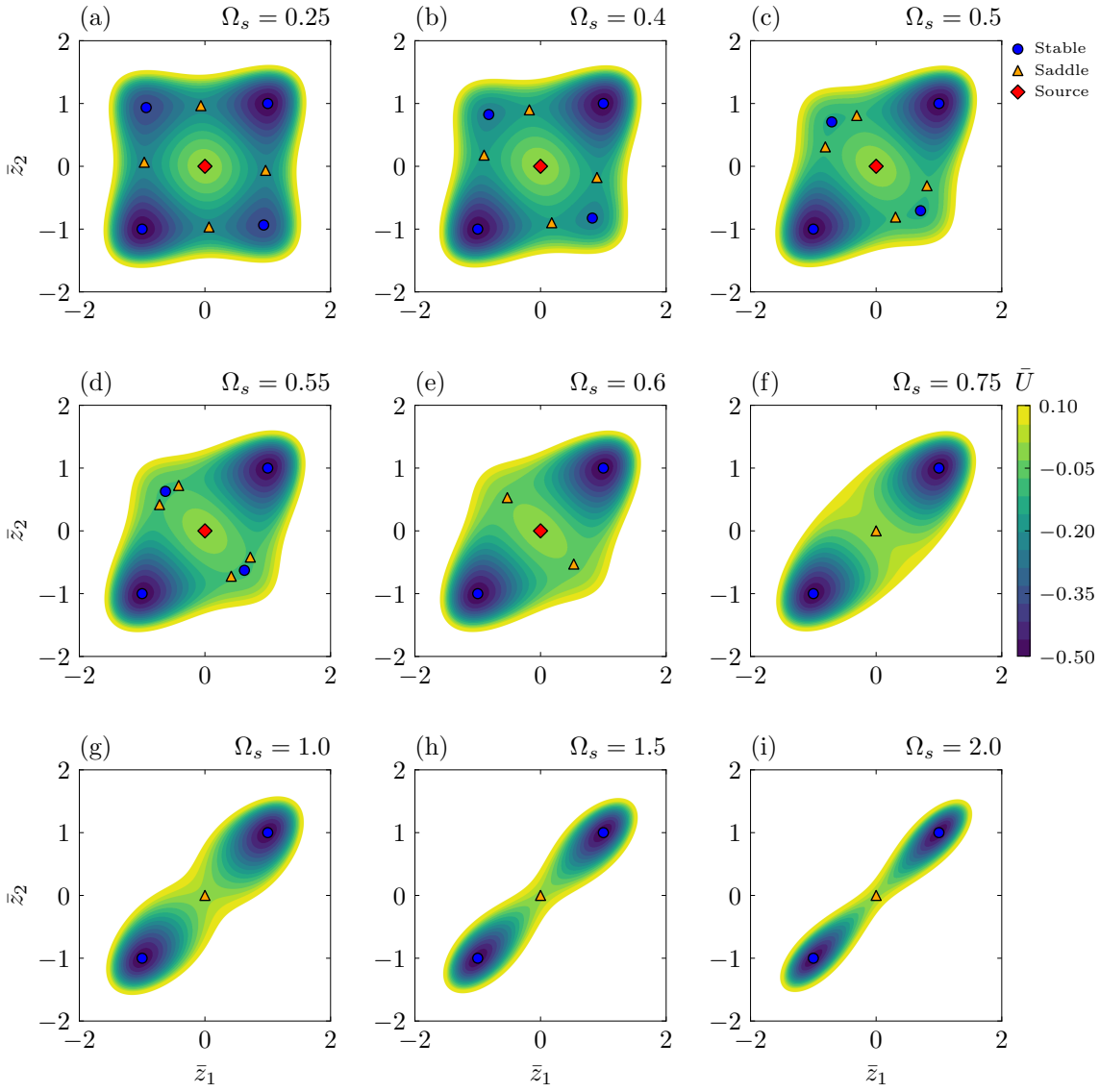

Figure 5.3: Stability configurations for a set of Ω_s values, with a fix mass ratio of $\rho = 1$. The colorbar indicates the potential energy level for each $\bar{z}_1$ and $\bar{z}_2$ positions. Blue dots represent stable equilibria, orange triangles represent unstable saddle-type equilibria, and red polygons represent unstable source-type equilibria.

5.4 presents the basins of attraction for different Ω_s using four colors to indicate attractors, which are the stable equilibrium points (SEP_i, $i = 1, \ldots, 4$) where the system converges to if released from initial conditions within the subspace domain $\bar{z}_1 \times \bar{z}_2$, where $\bar{z}_1 \in [-2, 2]$ and $\bar{z}_2 \in [-2, 2]$, and $\dot{\bar{z}}_1 = \dot{\bar{z}}_2 = \bar{v}_1 = \bar{v}_2 = 0$. In both Figures, blue dots indicate stable equilibria, orange triangles indicate unstable saddle-type equilibria and red polygons (diamonds) indicate unstable source-type equilibria. Also, a grid of 2000×2000 points is used in each basin plot.

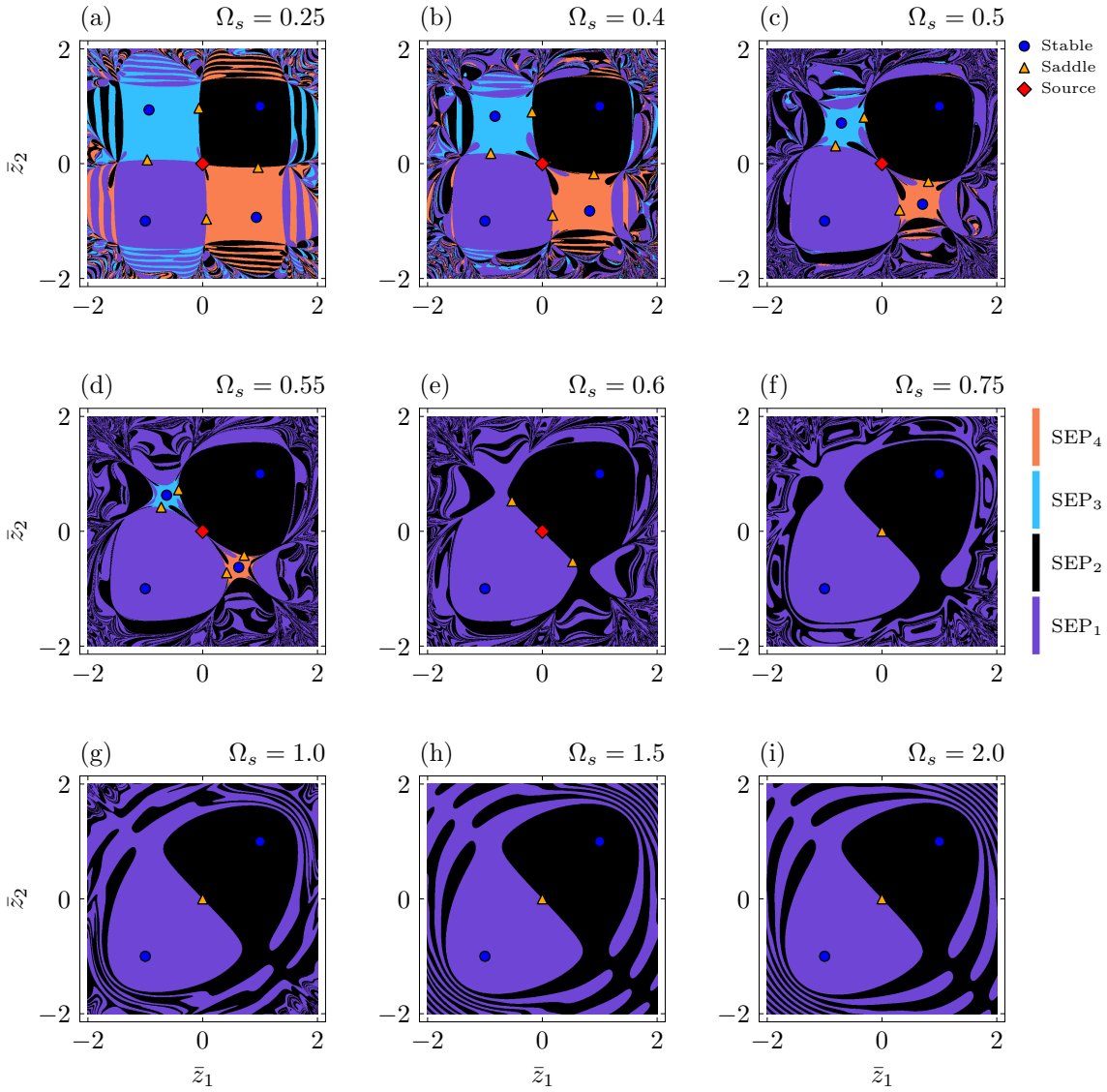

Figure 5.4: Basins of attraction for a set of Ω_s values, with a fix mass ratio of $\rho = 1$. Colors indicate the stable position the system is attracted to for each $\bar{z}_1$ and $\bar{z}_2$ initial positions. Blue dots represent stable equilibria, orange triangles represent unstable saddle-type equilibria and red polygons represent unstable source-type equilibria.

It is noticeable that for $\Omega_s < 0.6$, the system exhibits 9 equilibrium positions, 4 of which are stable, 4 are unstable saddle-type, and 1 is unstable source-type.

The increase of Ω_s results in a reduction of the distances between SEP_3, SEP_4, and the saddle-type points in their vicinity, which elevates the potential energy level of the local minima and decreases the likelihood of the system being attracted towards SEP_3 and SEP_4. When Ω_s reaches a value between 0.55 and 0.6, SEP_3 and SEP_4 disappear, becoming new saddle-type unstable points. This behavior defines 5 equilibrium points, with 2 stable, 2 saddle-type unstable, and 1 source-type unstable. Further, 2 of 3 unstable positions disappear between $0.6 < \Omega_s < 0.75$, resulting in a system with 3 equilibrium positions, of which 2 are stable and 1 is saddle-type unstable. The configuration remains the same for $\Omega_s > 0.75$ and the potential energy surface becomes thinner as Ω_s increases.

The impact of the mass ratio, ρ, on the stability of the system is analyzed in Figures 5.5 and 5.6, where Ω_s is kept constant at 0.5. Results show that the increase of ρ results in a slower reduction of the number of equilibrium points. This can be attributed to the term $\rho\Omega_s^2$ in Equations 12 and 13, where the influence of ρ is of first order and the influence of Ω_s is of second order. Furthermore, $\rho\Omega_s^2 = m_2\omega_2^2/(m_1\omega_1^2) = k_2/k_1$. By analyzing this term along with the results obtained in this section, it is concluded that a softer inner beam in comparison to the outer beam results in a more complex equilibrium state characterized by multistability, while stiffening the inner beam leads to bistability.

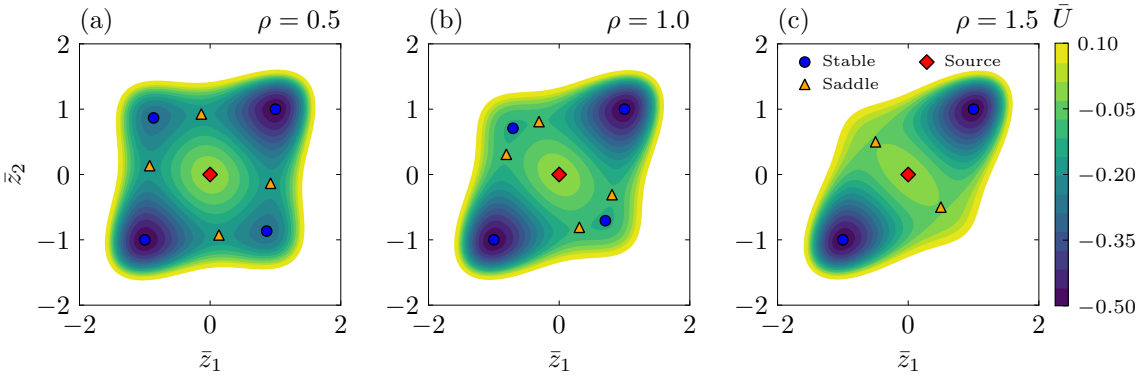

Figure 5.5: Stability configurations for a set of ρ values, with a fix natural frequency ratio of $\Omega_s = 0.5$. The colorbar indicates the potential energy level for each $\bar{z}_1$ and $\bar{z}_2$ position. Blue dots represent stable equilibria, orange triangles represent unstable saddle-type equilibria and red polygons represent unstable source-type equilibria.

Figure 5.7 presents an illustrative representation of the four possible stable equilibrium states of the system. As depicted in Figures 5.7a and 5.7b, the stable positions that persist under all stability configurations (SEP_1 and SEP_2) can be observed, while Figures 5.7c and 5.7d show the stable positions that vanish at elevated values of Ω_s (SEP_3 and SEP_4) according to this model.

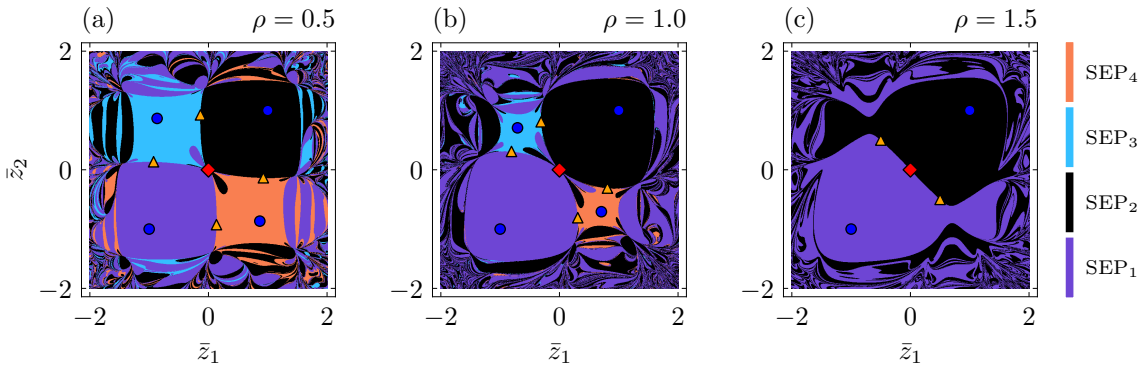

Figure 5.6: Basins of attraction for a set of ρ values, considering a fix natural frequency ratio of $\Omega_s = 0.5$. Colors indicate the stable position the system is attracted to for each $\bar{z}_1$ and $\bar{z}_2$ initial position. Blue dots represent stable equilibria, orange triangles represent unstable saddle-type equilibria, and red polygons represent unstable source-type equilibria.

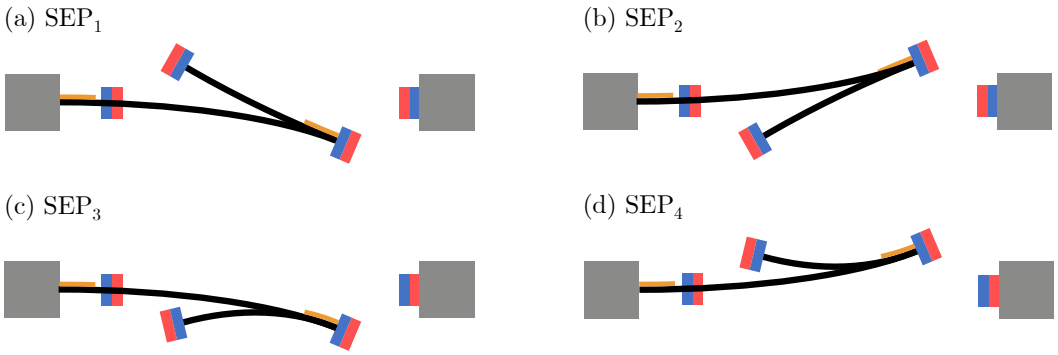

Figure 5.7: Representation of the four possible stable equilibrium states of the system: (a) SEP$_1$, (b) SEP$_2$, (c) SEP$_3$ and (d) SEP$_4$.

5.2.2 The Influence of Different Magnetic Configurations

The magnetic restitution parameters (α_1, α_2, β_1, and β_2) represent the effects of the magnetic field defined by the magnet positioning within the system and its material properties. Different combinations of these parameters can also lead to different stability conditions. Moreover, based on the previous analysis, it was shown that the stiffening/softening of the inner beam relative to the outer beam can alter significantly the stability characteristics of the system. This prior knowledge enables a better understanding of the coupling effects of the magnetic interactions and the elastic properties of the structure.

The relation $k_2/k_1 = \omega_2^2 m_2 / (\omega_1^2 m_1) = \Omega_s^2 \rho$ allows the elastic properties of the system to be represented either by Ω_s or ρ, as they change the k_2/k_1 relation at different rates. Therefore, for this analysis Ω_s is chosen to represent the stiffness

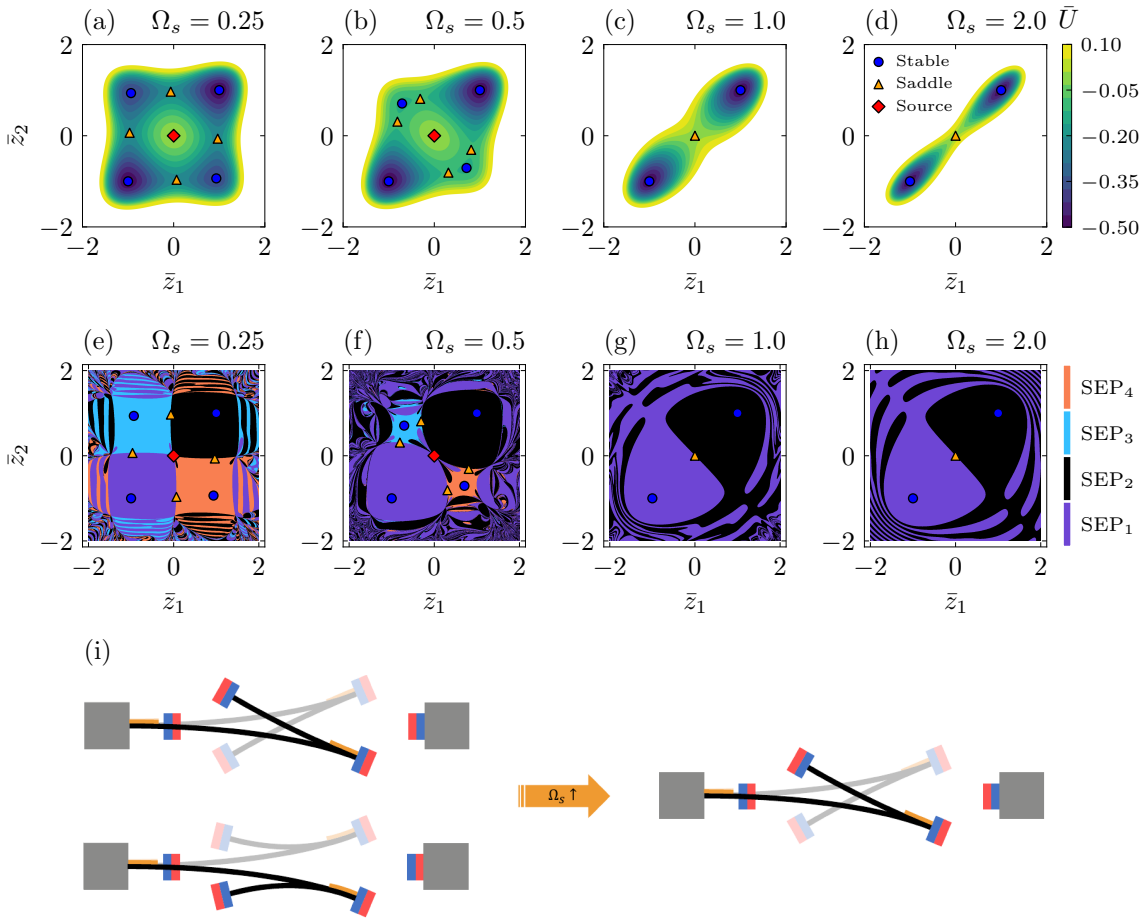

Figure 5.8: Stability configurations for a set of Ω_s values, with magnetic restitution coefficients $(\alpha_1, \alpha_2, \beta_1, \beta_2) = (-2, -1, 1, 1)$ and a fix mass ratio of $\rho = 1$. The first row shows potential energy levels for each configuration (a) $\Omega_s = 0.25$, (b) $\Omega_s = 0.5$, (c) $\Omega_s = 1$, and (d) $\Omega_s = 2$. The second row shows the basins of attraction evolution for each configuration (e) $\Omega_s = 0.25$, (f) $\Omega_s = 0.5$, (g) $\Omega_s = 1$, and (h) $\Omega_s = 2$. Blue, red and orange dots represent equilibria as previously described in the text. (i) One possible representation of the stable equilibrium states as Ω_s increases.

changes, and a constant value of $\rho = 1$ is assumed. With these assumptions in place, additional stability analyses are conducted and summarized in Figures 5.8, 5.9, 5.10 and 5.11. Each figure represents a different configuration defined by a set of values for the magnetic restitution parameters α_1, α_2, β_1, and β_2. In each case, the stability state is determined for different values of Ω_s. In the first row (letters a, b, c and d) the potential energy levels are associated with the equilibrium positions and their vicinity, while the second row (letters e, f, g and h) shows the respective basins of attraction of each potential energy plot. In both rows, blue dots, orange triangles, and red polygons represent the equilibrium position and its respective nature. Also, for each case, the stability plots are followed by a possible representation of the initial and final stable equilibrium states, related to the beam

structure, as Ω_s increases (letter i).

Figure 5.8 displays the case previously presented in subsection 5.2.1, with $(\alpha_1, \alpha_2, \beta_1, \beta_2) = (-2, -1, 1, 1)$, related to the configuration represented in Figure 5.8i where the two sets of magnets are set up in repulsive mode. In this case, for low values of $\Omega_s < 0.5$, that is, when the inner beam is softer than the outer beam, the system exhibits 9 equilibrium positions, 4 of them stable and 5 unstable, which means that a tetrastable system is of concern. By increasing the stiffness of the inner beam with respect to the outer beam, the structure's restitution force becomes stronger than the magnetic force, eliminating 6 equilibrium positions, and resulting in a bistable configuration with 2 stable equilibrium positions and 1 unstable.

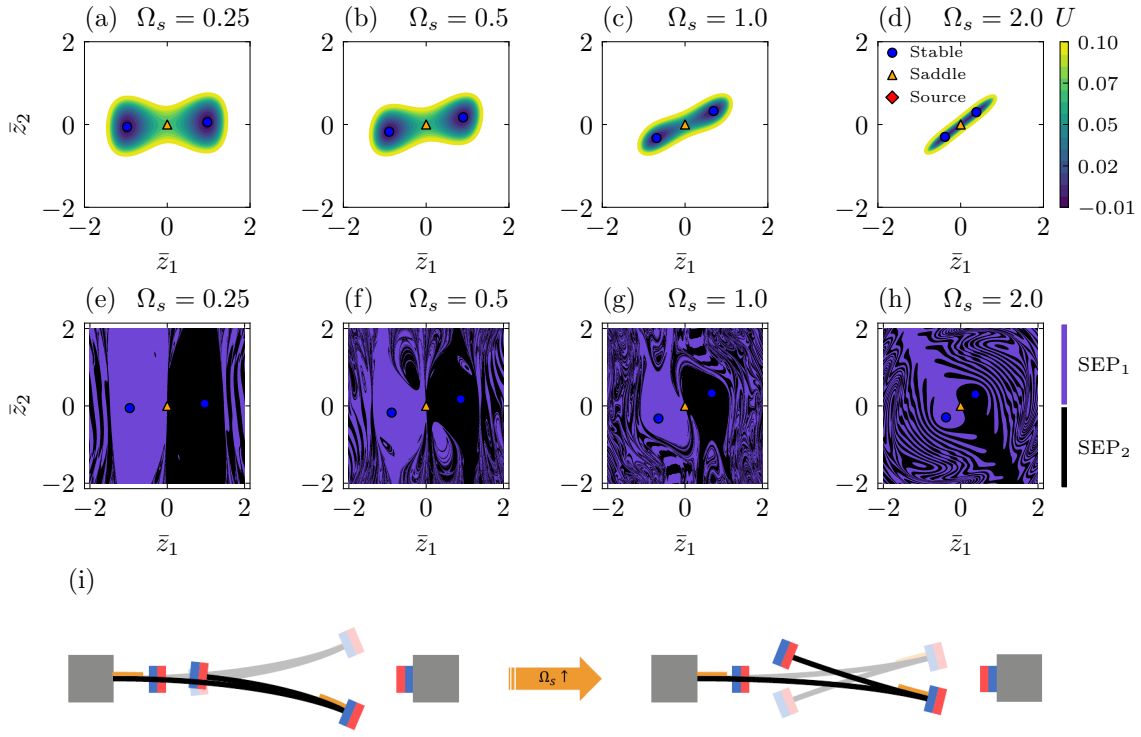

Figure 5.9: Stability configurations for a set of Ω_s values, with magnetic restitution coefficients $(\alpha_1, \alpha_2, \beta_1, \beta_2) = (-2, 1, 1, 1)$ and a fix mass ratio of $\rho = 1$. The first row represents the potential energy levels for each configuration (a) $\Omega_s = 0.25$, (b) $\Omega_s = 0.5$, (c) $\Omega_s = 1$, and (d) $\Omega_s = 2$. The second row represents the basins of attraction evolution for each configuration (e) $\Omega_s = 0.25$, (f) $\Omega_s = 0.5$, (g) $\Omega_s = 1$, and (h) $\Omega_s = 2$. Blue, red and orange dots represent equilibria as previously described in the text. (i) One possible representation of the stable equilibrium states as Ω_s increases.

Figure 5.9 shows a case with $(\alpha_1, \alpha_2, \beta_1, \beta_2) = (-2, 1, 1, 1)$. In this case, for all values of Ω_s, the system remains in bistable mode. A possible representation of this case is presented in Figure 5.9e, where the set of magnets attached to the outer beam remains in repulsive mode, while the set of magnets related to the inner

beam is set up to attractive mode. With a softer inner beam, it tends to retain the position of the inner beam close to zero as the magnetic force is stronger than the inner beam structure's restitution force. By increasing Ω_s, the enhancement in inner beam stiffness tends to increase the distance of its equilibrium position with respect to the neutral axis, while reducing the distance of the outer beam equilibrium position. Another possible representation of this case can retain the repulsive mode of the inner beam, but with an increased distance between the magnets, sufficient to not induce a change in stability of the inner beam, and remaining with the nonlinear characteristics. The final state of this configuration, represented in Figure 5.9d, is similar to the one shown in Figure 5.8d, but with a shorter distance between stable equilibrium positions.

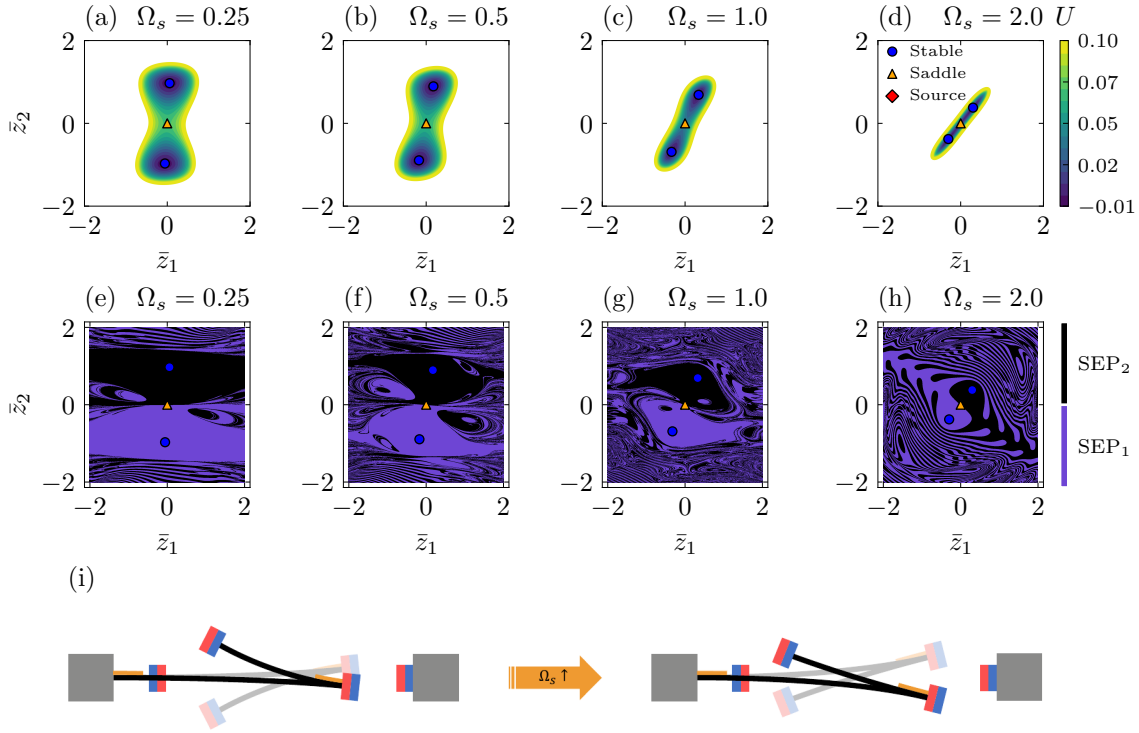

Figure 5.10: Stability configurations for a set of Ω_s values, with magnetic restitution coefficients $(\alpha_1, \alpha_2, \beta_1, \beta_2) = (0, -1, 1, 1)$ and a fix mass ratio of $\rho = 1$. The first row represents the potential energy levels for each configuration (a) $\Omega_s = 0.25$, (b) $\Omega_s = 0.5$, (c) $\Omega_s = 1$, and (d) $\Omega_s = 2$. The second row represents the basins of attraction evolution for each configuration (e) $\Omega_s = 0.25$, (f) $\Omega_s = 0.5$, (g) $\Omega_s = 1$, and (h) $\Omega_s = 2$. Blue, red and orange dots represent equilibria as previously described in the text. (i) One possible representation of the stable equilibrium states as Ω_s increases.

Figure 5.10 represent a case with $(\alpha_1, \alpha_2, \beta_1, \beta_2) = (0, -1, 1, 1)$. This case also consists of a bistable characteristic for all values of Ω_s analyzed. A possible representation for this configuration is presented in Figure 5.10e where the magnets related

to the outer beam are set up in attractive mode, while the magnets of the inner beam are arranged in repulsive mode. Similar to the previous case, a softer inner beam presents a higher amplitude than the outer beam. The force transmitted by the repulsive magnets to the beam structure causes a small deflection in the outer beam, translating its equilibrium position off the neutral axis. By increasing Ω_s, the stiffness of the inner beam increases, leading to an increase in the deflection of the outer beam, and a reduction in the reflection of the inner beam. Another representation of this state can retain the repulsive characteristics of the outer beam's magnets but with increased distance between them. This would retain the nonlinear characteristics but the forces between the magnets would not be sufficient to induce more equilibrium positions. The final state of this configuration, represented in Figure 5.10d, is similar to the final state configuration of the previous case, as shown in Figure 5.9d.

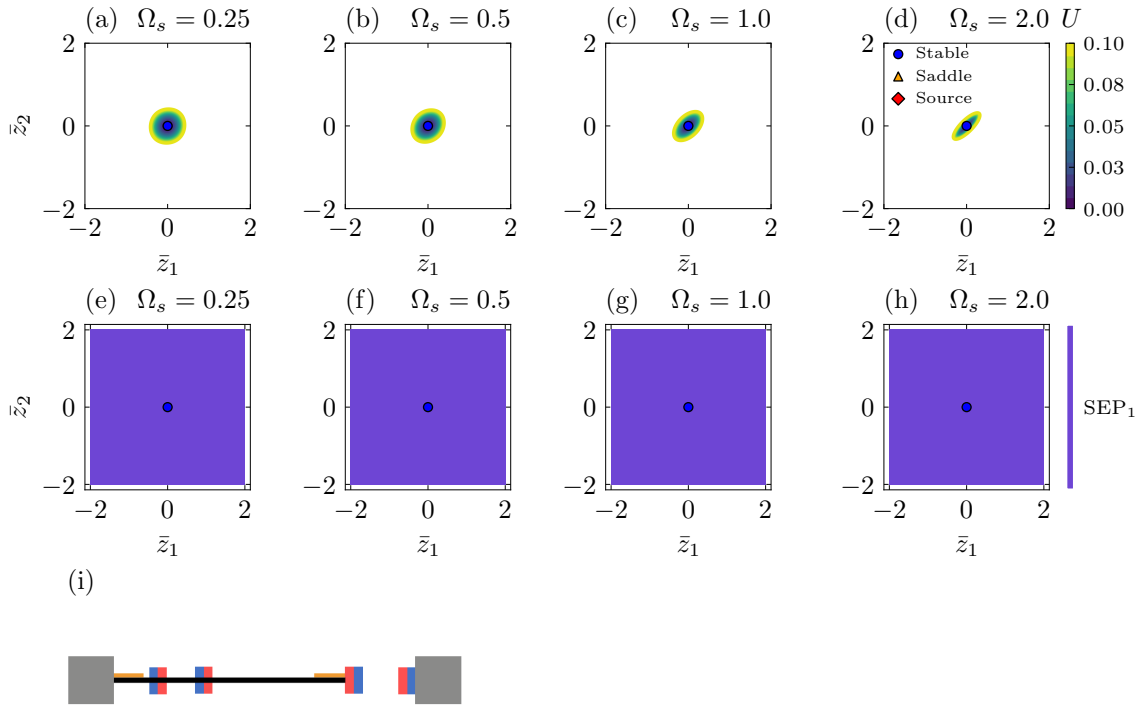

Figure 5.11: Stability configurations for a set of Ω_s values, with magnetic restitution coefficients $(\alpha_1, \alpha_2, \beta_1, \beta_2) = (0, 1, 1, 1)$ and a fix mass ratio of $\rho = 1$. The first row represents the potential energy levels for each configuration (a) $\Omega_s = 0.25$, (b) $\Omega_s = 0.5$, (c) $\Omega_s = 1$, and (d) $\Omega_s = 2$. The second row represents the basins of attraction evolution for each configuration (e) $\Omega_s = 0.25$, (f) $\Omega_s = 0.5$, (g) $\Omega_s = 1$, and (h) $\Omega_s = 2$. Blue, red and orange dots represent equilibria as previously described in the text. (i) One possible representation of the stable equilibrium states as Ω_s increases.

The last equilibrium state found is depicted in Figure 5.11. In this case, the

system presents monostable characteristics for all values of Ω_s. Possible representations of this state comprise the two sets of magnets set up in attractive mode or repulsive mode, but with increased distance between magnets to make the magnetic interactions weak, but remaining nonlinear.

5.3 Dynamical Analysis

This section presents a comprehensive analysis of the nonlinear dynamics and performance of the proposed harvester. Initially, the more complex configuration with $(\alpha_1, \alpha_2, \beta_1, \beta_2) = (-2, -1, 1, 1)$ is chosen and a general overview of its characteristics within the external excitation parameter domain is displayed. Subsequently, based on the conclusions of the stability analysis presented in Section 3.1.4, eight configurations with different magnetic and structural parameters are chosen and labeled and a detailed performance analysis is conducted to determine the best operational conditions of each configuration. These analyses allow the selection of a better magnetic configuration for energy harvesting purposes. Then, a performance comparison is performed between various designs within this configuration, each featuring distinct elastic properties, and the classical bistable energy harvester.

5.3.1 General Overview of the System's Dynamics and Performance

The stability analysis shows that stiffening the inner beam with respect to the outer beam changes completely the stability characteristics of the system. By changing either the value of ρ or the value of Ω_s, it tends to converge to the same result at different rates. Therefore, in the context of a dynamical perspective, it is reasonable to vary one parameter keeping the other constant as done before.

A harmonic excitation displacement of the form $\bar{z}_b = \gamma \sin(\Omega\tau)$ is adopted to represent the available ambient mechanical energy, being γ the normalized excitation amplitude, and Ω the normalized excitation frequency. Numerical analyses are carried out by evaluating the influence of the linearized natural frequency ratio parameter, Ω_s, with a constant $\rho = 1$. The other parameters are summarized in Table 5.1. The analyses are based on the theory and the diagrams established in Chapter 3. The diagrams are built with a grid of 1000×1000 sample points within the $\gamma \times \Omega$ parameter domain, each of which is obtained from a time series from numerical integration employing the fourth-order Runge-Kutta method considering time steps $\Delta\tau \propto (\mathrm{T} = 2\pi/\Omega)$. For each sample point, 4000 excitation periods (4000T) are imposed, with the last 500 considered to be the steady state, that is, when $\tau \geq 0.875\tau_f$. τ_f denotes the final time of integration.

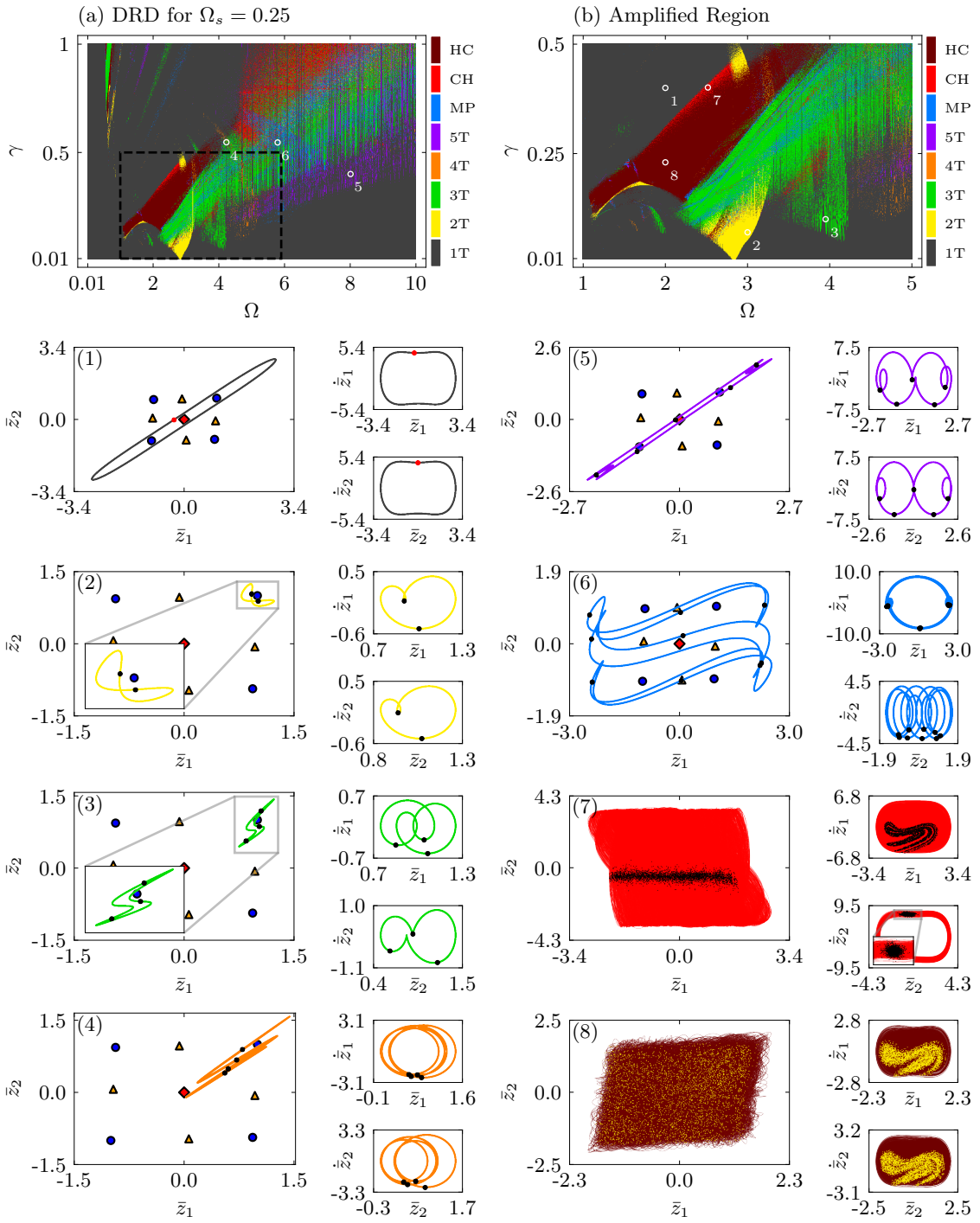

Figure 5.12: DRDs for a configuration with 4 stable and 5 unstable equilibria ($\Omega_s = 0.25$). (b) Amplified region delimited by the black dashed square in (a). Each color represents a dynamical attractor. White circles followed by numbers in (a) and (b) represent examples of the attractors contained in the DRD. Three phase subspaces of the system's steady-state response ($\bar{z}_1 \times \bar{z}_2$, $\bar{z}_1 \times \dot{\bar{z}}_1$ and $\bar{z}_2 \times \dot{\bar{z}}_2$) are plotted, colored and numbered according to the respective attractor marked in the DRDs.

The analysis is carried out by selecting two specific designs based on their stability characteristics: the first configuration features 4 stable equilibrium points,

being characterized by $\Omega_s = 0.25$; the second configuration has 2 stable equilibrium points, being represented by $\Omega_s = 1.0$. The initial conditions are $[\bar{z}_1(0), \dot{\bar{z}}_1(0), \bar{z}_2(0), \dot{\bar{z}}_2(0), \bar{v}_1(0), \bar{v}_2(0)] = [1, 0, 1, 0, 0, 0]$, which correspond to SEP_2, a stable position that persists throughout all stability configurations with $(\alpha_1, \alpha_2, \beta_1, \beta_2) = (-2, -1, 1, 1)$. Using these diagrams, a comprehensive overview of the system's dynamical characteristics and performance at different operational conditions are elucidated.

Figures 5.12, 5.13 and 5.14 depict examples of DRDs and LEDs for the two treated configurations. Examples of the dynamical attractor for each configuration are depicted in Figures 5.12 and 5.13, just below the corresponding DRDs. The chosen examples are identified by white circles with numbered labels within the DRDs. These labels represent the three phase subspaces ($\bar{z}_1 \times \bar{z}_2$, $\bar{z}_1 \times \dot{\bar{z}}_1$ and $\bar{z}_2 \times \dot{\bar{z}}_2$) of the system steady-state response, which are plotted, labeled, and color-coded according to the attractor designation in the DRDs. The Poincaré maps are depicted as dots in each phase subspace and the equilibrium positions discussed in Section 3.1.4 are useful for spatial references in the $\bar{z}_1 \times \bar{z}_2$ phase subspaces.

For the case of $\Omega_s = 0.25$, the orbits with periods of 2T, 3T and 4T are observed to be trapped around SEP_2, indicating that the system lacks sufficient energy to overcome the local potential energy minima (potential energy well). In contrast, the remaining examples display orbits with high amplitude displacements. The orbits with periods of 1T and 5T are characterized by synchronized or nearly synchronized behavior, where $\bar{z}_1$ and $\bar{z}_2$ show a coordinated motion, causing the system to oscillate around only three equilibrium positions. Conversely, the orbits characterized by multiple periods (MP), chaos (CH), and hyperchaos (HC) exhibit desynchronized or complex behavior, leading the system to visit all possible equilibrium points.

The case with $\Omega_s = 1.0$ reveals that the example orbits with periods of 1T and 5T are trapped around stable equilibrium positions, with the 5T orbit being confined around SEP_2, and the 1T orbit being confined around SEP_1. In general (for any case of Ω_s), this suggests that the system dynamics may start at one stable equilibrium position (SEP_2) and end up being trapped around another (SEP_1) due to transient motion. The remaining periodic example orbits show high amplitude displacements and visit all the equilibrium positions, leading to synchronized or nearly synchronized behavior as depicted in the phase subspaces $\bar{z}_1 \times \dot{\bar{z}}_1$ and $\bar{z}_2 \times \dot{\bar{z}}_2$ of each example. The chaotic (CH) and hyperchaotic (HC) examples, similar to previous cases, also show high amplitude displacements and exhibit desynchronized or complex behavior. Therefore, an effort is made to select orbits that differed from those chosen in the previous case, highlighting that these classified dynamical attractors merely indicate the periodicity of motion, and not necessarily the amplitude of motion or complex behaviors as synchronization.

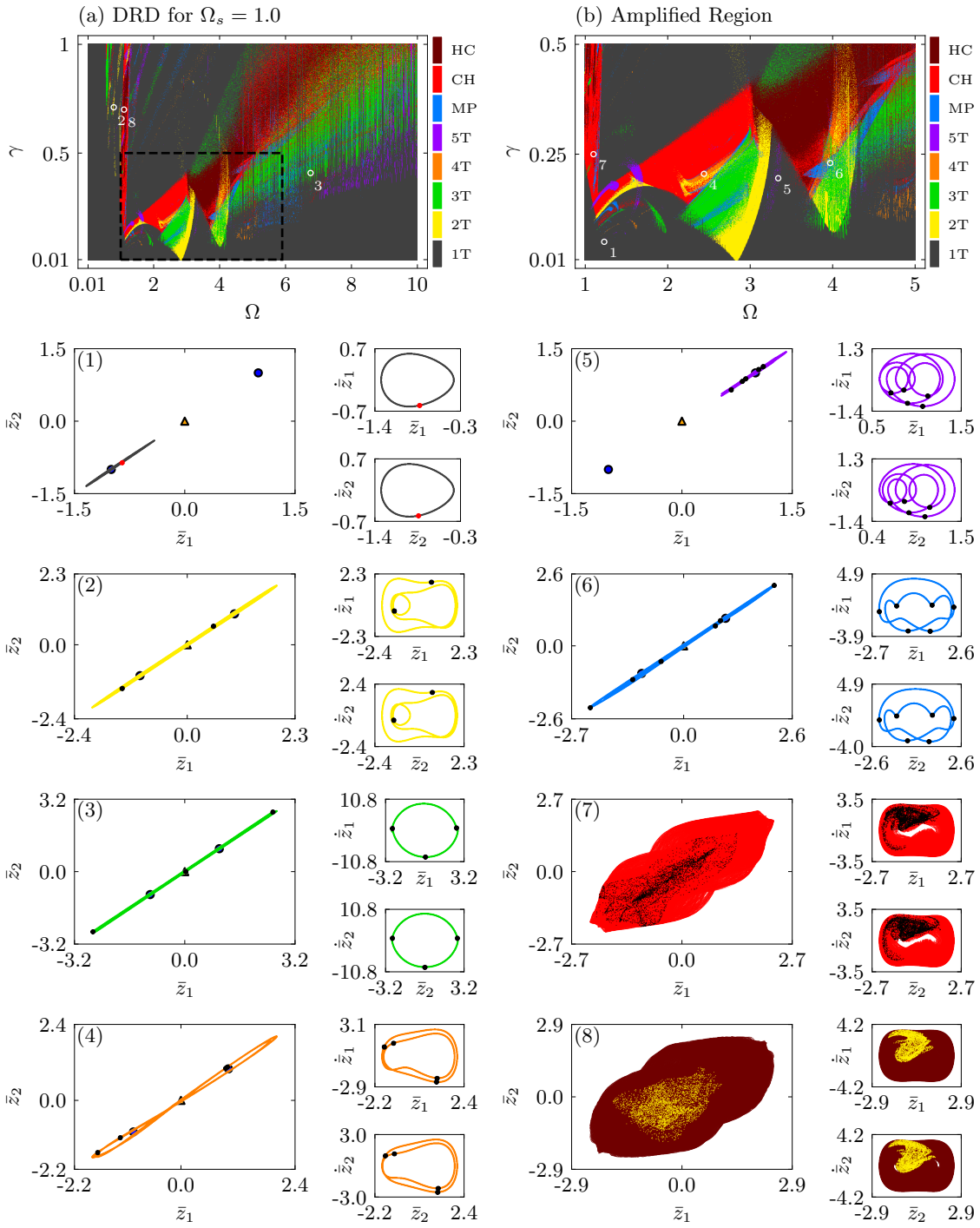

Figure 5.13: DRDs for a configuration with 2 stable and 1 unstable equilibrium points ($\Omega_s = 1.0$). (b) Amplified region delimited by the black dashed square in (a). Each color represents a dynamical attractor. White circles labeled by numbers in (a) and (b) represent examples of the attractors contained in the DRD. Three phase subspaces of the system's steady-state response ($\bar{z}_1 \times \bar{z}_2$, $\bar{z}_1 \times \dot{\bar{z}}_1$ and $\bar{z}_2 \times \dot{\bar{z}}_2$) are plotted, colored and numbered according to the respective attractor marked in the DRDs.

Finally, it is also important to note that the distinction between chaotic and hyperchaotic attractors is based on the number of instability directions. Chaotic attractors are represented by a single positive Lyapunov exponent ($\lambda_1 > 0$) with the remaining being negative, whereas hyperchaotic attractors have at least two positive exponents ($\lambda_1 > 0$ and $\lambda_2 > 0$). This can be observed in the Lyapunov Exponent Diagrams (LEDs) presented in Figure 5.14.

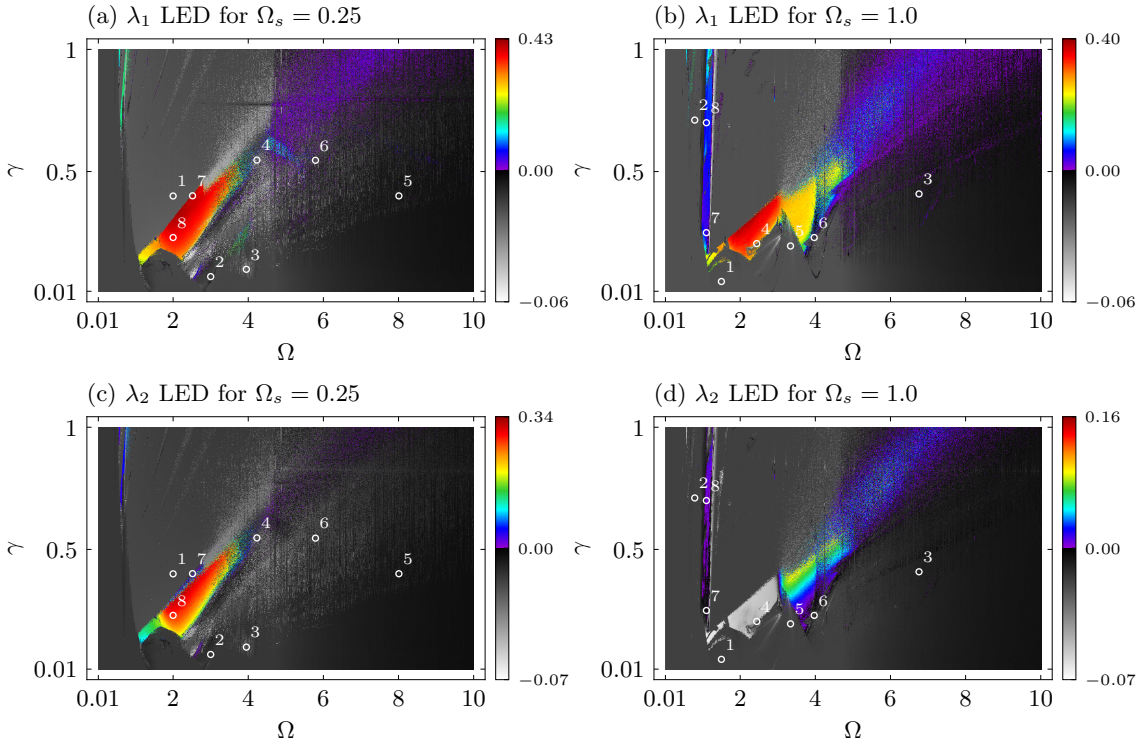

Figure 5.14: Lyapunov Exponent Diagrams (LEDs) for the two largest exponents (λ_1 and λ_2) for each case of Ω_s: (a) λ_1 for $\Omega_s = 0.25$, (b) λ_1 for $\Omega_s = 1.0$, (c) λ_2 for $\Omega_s = 0.25$, and (d) λ_2 for $\Omega_s = 1.0$. Rainbow colors represent positive exponents, while grayscale colors represent negative exponents. White circles followed by numbers represent the attractors exemplified in Figures 5.12 and 5.13.

Energy harvesting performance is now in focus. Figure 5.15 presents the average output power diagrams (OPDs) for the two configurations of $\Omega_s = 0.25$ and $\Omega_s = 1.0$. The OPDs are divided into six sub-figures, with Figures 5.15a and 5.15b showing the contribution of the first degree of freedom to the performance, Figures 5.15c and 5.15d displaying the contribution of the second degree of freedom, and Figures 5.15e and 5.15f showing the overall average output power converted by the harvester. The accompanying colorbars illustrate the quality of performance, with blue to red hues indicating good performance and purple hues indicating poor performance, as defined by the colormap. To facilitate interpretation, the range of each colorbar

is restricted to a specific limit value. The uppermost value on the peak of the top colorbar arrow represents the maximum average output power attained by the harvester.

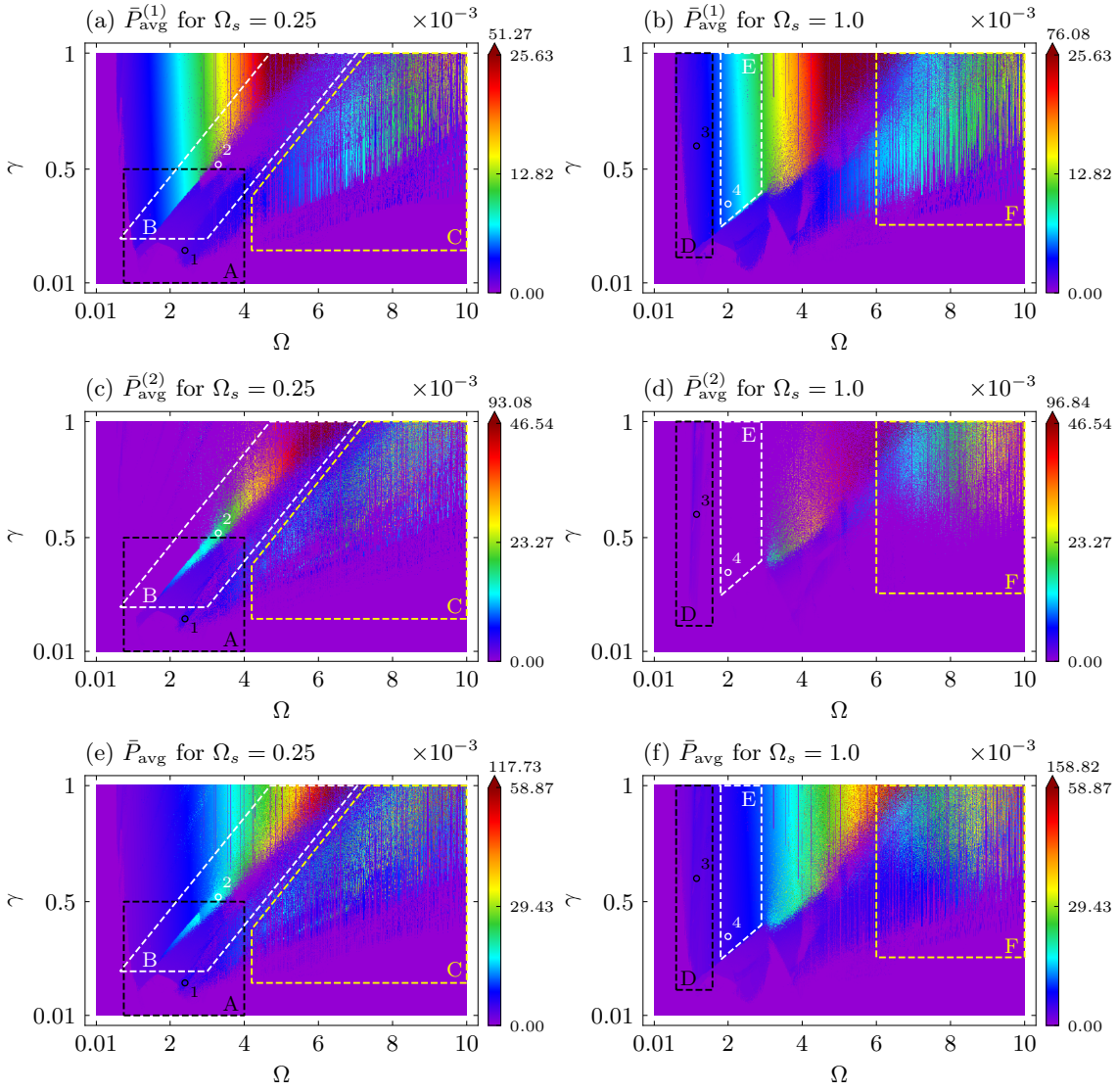

Figure 5.15: Average Output Power Diagrams (OPDs) for: $\Omega_s = 0.25$ (1^{st} column) and $\Omega = 1.0$ (2^{nd} column). The first row displays the contribution of the 1^{st} DoF to the average output power, while the second row shows the contribution of the 2^{nd} DoF. The third row displays the overall harvester $\bar{P}_{\text{avg}}$ for each value of Ω_s. The areas defined by dashed polygons and numbered circles are discussed in the text.

For the case of $\Omega_s = 0.25$, the first degree of freedom exerts greater influence in a large region in the parameter domain, and the second displays a considerable contribution in higher frequencies. Region B, delimited by the white dashed polygon, shows a scenario where the second degree of freedom presents high performance, while the first degree of freedom shows less performance, which illustrates a circum-

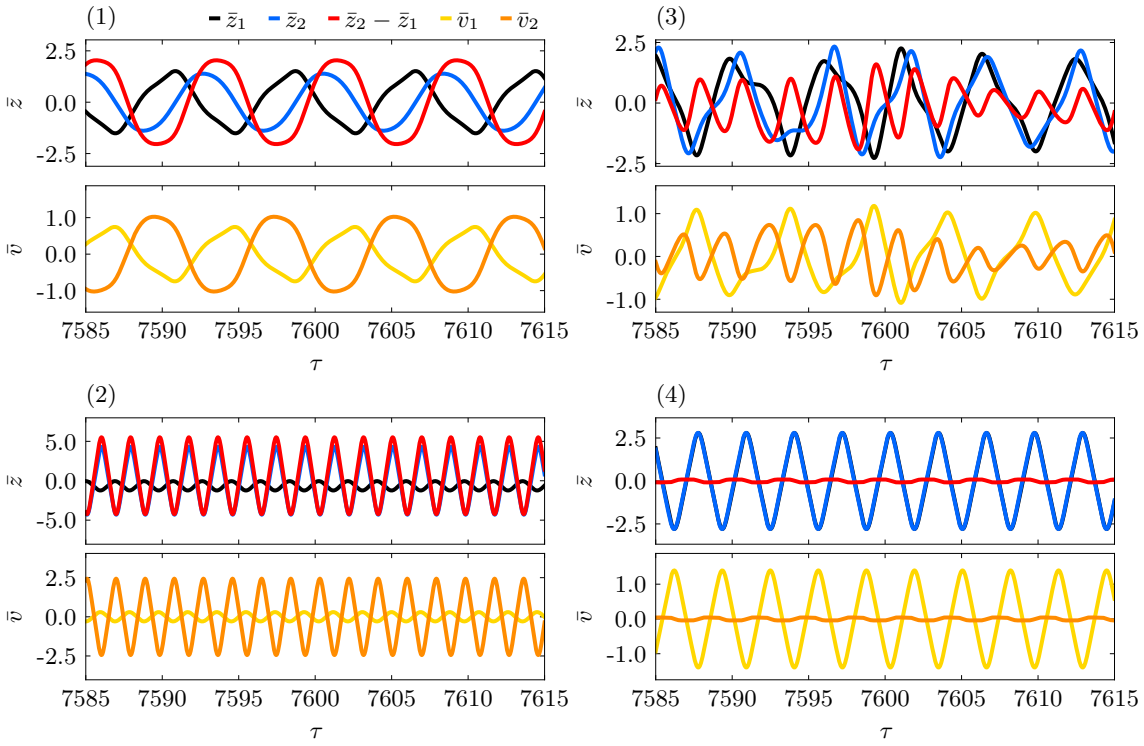

Figure 5.16: Steady state timeseries of each numbered point marked in Figure 5.15. The $\bar{z}_1$ and $\bar{z}_2$ positions, the $\bar{z}_2 - \bar{z}_1$ relative position, and the output voltages $\bar{v}_1$ and $\bar{v}_1$ and $\bar{v}_2$ are plotted and colored according to legend. Each one of the four groups of plots is numbered according to the respective point marked in the OPDs.

stance of transmissibility of energy within the system. In contrast, both degrees of freedom contribute effectively in region A, delimited by the black dashed rectangle. This result can be seen in the overall OPD in Figure 5.15e. In this region, hyperchaotic and periodic 3T attractors are predominant according to Figure 5.12.

In the second case of $\Omega_s = 1.0$, a similar scenario can be observed where the first degree of freedom exerts greater influence in the performance, and the second displays a good contribution in higher frequencies and a small frequency band in low frequencies. Similarly to the previous case, region D, delimited by a black dashed rectangle, is characterized by the effective contribution of both degrees of freedom to the performance, while the white dashed region, E, demonstrates a scenario in which only the first degree of freedom contributes effectively to the power conversion. The predominant attractors of these regions are 1T and chaotic according to Figure 5.13.

In terms of maximum output power, the case in which $\Omega_s = 1.0$ performs better, although the points of very high performance (near $\bar{P}_{\text{avg}}^{(\max)}$) for the second DoF are scarce. In contrast, the areas with high performance of the second DoF in the case of $\Omega_s = 0.25$ are more consistent. In general, the best overall power output regions of the two cases are similar. The yellow dashed areas labeled as C and F, respectively for each case, are characterized by a portion of intermittent irregular sparse points

of high and low performance. This is a characteristic of nonlinear systems that exhibit multiple solutions based on their initial conditions. This complexity is further illustrated by the DRDs in Figures 5.12 and 5.13, displaying a high probability of two or more attractors arising in these areas, instead of a concise area of a single dynamical attractor. In these areas, the knowledge of the probability of a dynamical attractor arising in each point of the diagram combined with a suitable smart control system needs to be incorporated into the system to ensure dynamical stability in these high-performance attractors at operation conditions. This specific zone and its properties will be further explored in Subsection 5.3.3.

Points were marked in Figure 5.15 for each white and black dashed area to exemplify the dynamics of interest of each region. Figure 5.16 displays the steady state time series for the positions $\bar{z}_1$ and $\bar{z}_2$, the relative position $\bar{z}_2 - \bar{z}_1$, and the output voltages $\bar{v}_1$ and $\bar{v}_2$ for each of these points. Plots (1) and (3) illustrate the behavior in which both degrees of freedom contribute effectively to the power conversion (black dashed regions A and D, respectively), while plots (2) and (4) exemplify the behavior in which only one degree of freedom contribute effectively for the power conversion (white dashed regions B and E, respectively).

In general, these examples indicate that the energy conversion is proportional to the displacements: the output voltage $\bar{v}_1$ is proportional to the displacement of the first DoF $\bar{z}_1$, while the output voltage $\bar{v}_2$ is proportional to the relative position, $\bar{z}_{\text{rel}} = \bar{z}_2 - \bar{z}_1$. This is expected as it is tangible to imagine that the resulting strain in

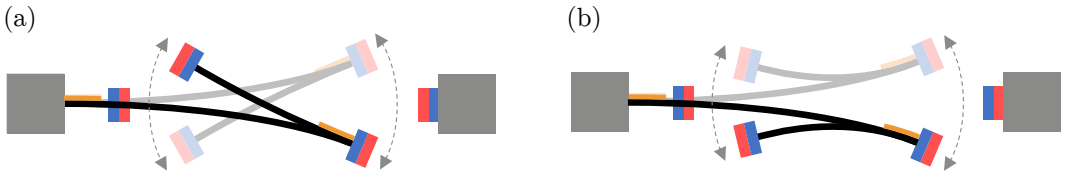

Figure 5.17: Representation of the possible linear vibration modes of the system.

the piezoelectric element of the second DoF depends on the relative position between DoFs, suggesting that in-phase synchronization between DoFs, that is, when the outer beam is moving upwards and the outer beam is moving downwards, makes only one DoF contribute effectively in the power conversion, while desynchronized, out-of-phase and anti-phase synchronized behavior makes the two DoFs contribute effectively in the power conversion. The way the system behaves in these cases is closely related to the linear modes of vibration of the structure, which are exemplified in Figure 5.17.

To further investigate the regions with high performance, the maximum power output, $\bar{P}_{\text{avg}}^{(\max)}$, for each value of excitation amplitude, γ, is marked as colorful points in the OPDs as shown in Figures 5.18a and 5.18b for the cases of $\Omega_s = 0.25$ and

$\Omega_s = 1.0$, respectively. Grayscale colors represent the OPD for reference. The colorbar next to the OPDs represents the value of the average output power of each point of maximum. For $\Omega_s = 0.25$, it is observed that $\bar{P}_{\text{avg}}^{(\text{max})}$ steadily grows as γ increases, with a larger occupation of the diagram. In addition, the region between $\Omega \approx 4 \rightarrow 7$ exhibits the maximum values of output power. In contrast, for $\Omega = 1.0$, the values of $\bar{P}_{\text{avg}}^{(\text{max})}$ are concentrated in the $\Omega \approx 1 \rightarrow 7$ interval of excitation frequency, with the maximum values occurring in a similar range of frequencies as the previous case.

Constant values of γ are selected in each diagram, labeled as G ($\gamma \approx 0.2$), H ($\gamma \approx 0.6$) and I ($\gamma \approx 0.9$) for the $\Omega_s = 0.25$ case, and J ($\gamma \approx 0.1$), K ($\gamma \approx 0.3$) and L ($\gamma \approx 0.5$) for the $\Omega_s = 1.0$ case. They are displayed in Figures 5.18c and 5.18d, showing similar bandwidths of operation. Three points of maximum output power for each case are marked with red circles and labeled with numbers 1 to 3. The three phase subspaces ($\bar{z}_1 \times \bar{z}_2$, $\bar{z}_1 \times \dot{\bar{z}}_1$ and $\bar{z}_2 \times \dot{\bar{z}}_2$) and their respective Poincaré maps are displayed below each case, labeled according to their respective point of maximum. The colors of the phase subspaces correspond to the dynamical attractors classified in Figures 5.12 and 5.13 and the respective equilibrium points of each case are included as a spatial reference in the $\bar{z}_1 \times \bar{z}_2$ phase subspaces.

These results show that the regions of high performance are characterized by a high amplitude displacement of each degree of freedom of the proposed harvester that courses around or through all equilibrium positions. However, point 1, which exhibits the $\bar{P}_{\text{avg}}^{(\text{max})}$ orbits for $\gamma \approx 0.1$, shows an exception to this statement, where the system does not have enough input energy to overcome the system potential barriers, being trapped around the stable equilibrium position. This represents a worst-case scenario for this type of harvester, presenting low power output, and is a characteristic present in several classical multistable harvesters in the literature.

In order to comprehensively characterize the high-performance dynamics of the harvester, the analysis presented in Figures 5.18 are extended to encompass a broader range of values for the parameter Ω_s. For each value of Ω_s, the points of maximum average output power as a function of γ are selected, and for each one of these points, the corresponding dynamical attractor is carefully accounted for. Results of this investigation are summarized in Figure 5.19, which provides a comprehensive overview of the occurrence of each dynamical attractor in points of maximum performance. It is observed that for cases where the harvester exhibits 9 equilibrium positions ($\Omega_s < 0.75$), maximum performance characteristics are associated with 3T attractors, followed by 1T attractors. While 2T and 5T, as well as high periodic (MP) and aperiodic (CH and HC) attractors, also occur, they are not predominant. In contrast, for systems with 3 equilibrium states ($\Omega_s \geq 0.75$), the predominance of 3T attractors decreases, while the occurrence of MP, CH and HC

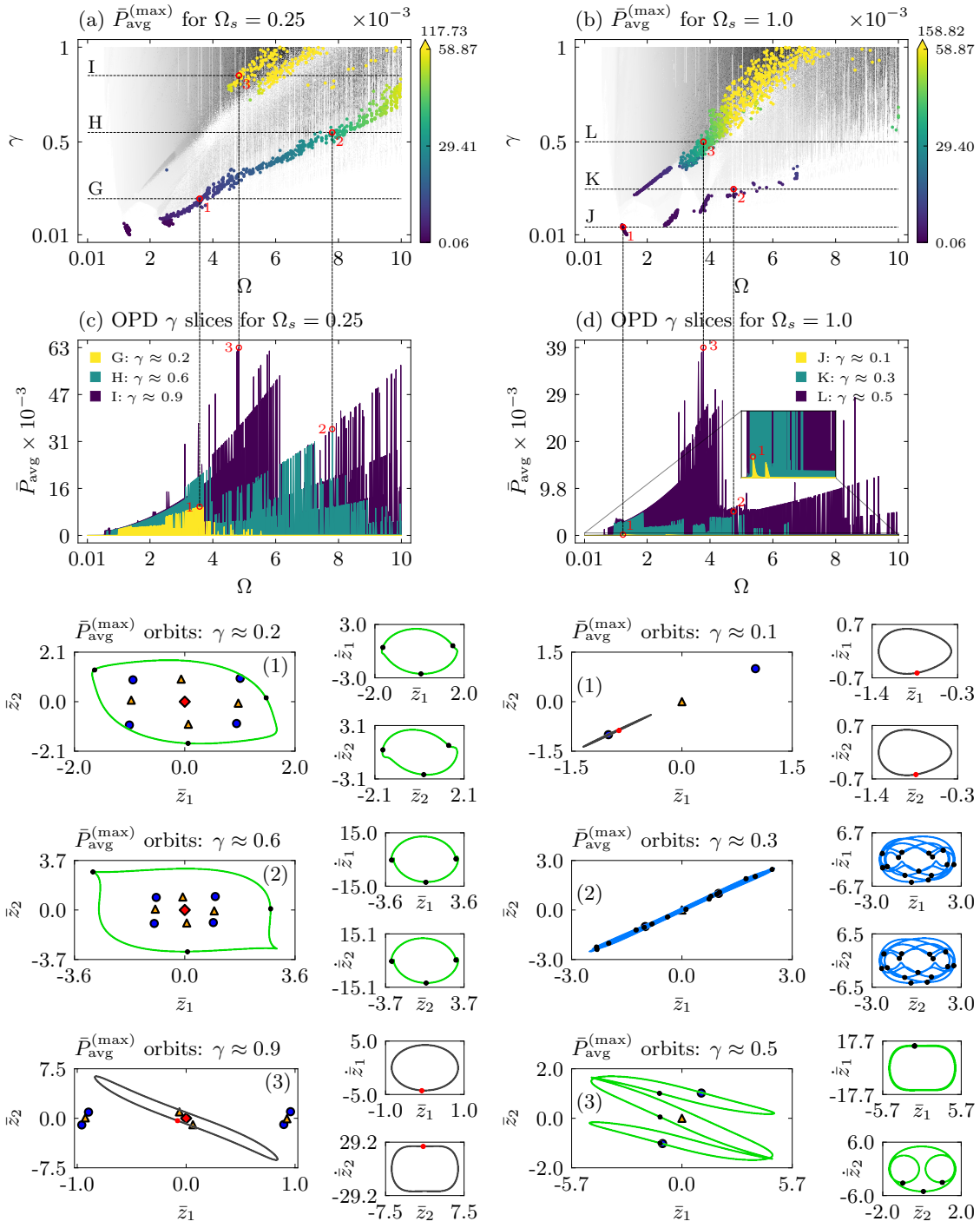

Figure 5.18: $\bar{P}_{\text{avg}}^{(\max)}$ as a function of γ for (a) $\Omega_s = 0.25$ and (b) $\Omega_s = 1.0$. Panels (c) and (d) display the slices G, H, I and J, K, L, respectively, of the OPDs for three values of γ in each case, with red circles marking the maximum power achieved for each slice. For further analysis of the system's steady state response under high-performance conditions, three phase subspaces ($\bar{z}_1 \times \bar{z}_2$, $\bar{z}_1 \times \dot{\bar{z}}_1$ and $\bar{z}_2 \times \dot{\bar{z}}_2$) and Poincaré maps are provided, labeled according to their respective points in the OPDs. To facilitate the visualization, the non-maximum values of the OPD are plotted in grayscale in (a) and (b).

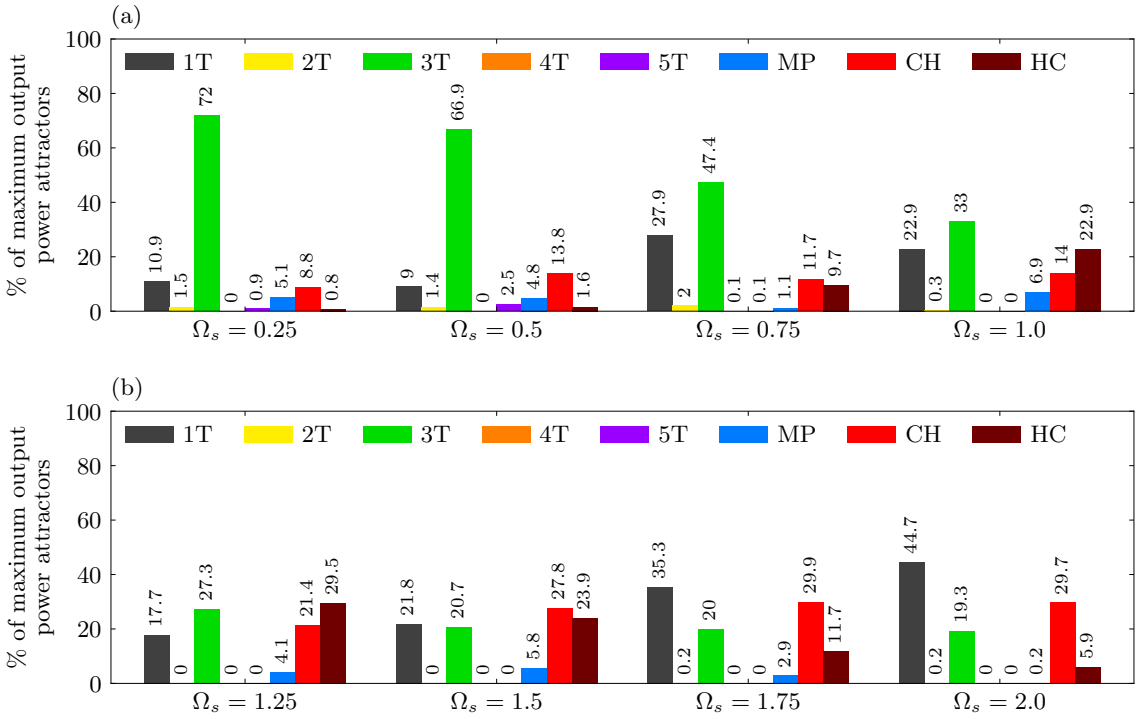

Figure 5.19: Characterization of the high-performance dynamics of the harvester: Percentage of occurrence of attractors of the points of maximum average output power as a function of γ for (a) $\Omega_s = \{0.25, 0.5, 0.75, 1.0\}$ and (b) $\Omega_s = \{1.25, 1.5, 1.75, 2.0\}$.

attractors increases. Notably, 2T, 4T and 5T attractors rarely appear in any of the cases studied.

5.3.2 Performance Considering Different Magnetic Configurations

In this subsection, the performance characteristics of the system considering different magnetic configurations are of concern. Based on the conclusions of the stability analysis, eight configurations with different magnetic and structural parameters are chosen and labeled, being summarized in Table 5.2. The choice of these parameters is based on the qualitative behavior of the multistability formulation presented in Chapter 4 and in value ranges already presented in prior investigations of multistable systems in the literature [5, 6, 65, 123, 193–197]. For each set of magnetic arrangements, two values of Ω_s are chosen (0.25 and 1), enabling a general overview of the system's performance across each set of magnetic restitution parameters. Furthermore, the analysis is divided into two aspects, considering lower and higher levels of input mechanical excitation amplitude, γ.

Table 5.2: Stability configurations based on the combination of different magnetic and structural parameters.

Magnetic				Structural		Stability	Configuration
α_1	α_2	β_1	β_2	ρ	Ω_s		
-2	-1	1	1	1	0.25	Tetrastable	I
					1	Bistable	II
-2	1	1	1	1	0.25	Bistable	III
					1	Bistable	IV
0	-1	1	1	1	0.25	Bistable	V
					1	Bistable	VI
0	1	1	1	1	0.25	Monostable	VII
					1	Monostable	VIII

Numerical investigations are performed employing average output power diagrams (OPDs). The initial conditions for each point within the diagrams are based on the stable position $\{\bar{z}_1, \dot{\bar{z}}_1, \bar{z}_2, \dot{\bar{z}}_2, \bar{v}_1, \bar{v}_2\} = \{\bar{Z}_1, 0, \bar{Z}_2, 0, 0, 0\}$ represented by the black basin of attraction (SEP_2) for the configurations I to VI at $\Omega_s = 0.25$, and the only stable position for the configurations VII and VIII. By utilizing these diagrams, a comprehensive overview of the qualitative performance characteristics of the system under different excitation conditions is presented.

Performance at High Amplitude Mechanical Excitation

Figure 5.20 depicts the OPDs for the configurations with $\Omega_s = 0.25$, as described in Table 5.2. The colorbars accompanying each diagram represent the average output power levels, restricted to a specific limit value to facilitate interpretation. The uppermost values indicated by the peak of the colorbar arrow represent the maximum normalized output power achieved by the harvester. By examining the OPDs at higher excitation amplitudes ($\gamma \geq 0.5$), it is evident that configurations I and III outperform the others for lower frequencies ($0.01 \leq \Omega < 3$). These configurations exhibit larger regions characterized by good output power values, represented by shades of blue. Moreover, configurations I and V demonstrate larger regions associated with very high output power (shades of red) for mid-range frequencies. It should be noted that configuration III displays shorter, scattered regions of very high performance, which can be primarily related to the presence of multiple solution branches (dynamical attractors) associated with low and high performance, these regions present similar behavior to the specific zones that will be further discussed in Subsection 5.3.3. Nonetheless, configuration III shows small regions of superior

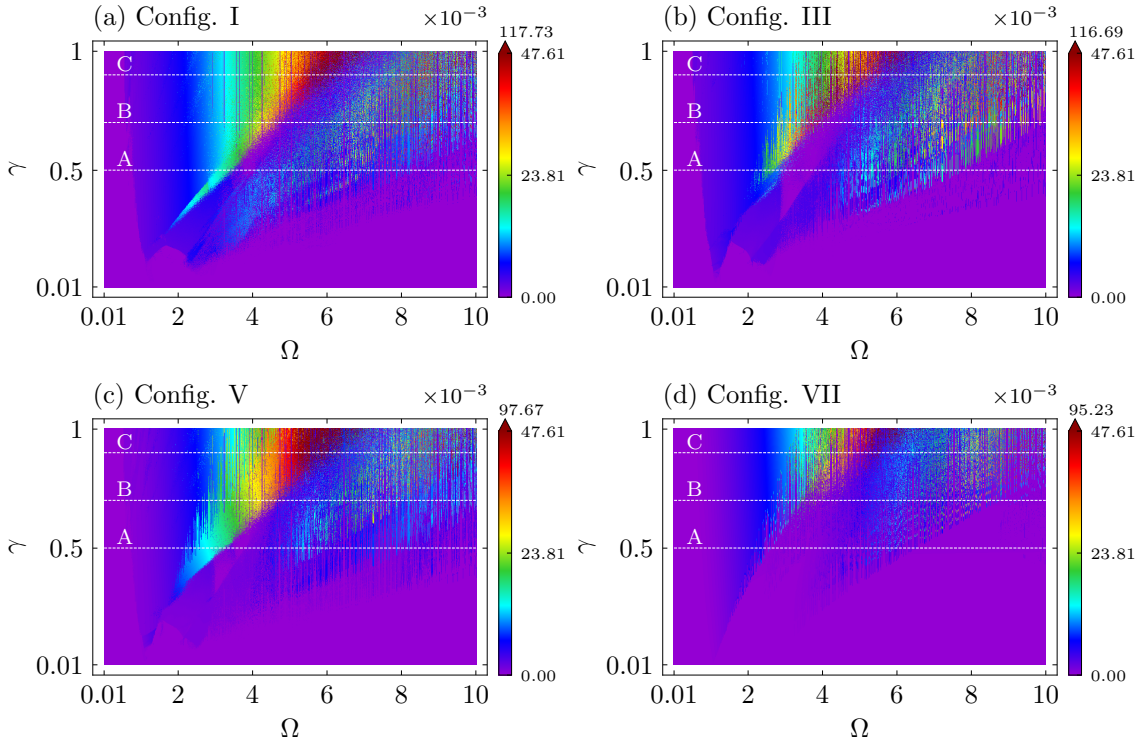

Figure 5.20: OPDs for the configurations with $\Omega_s = 0.25$: (a) Config. I, (b) config. III, (c) config. V, and (d) config. VII. Colorbars represent $\bar{P}_{\text{avg}}$ levels, restricted to a limit value. The peak value on the colorbar arrow signifies the maximum output power achieved by the harvester. White lines with capital letter labels are discussed in the text and are represented by the frequency response diagrams in Figure 5.21.

performance at lower γ values ($0.5 \leq \gamma \leq 0.6$) when compared to configurations I and V.

Notably, in the case of higher frequencies ($7 \leq \Omega \leq 10$), configuration III exhibits superior performance. Conversely, configuration VII consistently demonstrates the worst performance across all examined scenarios.

These findings can be further illustrated in Figure 5.21, which provides a visual representation of the output power for constant values of γ, denoted as A ($\gamma \approx 0.5$), B ($\gamma \approx 0.7$) and C ($\gamma \approx 0.9$) in each OPD presented in Figure 5.20. Notably, configuration I, characterized by tetrastability, demonstrates superior performance in terms of both bandwidth and maximum output power for $\gamma \approx 0.5$ and $\gamma \approx 0.7$. Conversely, configurations III and V, associated with bistability, exhibit similar performance characteristics, while configuration VII, associated with monostability, consistently displays the poorest performance. Furthermore, for values $\gamma \approx 0.9$, all configurations demonstrate comparable performance, although configuration VII exhibits a slightly lower maximum output power when compared to the other configurations.

Details about each kind of behavior can be observed in Figures 5.22 and 5.23

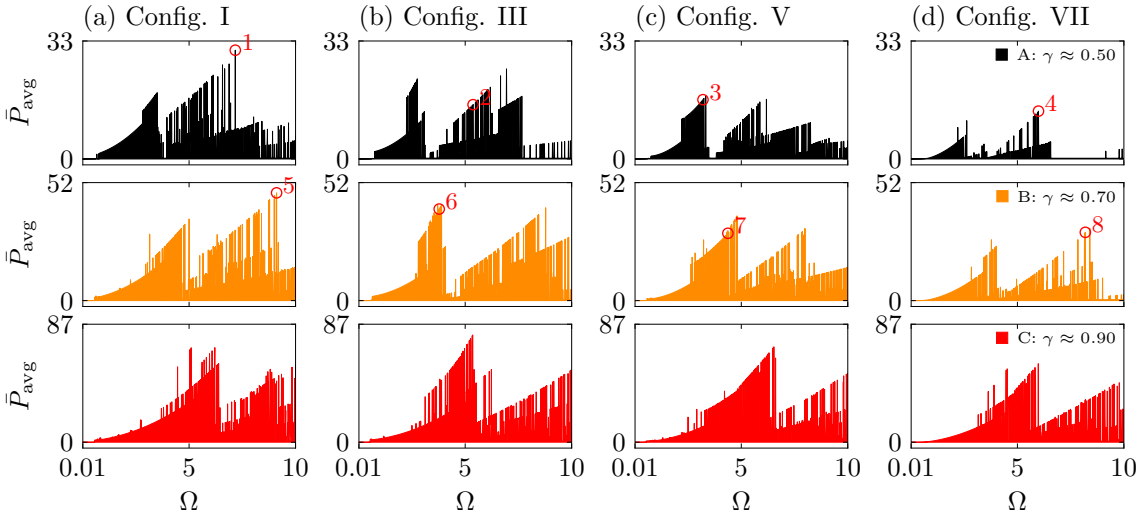

Figure 5.21: Average output power for different γ values. (a) Config. I, (b) config. III, (c) config. V, and (d) config. VII. Each level of γ is highlighted by a distinct color: black for $\gamma \approx 0.5$, orange for $\gamma \approx 0.7$, and red for $\gamma \approx 0.9$. γ values are represented in Figure 5.20 by labels A, B and C. Power values are scaled by $\times 10^{-3}$.

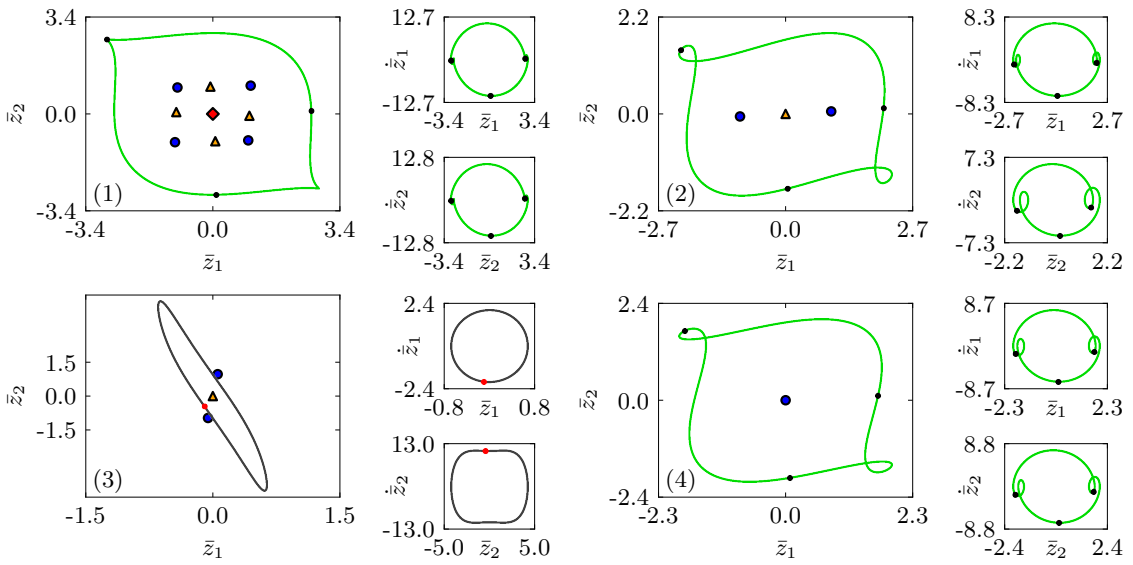

Figure 5.22: Phase subspaces $\bar{z}_1 \times \bar{z}_2$, $\bar{z}_1 \times \dot{\bar{z}}_1$ and $\bar{z}_2 \times \dot{\bar{z}}_2$ of the steady state response of the system. Each set of subspaces represents each red point marked and labeled as 1, 2, 3 and 4 in Figure 5.21. The associated equilibrium positions are displayed in each $\bar{z}_1 \times \bar{z}_2$ subspace for spatial reference. Poincaré maps are highlighted in red or black to indicate the type of dynamical response of the system.

that present phase subspaces $\bar{z}_1 \times \dot{\bar{z}}_1$, $\bar{z}_2 \times \dot{\bar{z}}_2$, and $\bar{z}_1 \times \bar{z}_2$ of points 1 to 8 situated at the vicinity of maximum output power values in Figure 5.21. Equilibrium points of the corresponding configuration in the $\bar{z}_1 \times \bar{z}_2$ are also displayed for spatial reference. These figures offer insights into the type of motion that leads to high performance

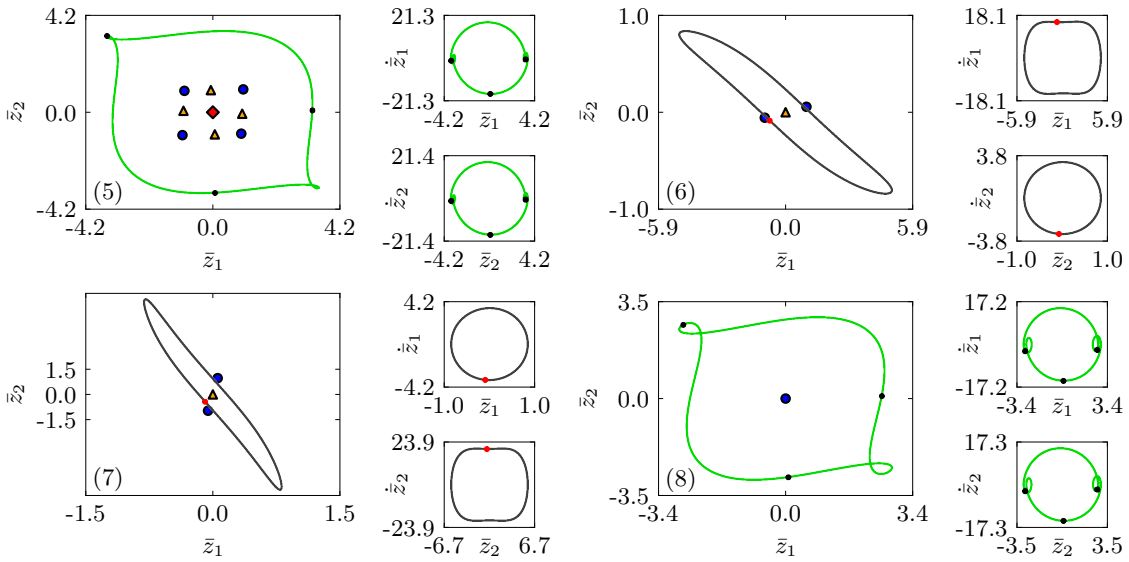

Figure 5.23: Phase subspaces $\bar{z}_1 \times \bar{z}_2$, $\bar{z}_1 \times \dot{\bar{z}}_1$ and $\bar{z}_2 \times \dot{\bar{z}}_2$ of the steady state response of the system. Each set of subspaces represents each red point marked and labeled as 5, 6, 7 and 8 in Figure 5.21. The associated equilibrium positions are displayed in each $\bar{z}_1 \times \bar{z}_2$ subspace for spatial reference. Poincaré maps are highlighted in red or black to indicate the type of dynamical response of the system.

under high-amplitude excitation. Essentially, the eight cases can be categorized into two sets based on the shape of the orbits. The 1T grey orbits of high performance are found in intermediary values of frequency, while the 3T orbits of high performance are found in higher values of frequency.

Figure 5.24 depicts the performance analysis for different configurations of the harvester with $\Omega_s = 1$, as shown in Table 5.2, considering values of $\gamma \geq 0.5$. In this scenario, the careful observation of the OPDs points to greater overall bandwidth and maximum output power for configuration II. Configurations IV and VI present very similar performance to each other, and configuration VIII displays the worst performance. In a supplementary manner, Figure 5.25 shows that the difference in performance between configurations II and configurations IV and VI is reduced as γ increases. Nevertheless, configuration VIII, associated with monostability, displays the worst performance.

Overall, this subsection demonstrates that in scenarios with higher amplitude excitations ($\gamma \geq 0.5$), the configurations associated with the magnetic parameters $(\alpha_1, \alpha_2, \beta_1, \beta_2) = (-2, -1, 1, 1)$ exhibit superior performance. Conversely, configurations associated with monostability consistently display the worst performance.

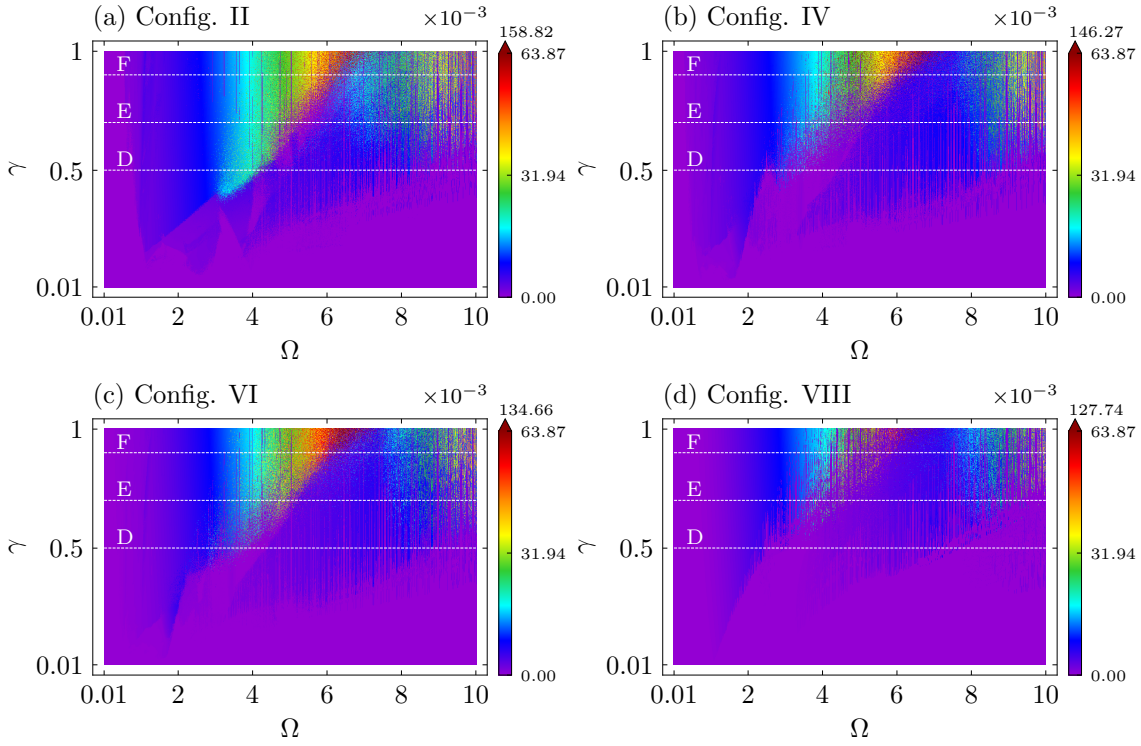

Figure 5.24: OPDs for the configurations with $\Omega_s = 1$: (a) Config. II, (b) config. IV, (c) config. VI, and (d) config. VIII. Colorbars represent $\bar{P}_{\text{avg}}$ levels, restricted to a limit value. The peak value on the colorbar arrow signifies the maximum output power achieved by the harvester. White lines with capital letter labels are discussed in the text and are represented by the frequency response diagrams in Figure 5.25.

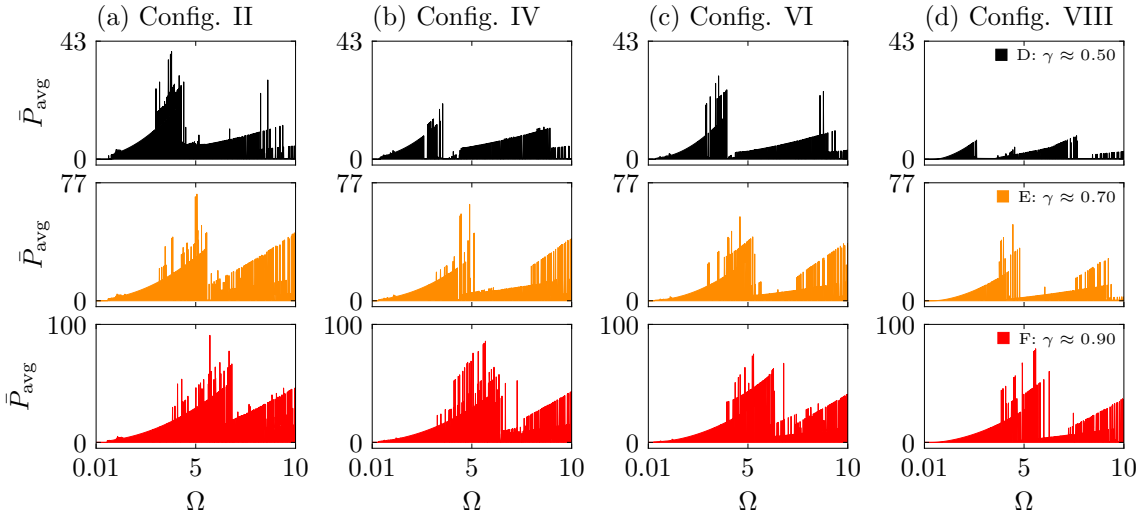

Figure 5.25: Average output power for different γ values. (a) Config. II, (b) config. IV, (c) config. VI, and (d) config. VIII. Each level of γ is highlighted by a distinct color: black for $\gamma \approx 0.5$, orange for $\gamma \approx 0.7$, and red for $\gamma \approx 0.9$. γ values are represented in Figure 5.24 by labels D, E and F. Power values are scaled by $\times 10^{-3}$.

Performance at Low Amplitude Mechanical Excitation

Henceforth, the performance associated with lower amplitude excitation scenarios is of concern. By analyzing Figures 5.20 and 5.24, it is noticeable that, for all cases, lower excitation amplitudes coupled with higher excitation frequencies results in negligible output power, configuring regions of poor performance. Therefore, to focus on the significant excitation parameters, the subsequent OPDs are constrained to the range of $0.01 \leq \gamma \leq 0.5$ and $0.01 \leq \Omega \leq 5$. This region exhibits substantial output power for all configurations analyzed under low amplitude excitation scenarios ($\gamma \leq 0.5$).

Building upon the methodology employed in the previous subsection, Figure 5.26 presents the OPDs for the configurations related to $\Omega_s = 0.25$. Subsequently, Figure 5.27 further investigates the performance by focusing on specific constant values of γ. These values, marked by dashed lines within the OPDs, are identified as G ($\gamma \approx 0.03$), H ($\gamma \approx 0.1$), and I ($\gamma \approx 0.35$).

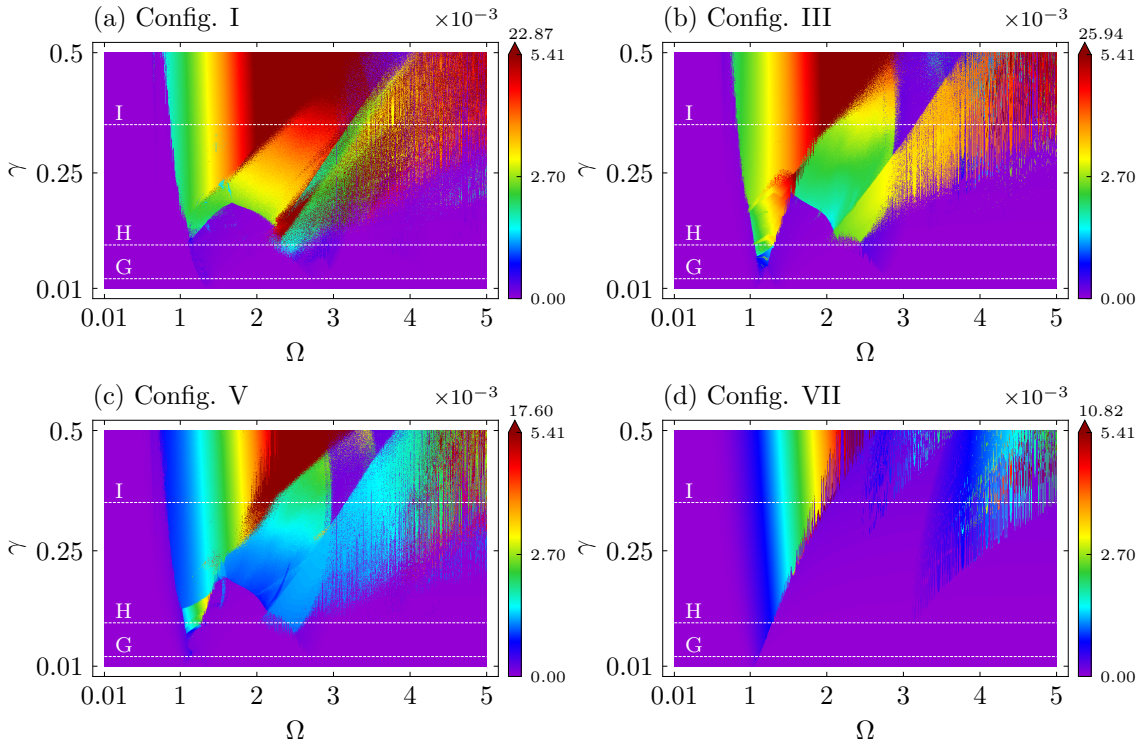

Figure 5.26: OPDs for the configurations with $\Omega_s = 0.25$: (a) Config. I, (b) config. III, (c) config. V, and (d) config. VII. Colorbars represent $\bar{P}_{\text{avg}}$ levels, restricted to a limit value. The peak value on the colorbar arrow signifies the maximum output power achieved by the harvester. White lines with capital letter labels are discussed in the text and are represented by the frequency response diagrams in Figure 5.27.

Overall, an overview of the OPDs points out that configuration I offers superior overall performance compared to the other configurations. This is evident from the

larger regions of high performance (represented by shades of red) observed in configuration I. In the same context, configurations III and V exhibit similar bandwidths, with configuration III displaying larger areas of high output power. Conversely, configuration VII exhibits the worst overall performance.

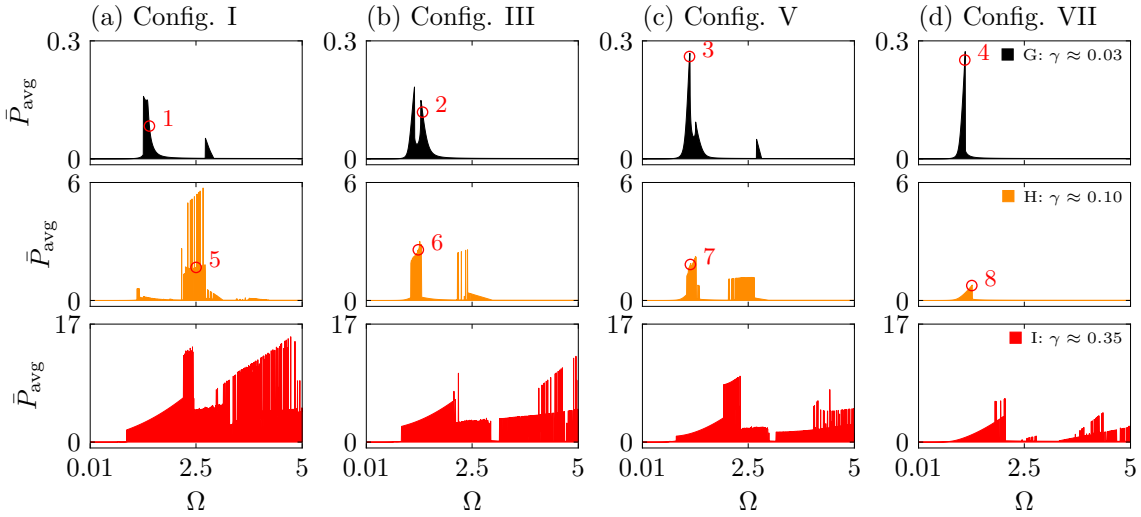

Figure 5.27: Average output power for different γ values. (a) Config. I, (b) config. III, (c) config. V and (d) config. VII. Each level of γ is highlighted by a different color: black for $\gamma \approx 0.03$, orange for $\gamma \approx 0.1$ and red for $\gamma \approx 0.35$. γ values are represented in Figure 5.24 by the labels I, H and J. Power values are scaled by $\times 10^{-3}$. Red points labeled with numbers are discussed in the text and are represented by the phase spaces in Figures 5.28 and 5.29.

Yet, a careful analysis of very low excitation levels ($\gamma \leq 0.1$) is crucial, as many practical applications exhibit this characteristic. When considering such scenarios, configurations V and VII demonstrate better performance in terms of maximum output power, while configurations III and V show superior performance in terms of bandwidth. Surprisingly, configuration I displays the worst performance for these excitation levels. In contrast, by increasing the excitation levels, a significant shift occurs, leading to configuration I exhibiting improved overall performance, while configuration VII shows the worst performance. Notably, the qualitative difference in performance remains consistent as γ increases. Figure 5.27 provides additional visual support for these findings through the frequency diagrams.

To deeply analyze this abrupt change in behavior, specific points in the vicinity of the maximum output powers within the frequency diagrams are carefully selected and highlighted in red. These points are labeled from 1 to 8. Figures 5.28 and 5.29 illustrate three phase subspaces ($\bar{z}_1 \times \bar{z}_2$, $\bar{z}_1 \times \dot{\bar{z}}_1$ and $\bar{z}_2 \times \dot{\bar{z}}_2$) of each selected point. Equilibrium points corresponding to each case in the $\bar{z}_1 \times \bar{z}_2$ phase subspaces are outlined for spatial reference. By comparing points 1 and 5, 2 and 6, 3 and 7, as well as 4 and 8 in Figures 5.28 and 5.29, it becomes evident that the performance at very

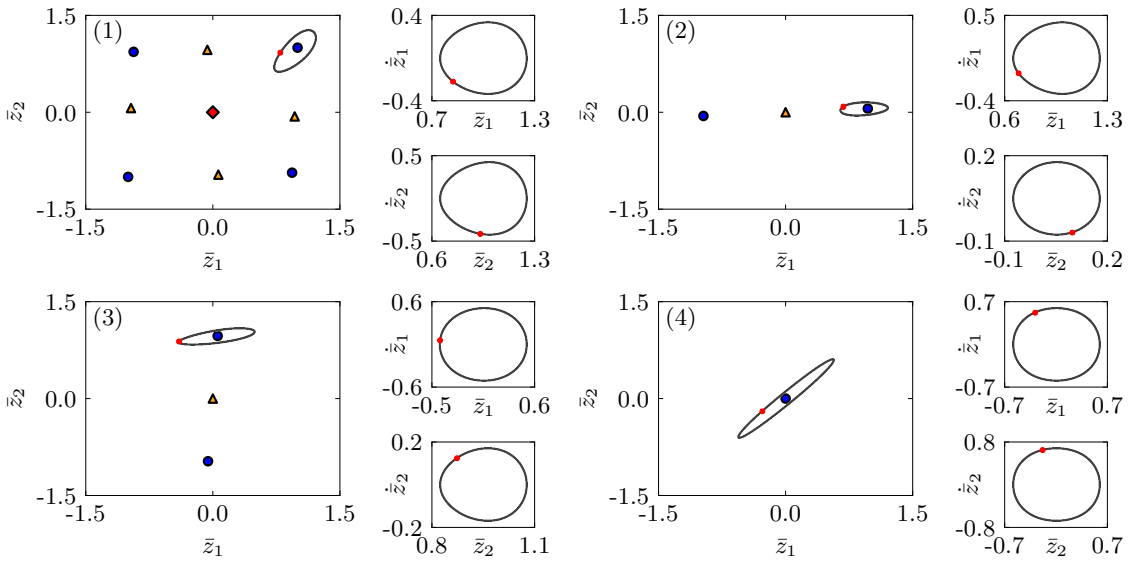

Figure 5.28: Phase subspaces $\bar{z}_1 \times \bar{z}_2$, $\bar{z}_1 \times \dot{\bar{z}}_1$ and $\bar{z}_2 \times \dot{\bar{z}}_2$ of the steady state response of the system. Each set of subspaces represents each red point marked and labeled as 1, 2, 3 and 4 in Figure 5.27. The associated equilibrium positions are displayed in each $\bar{z}_1 \times \bar{z}_2$ subspace for spatial reference. Poincaré maps are highlighted in red or black to indicate the type of dynamical response of the system.

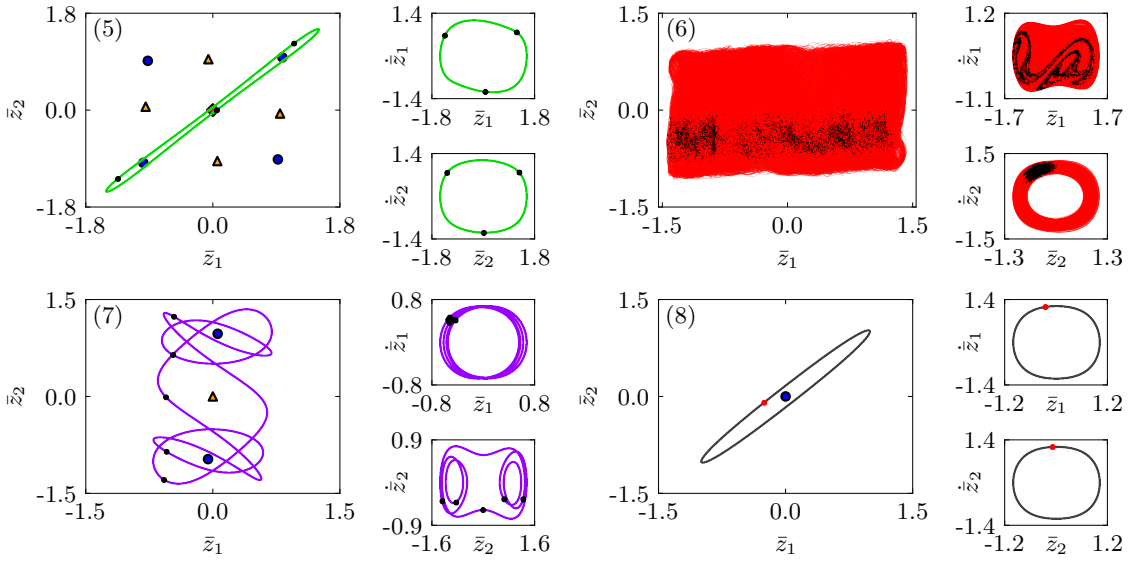

Figure 5.29: Phase subspaces $\bar{z}_1 \times \bar{z}_2$, $\bar{z}_1 \times \dot{\bar{z}}_1$ and $\bar{z}_2 \times \dot{\bar{z}}_2$ of the steady state response of the system. Each set of subspaces represents each red point marked and labeled as 5, 6, 7 and 8 in Figure 5.27. The associated equilibrium positions are displayed in each $\bar{z}_1 \times \bar{z}_2$ subspace for spatial reference. Poincaré maps are highlighted in red or black to indicate the type of dynamical response of the system.

low γ is constrained by the potential energy barriers inherent of multistable systems. In the case of bistable and tetrastable configurations, the system remains trapped

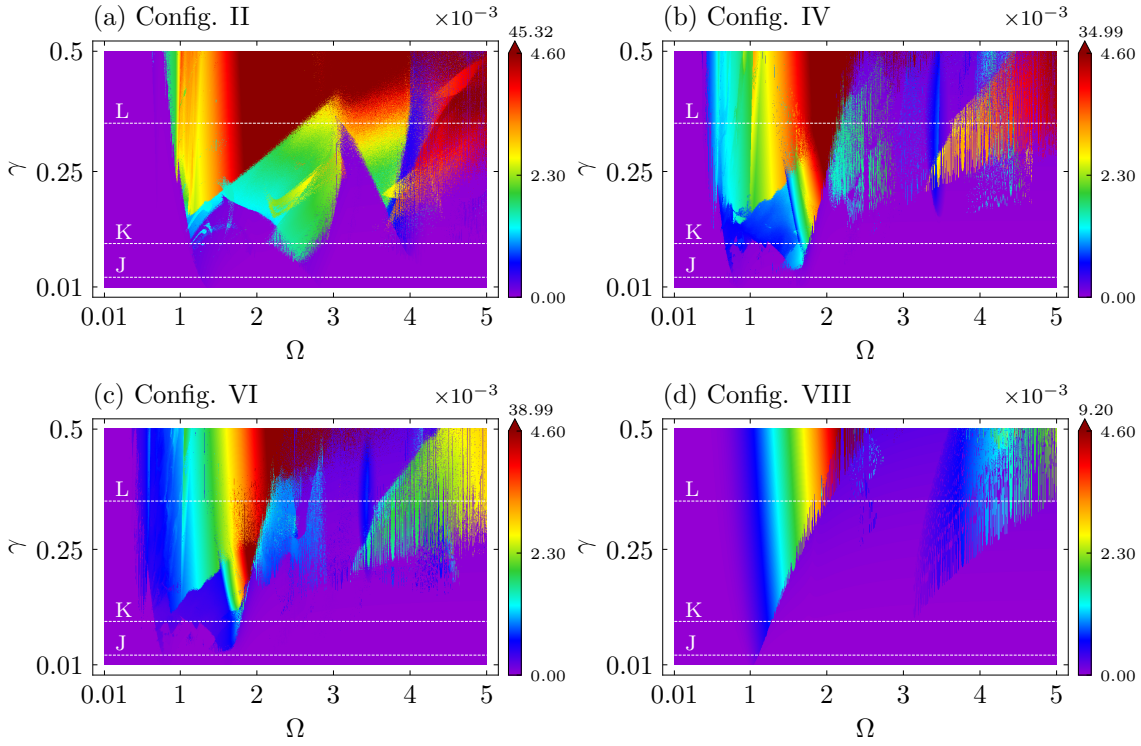

Figure 5.30: OPDs for the configurations with $\Omega_s = 1$: (a) Config. II, (b) config. IV, (c) config. VI, and (d) config. VIII. Colorbars represent $\bar{P}_{\text{avg}}$ levels, restricted to a limit value. The peak value on the colorbar arrow signifies the maximum output power achieved by the harvester. White lines with capital letter labels are discussed in the text and are represented by frequency response diagrams in Figure 5.31.

around a stable equilibrium position. As the system receives additional energy with increasing γ, it surpasses the potential barriers, leading to greater displacement and consequently improved performance. In this scenario, while the monostable configuration also experiences an increase in performance, it remains severely limited by the monostable potential. Additionally, in all subspaces, Poincaré maps are highlighted indicating the dynamical characteristics of the system, showing that enhanced performance is associated with higher displacement and complex phenomena, as indicating the orbits of periodicity 3T (green orbit), 5T (purple orbit), and chaotic (red orbit) in Figure 5.29, where T is the excitation period. These observations shed light on the underlying mechanisms responsible for the observed behavior.

Figures 5.30 and 5.31, related to the configurations associated with $\Omega_s = 1$, exhibit a similar qualitative behavior, whereby the bistable configurations display poorest maximum output power for very low γ. As γ increases, there is a notable surge in performance attributed to the high amplitude response of the system, surpassing the energy barriers.

Still, a careful analysis of the OPDs in Figure 5.30 reveals that configuration II demonstrates superior performance, characterized by larger regions of very high

performance (depicted by shades of red). Nevertheless, for operation at lower frequencies ($\Omega \leq 1$), configurations IV and VI outperform configuration II, as they encompass regions of good performance (indicated by shades of blue) while configuration II presents negligible performance (indicated by shades of purple). In contrast, configuration VIII, associated with monostability, exhibits by far the worst performance.

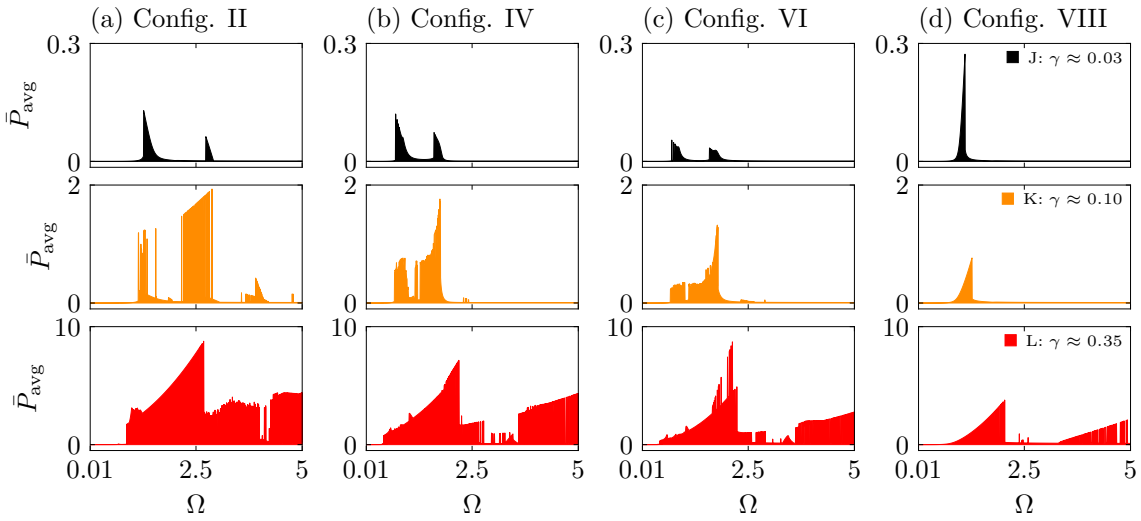

Figure 5.31: Average output power for different γ values. (a) Config. II, (b) config. IV, (c) config. VI and (d) config. VIII. Each level of γ is highlighted by a different color: black for $\gamma \approx 0.03$, orange for $\gamma \approx 0.1$ and red for $\gamma \approx 0.35$. γ values are represented in Figure 5.24 by the labels L, K and J. Power values are scaled by $\times 10^{-3}$.

In general, this subsection demonstrates that for very low excitation levels, configurations VII and VIII, associated with monostability, yield higher output powers. On the other hand, configurations III, V, and IV exhibit superior bandwidths. For low to medium excitation levels ($0.1 \leq \gamma \leq 0.5$), configurations I and II exhibit better performances, while configurations VII and VIII consistently perform poorly.

5.3.3 Multiple Solution Regions

In Subsection 5.3.2, output power diagrams (OPDs) are presented for all configurations. Across all these diagrams, a distinctive region becomes evident when examining high-frequency and high-amplitude values. Within these zones, a non-smooth, irregular distribution of data points, showcasing a wide range of high and low output powers can be observed. This subsection is devoted to a comprehensive exploration of this intriguing area, which, from this point forward, will be referred to as the 'scattered zone'. For that, consider Figure 5.32, where the OPD for Configuration I is selected. Here, a small region highlighted by the black dashed square

and labeled as "PS" is chosen and, within this region, four very close points with $\gamma = 0.5$ and distinct values of Ω are chosen to be analyzed.

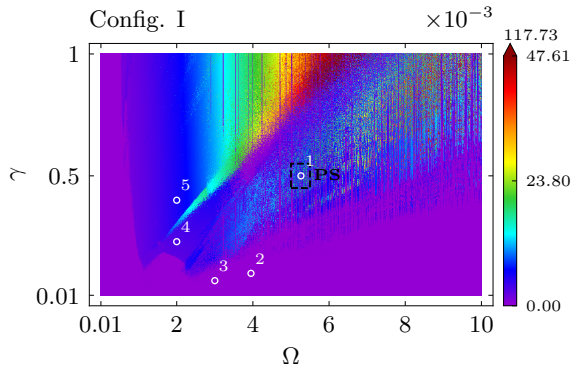

Figure 5.32: OPD for Config. I. Colorbars represent the average output power levels for each excitation condition. Colorbars represent $\bar{P}_{\text{avg}}$ levels, restricted to a limit value. The peak value on the colorbar arrow signifies the maximum output power achieved by the harvester. The black dashed rectangle region labeled as PS contains all the phase subspaces detailed in Figure 5.22. Numbered white circles mark the locations of each basin of attraction displayed in Figures 5.34 and 5.35.

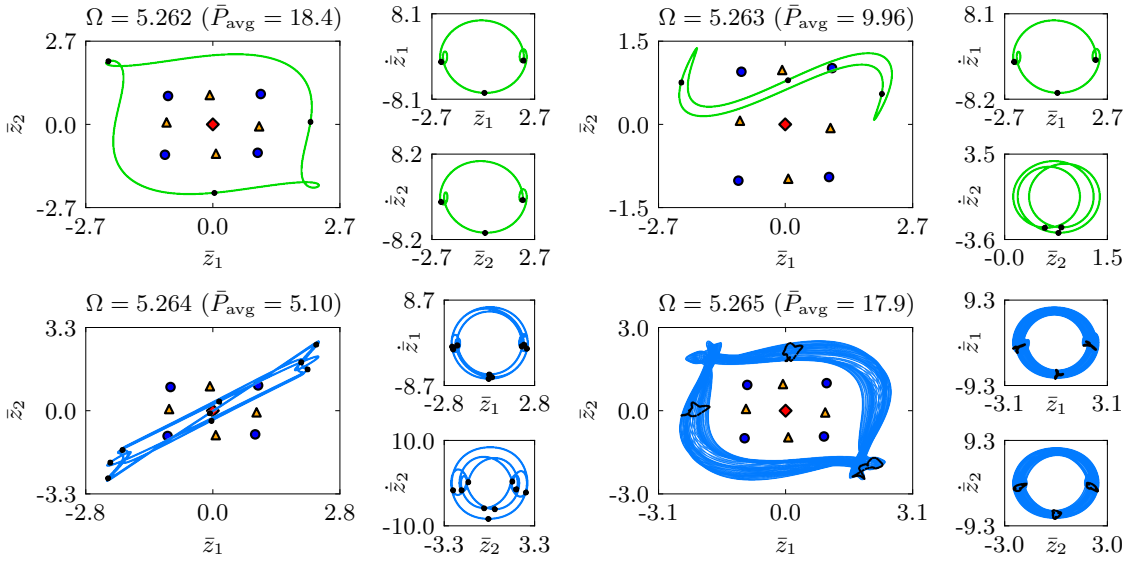

Figure 5.33: Phase subspaces $\bar{z}_1 \times \bar{z}_2$, $\bar{z}_1 \times \dot{\bar{z}}_1$ and $\bar{z}_2 \times \dot{\bar{z}}_2$ of the system's steady state response. Each set of subspaces represents a case with $\gamma = 0.5$ and a distinct Ω value within the PS zone highlighted in Figure 5.32. The associated equilibria are displayed in $\bar{z}_1 \times \bar{z}_2$ subspace for spatial reference. Poincaré maps are displayed in black dots. The $\bar{P}_{\text{avg}}$ manifested in each response is highlighted.

Figure 5.33 depicts the phase subspaces $\bar{z}_1 \times \bar{z}_2$, $\bar{z}_1 \times \dot{\bar{z}}_1$ and $\bar{z}_2 \times \dot{\bar{z}}_2$ of the steady-state response of the chosen points within the black dashed rectangle. For each case, the average output power, $\bar{P}_{\text{avg}}$, is highlighted, showing that a small perturbation in excitation parameters can alter significantly the system's response, influencing

its performance. In this case, four types of attractors are shown: 2 types of 3T attractors, a 9T attractor and a quasiperiodic-like attractor, each manifesting a distinct $\bar{P}_{\text{avg}}$. T, in this case, represents the period of excitation.

Results presented in Figure 5.33 suggest that the scattered zones are regions with many coexisting solutions. In order to confirm this hypothesis, consider an in-depth analysis of the basins of attraction of the forced system for the subspace $\bar{z}_1 \times \bar{z}_2$, as showcased in Figures 5.34 and 5.35. This analysis categorizes the basins into two distinct types: those on the left, which exclusively consider attractors based on the system's motion characteristics, and those on the right, which also incorporate the impact of average output power, as previously detailed in Chapter 3.

The left-sided basins employ a methodology based on the type of motion, the same procedure discussed in Section 3.2.1, to classify different types of dynamical attractors. These attractors are represented by a range of colors, each denoting different periodic or aperiodic behaviors. Dark gray corresponds to 1T periodic attractors, yellow to 2T attractors, green to 3T attractors, purple to 5T attractors, and light blue to multiple periods (MP), comprising all periodic attractors with a periodicity equal or greater than 6T. Additionally, red signifies chaotic (CH) attractors, while dark red indicates hyperchaotic (HC) attractors. This classification is summarized in the colorbars next to the left-sided basins in each row.

Furthermore, the right-sided basins employ a similar classification methodology, while also taking into consideration different values of $\bar{P}_{\text{avg}}$ to classify the attractors. To account for fluctuations and potential numerical errors associated with the integration scheme, the classification considers intervals with a margin of approximately 2% around the $\bar{P}_{\text{avg}}$ values. In other words, when identifying a value of $\bar{P}_{\text{avg}}$, any values falling within a range of $\pm 2\%$ of the original value associated with a single periodic or aperiodic attractor are grouped as a unique motion-power-attractor within this type of basin. Each plot is constructed with a grid of 1000×1000 points.

The motion-power attractors, which are based on the interplay of motion and power, are distinguished by various colors, as depicted in the horizontal bar plot adjacent to the right-sided basin. Additionally, the display includes information such as the type of motion, the $\bar{P}_{\text{avg}}$ value, and the area (A) occupied by the attractor within the basin. Moreover, when there is more than one attractor that occupies less than 1% of the basin area ($A < 1\%$), they are consolidated into a single color classification labeled as OT$\times N_{\text{attr}}$, where 'OT' signifies 'other attractors,' and N_{attr} represents the number of attractors combined in this manner. If a specific attractor motion name replaces 'OT', it indicates that all consolidated attractors share the same type of motion.

Figure 5.34a presents the basins of attraction corresponding to point 1, as indicated in Figure 5.32, chosen to represent the scattered zone within the OPD. These

basins reveal the potential for 39 distinct motion-power attractors to emerge depending on the displacement initial conditions, with 13 of them having a chance exceeding 1% to arise based on the occupied area. Among these 13 main attractors, four to five magnitudes of $\bar{P}_{\text{avg}}$ are observed. Furthermore, an examination of the basin morphology reveals that the most predictable responses originate from initial conditions situated at the corners of the plot. In these areas, the basin shapes are more consistent, and the values of $\bar{P}_{\text{avg}}$ are notably higher. Alternatively, the basin morphology near the stable equilibrium points is associated with an irregular fractal-like pattern, which can be associated with unpredictability. These characteristics can be associated with the existence of the scattered zone in the OPDs, as they were constructed utilizing a stable point as the initial condition for all its points.

In a similar manner, Figure 5.34b displays a case below the scattered zone, with still a mid-high Ω but with a lower γ. This region shows 32 motion-power attractors, with 7 of them occupying more than 1% of the plot area. Although this still represents a substantial number of attractors, it is fewer in comparison to point 1. The basin morphology, however, shows the opposite of the previous basin. In this case, the basin shapes near the equilibrium positions exhibit greater consistency, suggesting a higher degree of predictability, whereas the surroundings of the plot are characterized by fractal-like patterns, signifying a higher degree of unpredictability. Additionally, it's worth noting that in this case, the predictable zones with larger areas exhibit lower values of $\bar{P}_{\text{avg}}$, while the zones associated with unpredictability demonstrate higher performance.

Figure 5.34c shows the basin of point 4 located in the OPD. In this case, the basins show characteristics that, in terms of output power and morphology, closely resemble those observed in the basin presented in Figure 5.34b. Nevertheless, it implies that a significant reduction in the number of motion-power attractors can be achieved by reducing the frequency and amplitude of excitation. This reduction leads to an expansion of the overall area occupied by each attractor, enhancing the predictability of those with more consistent areas.

This hypothesis is strengthened by the basins presented in Figure 5.35, which represents the points 4 and 5 highlighted in Figure 5.32. These basins reveal that as the excitation frequency is decreased towards values closer to the linear natural frequency of the structure, a significant reduction in the number of attractors occurs. In point 5, there is only one attractor, while in point 4, there is virtually one. It's worth noting that the term 'virtually one' is used for point 4 because the basin of point 4 reveals the presence of hyperchaotic responses, indicating that each point of the attractor represents a distinct, but very similar response, in qualitative terms. This is supported by the right-sided basin which shows the classification of distinct hyperchaotic attractors with very similar $\bar{P}_{\text{avg}}$ values and amorphous morphology

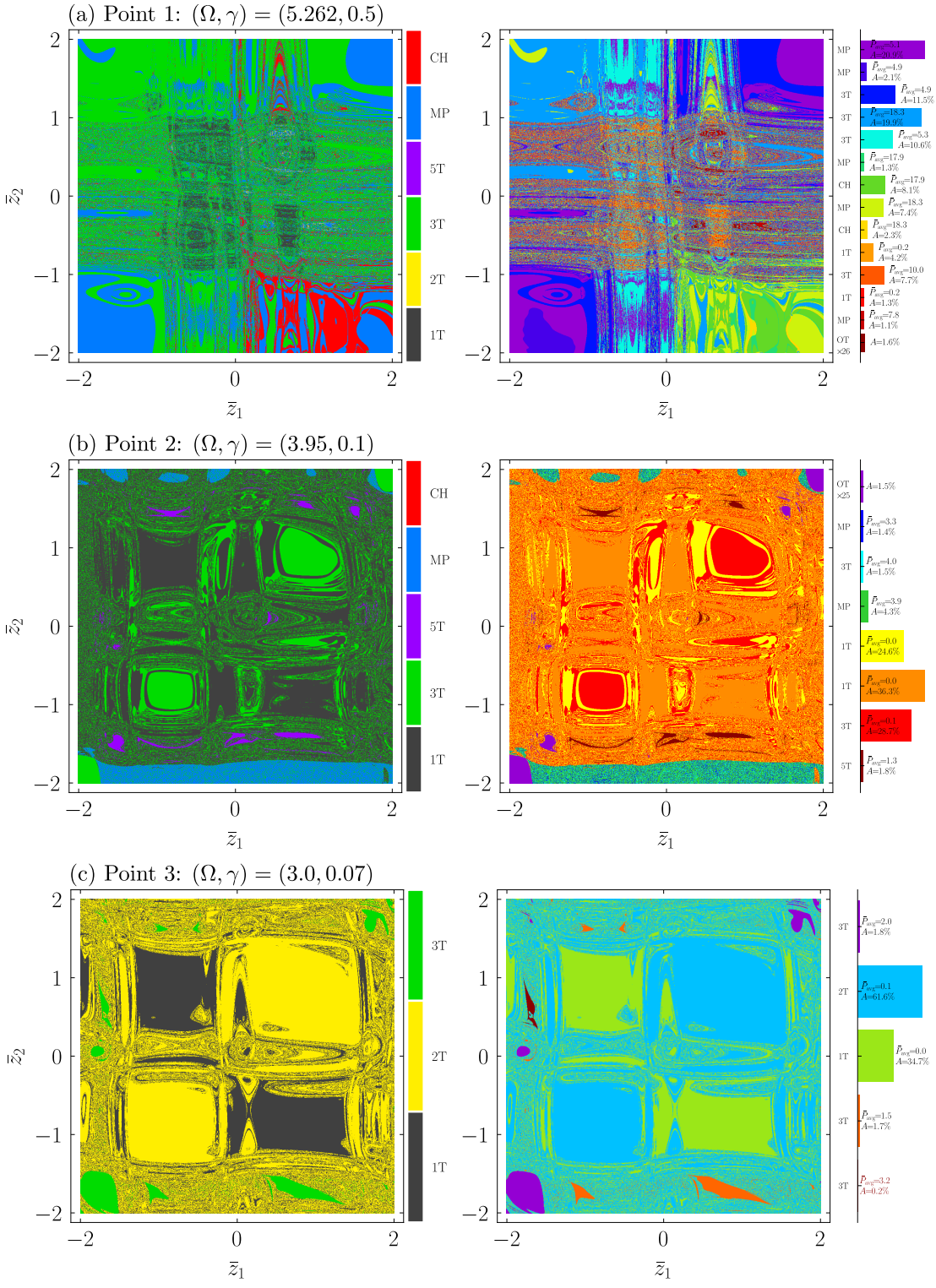

Figure 5.34: Basins of attraction of the forced system for the subspace $\bar{z}_1 \times \bar{z}_2$: (a) Point 1, (b) Point 2, and (c) Point 3 (as highlighted in Figure 5.32). The left-sided basins show the attractors related to the type of motion of the system, with the colorbar representing each attractor. The right-sided basins also incorporate the value of $\bar{P}_{\text{avg}}$ as a mean of classification, with the bar plot representing all the distinct motion-power attractors.

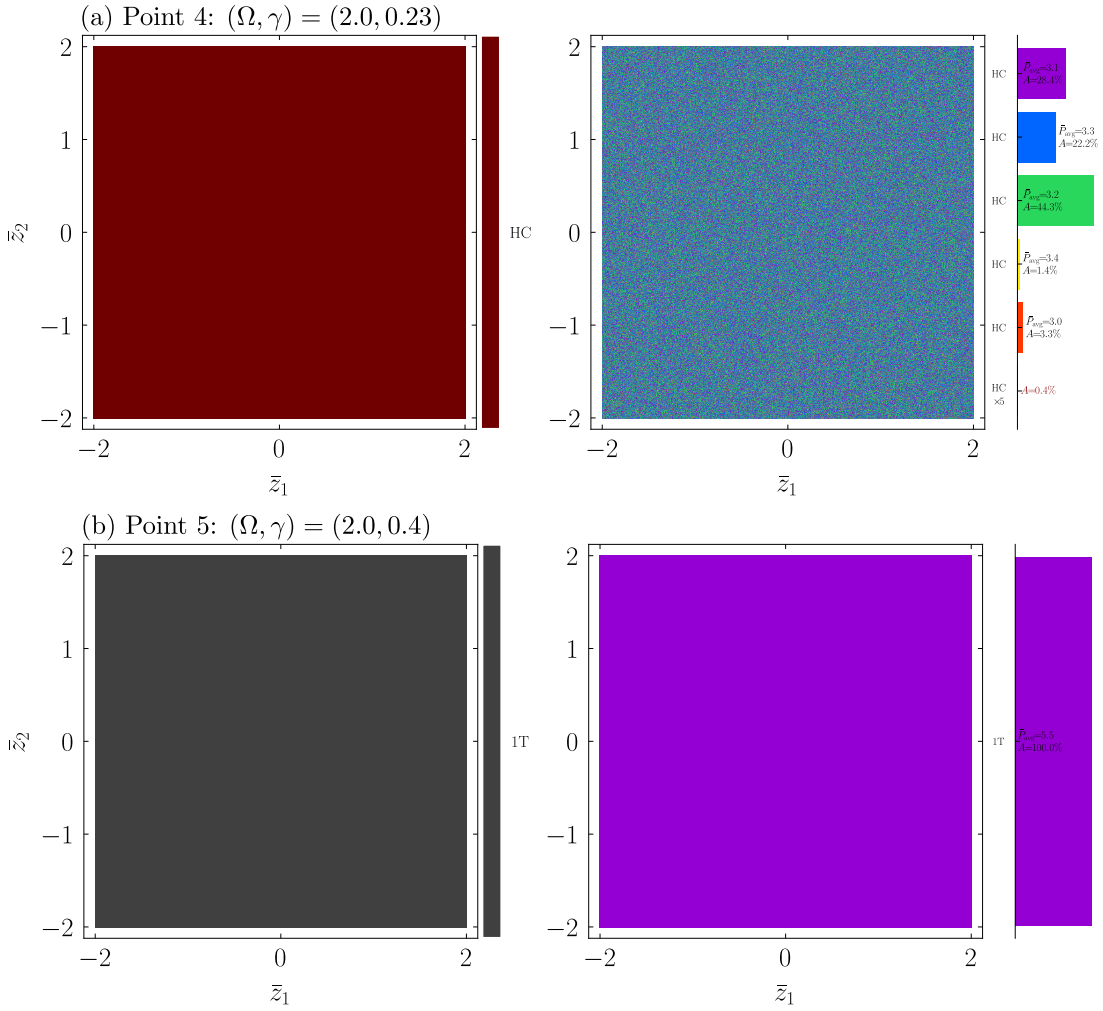

Figure 5.35: Basins of attraction of the forced system for the subspace $\bar{z}_1 \times \bar{z}_2$: (a) Point 4 and (b) Point 5 (as highlighted in Figure 5.32). The left-sided basins show the attractors related to the type of motion of the system, with each color of the colorbar representing one attractor. The right-sided basins also incorporate the value of $\bar{P}_{\text{avg}}$ as a mean of classification, with the bar plot representing all the distinct motion-power attractors.

of the basin. In these two instances, it becomes evident that the system's response and performance exhibit a remarkable level of predictability in point 4, and is 100% predictable in point 5.

Therefore, the scattered zone is a region with a high amount of coexisting solutions, which reduces the predictability of the system's performance. It seems that a control scheme is needed for the system to effectively operate within this region, ensuring good performance. Moreover, it is noticeable that the reduction of the frequency of excitation to a value near the linear natural frequencies can drastically improve its predictability. As a final point, the findings for Configuration I can be extrapolated for other configurations, however, further analyses of the remaining

configurations must be carried out in order to be sure of that.

5.3.4 Performance Comparisons

This Subsection presents a comparison analysis between the compact multistable energy harvester and the classic bistable energy harvester. In light of the results presented in the previous Subsections, it is reasonable to determine that configurations I and II present superior performance in almost all operational conditions, while not true for very low input mechanical energy. Therefore, the magnetic configuration represented by the restitution parameters $(\alpha_1, \alpha_2, \beta_1, \beta_2) = (-2, -1, 1, 1)$ is chosen in this analysis.

The comparisons are performed using the performance comparison diagrams (PCD), where the metric is defined as the percentage difference of the average output power, denoted as $\Delta\bar{P}_{\text{avg}}(\%)$, between the average output power of each harvester ($\bar{P}_{\text{avg}}^{(\text{CMEH})}$ and $\bar{P}_{\text{avg}}^{(\text{CBEH})}$), where CMEH refer to the proposed multistable harvester in this work and CBEH is the classical bistable harvester. Equation 5.25 is used to calculate the percentage difference, which allows a classification based on three sets:

- $\Delta\bar{P}_{\text{avg}}(\%) > 0$: CMEH shows better performance;
- $\Delta\bar{P}_{\text{avg}}(\%) = 0$: CMEH and CBEH shows the same performance;
- $\Delta\bar{P}_{\text{avg}}(\%) < 0$: CBEH shows better performance.

$$\Delta\bar{P}_{\text{avg}}(\%) = \frac{\bar{P}_{\text{avg}}^{(\text{CMEH})} - \bar{P}_{\text{avg}}^{(\text{CBEH})}}{\bar{P}_{\text{avg}}^{(\text{CBEH})}} \times 100. \tag{5.25}$$

On this basis, this estimation is applied to each point of the 1000×1000 OPD grid of each harvester, resulting in a performance comparison diagram (PCD).

Multistable 2-DoF vs Classical Bistable

The overall characteristics of the classical bistable energy harvester are analyzed by considering the same approach employed for the 2-DoF system, building DRD and OPD by setting the parameters of the second degree of freedom to zero ($\alpha_2 = \beta 2 = \zeta_2 = \rho = \Omega_s = \chi_2 = \varphi_2 = \kappa_2 = 0$). Results observed in Figure 5.36 show consistent regions of dynamical attractors at lower excitation frequencies and sparser regions at higher frequencies, with the 1T, 3T, and CH being the predominant dynamical attractors in the DRD. Qualitatively, the OPD in Figure 5.36b displays a similar structure compared to the multistable 2-DoF harvester, showing however, lower maximum average output power: while the classical bistable harvester displays a maximum $\bar{P}_{\text{avg}} = 65.92$, the multistable harvester converts up to $\bar{P}_{\text{avg}} = 117.73$ with

$\Omega_s = 0.25$, and $\bar{P}_{\text{avg}} = 158.82$ with $\Omega_s = 1.0$, a performance enhancement of 78.6% and 140.92%, respectively.

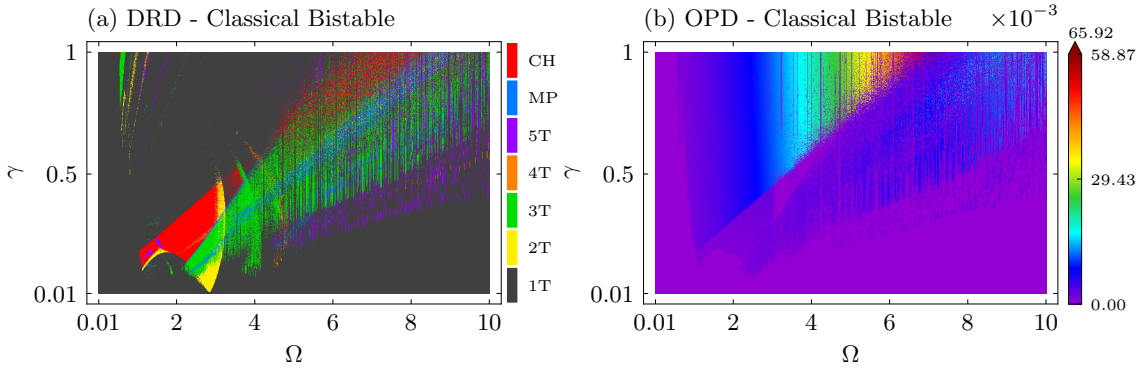

Figure 5.36: (a) DRD and (b) OPD for the classical bistable energy harvester. Colors in (a) represent dynamical attractors while colors in (b) represent the average output power of the harvester ($\bar{P}_{\text{avg}}$).

An overall comparison of the performance of the classical bistable energy harvester with the multistable 2-DoF energy harvester is established considering eight configurations related to the value of Ω_s: 0.25, 0.5, 0.75, 1.0, 1.25, 1.5, 1.75, 2.0. The performance comparison diagrams (PCDs) in Figure 5.37 illustrate the analysis, where red colors indicate regions in which the multistable 2-DoF energy harvester outperforms the classical bistable energy harvester, and black colors indicate regions where the classical bistable energy harvester performs better. Besides, the red areas of the diagram are accounted, represented by A_{red}.

By increasing the value of Ω_s causes the regions where the multistable 2-DoF energy harvester most outperforms the bistable harvester to shift towards higher frequencies, as expected given $\Omega_s = \omega_2/\omega_1$. Moreover, as Ω_s increases, the darker regions representing the narrow frequency ranges where the bistable harvester most outperforms the multistable also become more prominent in higher frequency ranges, augmenting the range of frequencies where the classical bistable harvester outperforms the multistable one in key regions of interest. This can be observed by examining the structures enclosed within the white dashed rectangles shown in the PCDs, which progressively shift towards higher frequencies with increasing Ω_s. Additionally, by increasing Ω_s, it is observed an increase in the area, A_{red}, that represents the better performance of the 2 DoF multistable energy harvester.

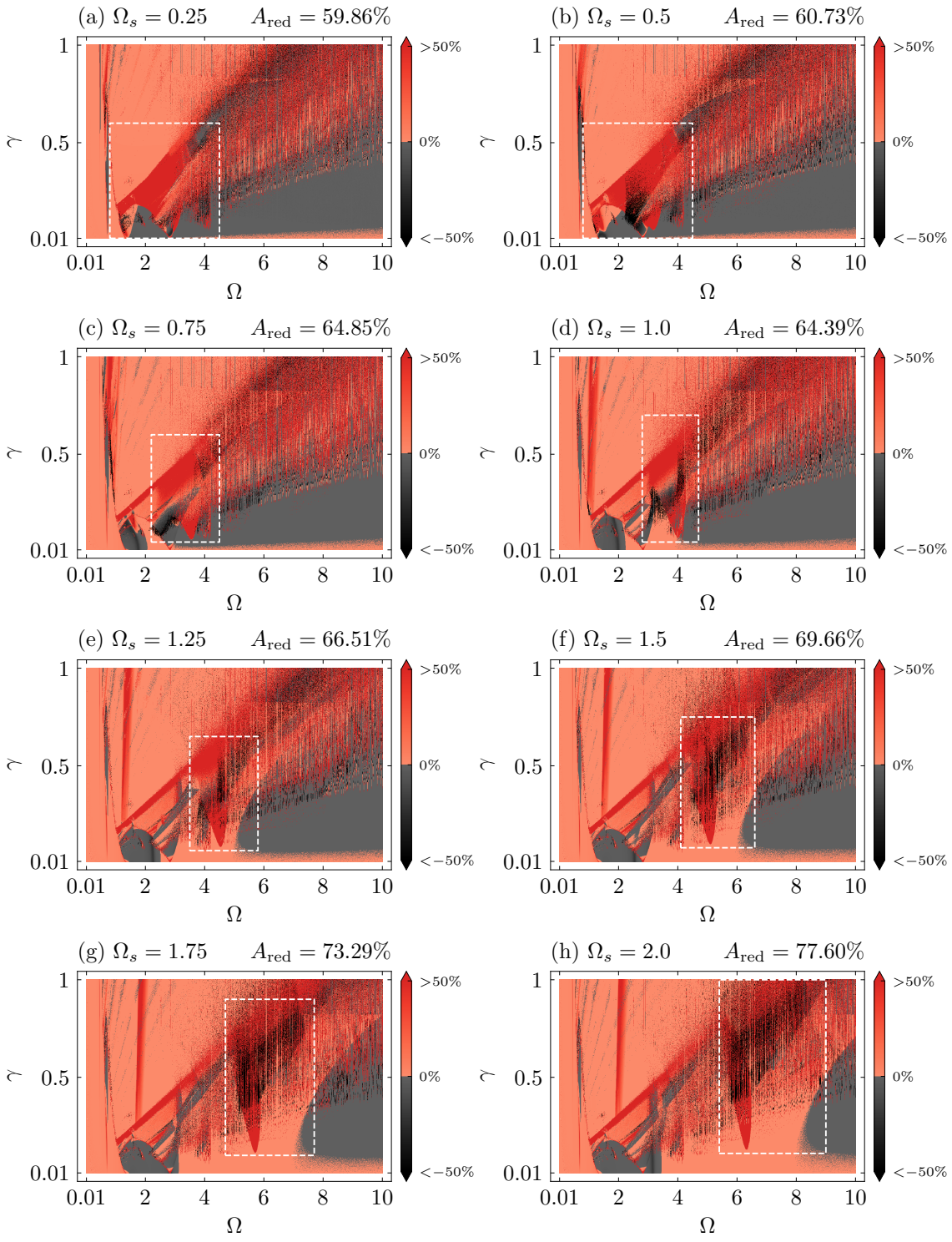

Figure 5.37: Performance comparison between the CMEH and the CBEH: PCD for (a) $\Omega_s = 0.25$, (b) $\Omega_s = 0.5$, (c) $\Omega_s = 0.75$, (d) $\Omega_s = 1$, (e) $\Omega_s = 1.25$, (f) $\Omega_s = 1.5$, (g) $\Omega_s = 1.75$, (h) $\Omega_s = 2$. Colorbars represent $\Delta\bar{P}_{\text{avg}}(\%)$. Regions in red represent where the CMEH outperforms the CBEH, while black regions show where the CBEH performs better. White dashed rectangle regions are discussed in the text.

Having identified the regions in the excitation parameter domain where the proposed harvester outperforms the classical bistable harvester, it is crucial to evaluate the quality of these regions. To this end, consider the introduction of a normalization of the output power for each output power diagram (OPD) analyzed with different values of $\Omega_s = (0.25, 0.5, 0.75, 1.0, 1.25, 1.5, 1.75, 2.0)$. Specifically, the normalized power, $\bar{P}_{\text{norm}_{ij}}$, is defined as the ratio of the average output power at each point in the OPD, denoted by $\bar{P}_{\text{avg}_{ij}}$, to the maximum average output power across all points in that same OPD, denoted by $\bar{P}_{\text{avg}}^{(\text{max})}$, where i and j are the indexes of the points within the diagram:

$$\bar{P}_{\text{norm}_{ij}} = \frac{\bar{P}_{\text{avg}}}{\bar{P}_{\text{avg}}^{(\text{max})}}. \tag{5.26}$$

This normalization procedure results in all OPDs being scaled to the range $[0, 1]$, providing a measure of the quality of each frequency range. Subsequently, the occurrence of $\bar{P}_{\text{norm}} \geq 0.01$ for each case is analyzed, which indicates the instances where the normalized output power is at least 1% of the output power range while excluding very low power values. The outcome of the analysis is summarized in Figure 5.38a, where the occurrence diagram is presented. By analyzing this diagram, four areas of interest can be delimited, as shown in Figure 5.38b. The green area denoted by the letter A can be classified as the region with the best performance, exhibiting a high occurrence of good performance. In contrast, the yellow region labeled as B represents the region with many fluctuations due to the presence of intermittent irregular sparse points of high and low performance, caused by the numerous attractors in its basin of attraction. Although region B can present high performance at higher frequencies of operation, it should be classified as a region of moderate performance as it needs to be associated with a control scheme to stabilize

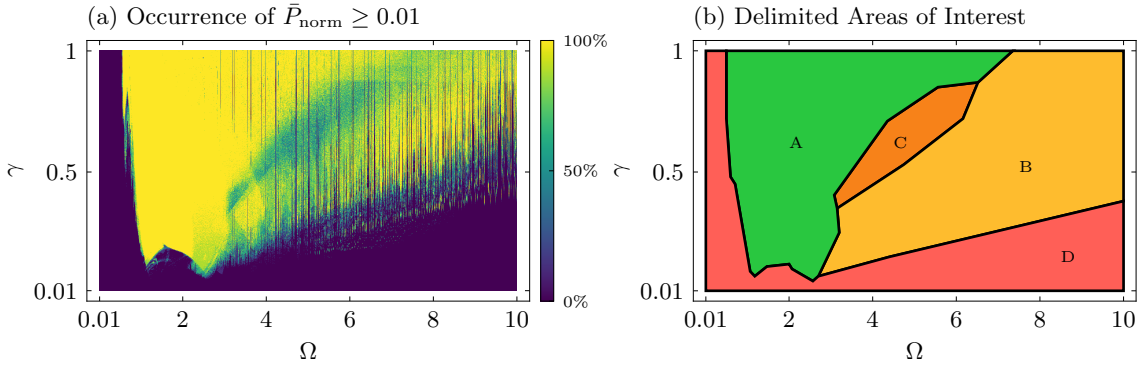

Figure 5.38: (a) Occurrence diagram (OCD) for $\bar{P}_{\text{norm}} \geq 0.01$. (b) identified regions of interest. The colorbar in (a) represents the occurrence percentage. Labels A, B, C and D represent each colored region, being A the region of best performance, B and C the regions of moderate performance, and D the region of poor performance in the $\gamma \times \Omega$ parameter domain.

in a suitable attractor. Region C, represented in orange, is similar to region B but shows lower occurrence in the occurrence diagram of 5.38a. Lastly, the red region labeled as D is characterized by poor harvester performance and should be avoided in the design of this type of harvester. Therefore regions A, B and C can be classified as regions of interest.

By comparing Figures 5.37 and 5.38, it is clear that, in terms of overall average output power, the multistable 2-DoF energy harvester outperforms the bistable harvester in almost every region of interest. This improved performance can be attributed to the multistable harvester's more efficient use of available free space, which is achieved by incorporating a second piezoelectric patch.

In contrast, in terms of power density, $\bar{P}_{\text{avg}}^{\text{den}}$, as defined by Equation 5.22, the proposed system outperforms the classical bistable energy harvester only in specific zones of the diagram, as depicted in Figure 5.39. This is further explicit by the measure of the area in red, A_{red}. These zones are mainly associated with regions B and C of moderate performance, as classified in Figure 5.38b, suggesting that these zones are associated with the high performance of both degrees of freedom. This indicates that the transmission of energy from the external source to the structure, and from the structure to the piezoelectric elements is done more efficiently in these regions. In the black zones, the superior performance of the classical bistable harvester can be attributed to the insertion of an additional source of damping by introducing the second degree of freedom. In these regions, this extra degree of freedom acts as an energy sink that does not transmit the energy efficiently to the transducer element.

Different 2-DoF multistable configurations

This subsection establishes a comparison between two different configurations within the group of cases analyzed in this work ($\Omega_s = \{0.25, 0.5, 0.75, 1.0, 1.25, 1.5, 1.75, 2.0\}$). Equation 5.25 is used, but instead of comparing with the CBEH, now the comparison is done regarding the device with $\Omega_s = 0.25$. Figure 5.40 presents a comparison between the device with $\Omega_s = 0.25$ and its counterparts with increasing values of Ω_s. Black regions depict where the multistable 2-DoF harvester with $\Omega_s = 0.25$ outperforms its counterparts, while black regions where it underperforms. It is noteworthy that the increase of Ω_s promotes enhanced performance at higher frequencies as depicted by the performance comparison diagrams (PCDs). As expected, the difference in performance between the compared harvesters increases in regions where each one performs better.

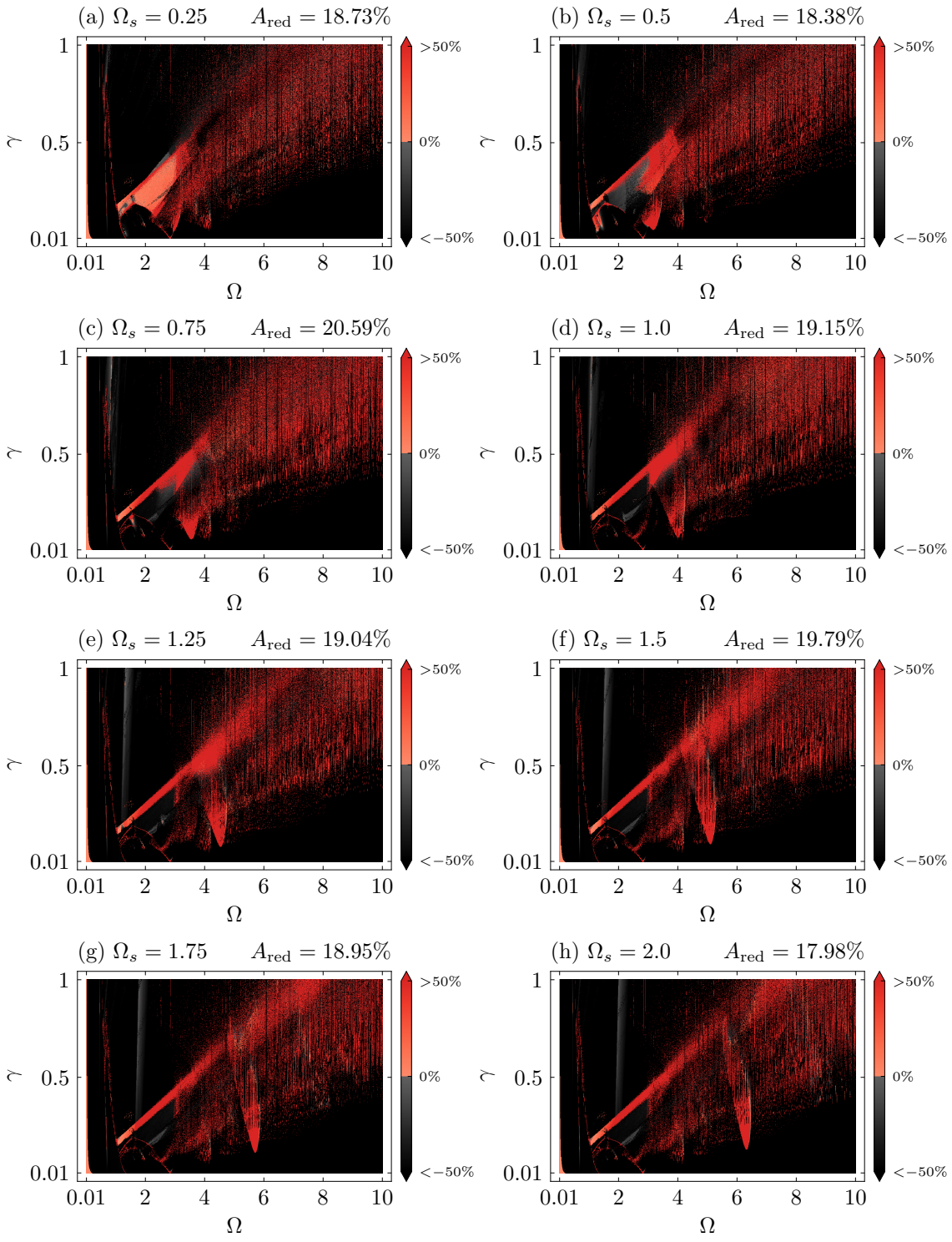

Figure 5.39: Performance comparison between the CMEH and the CBEH using the average output power density $\bar{P}^{\text{den}}_{\text{avg}}$. PCD for (a) $\Omega_s = 0.25$, (b) $\Omega_s = 0.5$, (c) $\Omega_s = 0.75$, (d) $\Omega_s = 1.0$, (e) $\Omega_s = 1.25$, (f) $\Omega_s = 1.5$, (g) $\Omega_s = 1.75$, (h) $\Omega_s = 2.0$. Colorbars represent $\Delta\bar{P}^{\text{den}}_{\text{avg}}(\%)$. Regions in red represent where the CMEH outperforms the CBEH, while black regions show where the CBEH performs better.

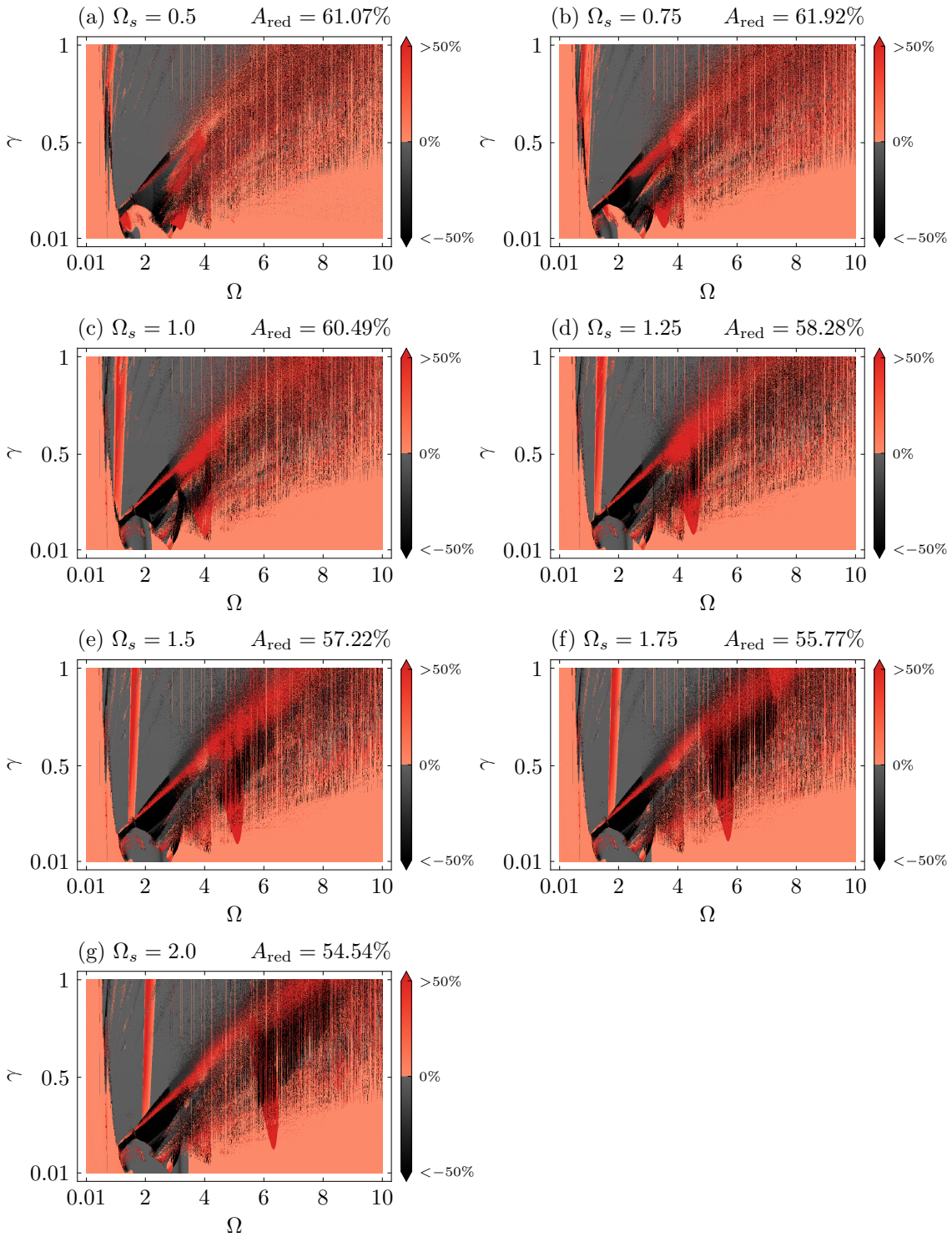

Figure 5.40: Performance comparison between the CMEH $\bar{P}_{\text{avg}}$ with $\Omega = 0.25$ and the CMEH with different Ω_s values: (a) $\Omega_s = 0.5$, (b) $\Omega_s = 0.75$, (c) $\Omega_s = 1.0$, (d) $\Omega_s = 1.25$, (e) $\Omega_s = 1.5$, (f) $\Omega_s = 1.75$, (g) $\Omega_s = 2.0$. Colorbars represent $\Delta\bar{P}_{\text{avg}}(\%)$. Red regions indicate where the CMEH with $\Omega_s = 0.25$ outperforms its counterparts, while black regions show where it underperforms. The PCDs use Equation 5.25 modified with the reference harvester being the one with $\Omega_s = 0.25$, instead of the CBEH.

Chapter 6

The Multidirectional Hybrid Energy Harvester

Pendulum structures have been widely used in mechanical energy harvesting systems, as demonstrated in recent review studies [115, 198]. Additionally, although numerous enhancements to the classic cantilever harvester design have been developed to date, the capability for multidirectional energy harvesting remains a challenge that needs to be properly addressed. This Chapter is dedicated to exploring the usage of pendulum structures to achieve multidirectional capabilities in classical energy harvesting systems. A multidirectional hybrid energy harvester (MHEH) is proposed. Specifically, the MHEH is a modified version of the classical cantilever-based piezoelectric energy harvester (CPEH), where a pendulum is attached to the free end of the cantilever design. Moreover, a piezoelectric transducer is attached to the vertical direction of the harvester to convert energy from axial oscillations, while an electromagnetic converter is attached to the pendulum to harness the rotational energy, resulting in a hybrid transduction scheme. The next sections show that the utilization of the hybrid transduction strategy is necessary to mitigate the effects of the pendulum as an energy absorber, harnessing the rotational energy that would otherwise be lost.

6.1 Design and Theoretical Model

Consider the conceptual representation of three cantilever-based energy harvesters presented in Figure 6.1. The first shown in Figure 6.1(a), represents the classical cantilever-based piezoelectric energy harvester (CPEH), composed by a piezoelectric transducer attached to a structural beam element, a support where the beam is embedded, and a tip mass at its free end. The second design, displayed in Figure 6.1(b), shows the multidirectional piezoelectric harvester (MPEH), which

incorporates the pendulum in the classical design. This layout leverages the planar motion of the pendulum to transmit the input energy from one Cartesian direction to another. Finally, Figure 6.1(c) displays the proposed multidirectional hybrid energy harvester (MHEH), which incorporates an additional electromagnetic transducer at the support of the pendulum in order to harness its rotational energy.

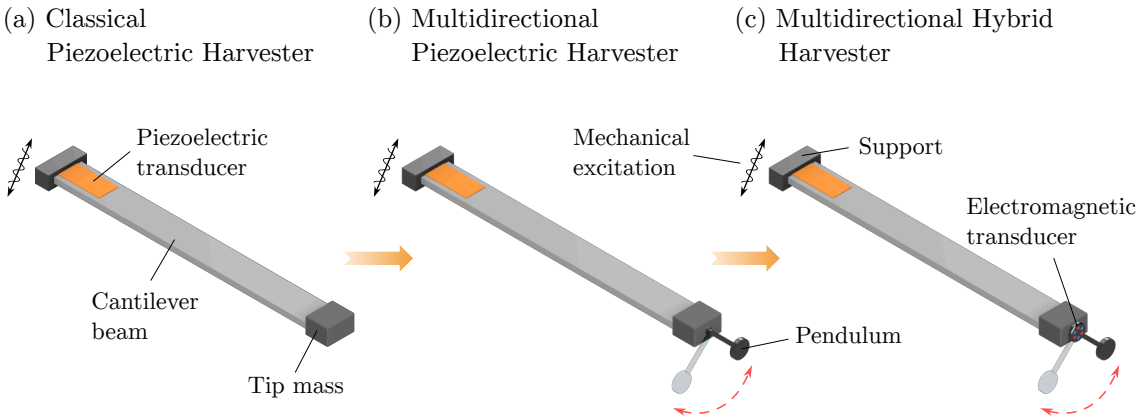

Figure 6.1: Conceptual representation of the three types of energy harvesters. (a) The classical piezoelectric energy harvester (CPEH), composed of a piezoelectric transducer and a cantilever beam structure with a tip mass. (b) the multidirectional piezoelectric energy harvester (MPEH), composed by the CPEH plus the addition of a pendulum structure. (c) The proposed multidirectional hybrid energy harvester (MHEH) composed of the MPEH plus the addition of an electromagnetic transducer at the pendulum's support.

6.1.1 Physical Modeling

Given the designs presented in Figure 6.1, they can be represented by the general archetype model depicted in Figure 6.2. The model considers the beam main structure of effective mass m_s, and a pendulum-type element of effective mass m_p attached to it. The equivalent stiffness and damping coefficients are represented by k_j $(j = x, z, pz)$ and c_j $(j = x, z, em, p)$, in which subscripts are related to the direction or an element within the system. Subscript x and z refer to the plane directions, while subscript p refers to the pendulum; subscripts pz and em refer to the piezoelectric and electromagnetic transducers, respectively. Two transducers are attached to the system: a piezoelectric element with an electromechanical coupling term, θ_{pz} and an equivalent stiffness, k_{pz}, in the z direction of the structure; and an electromagnetic energy converter attached to the support of the pendulum with an electromagnetic coupling term, θ_{em}, and a magnetic damping coefficient c_{em}. The transducers are represented by an equivalent circuit. The piezoelectric

element can be represented by a circuit depicted in Figure 6.2(b), with an internal capacitance, C_{pz}, connected in parallel to internal resistance, R_{ipz}, and an induced current related to the electromechanical coupling, $I_{pz}(t) = \theta_{pz}\dot{z}_s(t)$. An external load resistance, R_{lpz}, is also attached to the piezoelectric element. Additionally, the electromagnetic transducer is represented by the circuit depicted in Figure 6.2(c), with a voltage source, $v_{em}(t) = \theta_{em}\dot{\phi}(t)$, connected in series with an equivalent internal inductance, L_m, an internal resistance R_{iem}, and external load resistance, R_{lem}. The equivalent resistance of the piezoelectric circuit is represented by $R_{pz} = R_{ipz}R_{lpz}/\left(R_{lpz} + R_{ipz}\right)$, while the equivalent resistance of the electromagnetic circuit is represented by $R_{em} = R_{iem} + R_{lem}$.

The effects of gravity, g, are considered, and the system is subjected to a multidirectional excitation represented by the vector $\mathbf{r_b}(t) = r_b(t)\left[\sin\left(\mu\right)\hat{\mathbf{e}}_x + \cos\left(\mu\right)\hat{\mathbf{e}}_z\right]$, where the bold notation refers to vectors and italic notation refers to scalars; μ is the angle between the external excitation vector $\mathbf{r_b}(t)$ and the z direction, and $r_b(t)$ is the excitation function; the vectors $\hat{\mathbf{e}}_x$ and $\hat{\mathbf{e}}_z$ are the base vectors of each Cartesian direction, x and z, respectively.

The absolute structure position can be written as follows,

$$\begin{aligned}\mathbf{r}_s(t) &= \left[x_b(t) + x_s(t)\right]\hat{\mathbf{e}}_x + \left[z_b(t) + z_s(t)\right]\hat{\mathbf{e}}_z \\ &= \left[x_b(t) + x(t)\right]\hat{\mathbf{e}}_x + \left[z_b(t) + z(t) + z_{st}\right]\hat{\mathbf{e}}_z,\end{aligned} \tag{6.1}$$

where $x(t)$ and $z(t)$ are the relative positions in which the system oscillates with respect to the equilibrium position, and $z_{st} = \left(m_s + m_p\right)g/\left(k_z + k_{pz}\right)$ is the static deflection of the structure due to gravity action. Also, the absolute position of the pendulum is given by

$$\begin{aligned}\mathbf{r}_p(t) &= \left[x_b(t) + x(t) + x_p(t)\right]\hat{\mathbf{e}}_x + \left[z_b(t) + z(t) + z_{st} + z_p(t)\right]\hat{\mathbf{e}}_z \\ &= \left[x_b(t) + x(t) + L_p\sin\left(\phi(t)\right)\right]\hat{\mathbf{e}}_x + \left[z_b(t) + z(t) + z_{st} + L_p\cos\left(\phi(t)\right)\right]\hat{\mathbf{e}}_z,\end{aligned} \tag{6.2}$$

where L_p is the pendulum length and ϕ is the pendulum angle.

By considering an energetic approach, the total kinetic energy can be written as the composition of the structure and the pendulum kinetic energies as follows,

$$\begin{aligned}T &= T_s + T_p \\ &= \frac{1}{2}m_s\dot{\mathbf{r}}_s(t)\cdot\dot{\mathbf{r}}_s(t) + \frac{1}{2}m_p\dot{\mathbf{r}}_p(t)\cdot\dot{\mathbf{r}}_p(t) \\ &= \frac{1}{2}m_p\left\{\left[\dot{x}(t) + \dot{x}_b(t) + L_p\dot{\phi}(t)\cos\left(\phi(t)\right)\right]^2 + \left[\dot{z}(t) + \dot{z}_b(t) - L_p\dot{\phi}(t)\sin\left(\phi(t)\right)\right]^2\right\} \\ &\quad + \frac{1}{2}m_s\left\{\left[\dot{x}(t) + \dot{x}_b(t)\right]^2 + \left[\dot{z}(t) + \dot{z}_b(t)\right]^2\right\}.\end{aligned} \tag{6.3}$$

The structure and piezoelectric element constitutive behaviors are assumed to be

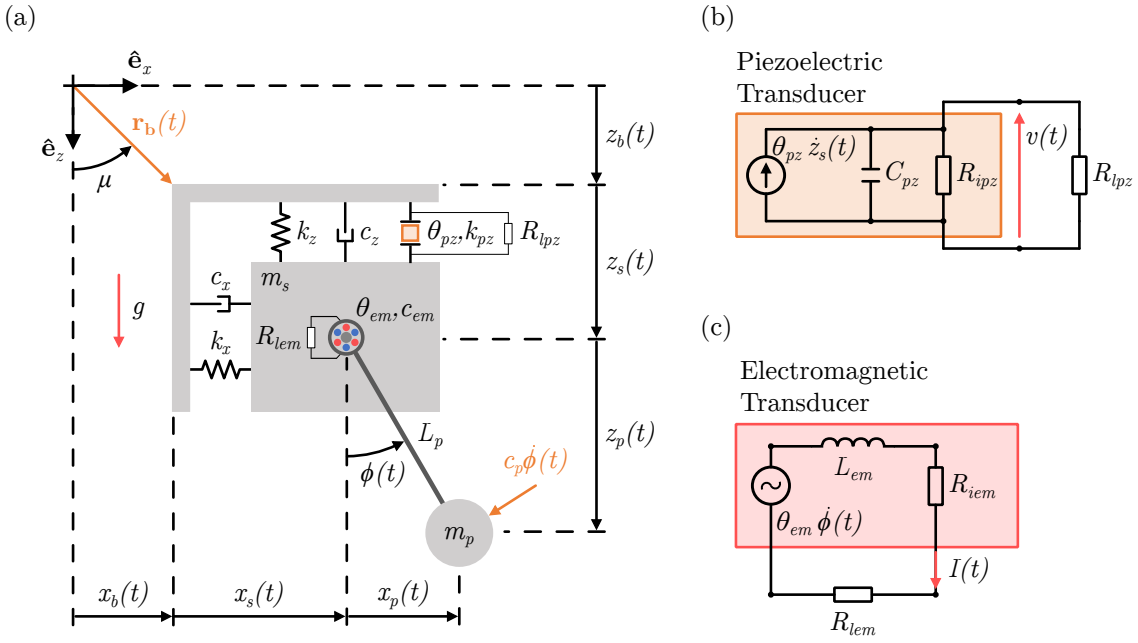

Figure 6.2: (a) Archetype representing the Hybrid Multidirectional Energy Harvester. (b) The equivalent circuit of the piezoelectric transducer attached to a resistance. (c) The equivalent circuit of the electromagnetic transducer attached to a resistance.

linear and, therefore, the total restitution forces of the structure and the piezoelectric elements are defined in Equations 6.4, 6.5, and 6.6,

$$f_x(t) = -k_x x(t), \tag{6.4}$$

$$f_z(t) = -k_z z(t), \tag{6.5}$$

$$f_{pz}(t) = -k_{pz} z(t), \tag{6.6}$$

resulting in the total potential energy, written as the sum of the main structure, piezoelectric element, and pendulum potential energies,

$$\begin{aligned} U &= U_s + U_p \\ &= -\int_0^{x_s(t)} f_x(t)\,dx - \int_0^{z_s(t)} \left[f_z(t) + f_{pz}(t)\right]\,dz - \int_0^{z_b(t)+z_s(t)} m_s g\,dz \\ &\quad - \int_0^{z_b(t)+z_s(t)+z_p(t)} m_p g\,dz \\ &= \frac{1}{2}k_x x(t)^2 + \frac{1}{2}\left(k_z + k_{pz}\right)\left[z(t) + z_{st}\right]^2 - m_s g\left[z_b(t) + z(t) + z_{st}\right] \\ &\quad - m_p g\left[z_b(t) + z(t) + z_{st} + L_p\cos\left(\phi(t)\right)\right]. \end{aligned} \tag{6.7}$$

The electromechanical coupling of the piezoelectric transducer, θ_{pz}, is related to the induced current, $I_{pz}(t)$. In contrast, the electromechanical coupling of the

electromagnetic transducer, θ_{em}, is related to the induced voltage, $v_{em}(t)$. The electromechanical coupling, θ_{pz}, is determined by the properties of the piezoelectric material, its geometry and dimensions. In contrast, the electromechanical coupling due to the electromagnetic converter, θ_{em}, can be determined by the geometric characteristics of the coil(s), the properties of the magnet(s) within the converter, the intensity of its magnetic field(s) and how these elements are positioned and distributed within the transducer. Often, it is possible to determine these two quantities analytically, nevertheless, either finite element analysis or experimental methods are required for complex structures. Another possibility is that these coupling mechanisms can dynamically change depending on the state of the system. For the sake of simplicity, this work considers constant coupling coefficients.

From this perspective, consider the linear relation between the flux linkage, $\psi(t)$, and the voltage, $v(t)$, across the piezoelectric circuit as $\dot{\psi}(t) = v(t)$, and the linear relation between the charge, $q(t)$, and the current, $I(t)$, flowing in the electromagnetic circuit as $\dot{q}(t) = I(t)$. Considering that the total energy, W, of the electrical domain can be represented by the sum of the electric energy of the piezoelectric element, W_e, and the magnetic energy of the electromagnetic transducer, W_m, as described by Equation 6.8, where W_C, W_{pz}, W_L and W_{em} are the electric energy in the capacitance, the piezoelectric energy, the magnetic energy in the inductance and the electromagnetic energy, respectively. The details of this formulation can be seen in PREUMONT [191].

$$W = W_e + W_m \tag{6.8}$$

$$= W_C + W_{pz} + W_L + W_{em} \tag{6.9}$$

$$= \frac{1}{2}C_{pz}\dot{\psi}(t)^2 + \theta_{pz}\dot{\psi}(t)z(t) + \frac{1}{2}L_{em}\dot{q}(t)^2 + \theta_{em}\dot{q}(t)\phi(t). \tag{6.10}$$

The system dissipation is expressed from four major sources: viscous dissipation of the main structure; viscous dissipation related to the pendulum structure; magnetic dissipation of the electromagnetic transducer, resulting from the interactions between the magnet(s) and coil(s); and electrical resistances within the circuits. These sources can be modeled through dissipation functions [191, 192], as depicted in Equation 6.11, where D_x and D_z are the dissipation functions associated with the nonconservative viscous force in x and z directions. D_{ϕ_e} is the dissipation function associated with the interaction between the pendulum structure and the surrounding media, while D_{ϕ_i} is the electromechanical dissipation associated with the magnetic forces within the electromagnetic transducer. D_{pz} and D_{em} are the dissipation func-

tions that account for the resistive elements of the circuits.

$$\begin{aligned} D &= D_x + D_z + D_{\phi_e} + D_{\phi_i} + D_{pz} + D_{em} \\ &= \frac{1}{2}c_x\dot{x}(t)^2 + \frac{1}{2}c_z\dot{z}(t)^2 + \frac{1}{2}c_pL_p\dot{\phi}(t)^2 + \frac{1}{2}c_{em}\dot{\phi}(t)^2 + \frac{1}{2}\frac{\dot{\psi}(t)^2}{R_{pz}} + \frac{1}{2}R_{em}\dot{q}(t)^2. \end{aligned} \tag{6.11}$$

On this basis, the Lagrangian can be defined as $\mathcal{L} = T - U + W$, where the electromechanical system is associated with five generalized coordinates (three mechanical and two electrical), $\mathbf{Q} = [x(t), z(t), \phi(t), \psi(t), q(t)]$. Therefore, by applying the Euler-Lagrange method, the following equation is achieved,

$$\frac{d}{dt}\left(\frac{\partial \mathcal{L}}{\partial \dot{Q}_i}\right) - \frac{\partial \mathcal{L}}{\partial Q_i} + \frac{\partial D}{\partial \dot{Q}_i} = 0. \tag{6.12}$$

Suppressing the (t) in the notation of the generalized coordinates, the electromechanical equations of motion can be written as a system of equations related to the state variables x, z, ϕ, v and I:

$$(m_s + m_p)\,\ddot{x} + c_x\dot{x} + k_x x + m_pL_p\left[\ddot{\phi}\cos(\phi) - \dot{\phi}^2\sin(\phi)\right] = -(m_s + m_p)\,\ddot{x}_b; \tag{6.13}$$

$$\begin{aligned} (m_s + m_p)\,\ddot{z} + c_z\dot{z} + (k_z + k_{pzt})\,z - \theta_{pz}v - m_pL_p\left[\ddot{\phi}\sin(\phi) + \dot{\phi}^2\cos(\phi)\right] = \\ -(m_s + m_p)\,\ddot{z}_b; \end{aligned} \tag{6.14}$$

$$\begin{aligned} m_pL_p^2\ddot{\phi} + (c_{em} + c_pL_p)\dot{\phi} + m_pL_p[\ddot{x}\cos(\phi) + (g - \ddot{z})\sin(\phi)] - \theta_{em}I = \\ m_pL_p\left[\ddot{z}_b\sin(\phi) - \ddot{x}_b\cos(\phi)\right]; \end{aligned} \tag{6.15}$$

$$C_{pz}\dot{v} + \frac{v}{R_{pz}} + \theta_{pz}\dot{z} = 0; \tag{6.16}$$

$$L_{em}\dot{I} + R_{em}I + \theta_{em}\dot{\phi} = 0. \tag{6.17}$$

By assuming a harmonic external stimulus:

$$\mathbf{r_b} = x_b\hat{\mathbf{e}}_x + z_b\hat{\mathbf{e}}_z = A_b\sin(\omega t)\left[\sin(\mu)\hat{\mathbf{e}}_x + \cos(\mu)\hat{\mathbf{e}}_z\right]. \tag{6.18}$$

Thus,

$$\ddot{\mathbf{r}}_\mathbf{b} = \ddot{x}_b\hat{\mathbf{e}}_x + \ddot{z}_b\hat{\mathbf{e}}_z = -A_b\omega^2\sin(\omega t)\left[\sin(\mu)\hat{\mathbf{e}}_x + \cos(\mu)\hat{\mathbf{e}}_z\right]. \tag{6.19}$$

In order to generalize the analysis, a normalization approach is performed by considering a reference length, L, a reference voltage V, and a reference current $\mathcal{I}$,

resulting in the following dimensionless electromechanical equations:

$$(1+\rho)\,\ddot{\bar{x}} + 2\zeta_x\dot{\bar{x}} + \Omega_s^2\bar{x} + \rho\ell\left[\ddot{\bar{\phi}}\cos(\bar{\phi}) - \dot{\bar{\phi}}^2\sin(\bar{\phi})\right] = -(1+\rho)\ddot{\bar{x}}_b; \tag{6.20}$$

$$(1+\rho)\,\ddot{\bar{z}} + 2\zeta_z\dot{\bar{z}} + \bar{z} - \chi_{pz}\bar{v} - \rho\ell\left[\ddot{\bar{\phi}}\sin(\bar{\phi}) + \dot{\bar{\phi}}^2\cos(\bar{\phi})\right] = -(1+\rho)\ddot{\bar{z}}_b; \tag{6.21}$$

$$\ddot{\bar{\phi}} + 2\zeta_\phi\dot{\bar{\phi}} + \Omega_\phi^2\sin(\bar{\phi}) - \chi_{em}\bar{I} + \frac{1}{\ell}\left[\ddot{\bar{x}}\cos(\bar{\phi}) - \ddot{\bar{z}}\sin(\bar{\phi})\right] = \frac{1}{\ell}\left[\ddot{\bar{z}}_b\sin(\bar{\phi}) - \ddot{\bar{x}}_b\cos(\bar{\phi})\right]; \tag{6.22}$$

$$\dot{\bar{v}} + \frac{\bar{v}}{\varphi_{pz}} + \kappa_{pz}\dot{\bar{z}} = 0; \tag{6.23}$$

$$\dot{\bar{I}} + \varphi_{em}\bar{I} + \kappa_{em}\dot{\bar{\phi}} = 0. \tag{6.24}$$

These equations are related to the dimensionless parameters presented in Table 6.1 together with typical values.

Table 6.1: System parameters and values used in the analyses

Parameter Description	Symbol	Definition	Value
Natural frequency of the main structure in x	ω_x	$\sqrt{k_x/m_s}$	-
Natural frequency of the main structure in z	ω_z	$\sqrt{k_z/m_s}$	-
Linearized natural frequency of the pendulum	ω_ϕ	$\sqrt{g/L_p}$	-
Normalized time	τ	$\omega_z t$	-
Normalized x displacement of the main structure	$\bar{x}(\tau)$	$x(t)/L$	-
Normalized z displacement of the main structure	$\bar{z}(\tau)$	$z(t)/L$	-
Normalized angle of the pendulum structure	$\bar{\phi}(\tau)$	$\phi(t)$	-
Normalized voltage of the piezoelectric circuit	$\bar{v}(\tau)$	$v(t)/V$	-
Normalized current of the electromagnetic circuit	$\bar{I}(\tau)$	$I(t)/\mathcal{G}$	-
Normalized base excitation frequency	Ω	ω/ω_z	$0.01 \rightarrow 2$
Normalized base excitation amplitude	γ	A_b/L	$0.01 \rightarrow 0.5$
Normalized angle of the base excitation vector $\mathbf{r_b}(t)$	$\bar{\mu}$	μ	$0°, 45°, 90°$
Normalized base excitation displacement in the x direction	$\bar{x}_b(\tau)$	$\gamma\sin(\Omega\tau)\sin(\bar{\mu})$	-
Normalized base excitation displacement in the z direction	$\bar{z}_b(\tau)$	$\gamma\sin(\Omega\tau)\cos(\bar{\mu})$	-
Ratio of masses	ρ	m_p/m_s	0.5
Normalized damping coefficient of the main structure in x	ζ_x	$c_x/(2\omega_z m_s)$	0.025
Normalized damping coefficient of the main structure in z	ζ_z	$c_z/(2\omega_z m_s)$	0.025
Normalized total damping coefficient of the pendulum structure	ζ_ϕ	$\frac{[(c_{em}/L_p)+c_p]}{2\omega_z L_p m_s}$	0.0025
Ratio of natural frequencies of the main structure	Ω_s	ω_x/ω_z	$0.01 \rightarrow 2$
Ratio of natural frequencies of the pendulum and the z direction	Ω_ϕ	ω_ϕ/ω_z	$0.01 \rightarrow 2$
Normalized pendulum length	ℓ	L_p/L	1
Normalized piezoelectric coupling in the mechanical ODE	χ_{pz}	$\theta_{pz}V/(k_z L)$	0.05
Normalized electromagnetic coupling in the mechanical ODE	χ_{em}	$\theta_{em}\mathcal{G}/(\rho k_z L_p^2)$	$\eta\chi_{pz}$
Normalized piezoelectric coupling in the piezo circuit ODE	κ_{pz}	$\theta_{pz}L/(C_{pz}V)$	0.5
Normalized EM coupling in the electromagnetic circuit ODE	κ_{em}	$\theta_{em}/(L_{em}\mathcal{G})$	$\eta\kappa_{pz}$
Normalized equivalent resistance of the piezoelectric circuit	φ_{pz}	$C_{pz}R_{pz}\omega_z$	$0.2 \rightarrow 100$
Normalized equivalent resistance of the electromagnetic circuit	φ_{em}	$R_{em}/(L_{em}\omega_z)$	$0.01 \rightarrow 5$
Ratio between electromechanical couplings	η	$\chi_{em}/\chi_{pz} = \kappa_{em}/\kappa_{pz}$	$0.2 \rightarrow 1$
Normalized electrical output power of the piezoelectric circuit	$\bar{P}_{pz}(\tau)$	$P_{pz}(t)/(C_{pz}\omega_z V^2)$	-
Normalized electrical output power of the electromagnetic circuit	$\bar{P}_{em}(\tau)$	$P_{em}(t)/(L_{em}\omega_z\mathcal{G}^2)$	-

This model allows the representation of all three harvesters depicted in Figure 6.1, enabling further comparison among them. The modeling of the CPEH is achieved by maintaining the pendulum mass, reducing the pendulum length to zero, and removing the electromagnetic transducer as illustrated in Figure 6.3a, denoted as Case I. This is equivalent of making the parameters $\zeta_\phi = \Omega_\phi = \ell = \chi_{em} = \kappa_{em} =$

$\varphi_{em} = 0$. Case II, depicted in Figure 6.3b, represents the model for the MPEH. This configuration can be achieved by removing the electromagnetic transducer, making $\chi_{em} = \kappa_{em} = \varphi_{em} = 0$. Finally, Case III refers to the proposed MHEH, with the pendulum structure and the electromagnetic converter, being represented in Figure 6.3c.

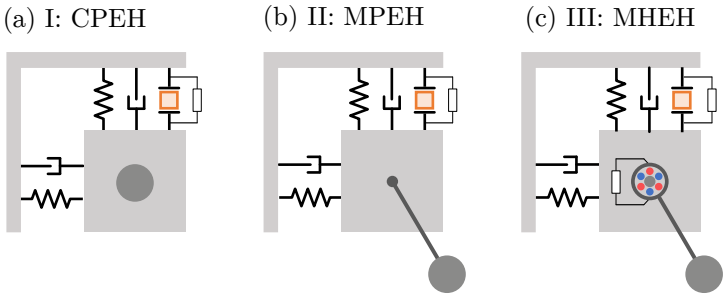

Figure 6.3: Equivalent models of (a) Case I: The classical linear piezoelectric energy harvester (CPEH). (b) Case II: The multidirectional piezoelectric energy harvester (MPEH). (c) Case III: The multidirectional hybrid energy harvester (MHEH), proposed in this work.

6.1.2 Performance Metrics

The performance of the energy harvesting system is evaluated with the definition of the electrical power associated with both piezoelectric and electromagnetic circuits. The total instantaneous electrical power consists of the sum of the instantaneous electrical power in each circuit, as represented by Equation 6.25. Thus, the average electrical power, defined over the interval $t_0 \leq t \leq t_f$, is represented by Equation 6.26, where v^{RMS} and I^{RMS} are the root-mean-square (RMS) of the output voltage of the piezoelectric circuit and the output current of the electromagnetic circuit, respectively, and is defined as depicted in Equation 6.27.

$$P_{\text{inst}} = P_{\text{inst}_{pz}} + P_{\text{inst}_{em}} = \frac{1}{R_{pz}} v^2 + R_{em} I^2, \tag{6.25}$$

$$P_{\text{avg}} = \frac{1}{t_f - t_0} \int_{t_0}^{t_f} P_{\text{inst}}\, dt = \frac{1}{R_{pz}} \left(v^{\text{RMS}}\right)^2 + R_{em} \left(I^{\text{RMS}}\right)^2, \tag{6.26}$$

where the RMS of any quantity can be defined as:

$$\square^{\text{RMS}} = \sqrt{\frac{1}{t_f - t_0} \int_{t_0}^{t_f} \left[\square(t)\right]^2 \, dt}. \tag{6.27}$$

Furthermore, based on these concepts and according to Table 6.1, the normalized

average electrical output power can be determined as described in Equation 6.28.

$$\bar{P}_{\text{avg}} = \bar{P}_{pz} + \bar{P}_{\text{em}} = \frac{1}{\varphi_{pz}} \left(\bar{v}^{\text{RMS}}\right)^2 + \varphi_{em} \left(\bar{I}^{\text{RMS}}\right)^2. \tag{6.28}$$

6.2 Multidirectional Energy Harvesting

This section evaluates the main characteristics of the energy harvester showing that the pendulum structure can be used to achieve multidirectionality in mechanical structures due to its capability to diffuse energy between different directions within the system. Numerical simulations carried out employing the fourth order Runge-Kutta scheme, considering a time step $\Delta\tau \propto 2\pi/\Omega$ defined after a convergence analysis. Dynamical observations are treated together with performance.

In order to illustrate the multidirectionality concept, consider the free responses of the system ($\gamma = \Omega = \bar{\mu} = 0$), presented in Figures 6.4, 6.5 and 6.6 with the following structural parameters: $\Omega_s = 1.5$ and $\Omega_\phi = 0.05$. For clarity, the piezoelectric and electromagnetic transducers are excluded from the analysis, setting $\chi_{pz} = \kappa_{pz} = \varphi_{pz} = \chi_{em} = \kappa_{em} = \varphi_{em} = 0$. The remaining parameters are listed in Table 5.1.

Figure 6.4 demonstrates a scenario in which the structure is perturbed with an arbitrary initial position in the $\bar{z}$ direction, while the pendulum and the position of the structure's $\bar{x}$ direction remain stationary at their respective initial condition. As time progresses, it is observed that the structure oscillates in the $\bar{z}$ direction, while the pendulum and the structure's $\bar{x}$ direction remain stationary at rest. This

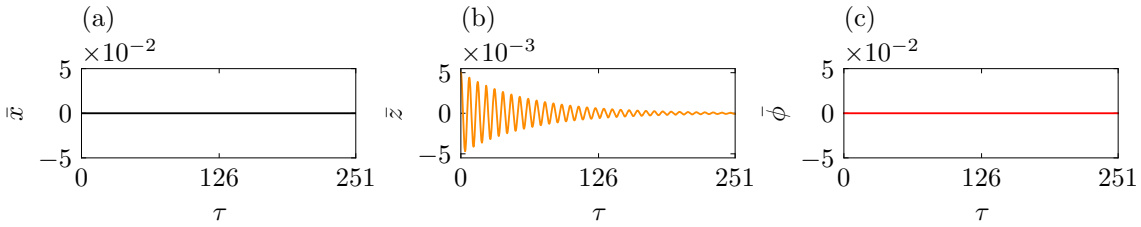

Figure 6.4: Free response of the system as the structure is released from an arbitrary $\bar{z}$ initial position. The piezoelectric and electromagnetic transducers are excluded from the analysis, that is, $\chi_{pz} = \kappa_{pz} = \varphi_{pz} = \chi_{em} = \kappa_{em} = \varphi_{em} = 0$.

behavior is expected since the system is ideal and unperturbed in the other directions. In contrast, when the $\bar{x}$ direction is perturbed, energy is transmitted from the $\bar{x}$ direction to the pendulum, and from the pendulum to the $\bar{z}$ direction. This scenario is depicted in Figure 6.5. Furthermore, Figure 6.6 demonstrates that when the pendulum is released from an arbitrary $\bar{\phi}$ initial angle, the energy is simultaneously transferred from the pendulum to both $\bar{x}$ and $\bar{z}$ directions. This analysis

highlights the pendulum as an energy bridge between directions.

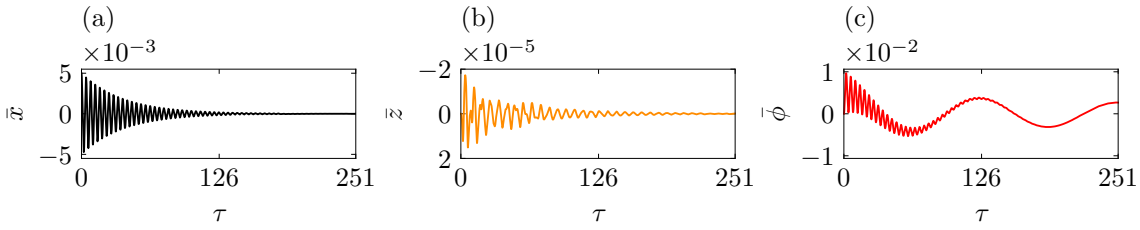

Figure 6.5: Free response of the system as the structure is released from an arbitrary $\bar{x}$ initial position. The piezoelectric and electromagnetic transducers are excluded from the analysis, that is, $\chi_{pz} = \kappa_{pz} = \varphi_{pz} = \chi_{em} = \kappa_{em} = \varphi_{em} = 0$.

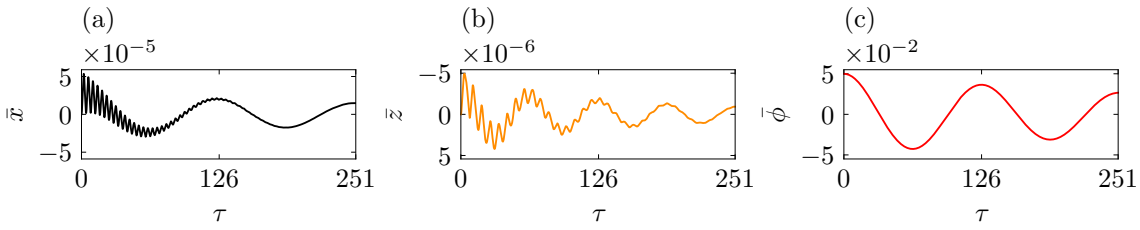

Figure 6.6: Free response of the system as the pendulum is released from an arbitrary $\bar{\phi}$ initial angle. The piezoelectric and electromagnetic transducers are excluded from the analysis, that is, $\chi_{pz} = \kappa_{pz} = \varphi_{pz} = \chi_{em} = \kappa_{em} = \varphi_{em} = 0$.

Energy harvesting assessment is now in focus. In this phase, the energy harvesters illustrated in Figure 6.1 are compared. For that, consider their equivalent models as established in Figure 6.3. The electromagnetic transducer parameters utilized are of the following: $\chi_{em} = 0.04$, $\varphi_{em} = 0.25$, $\kappa_{em} = 0.4$. The remaining non-zero parameters are utilized as presented in Table 5.1.

The performance of each system is assessed across a range of frequencies by imposing three different excitation angles for each case, defining different multidirectional energy sources: $\bar{\mu} = 0°$, a unidirectional case; $\bar{\mu} = 45°$, a multidirectional case; and $\bar{\mu} = 90°$, an opposite case of the unidirectional source. Diagrams $\bar{P}_{\text{avg}} \times \Omega$ presented in Figures 6.7, 6.8 and 6.9, are built using $\bar{x} = \dot{\bar{x}}_0 = \bar{z}_0 = \dot{\bar{z}}_0 = \bar{\phi}_0 = \dot{\bar{\phi}}_0 = \bar{v}_0 = \bar{I}_0 = 0$ as initial conditions. An up-sweep test with 500 steps of the normalized frequency, Ω, is performed. For each step, $d\Omega$, 800 excitation periods, T, are imposed at each integration, with the last 150 considered to be steady state. The value of the steady state average output power, $\bar{P}_{\text{avg}}$, is computed for each step. As Ω increases, the dynamics of the system are maintained, that is, besides for the first value of Ω, the initial conditions of each point in the diagram correspond to the end state of the preceding point. Different excitation levels of $\gamma = 0.1$, $\gamma = 0.25$, and $\gamma = 0.5$ are considered.

In each Figure, the first column (a) illustrates the performance of Case I: CPEH. It is observed that when the excitation angle, $\bar{\mu}$, is set to 0°, the system achieves maximum performance as the direction of excitation aligns parallel to the $\hat{\mathbf{e}}_z$ axis. However, as the angle $\bar{\mu}$ increases, the maximum power output diminishes gradually until it reaches zero at $\bar{\mu} = 90°$ when the excitation becomes perpendicular to the $\hat{\mathbf{e}}_z$ axis. Consequently, for excitation angles other than $\bar{\mu} = 0°$ and $\bar{\mu} = 180°$, the CPEH system experiences a loss of valuable energy from the environment.

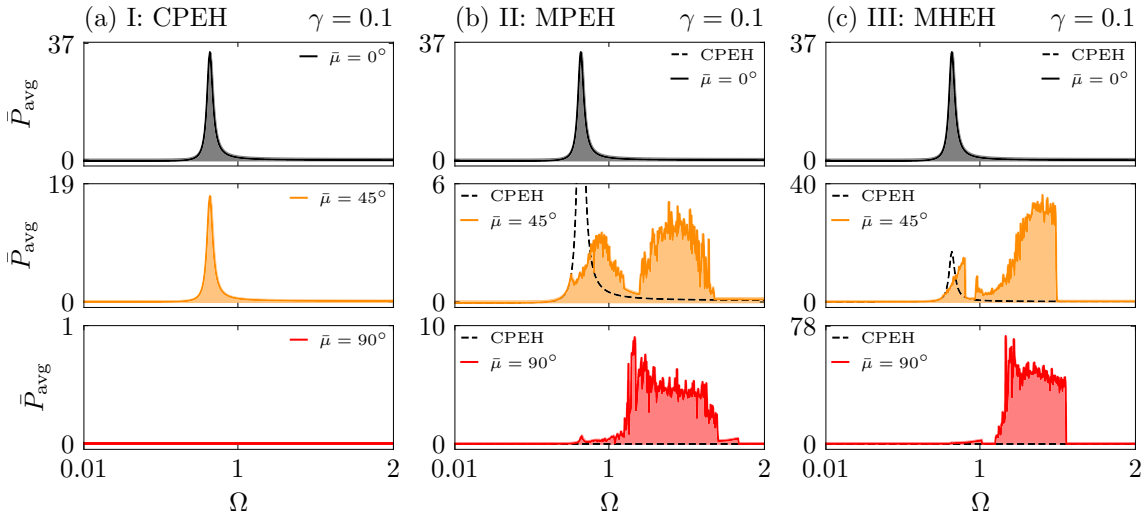

Figure 6.7: $\bar{P}_{\text{avg}} \times \Omega$ diagrams for the Cases I, II, and III represented in Figure 6.3 excited with different angles, $\bar{\mu}$, $\gamma = 0.1$. (a) CPEH. (b) Comparison between the CPEH (dashed black lines) and the MPEH. (c) Comparison between the CPEH (dashed black lines) and the proposed MHEH. The $\bar{P}_{\text{avg}}$ values are scaled by $\times 10^{-3}$.

This issue is addressed by incorporating a pendulum structure that achieves multidirectionality (referred to as Case II: MPEH) as demonstrated by XU & TANG [199], as well as PAN *et al.* [200, 201]. Figures 6.7(b), 6.8(b) and 6.9(b) display the performance for this kind of harvester. For an excitation angle of $\bar{\mu} = 0°$, the performance of the MPEH is identical to that of the CPEH as there is no resulting motion from the pendulum. In contrast, for an excitation angle of $\bar{\mu} = 90°$ the advantages of utilizing a pendulum structure to facilitate energy transfer between directions become evident. In this scenario, the system is capable of effectively harvesting energy from all directions. However, for intermediate angles between $0° < \bar{\mu} < 90°$ it exhibits a drawback, demonstrating lower performance (lower maximum output power) compared to the CPEH in certain scenarios. This is due to the pendulum acting as an energy absorber.

In order to deal with this matter, an electromagnetic transducer has been integrated into the system to harness the rotational energy, enabling a portion of the mechanical energy absorbed by the pendulum to be converted into electrical energy.

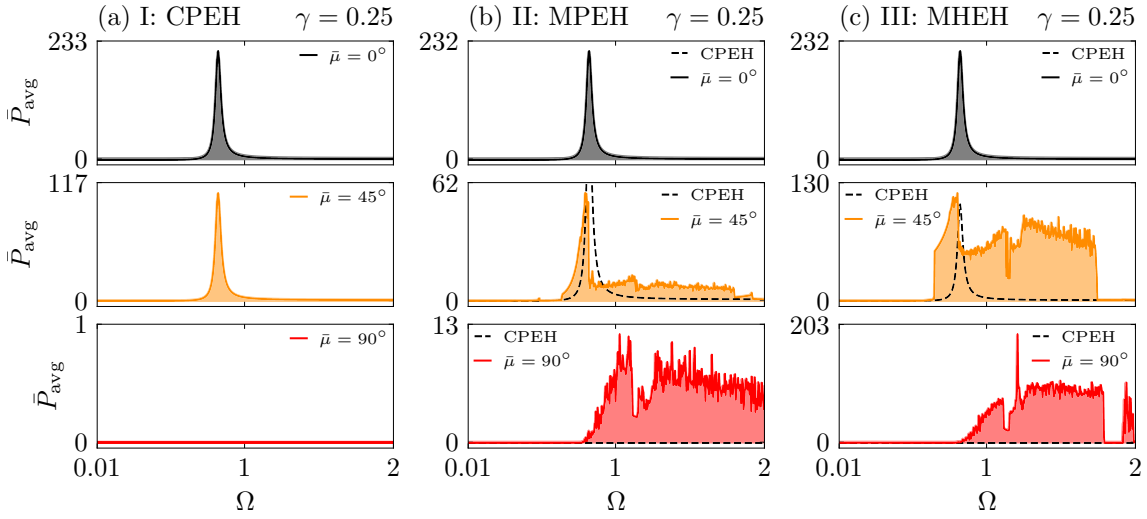

Figure 6.8: $\bar{P}_{\text{avg}} \times \Omega$ diagrams for the Cases I, II, and III represented in Figure 6.3 excited with different angles, $\bar{\mu}$, $\gamma = 0.25$. (a) CPEH. (b) Comparison between the CPEH (dashed black lines) and the MPEH. (c) Comparison between the CPEH (dashed black lines) and the proposed MHEH. The $\bar{P}_{\text{avg}}$ values are scaled by $\times 10^{-3}$.

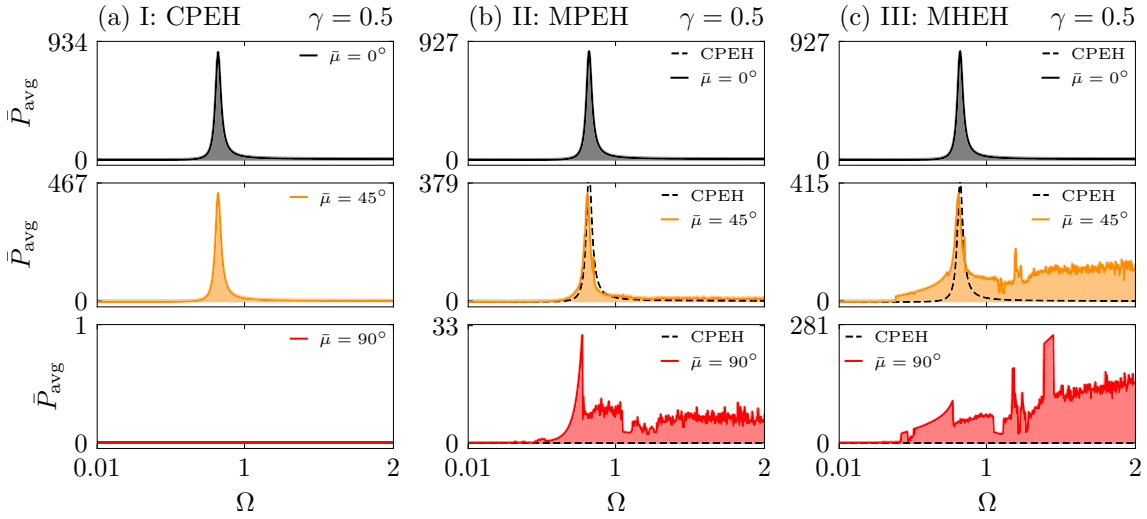

Figure 6.9: $\bar{P}_{\text{avg}} \times \Omega$ diagrams for the Cases I, II, and III represented in Figure 6.3 excited with different angles, $\bar{\mu}$, $\gamma = 0.5$. (a) CPEH. (b) Comparison between the CPEH (dashed black lines) and the MPEH. (c) Comparison between the CPEH (dashed black lines) and the proposed MHEH. The $\bar{P}_{\text{avg}}$ values are scaled by $\times 10^{-3}$.

On this basis, a hybrid system is of concern, represented by Case III: MHEH. The performance of this harvester is presented in Figures 6.7(c), 6.8(c) and 6.9(c). Similar to the previous case, for an angle of $\bar{\mu} = 0°$, the performance of the MHEH is equivalent to the CPEH as there is no resulting motion of the pendulum. However, for angles of $\bar{\mu} = 45°$ and $\bar{\mu} = 90°$, there is an impressive increase of performance in both maximum output power and bandwidth when compared to the CPEH.

These results clearly show that the MHEH (Multidirectional Hybrid Energy Harvester) not only retains the desirable characteristics of the MPEH (Multidirectional Piezoelectric Energy Harvester) but can also effectively address its limitations. This highlights the importance of incorporating the additional strategy to harness the rotational energy when utilizing pendulum structures for efficient multidirectional piezoelectric energy harvesting applications.

6.3 MHEH Key Characteristics

The next sections are focused on exploring the performance characteristics of the MHEH by parametrically varying some parameters. Thus, it is important to contextualize the meaning of these key parameters and how they can influence the dynamical behavior and harvester performance.

6.3.1 Electrical Parameters

First, the electromechanical couplings of the electromagnetic transducer, χ_{em} and κ_{em}, are important to be addressed. As discussed in Section 6.1.1, the value of these couplings is influenced by many construction characteristics of the transducer, especially the disposal of coils and internal magnet properties. In order to perform a general qualitative analysis of the MHEH, a variable is defined containing information of the electromagnetic transducer, based on the piezoelectric transducer. On this basis, consider the ratio between electromechanical couplings as

$$\eta = \frac{\chi_{em}}{\chi_{pz}} = \frac{\kappa_{em}}{\kappa_{pz}}. \tag{6.29}$$

Note that if $\eta = 1$, both transducers have the same coupling, while if $\eta < 1$, electromagnetic couplings have a lower value than the corresponding piezoelectric coupling. Alternatively, if $\eta > 1$, the electromagnetic couplings have a larger value than the corresponding piezoelectric couplings.

Additionally, φ_{pz} and φ_{em} represent the normalized resistance of the circuit, meaning that there is an optimal value to be used in order to maximize the output power of the harvester.

6.3.2 Mechanical Parameters

Mechanical available ambient energy constitutes input parameters, γ - the normalized magnitude of excitation and Ω - the normalized excitation frequency. Note that $\Omega = 1$ means that the excitation frequency matches the beam's natural frequency in the z-direction. On the other hand, Ω_s is the ratio between the natural

frequency of the beam's x-direction and z-direction; Ω_ϕ is the ratio between the linearized natural frequency of the pendulum and the beam's natural frequency in z-direction. Note that $\Omega_s = 1$ means that the natural frequencies of the beam structure are the same in x and z directions; $\Omega_s > 1$ means that the x-direction is stiffer than the z-direction. This characteristic is illustrated in Figure 6.10, where a simplified frontal view of the MHEH beam structure is depicted. Furthermore, Figure 6.11 represents the meaning of Ω_ϕ parameter, which is closely related to the pendulum's length, L_p. A higher value of Ω_ϕ means a shorter pendulum length.

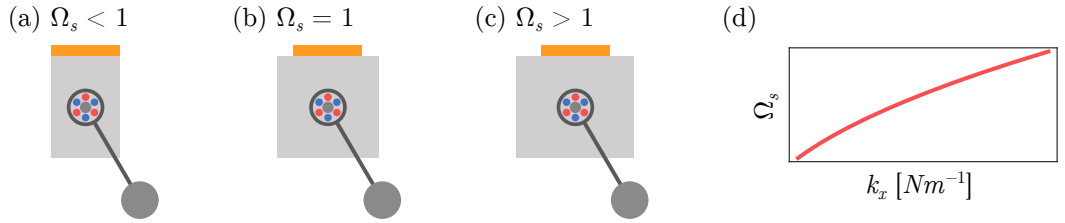

Figure 6.10: Illustrative representation of the natural frequencies ratio, Ω_s. (a) $\Omega_s < 1$ indicates lower stiffness in the x direction, shown by a narrower beam width. (b) $\Omega_s = 1$ represents equal stiffness in both x and z directions, with identical width and height. (c) $\Omega_s > 1$ demonstrates higher stiffness in x direction, depicted by a wider beam width. (d) Changes in Ω_s as the stiffness in x direction, k_x, increases.

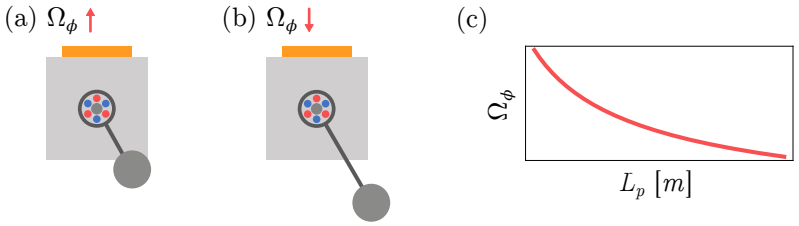

Figure 6.11: Illustrative representation of the ratio of natural frequencies of the pendulum and the z direction, Ω_ϕ. (a) Representation of a higher Ω_ϕ, corresponding to a shorter pendulum length. (b) Representation of a lower Ω_ϕ, indicating a wider pendulum length. (d) Change in Ω_ϕ as the pendulum length, L_p, increases.

6.4 Electrical Parameters and Performance

This section develops a characterization of the system's performance by evaluating the influence of different electrical parameters. Subsection 6.4.1 evaluates the influence of the electrical resistance parameters on the transducer output powers. On the other hand, the second subsection evaluates the effects of parameter η in the average output power of the MHEH. The analyses are carried out by considering three different configurations with different ratios of natural frequencies, Ω_s: 0.5, 1.0

and 1.5, and a fixed value of $\Omega_\phi = 0.05$. The angle of excitation is also maintained constant at $\bar{\mu} = 45°$ and the values of the remaining parameters are summarized in Table 5.1.

6.4.1 Influence of the Electrical Resistances, φ_{pz} and φ_{em}

The influence of the electrical resistance parameters is now of concern, establishing their effects on the average output power of the system. By considering a constant value of $\eta = 1$ and $\gamma = 0.1$, Average Output Power Diagrams (OPDs) are constructed to analyze the influence of the normalized electrical resistance parameters, φ_{pz}, and φ_{em}, and the excitation frequency, Ω, in the output power of the system. These diagrams are built with a grid of 500×500 sample points, each of which is obtained from a time series integration. As in the previous diagrams, for each sample point, 800 excitation periods, T, are imposed at each integration, with the last 150 considered to be steady state. Then, the value of the output power is computed based on the instantaneous output power of the steady state part. Additionally, all sample points have the same initial conditions of $\bar{x} = \dot{\bar{x}}_0 = \bar{z}_0 = \dot{\bar{z}}_0 = \bar{\phi}_0 = \dot{\bar{\phi}}_0 = \bar{v}_0 = \bar{I}_0 = 0$ to standardize the analysis.

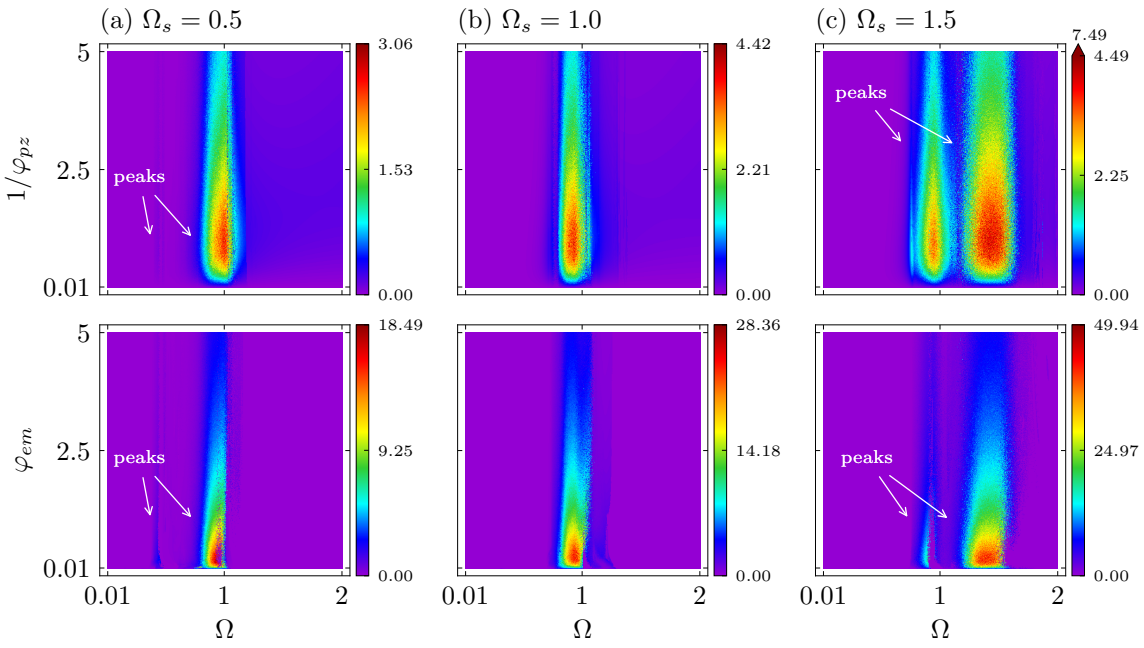

Figure 6.12: OPDs for the normalized electrical resistance analysis, using $\gamma = 0.1$ and $\bar{\mu} = 45°$. Three groups are defined with: (a) $\Omega_s = 0.5$, (b) $\Omega_s = 1$, and (c) $\Omega_s = 1.5$. The first row shows the performance for distinct conductance values in the piezoelectric circuit ($1/\varphi_{pz}$). The second row shows the performance for different resistance values in the electromagnetic circuit (φ_{em}). Colorbars indicate the average output power level, $\bar{P}_{\text{avg}}$, achieved in each case. $\bar{P}_{\text{avg}}$ values are scaled by $\times 10^{-3}$.

Figure 6.12 shows these diagrams considering three configurations with different

values of Ω_s. Each column of Figure 6.12 is related to one different configuration: Figure 6.12(a) for $\Omega_s = 0.5$, that is, the $\bar{z}$ direction is stiffer than the $\bar{x}$ direction; Figure 6.12(b) for $\Omega_s = 1.0$, where both stiffness of each direction are equal; and Figure 6.12(c) for $\Omega = 1.5$, showing a configuration with a stiffer $\bar{x}$ direction than the $\bar{z}$ direction. The first row of each configuration shows the OPD for the values of the normalized conductance of the piezoelectric circuit, $1/\varphi_{pz}$. For all configurations, the optimal value of the normalized conductance is shown to be around $1/\varphi_{pz} = 1$. Additionally, the second row of each configuration shows the OPD for the values of the normalized resistance of the electromagnetic circuit, φ_{em}. As in the previous case, the three configurations show similar regions of optimal resistance around $\varphi_{em} = 0.25$.

In this case, it should be pointed out that the increase of Ω_s produces an increase in the maximum output power of both piezoelectric and electromagnetic transducers. Additionally, the presence of two peaks of output power in the first and third cases, as pointed out by the white arrows, occurs due to the shift of the resonance regions caused by the change of Ω_s.

6.4.2 Influence of the Ratio Between Electromechanical Couplings, η

The ratio between electromechanical couplings, η, is now of concern addressing the evaluation of its effects on the average output powers of the MHEH. Three values of η are selected: 0.2, 0.5 and 0.8. For each value of η, the same three configurations with different Ω_s values are evaluated, as discussed in the previous subsection. Results are summarized in $\bar{P}_{\text{avg}} \times \Omega$ diagrams displayed in Figures 6.13, 6.14, and 6.15, which are divided into three sections based on different values of normalized excitation amplitude of $\gamma = 0.1$, $\gamma = 0.25$, and $\gamma = 0.5$. In these Figures, dashed lines represent the $\bar{P}_{\text{avg}}$ for the CPEH, serving as a reference for comparison. Additionally, these diagrams include red curves that represent the average output power associated with the piezoelectric element, $\bar{P}_{pz}$, orange curves that represent the average output power of the electromagnetic transducer, $\bar{P}_{em}$, and purple curves that represent the total average output power of the MHEH, $\bar{P}_{\text{avg}}$. Note that all values of power are scaled by $\times 10^3$ for better representation.

Figure 6.13 represents the case with $\eta = 0.2$. Figure 6.13(a) illustrates that, given this particular value of η and low excitation amplitudes ($\gamma = 0.1$), the MHEH does not enhance energy conversion to a degree that justifies its use over the CPEH. This observation holds true for $\gamma = 0.25$ and $\gamma = 0.5$, as displayed in Figures 6.13(b) and 6.13(c). However, under these conditions, the piezoelectric output power, denoted as $\bar{P}_{pz}$, exhibits a significant increase.

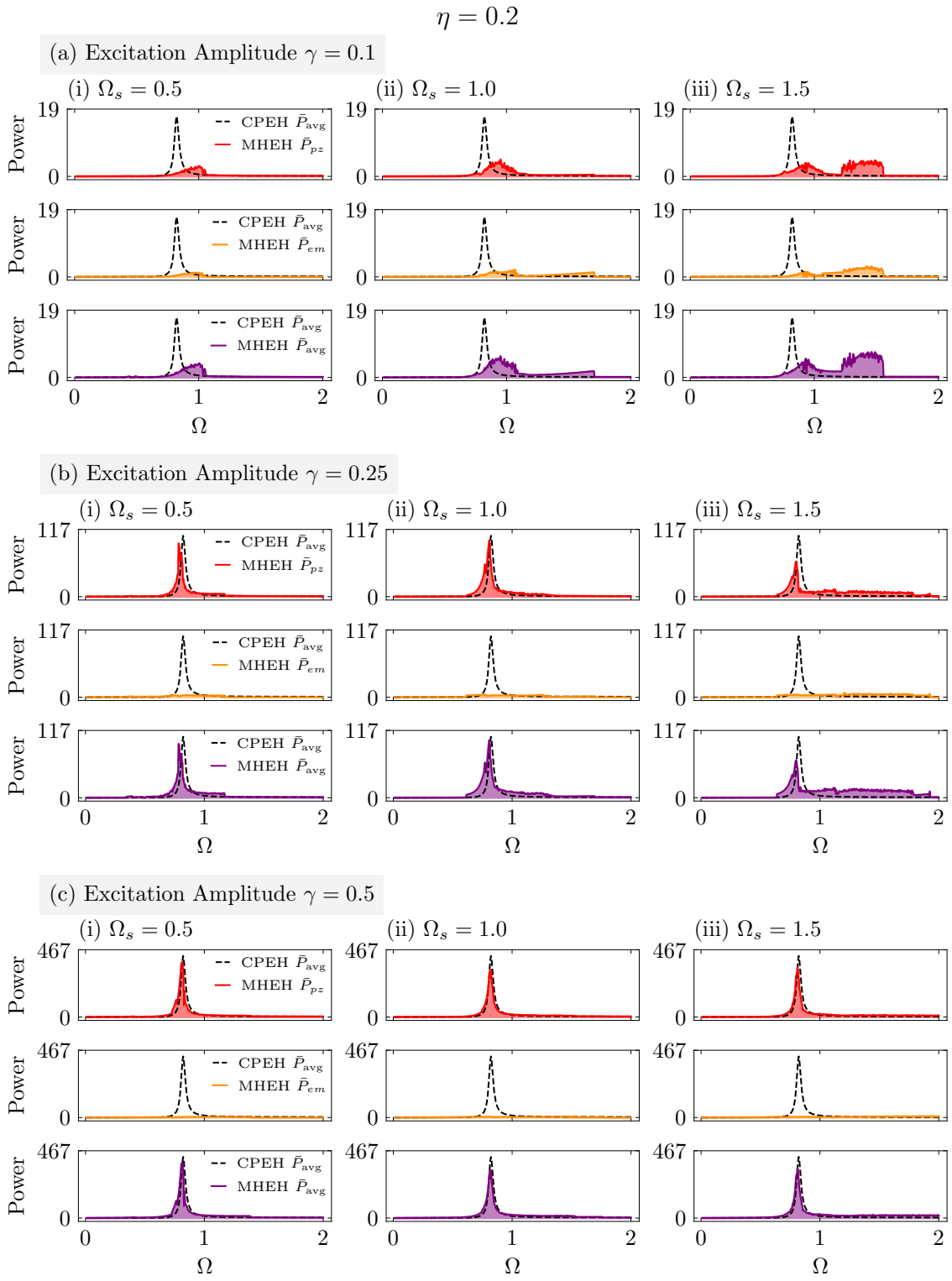

Figure 6.13: $\Omega \times \bar{P}$ diagrams for $\eta = 0.2$. Three excitation amplitudes are chosen: (a) $\gamma = 0.1$, (b) $\gamma = 0.25$, and (c) $\gamma = 0.5$. For each γ, three configurations are selected with (i) $\Omega_s = 0.5$, (ii) $\Omega_s = 1$ and (iii) $\Omega_s = 1.5$. Dashed lines represent CPEH $\bar{P}_{\text{avg}}$. Red curves represent $\bar{P}_{pz}$, orange curves represent $\bar{P}_{em}$, and purple curves represent $\bar{P}_{\text{avg}}$, all for the MHEH. Power values are scaled by $\times 10^{-3}$.

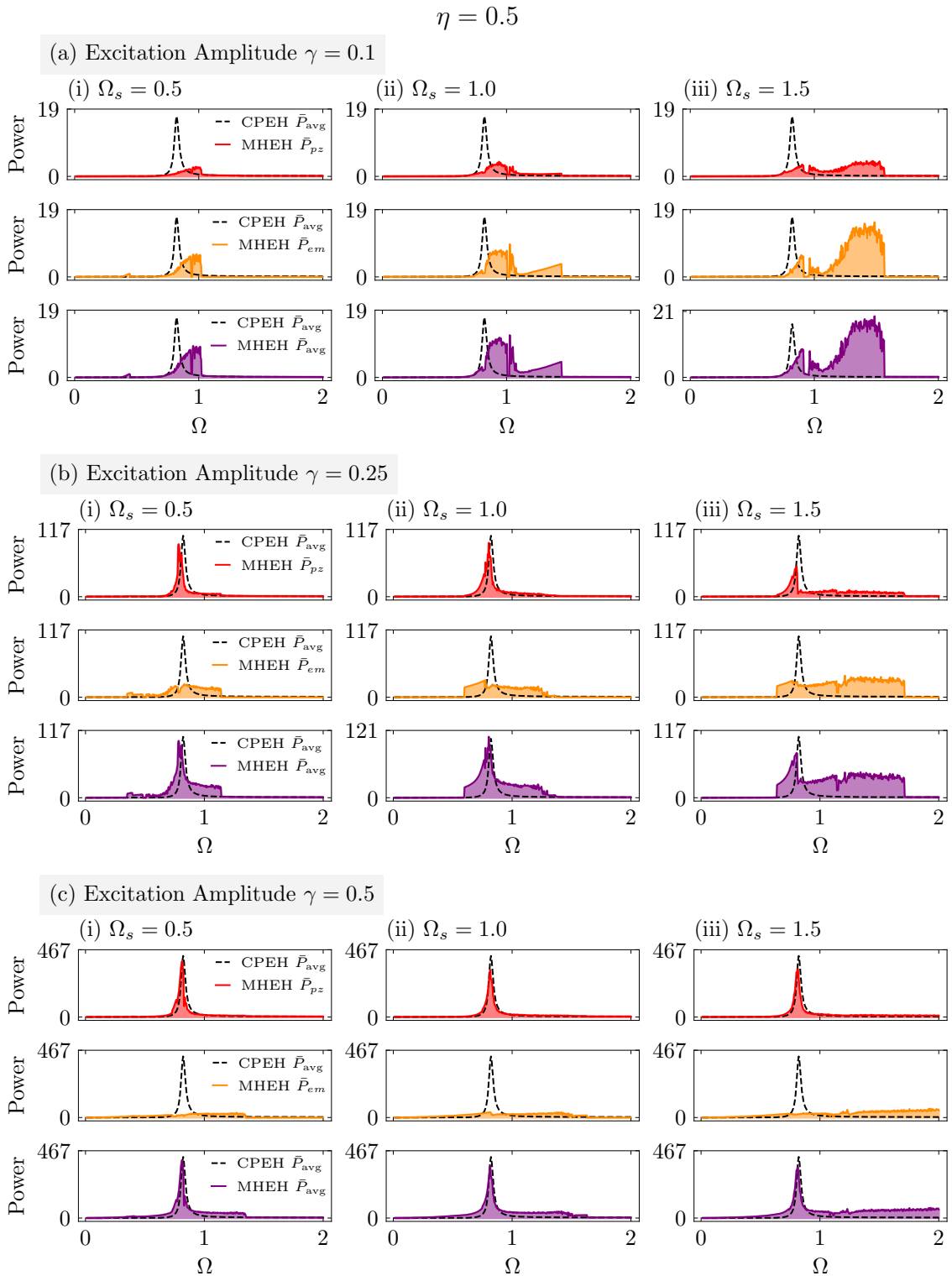

Figure 6.14: $\Omega \times \bar{P}$ diagrams for $\eta = 0.5$. Three excitation amplitudes are chosen: (a) $\gamma = 0.1$, (b) $\gamma = 0.25$, and (c) $\gamma = 0.5$. For each γ, three configurations are selected with (i) $\Omega_s = 0.5$, (ii) $\Omega_s = 1$ and (iii) $\Omega_s = 1.5$. Dashed lines represent CPEH $\bar{P}_{\text{avg}}$. Red curves represent $\bar{P}_{pz}$, orange curves represent $\bar{P}_{em}$, and purple curves represent $\bar{P}_{\text{avg}}$, all for the MHEH. Power values are scaled by $\times 10^{-3}$.

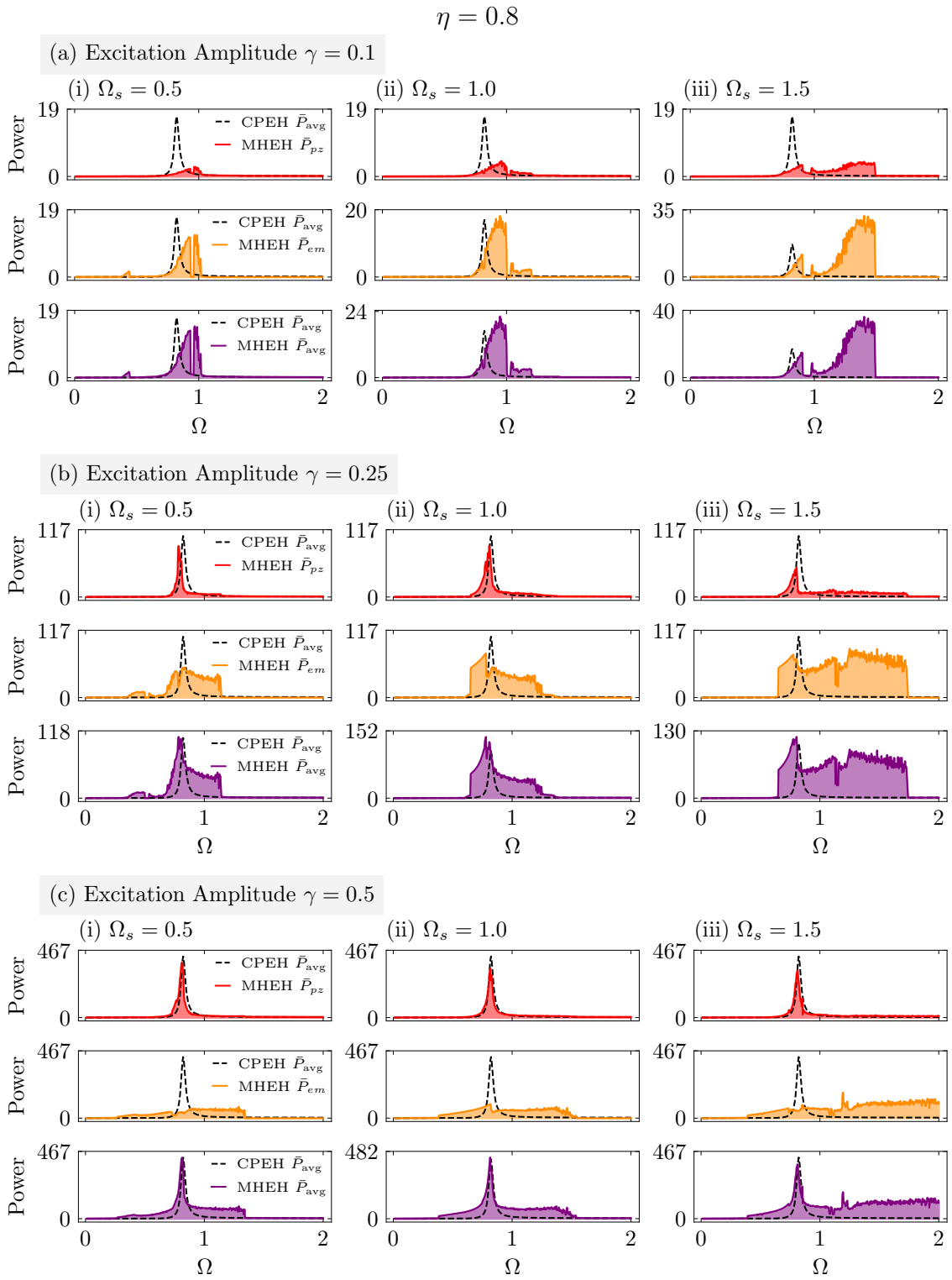

Figure 6.15: $\Omega \times \bar{P}$ diagrams for $\eta = 0.8$. Three excitation amplitudes are chosen: (a) $\gamma = 0.1$, (b) $\gamma = 0.25$, and (c) $\gamma = 0.5$. For each γ, three configurations are selected with (i) $\Omega_s = 0.5$, (ii) $\Omega_s = 1$ and (iii) $\Omega_s = 1.5$. Dashed lines represent CPEH $\bar{P}_{\text{avg}}$. Red curves represent $\bar{P}_{pz}$, orange curves represent $\bar{P}_{em}$, and purple curves represent $\bar{P}_{\text{avg}}$, all for the MHEH. Power values are scaled by $\times 10^{-3}$.

Additionally, Figure 6.14 shows the results for a scenario with $\eta = 0.5$. For low excitation amplitude values ($\gamma = 0.1$), the CPEH is still advantageous for $\Omega_s = 0.5$. Alternatively, for the cases with $\Omega_s = 1.0$ and $\Omega_s = 1.5$, the performance became comparable or even better than the CPEH. For medium values of excitation amplitude ($\gamma = 0.25$), as displayed in Figure 6.14(b), this value of η is suitable for replacing the CPEH as both piezoelectric and electromagnetic transducers contribute effectively for the energy conversion. For greater values of excitation amplitude ($\gamma = 0.5$), as displayed in Figure 6.14(c), only the piezoelectric transducer contributes effectively to the energy conversion.

Furthermore, Figure 6.15 illustrates the case where the value of η is increased to 0.8. In this case, nearly all combinations of Ω_s and γ demonstrate the benefits of employing the MHEH. This is because, in every scenario, the output powers are comparable to or exceed those presented by the CPEH. Consequently, it follows that the optimal ratio of electromechanical couplings is around $\eta = 0.8$, given this set of parameters, where both piezoelectric and electromagnetic transducers contribute effectively to the energy conversion. For higher values of η, the electromagnetic transducer should convert much more than the piezoelectric element.

Finally, by observing the values of output power presented in Figures 6.13, 6.14, and 6.15, as well as in Figure 6.12 of the previous section, it is revealed that the increase of Ω_s tends to increase the bandwidth.

6.5 Dynamics and Performance

This section presents a parametric analysis considering four key parameters: the ratio between natural frequencies of the main structure, Ω_s; the ratio between natural frequencies of the pendulum and the structure's z-direction, Ω_ϕ; the normalized excitation amplitude, γ; and the normalized excitation frequency, Ω. The main objective of the analysis is to identify the best and the worst combinations of Ω_s and Ω_ϕ parameters in terms of overall performance by considering a wide range of excitation parameters, γ and Ω. Besides, the angle of base excitation, $\bar{\mu}$, is maintained at 45° in order to subject the system to a symmetric multidirectional excitation of which the magnitude components of each direction, z and x, are equal. The electrical parameters are based on the values established in the previous sections ($\eta = 0.8$, $\varphi_{em} = 0.25$, $1/\varphi_{pz} = 1$) and the remaining constant parameter values are listed in Table 5.1.

The parametric analysis is based on the nonlinear dynamics perspective framework employing five types of diagrams: the Dynamical Responses Diagrams (DRDs), the Lyapunov Exponents Diagrams (LEDs), the Average Output Power Diagrams (OPDs), the Occurrence Diagrams (OCDs), and the Dynamical Pattern Diagrams

(DPDs). Each diagram shows an important characteristic of the MHEH in a two-dimensional parameter space of choice in order to characterize the system's dynamics and performance with robustness. Different excitation parameters are of concern.

Each point in the diagrams is related to a time series from the integration of the governing equations from an initial time, τ_0, to a final time, τ_f, considering a suitable integration time step, $\Delta\tau = 2\pi/(\Omega N_{\text{div}})$, with $N_{\text{div}} = 6000$ determined by a convergence analysis. A specific point in time, $\tau_{\text{trans}} = 0.8125\tau_f$, is chosen to define the beginning of a steady-state response. All sample points have the same initial condition of $\bar{x} = \dot{\bar{x}} = \bar{z} = \dot{\bar{z}} = \bar{\phi} = \dot{\bar{\phi}} = \bar{v} = \bar{I} = 0$ to standardize the analyses.

6.5.1 Dynamical Responses

This subsection presents a discussion about the distinct dynamical responses of the MHEH. Diagrams are built assuming constant values of excitation parameters γ and Ω, employing a grid of 500×500 sample points within the $\Omega_s \times \Omega_\phi$ parameter space, each from 0.01 to 2.

Figure 6.16 shows the DRD, LEDs and OPDs for excitation parameters $\gamma = 0.1$ and $\Omega = 1.2$. Figure 6.16a displays the DRD, where different steady-state dynamical behaviors are classified for each time series sample following the color code established in previous sections of this text. Notably, for this specific system, after an intensive session of testing and examination of the phase subspaces, it was observed that the MP classification also includes quasi-periodic responses successfully, although the algorithm does not always guarantee this behavior as discussed in Appendix B.

LEDs are presented in Figures 6.16c and 6.16d, being complementary diagrams to the DRD that showing the delimitation of periodic, chaotic and hyperchaotic regions. Moreover, Figures 6.16b, 6.16d and 6.16f show the OPDs for the overall average output power, $\bar{P}_{\text{avg}}$, the average output power of the piezoelectric transducer, $\bar{P}_{pz}$, and the average output power of the electromagnetic transducer, $\bar{P}_{em}$. All these quantities are computed considering the steady-state responses ($\tau > \tau_{\text{trans}}$) of each time series sample, being essential to define system performance.

It should be pointed out that the attractors present a predominance of 1T periodic responses, followed by hyperchaotic responses in the bottom right part of the diagrams. The analysis of these diagrams together indicates that more complex regions, associated with many types of dynamical responses, produce better performance, especially the central part of the hyperchaotic zone. Also, this case shows the output power predominance of the electromagnetic transducer, showing a maximum value of 7.5 times greater than the piezoelectric element.

Eight points, labeled from 1 to 8, are marked on the diagrams to illustrate

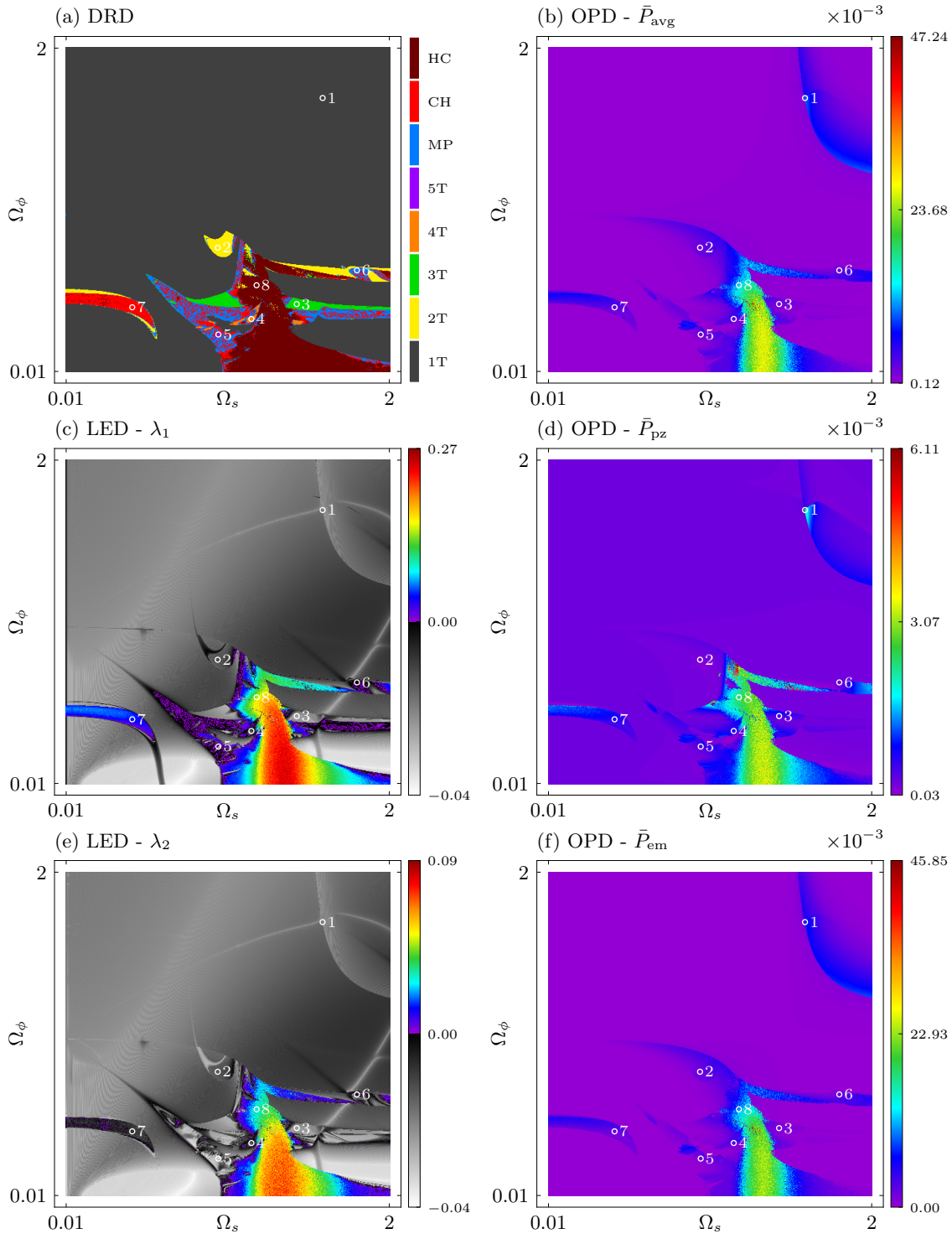

Figure 6.16: Diagrams for the $\Omega_s \times \Omega_\phi$ parameter space, considering excitation parameters of $\gamma = 0.1$ and $\Omega = 1.2$: (a) DRD with the classification of distinct attractor types, color-coded according to text description. (b) OPD for the overall average output power, $\bar{P}_{\text{avg}}$. (c) LED for largest exponent, λ_1. (d) OPD for the piezoelectric transducer output power, $\bar{P}_{pz}$. (e) LED for the second largest exponent, λ_2. (f) OPD for the electromagnetic transducer output power, $\bar{P}_{em}$. OPD colorbars represent output power values; LEDs colorbars indicate exponent value (rainbow for positive, grayscale for negative). Diagrams are built with a grid of 500×500 points.

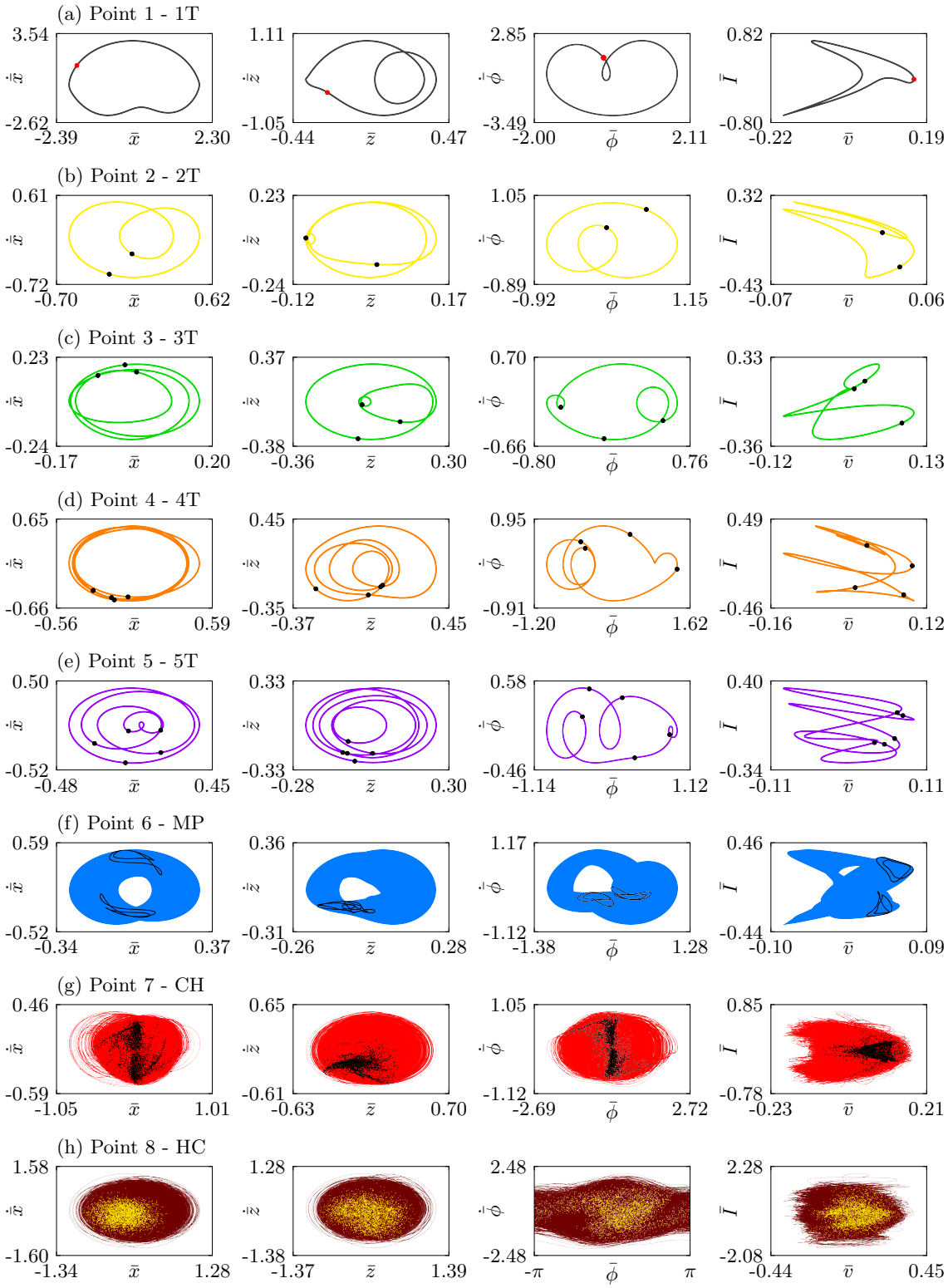

Figure 6.17: Corresponding phase subspaces and Poincaré maps of the steady-state response of points 1 to 8, as referenced in Figure 6.16 and detailed in Table 6.2. Each color represents distinct dynamical responses. (a) dark gray: 1T, (b) yellow: 2T, (c) light green: 3T, (d) orange: 4T, (e) purple: 5T, (d) light blue: MP - in this case, quasi-periodic, (g) red: chaotic - CH, and (h) dark red: hyperchaotic - HC. Poincaré maps are displayed by black dots, except for red in (a) and yellow in (h).

each dynamical response classified within the DRD. These points are meticulously documented in Table 6.2 for reproducibility. Figure 6.17 showcases the distinct dynamical responses corresponding to each point. Each example is depicted through four steady state phase subspaces: $\bar{x} \times \dot{\bar{x}}$, representing the x-direction, $\bar{z} \times \dot{\bar{z}}$, representing the z-direction, $\bar{\phi} \times \dot{\bar{\phi}}$, representing the pendulum motion. Notably, the ϕ-direction is constrained to the range of the remainder of the actual value of $\bar{\phi}$ divided by 2π. This treatment aligns with the topological view of the pendulum's phase subspace as a cylinder, where π and $-\pi$ represent the same position (upward vertical position) [171, 202]. Finally, $\bar{v} \times \bar{I}$ represents the electrical coordinate domain. It is noticeable that the first seven points, from Figures 6.17a to 6.17g, show dynamical behaviors where the pendulum does not rotate, but oscillates between a maximum and a minimum position. A variety of responses are observable with this characteristic, remarkably the quasi-periodic behavior showed in Figure 6.17f and the chaotic response in Figure 6.17g where the system exhibits a complex aperiodic pattern of motion. Alternatively, the example presented in Figure 6.17h shows a hyperchaotic complex response where the pendulum shows an irregular pattern, including rotation. This result indicates that the MHEH exhibits better performance when the pendulum has some kind of high-amplitude motion.

Table 6.2: Exact corresponding values of Ω_s and Ω_ϕ marked in the diagrams of Fig. 6.16 used to exemplify the different dynamical responses in Fig. 6.17.

Point	Classification	Ω_s	Ω_ϕ
1	1T	1.589238476953908	1.692925851703407
2	2T	0.943186372745491	0.771703406813627
3	3T	1.429719438877756	0.424749498997996
4	4T	1.150561122244489	0.333026052104208
5	5T	0.947174348697395	0.237314629258517
6	MP	1.80060120240481	0.632124248496994
7	CH	0.416773547094188	0.404809619238477
8	HC	1.18246492985972	0.540400801603206

6.5.2 Global Dynamics

In order to determine the best and worst combinations of Ω_s and Ω_ϕ across various excitation scenarios, the analysis presented in Figure 6.16 is conducted across 100 scenarios, each distinguished by different excitation values. Initially, five specific values of γ ranging from $\gamma = 0.1$ to $\gamma = 0.5$ are selected, with an interval of $\Delta\gamma = 0.1$ between each value. Subsequently, for each value of γ, 20 distinct values of parameter Ω are examined, ranging from $\Omega = 0.1$ to $\Omega = 2$, with an interval of $\Delta\Omega = 0.1$. This

extensive range allows the evaluation of the system performance under a broader spectrum of conditions. A subset of these scenarios, specifically forty (40), are depicted in Figures 6.18, 6.19, 6.20, and 6.21.

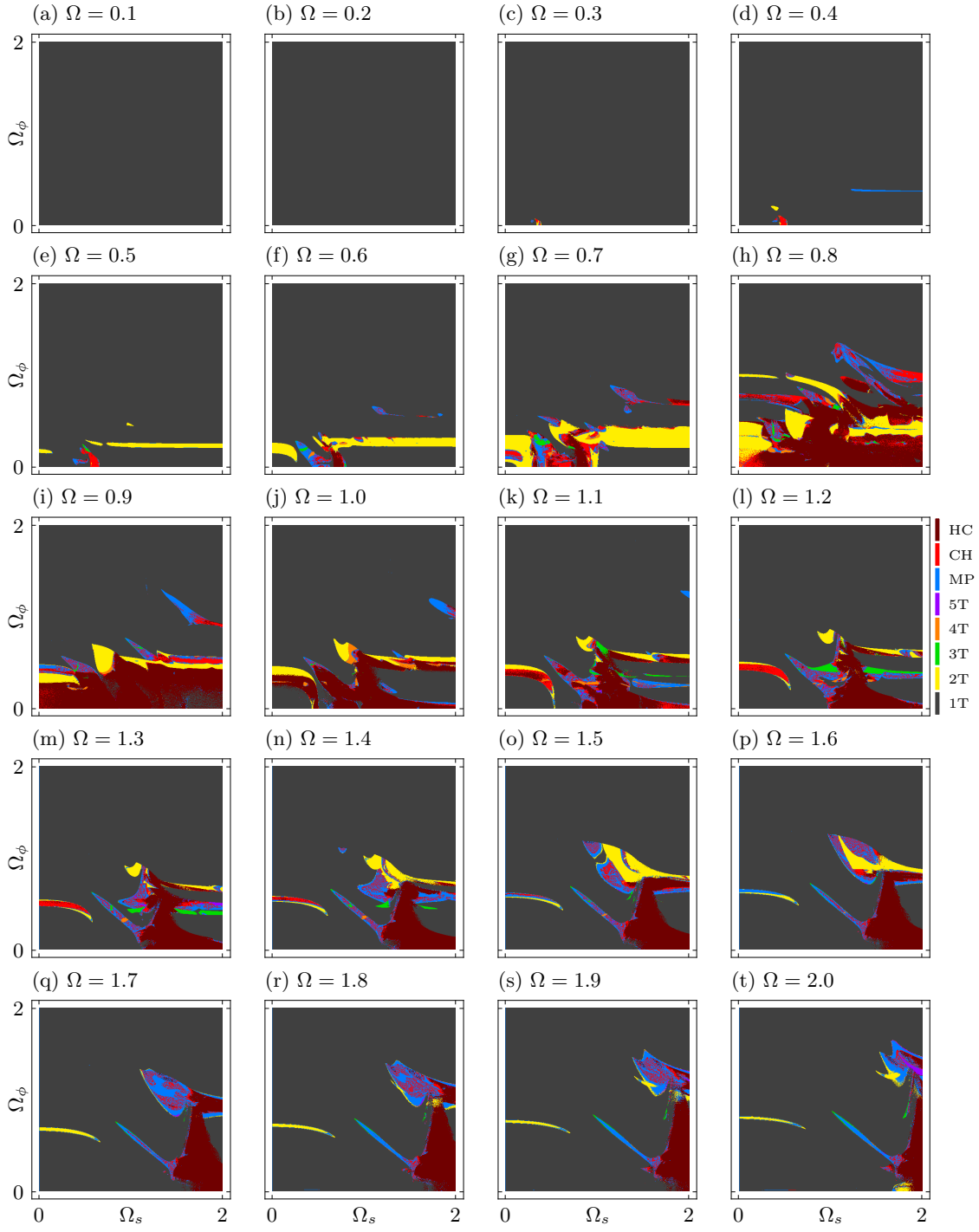

Figure 6.18: DRDs for a fixed value of excitation amplitude of $\gamma = 0.1$, showing different values excitation frequency, from (a) $\Omega = 0.1$ to (t) $\Omega = 2$, with an interval of $\Delta\Omega = 0.1$. Different colors represent distinct dynamical behaviors summarized in the accompanying colorbar. Each diagram is built with 500×500 sample points.

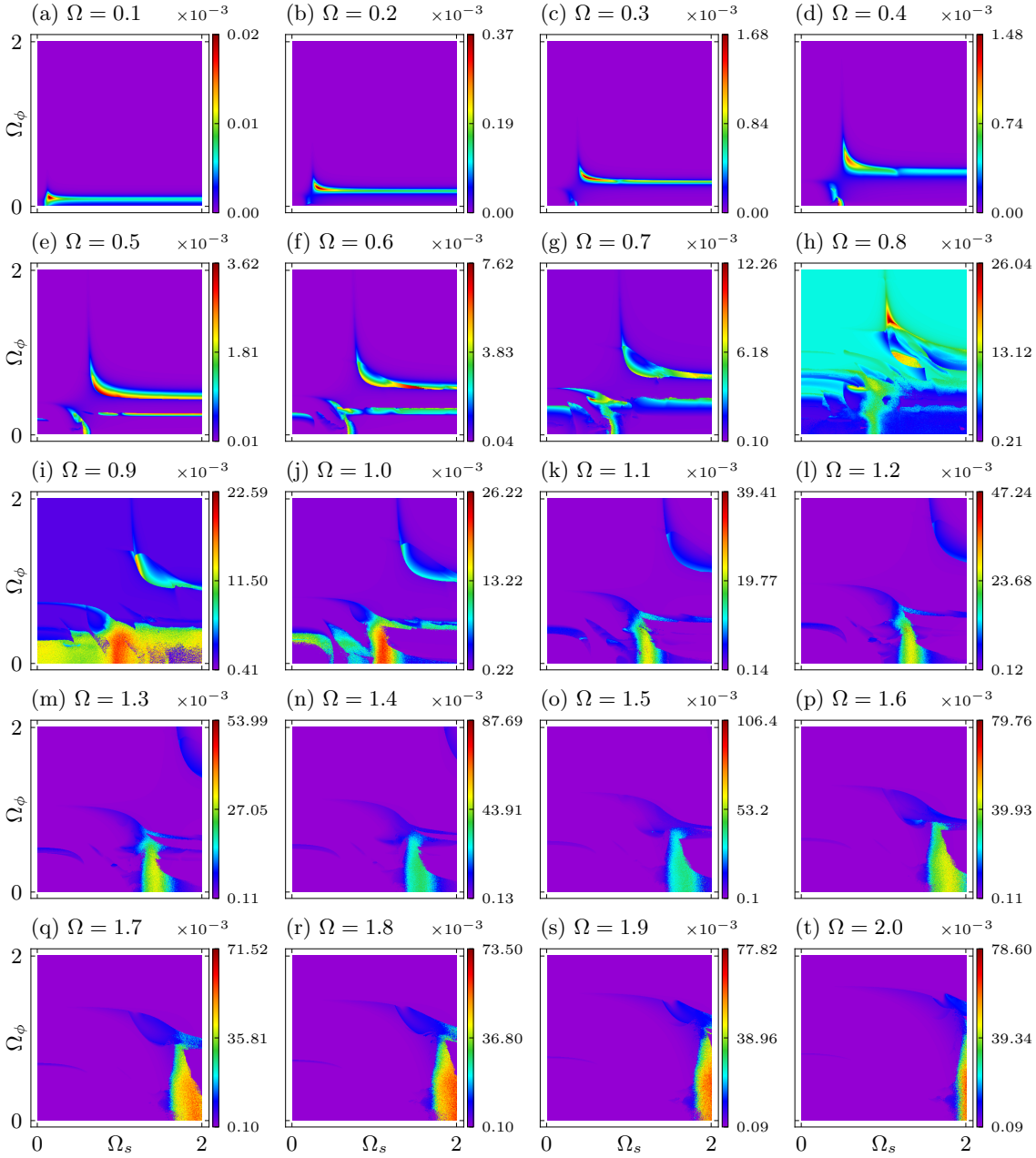

Figure 6.19: $\bar{P}_{\text{avg}}$ OPDs for a fixed value of excitation amplitude of $\gamma = 0.1$, showing different values excitation frequency, from (a) $\Omega = 0.1$ to (t) $\Omega = 2$, with an interval of $\Delta\Omega = 0.1$. Accompanying rainbow colorbars show the range of values of $\bar{P}_{\text{avg}}$ for each scenario. Each diagram is built with 500×500 sample points.

Figure 6.18 showcases 20 unique instances of $\Omega_s \times \Omega_\phi$ DRDs, achieved by varying Ω while maintaining a fixed the value of $\gamma = 0.1$. It is observed that lower Ω values, represented in the first row of Figure 6.18 (Figures 6.18a to 6.18d - ranging from $\Omega = 0.1$ to $\Omega = 0.4$), lead to a simpler system behavior when altering Ω_s and Ω_ϕ, primarily exhibiting 1T dynamical responses. As the excitation frequency increases from $\Omega = 0.5$ to $\Omega = 1.2$, the complexity intensifies, especially near the z-direction resonance (around the vicinity of $\Omega = 1$). However, a further increase in the excitation frequency from $\Omega = 1.3$ to $\Omega = 2$ results in a reduction in complexity.

Figure 6.19 presents the corresponding OPDs for the DRDs depicted in Figure 6.18. Several observations can be made by comparing these two Figures. Firstly, an increase in complexity is indicative of improved performance according to these results. Secondly, near z-direction resonance ($0.8 \leq \Omega \leq 1.0$), the regions of good performance expand within the OPDs, as expected. Thirdly, 1T, 2T, and HC responses are the most prevalent dynamical behaviors observed, followed by CH and MP responses. Upon examination of these results, it is noted that the majority of hyperchaotic regions show superior performance, while the majority of 1T regions (though not all) exhibit poor performance. For instance, the top-right regions of Figures 6.19i to 6.19l (from $\Omega = 0.9$ to $\Omega = 1.2$) show an arc-shaped strip with elevated output power values. In fact, this strip seems to move from the bottom region (Figure 6.19a) to the top right region of the diagrams, while other more complex regions emerge at the bottom as Ω increases. Fourthly, the peak power moves from smaller to larger Ω_s values as Ω increases, as expected, due to the change in the beam's resonance frequency region. In this regard, the peak output power region of the OPDs from $\Omega = 0.1$ to $\Omega = 0.8$ (Figures 6.19a to 6.19h) are well-defined regular 1T attractors. Alternatively, from $\Omega = 0.9$ to $\Omega = 2$ (Figures 6.19i to 6.19t), the regions that display the best performances are hyperchaotic ones. Finally, as the resonance shifts from a lower to a higher Ω_s value, an increase in maximum average output power, $\bar{P}_{\text{avg}}^{(\text{max})}$, is observed in almost all cases.

Several of the previously discussed observations hold for scenarios with a higher excitation amplitude of $\gamma = 0.3$, as presented in Figures 6.20 and 6.21. Nevertheless, some new behaviors also emerge. In this case, due to the larger excitation magnitude, some of the described phenomena start to appear at lower Ω values compared to the previous case. In the scenario with low Ω values from $\Omega = 0.1$ to $\Omega = 0.3$, the peak power regions are characterized by 1T regular attractors. For $\Omega = 0.3$ and $\Omega = 0.4$, 2T and CH attractors also appear in the peak output power zone. These attractors form a strip, similar to the one in the previous case, that moves towards the top right region of the diagram. As Ω increases from $\Omega = 0.4$ to $\Omega = 2$, the complexity increases, and new regions with distinct dynamical responses emerge. From the scenario with $\Omega = 0.4$ to $\Omega = 0.8$ (from Subfigures 6.21d to 6.21h), high-

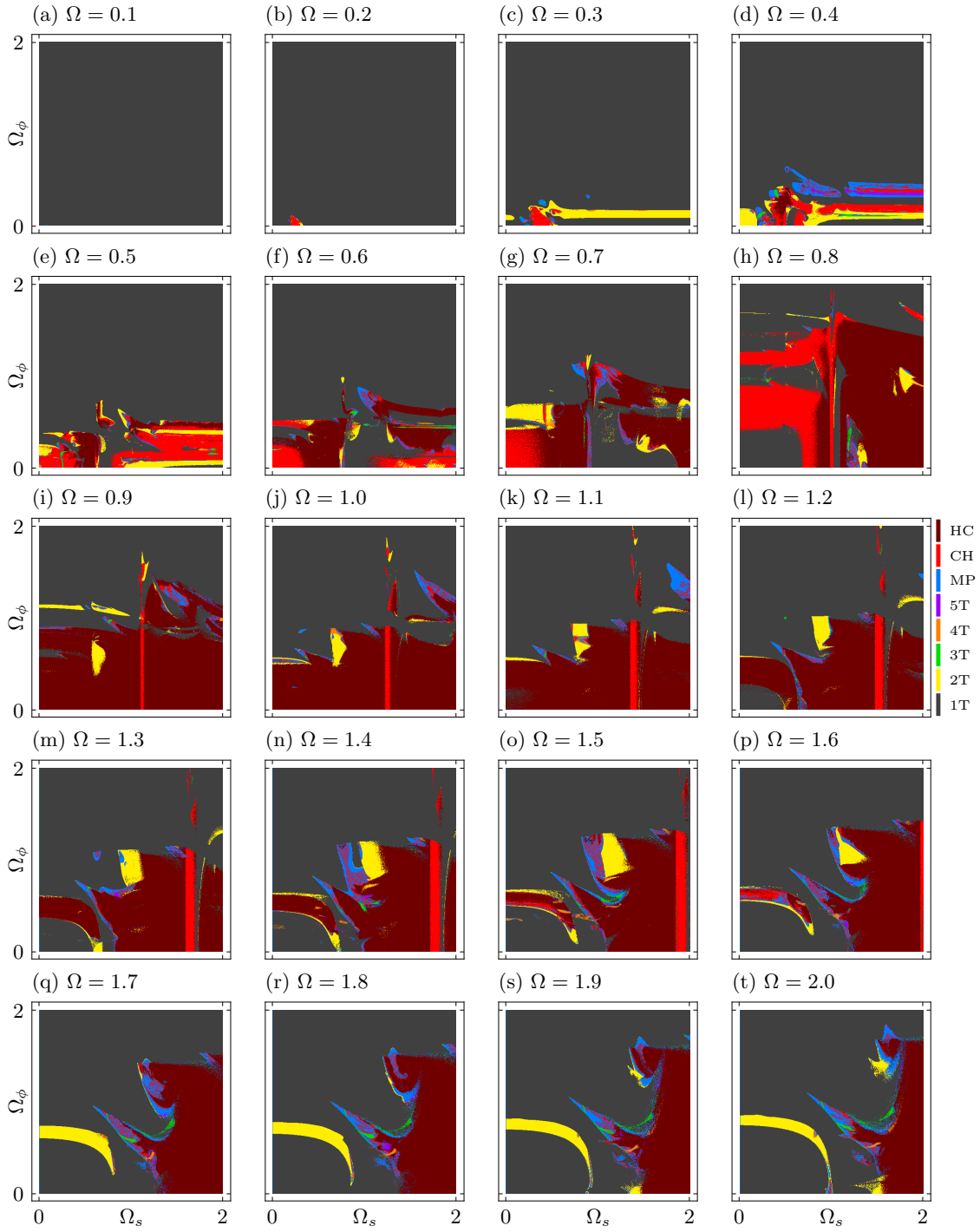

Figure 6.20: DRDs for a fixed value of excitation amplitude of $\gamma = 0.3$, showing different values excitation frequency, from (a) $\Omega = 0.1$ to (t) $\Omega = 2$, with an interval of $\Delta\Omega = 0.1$. Different colors represent distinct dynamical behaviors summarized in the accompanying colorbar. Each diagram is built with 500×500 sample points.

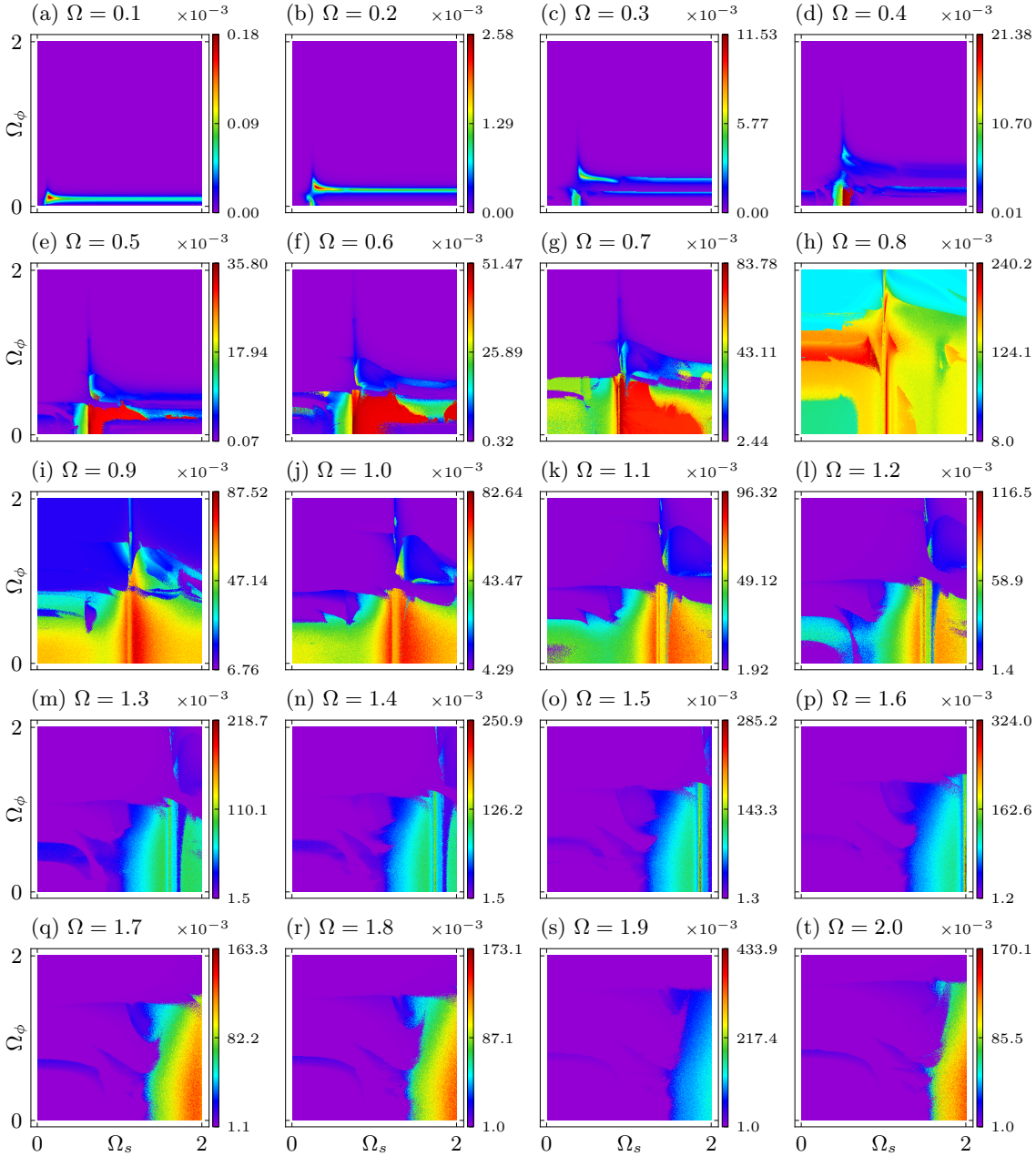

Figure 6.21: $\bar{P}_{\text{avg}}$ OPDs for a fixed value of excitation amplitude of $\gamma = 0.3$, showing different values excitation frequency, from (a) $\Omega = 0.1$ to (t) $\Omega = 2$, with an interval of $\Delta\Omega = 0.1$. Accompanying rainbow colorbars show the range of values of $\bar{P}_{\text{avg}}$ for each scenario. Each diagram is built with 500×500 sample points.

performance regions (red regions) exhibit a greater number of distinct attractors, but with the 1T attractor being predominant. From $\Omega = 0.9$ to $\Omega = 2$ (from Figures 6.21i to 6.21t), the majority of attractors appearing in high-performance zones (red regions) are aperiodic ones (CH and HC). As before, the increase in Ω shifts the peak output power region to higher Ω_s values due to the change in the system's resonance characteristics. Also, the increase in γ results in an overall increase in the maximum output power displayed across all scenarios.

6.5.3 The Best Key Structural Parameters

The previous analysis, represented by Figures 6.18, 6.19, 6.20 and 6.21, provide numerous valuable insights concerning energy harvesting, being useful for design decision making through the determination of the combinations of Ω_s and Ω_ϕ that yields the best performances. Nevertheless, the analysis and design is a complex task that requires more sophisticated tools. An interesting tool for that is the Occurrence Diagram (OCD) which is a two-dimensional parameter diagram that monitors how many times a certain characteristic occurs in a certain region of the parameter space. A comprehensive explanation of the method used to build the OCDs is provided in Chapter 3. By employing this approach, it is possible to effectively identify regions within the $\Omega_s \times \Omega_\phi$ parameter space where higher and lower performances are more likely to occur.

In the process of analyzing 100 distinct scenarios, each with its unique set of OPDs (one for the $\bar{P}_{pz}$, one for $\bar{P}_{em}$ and one for $\bar{P}_{\text{avg}}$), it is crucial to normalize the power ranges prior to constructing the OCDs. This normalization ensures that the values representing the lowest and highest performances of each OPD are scaled to 0 and 1, respectively. This step is necessary as each OPD possesses its own unique minimum and maximum values of average output power, and constructing the OCDs without this normalization could lead to biased results.

The normalization is carried out for three sets of 100 OPDs: one set regarding the average output power of the piezoelectric transducer, $\bar{P}_{pz}$, one related to the average output power of the electromagnetic transducer, $\bar{P}_{em}$, and the last concerning the overall average output power of the MHEH, $\bar{P}_{\text{avg}}$. For each point within an OPD, a normalized output power is defined, $\bar{P}_{\text{norm}}$, defined from the average output power, $\bar{P}$, associated with a specific point within the OPD, defined by indexes i and j; and the maximum average output power occurring within the current OPD, $\bar{P}^{(\max)}$. This is represented as follows

$$\bar{P}_{\text{norm}_{ij}} = \frac{\bar{P}_{ij}}{\bar{P}^{(\max)}}, \qquad (i = 1, \cdots, 500); (j = 1, \cdots, 500) \tag{6.30}$$

For the current analysis, it has been established that the OCDs should monitor

instances where $\bar{P}_{\text{norm}} \geq 0.3$. In other words, any sample within the OPD that exhibits an output power value exceeding 30% of the maximum output power of the current OPD is recorded by the occurrence diagram. This threshold is selected as it effectively identifies regions demonstrating good to excellent performance in terms of output power and bandwidth.

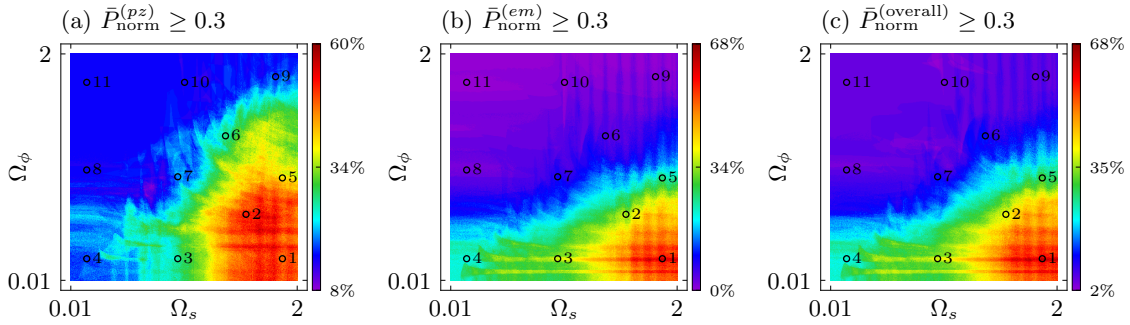

Figure 6.22: Occurrence Diagrams (OCDs) of the $\Omega_s \times \Omega_\phi$ parameter space for a threshold of (a) $\bar{P}_{\text{norm}}^{(pz)} \geq 0.3$, (b) $\bar{P}_{\text{norm}}^{(em)} \geq 0.3$, and (c) $\bar{P}_{\text{norm}}^{(\text{overall})} \geq 0.3$. The accompanying colorbar in each OCD represents the likelihood of the corresponding threshold to occur. Black circles labeled with numbers from 1 to 11 represent combined Ω_s and Ω_ϕ values of interest.

The resulting OCDs are displayed in Figure 6.22. Figure 6.22c makes evident that the optimal overall combinations of Ω_s and Ω_ϕ are situated in the bottom right region of the diagrams, while the least favorable combination is located in the top left. Specifically, approximately 60% to 68% of the cases with performance exceeding a threshold of 30% ($\bar{P}_{\text{norm}}^{(\text{overall})} \geq 0.3$) occur at higher Ω_s values and lower Ω_ϕ values. Conversely, about 2% to 5% of the cases with similar performance levels occur at lower Ω_s values and higher Ω_ϕ values. Moreover, medium occurrence values are displayed at lower to mid-range Ω_ϕ values, spanning all Ω_s values. Additionally, the OCD for the $P_{\text{norm}}^{(em)}$, associated with the electromagnetic transducer, exhibits similar qualitative behavior, as depicted in Figure 6.22b. Alternatively, Figure 6.22a presents the OCD for the $P_{\text{norm}}^{(pz)}$, associated with the piezoelectric transducer. Although the region of high occurrence of good performance still appears in the bottom right region of the OCD, it covers a larger area within the diagram. Also, the regions of medium occurrence values are dispersed around the high occurrence region, occupying a range of approximately $0.7 \leq \Omega_s \leq 1.3$ and $0.01 \leq \Omega_\phi \leq 1.8$.

In summary, this discussion reveals that an MHEH with a stiffer x direction, k_x, and a longer pendulum length, L_p, outperforms an MHEH with opposite configurations. To corroborate this point, 11 configurations are selected within the OCDs, each possessing unique structural characteristics (distinct Ω_s and Ω_ϕ values). The location of these configurations within the OCD is marked as black circles labeled

Table 6.3: Exact corresponding values of Ω_s and Ω_ϕ marked in the OCDs of Figure 6.22 used to determine the configurations analyzed in Figures 6.23, 6.24, 6.25. Region colors are associated with the occurrence percentage as displayed in the OCDs.

Configuration	Ω_s	Ω_ϕ	Region Color in the OCD		
			$\bar{P}_{\text{norm}}^{(pz)}$	$\bar{P}_{\text{norm}}^{(em)}$	$\bar{P}_{\text{norm}}^{(\text{overall})}$
1	1.87	0.20			
2	1.55	0.59			
3	0.95	0.20			
4	0.15	0.20			
5	1.87	0.91			
6	1.37	1.28			
7	0.95	0.92			
8	0.15	0.98			
9	1.81	1.80			
10	1.01	1.75			
11	0.15	1.75			

from 1 to 11, as displayed in Figure 6.22, and listed in Table 6.3 for reproducibility. For each configuration, a new set of DRDs and OPDs are constructed within the $\gamma \times \Omega$ parameter space to assess performance under a broad range of external excitation conditions, where the values of γ are varied from 0.01 to 0.5, and the values of Ω are varied from 0.01 to 2, both contained in a grid of 1000×1000 points. In this regard, many aspects of this analysis are visual representations of a qualitative characteristic, with different colors or gradients representing different characteristics. Consequently, in this analysis, any output power value classified from blue to red is considered part of the harvester's operational bandwidth, while purple values are considered poor performance.

Figure 6.23 showcases the result for Configurations 1, 2, 3, and 5. These configurations reside in the region of medium to high occurrences of $\bar{P}_{\text{norm}} \geq 0.3$ in the OCDs, spanning from green to red-colored regions. Each case displays the DRD, the OPD, and the percentage contribution of each transducer to the average output power of the OPD. Here, EM (light red bar) represents the electromagnetic transducer, and PZ (orange bar) represents the piezoelectric transducer. Overall, this first set of configurations exhibits a wider bandwidth characterized by complex dynamical patterns, observable even at the lowest excitation amplitude values. Upon visual examination and comparison of the DRDs with the OPDs of each case, regions of good performance are characterized by complex dynamical patterns, especially hyperchaotic (HC) attractors. The majority of poor performance regions are associated with 1T regular responses. 2T and chaotic (CH) are also common and appear

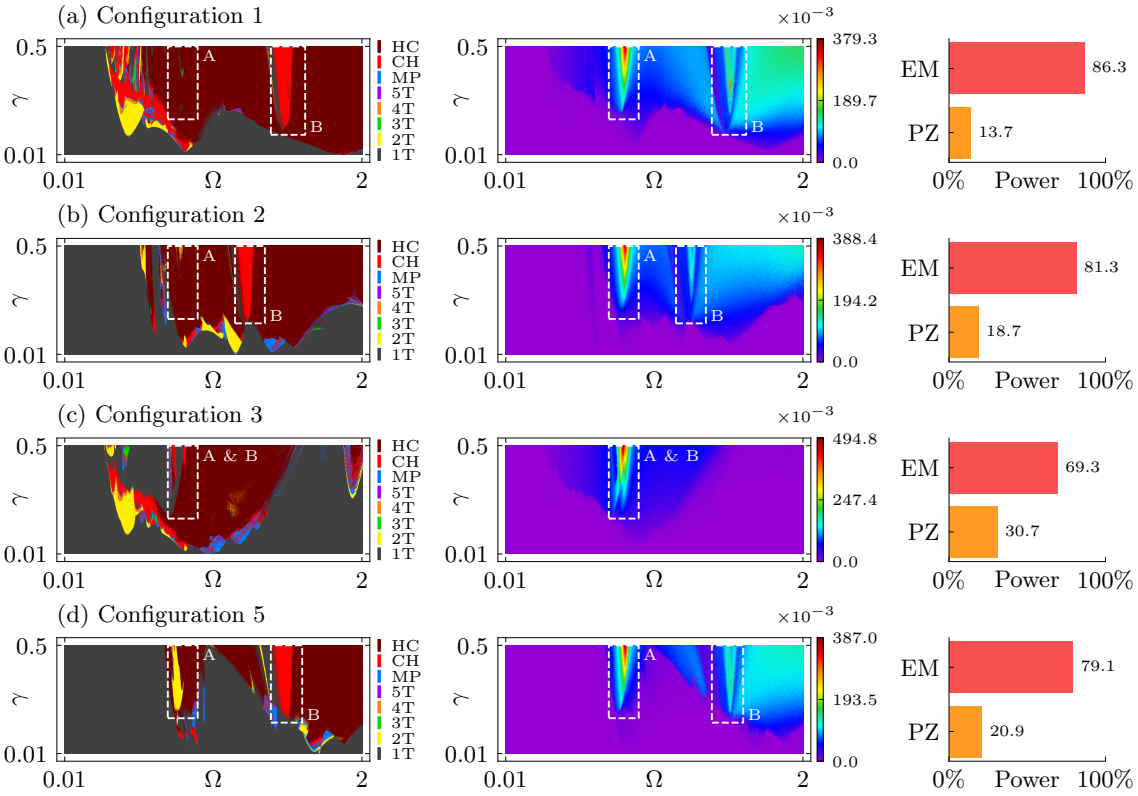

Figure 6.23: DRD, OPD for the overall average output power, $\bar{P}_{\text{avg}}$, and the contribution of each transducer in power conversion for (a) Config. 1, (b) Config. 2, (c) Config. 3, and (d) Config. 5. DRD colorbars represent different types of dynamical responses, and OPD colorbars represent the range of $\bar{P}_{\text{avg}}$ displayed by each configuration. Light red and orange bars are the % contribution of the piezoelectric and electromagnetic transducers in the overall conversion, respectively. Diagrams are constructed with a grid of 1000×1000 points of the $\gamma \times \Omega$ parameter space.

in certain clusters within the parameter domain. The main peak power occurs in a concentrated region (labeled as A) associated with the resonance of the $\bar{z}$-direction, followed by a secondary peak (labeled as B) associated with the resonance of the $\bar{x}$-direction that transmits more energy to the pendulum. This secondary peak arises in different positions of the diagram and is associated with the value of Ω_s. That is, a configuration with higher Ω_s presents a secondary peak at higher excitation amplitudes, and vice-versa. Configuration 1 presents the wider bandwidth, while configuration 3 presents the highest maximum output power, despite the reduced bandwidth. Additionally, for all cases in this set of configurations, the electromagnetic transducer predominantly contributes to the power conversion of the MHEH.

Figure 6.24 presents results of Configurations 4, 6 and 7. These configurations are situated in the blue regions (both light and navy blue) of the $\bar{P}_{\text{norm}}^{(\text{overall})}$ and $\bar{P}_{\text{norm}}^{(em)}$ OCDs of Figure 6.22b and 6.22c, and in the blue to green regions of the $\bar{P}_{\text{norm}}^{(pz)}$ OCD of Figure 6.22a. In this set of configurations, it is observed that the complex regions

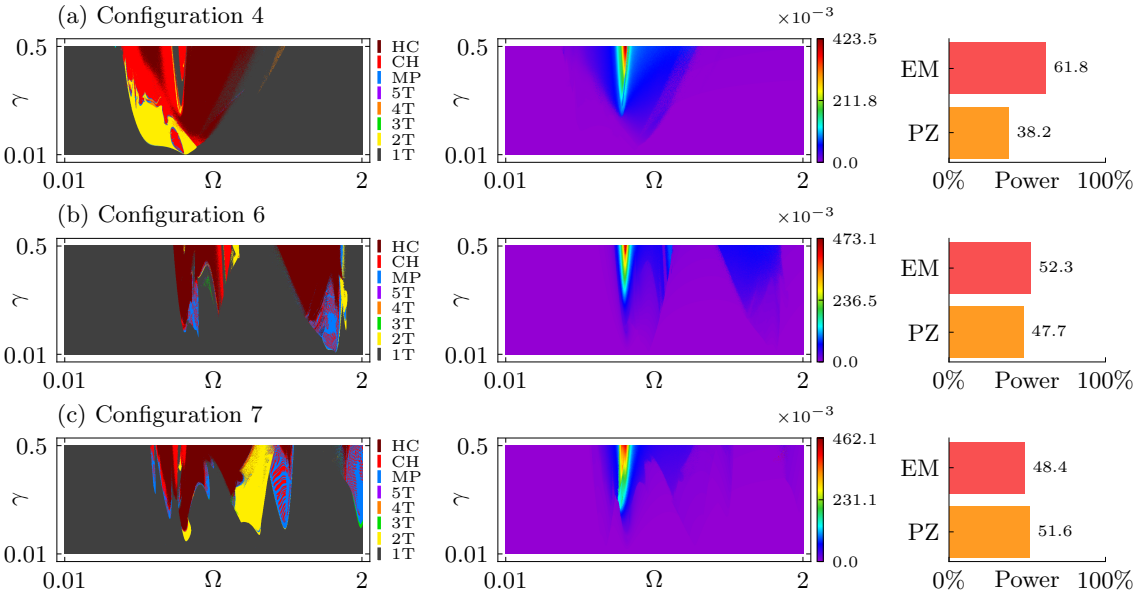

Figure 6.24: DRD, OPD for the overall average output power, $\bar{P}_{\text{avg}}$, and the contribution of each transducer in power conversion for (a) Config. 4, (b) Config. 6, and (c) Config. 7. DRD colorbars represent different types of dynamical responses, and OPD colorbars represent a range of $\bar{P}_{\text{avg}}$ displayed by each configuration. Light red and orange bars represent the % contribution of the piezoelectric and electromagnetic transducers in the overall conversion, respectively. Diagrams are constructed with a grid of 1000×1000 points of the $\gamma \times \Omega$ parameter space.

associated with higher performances are distributed in small clusters, showing a reduced, yet significant, bandwidth. Moreover, the maximum output powers achieved surpass those of the majority of the previous configurations presented in Figure 6.23. They are concentrated in the $\bar{z}$-direction resonance region. Additionally, these configurations exhibit a more balanced distribution of converted power between the two transducers.

On the other hand, Figure 6.25 presents a set of four configurations that are located in the blue regions of the $\bar{P}^{(pz)}_{\text{norm}}$ OCD in Figure 6.22a, and in the purple regions of the remaining OCDs in Figures 6.22b and 6.22c. In general, these configurations are characterized by the dominance of the piezoelectric transducer in energy conversion. In fact, Configurations 10 and 11 exhibit a predominance exceeding 96%. They also display very narrow bandwidths associated with the peak power in the $\bar{z}$-direction resonance region, except for Configuration 9, which shows another narrow secondary peak at higher excitation frequencies due to the higher Ω_s values. This group of configurations represents the worst-case scenario in the utilization of MHEH, as it offers minimal advantages in terms of performance when attaching the pendulum to the classic piezoelectric energy harvester (CPEH).

The analysis outlined in this subsection demonstrates that the Occurrence Di-

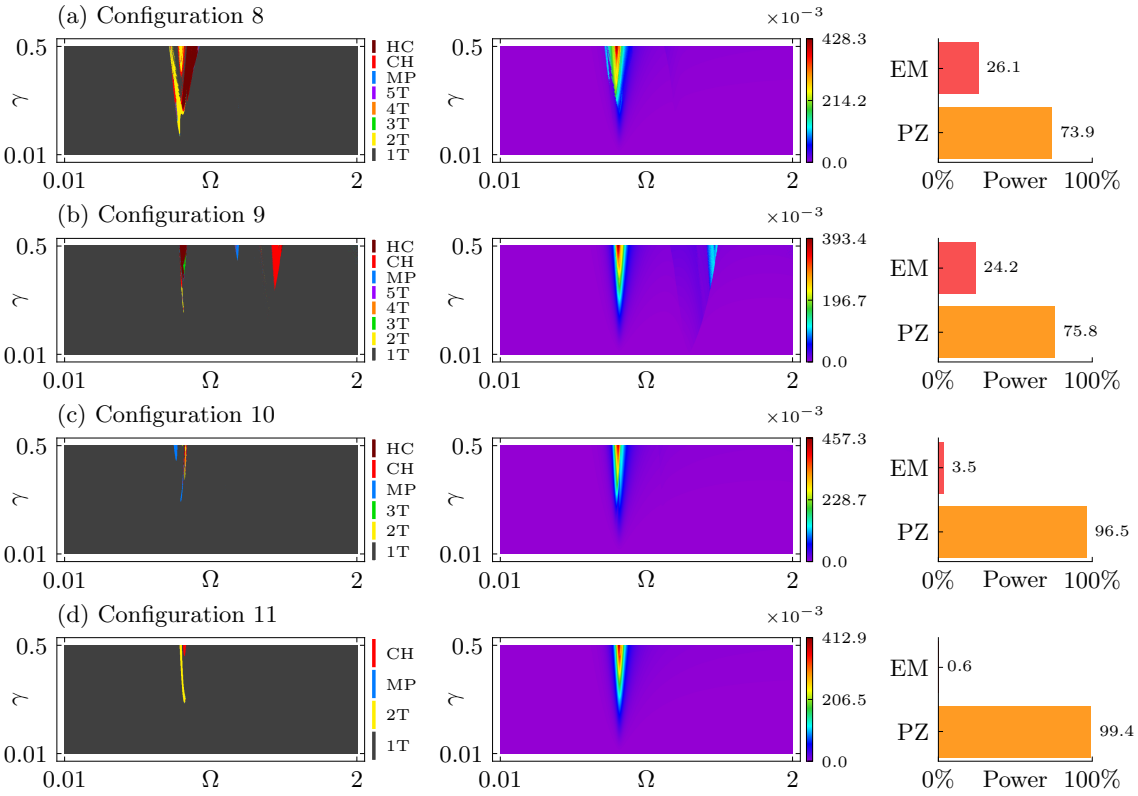

Figure 6.25: DRD, OPD for the overall average output power, $\bar{P}_{\text{avg}}$, and the contribution of each transducer in the power conversion for (a) Config. 8, (b) Config. 9, (c) Config. 10, and (d) Config. 11. DRD colorbars represent different types of dynamical responses, and OPD colorbars represent a range of $\bar{P}_{\text{avg}}$ displayed by each configuration. Light red and orange bars represent the percentage contribution of the piezoelectric and electromagnetic transducers in the overall conversion, respectively. Diagrams are constructed with a grid of 1000×1000 points of the $\gamma \times \Omega$ parameter space.

agram (OCD) is a powerful tool for mapping and determining the optimal and suboptimal combinations of parameters within a specific parameter space. Despite its substantial computational resource requirements, needing the prior assembly of a considerable number of diagrams for its accurate construction, the OCD offers an effective method to map and identify the frequency of occurrence of key characteristics of a dynamical system.

6.5.4 Dynamical Patterns vs Performance

The correlation between dynamics and performance is an essential key to the energy harvesting analysis. In this regard, it is important to identify the types of responses and patterns. Besides, it is interesting to evaluate the influence of pendulum incorporation on the harvester response that indeed has demonstrated the potential to significantly enhance operational bandwidth, as presented in Figures 6.23,

6.24 and 6.25. On this basis, one of the key points to address is to identify which pendulum dynamical patterns produce these regions of enhanced performance. To this end, Figure 6.26 presents the concept of a Dynamical Pattern Diagram (DPD) for Configuration 1. A DPD is an extension of the Dynamical Responses Diagram (DRD) that accounts for the classification and mapping of specific dynamical patterns of a dynamical system in a two-dimensional parameter space. In this case, the DPDs monitor whether the pendulum rotates or not. Six patterns are identified: RO (Light Cyan), when the pendulum oscillates with regular motion and does not rotate; IO (Dark Cyan), when it oscillates with an irregular motion and does not rotate; RR (Light Lime Green), when it rotates with a regular motion; IR (Lime Green), when it rotates with an irregular motion; RM (Light Salmon), when it presents a regular intermittent mix of oscillatory and rotatory motions; and IM (Lava Red), when it presents a mix of oscillatory and rotatory irregular motions.

Table 6.4: Conditions for each dynamical pattern classification of the MHEH.

Dynamical Pattern Classification	Conditions
RO (Regular Oscillation)	• $\bar{\phi}_{\min} > -\pi$ and $\bar{\phi}_{\max} < \pi$ • $\text{sgn}(\dot{\bar{\phi}}_{\min}) \neq \text{sgn}(\dot{\bar{\phi}}_{\max})$ • Attractor $\neq$ CH and Attractor $\neq$ HC
IO (Irregular Oscillation)	• $\bar{\phi}_{\min} > -\pi$ and $\bar{\phi}_{\max} < \pi$ • $\text{sgn}(\dot{\bar{\phi}}_{\min}) \neq \text{sgn}(\dot{\bar{\phi}}_{\max})$ • Attractor = CH or Attractor = HC
RR (Regular Rotation)	• $\bar{\phi}_{\min} \leq -\pi$ and $\bar{\phi}_{\max} \geq \pi$ • $\text{sgn}(\dot{\bar{\phi}}_{\min}) = \text{sgn}(\dot{\bar{\phi}}_{\max})$ • Attractor $\neq$ CH and Attractor $\neq$ HC
IR (Irregular Rotation)	• $\bar{\phi}_{\min} \leq -\pi$ and $\bar{\phi}_{\max} \geq \pi$ • $\text{sgn}(\dot{\bar{\phi}}_{\min}) = \text{sgn}(\dot{\bar{\phi}}_{\max})$ • Attractor = CH or Attractor = HC
RM (Regular Mixed)	• $\bar{\phi}_{\min} \leq -\pi$ and $\bar{\phi}_{\max} \geq \pi$ • $\text{sgn}(\dot{\bar{\phi}}_{\min}) \neq \text{sgn}(\dot{\bar{\phi}}_{\max})$ • Attractor $\neq$ CH and Attractor $\neq$ HC
IM (Irregular Mixed)	• $\bar{\phi}_{\min} \leq -\pi$ and $\bar{\phi}_{\max} \geq \pi$ • $\text{sgn}(\dot{\bar{\phi}}_{\min}) \neq \text{sgn}(\dot{\bar{\phi}}_{\max})$ • Attractor = CH or Attractor = HC

Specifically, it monitors the coordinate transformed state space of the pendulum $\bar{\phi} \times \dot{\bar{\phi}}$ and its associated dynamical attractor. The process of coordinate transformation of $\bar{\phi}$ is discussed in Section 6.5.1, and it is done due to the phase subspace of the pendulum being characterized by a cylinder topology. Based on the minimum

and maximum values of the angular position of the pendulum, $\bar{\phi}_{\min}$ and $\bar{\phi}_{\max}$, respectively, on the signal of the angular velocity $\dot{\bar{\phi}}$, and on the dynamical response classification of the DRD, it classified six different dynamical patterns of rotation as summarized in Table 6.4. Each classification is represented by a distinct color as presented in Figure 6.27.

Each pattern is exemplified by selected points, labeled with numbers from 1 to 6, as marked by black circles within the DPD in Figure 6.26a. Four phase subspaces and Poincaré maps ($\bar{x} \times \dot{\bar{x}}$, $\bar{z} \times \dot{\bar{z}}$, $\bar{\phi} \times \dot{\bar{\phi}}$, and $\bar{v} \times \bar{I}$) for each point are depicted in Figures 6.26b to 6.26g, representing each different pattern. The color of each phrase subspace is associated with the color used to classify the pattern, and the exact γ and Ω values used for the selected points are described in Table 6.5 for reproducibility.

Table 6.5: Exact corresponding values of γ and Ω marked in the DPD of Figure 6.26 used to exemplify the different dynamical patterns.

Point	Classification	γ	Ω
1	RO	0.21012012012012	0.45023023023023
2	IO	0.05022022022022	0.814764764764765
3	RR	0.311161161161161	0.563773773773774
4	IR	0.384244244244244	0.370550550550551
5	RM	0.377377377377377	0.796836836836837
6	IM	0.25034034034034	0.860580580580581

Figure 6.27 presents a series of DPDs associated with each configuration previously described in Table 6.2. By comparing with the OPDs previously presented in Figures 6.23, 6.24 and 6.25, it is noticeable that triggering a rotational or a mixed dynamical pattern in the pendulum results in an enhanced performance outside the typical $\bar{z}$-direction resonance zone due to the contribution of the electromagnetic transducer. In fact, this is the reason for the configurations with larger bandwidths display a greater contribution to energy conversion from the electromagnetic transducer. Furthermore, Figure 6.27l supports the previous conclusions by showing the percentage of each dynamical pattern within the DPD for each distinct configuration.

Another crucial topic is the type of dynamical response that yields the best performances. In this regard, from the 100 unique scenarios examined in Subsection 6.5.2, the total percentage of attractors is accounted for, as displayed in Figure 6.28a. In essence, 25×10^6 time series, considering different combination of γ, Ω, Ω_s and Ω_ϕ parameters, are analyzed. It is observed that 72% of the dynamical responses are regular 1T attractors, followed by 19.2% of hyperchaotic (HC) ones. Chaotic (CH),

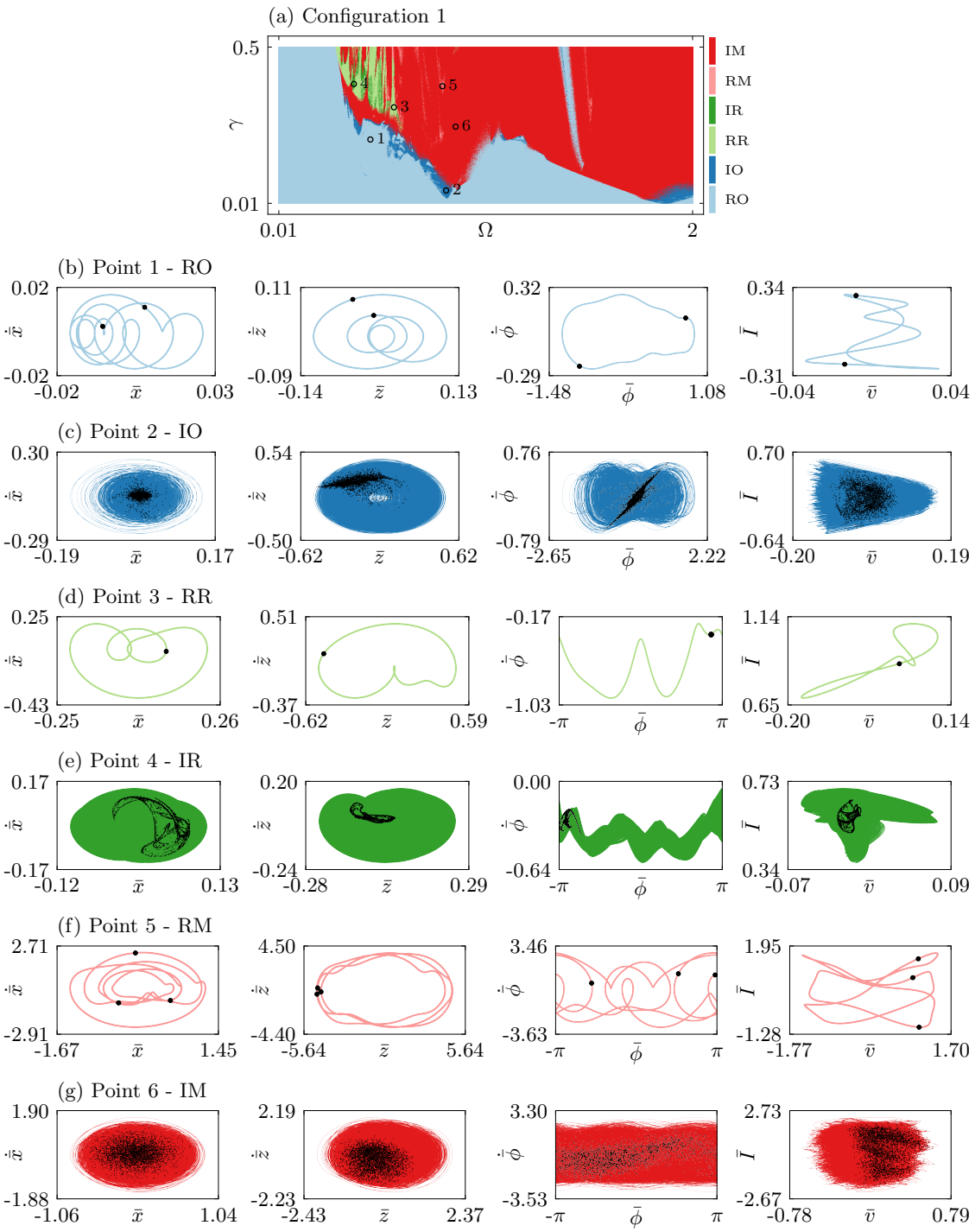

Figure 6.26: Classification of different pendulum dynamical patterns. (a) Dynamical Pattern Diagrams (DPD) of Config. 1 classifying six distinct patterns: RO (light cyan) - Regular Oscillation, IO (dark cyan) - Irregular Oscillation, RR (light lime green) - Regular Rotation, IR (lime green) - Irregular Rotation, RM (light salmon) - Regular Mixed, and IM (lava red) - Irregular Mixed. Black circle points are associated with different patterns. Phase subspaces representation of the (b) RO pattern (point 1), (c) IO pattern (point 2), (d) RR pattern (point 3), (e) IR pattern (point 4), (f) RM pattern (point 5), and (g) IM pattern (point 6). The DPD is constructed with a grid of 1000×1000 points of the $\gamma \times \Omega$ parameter space.

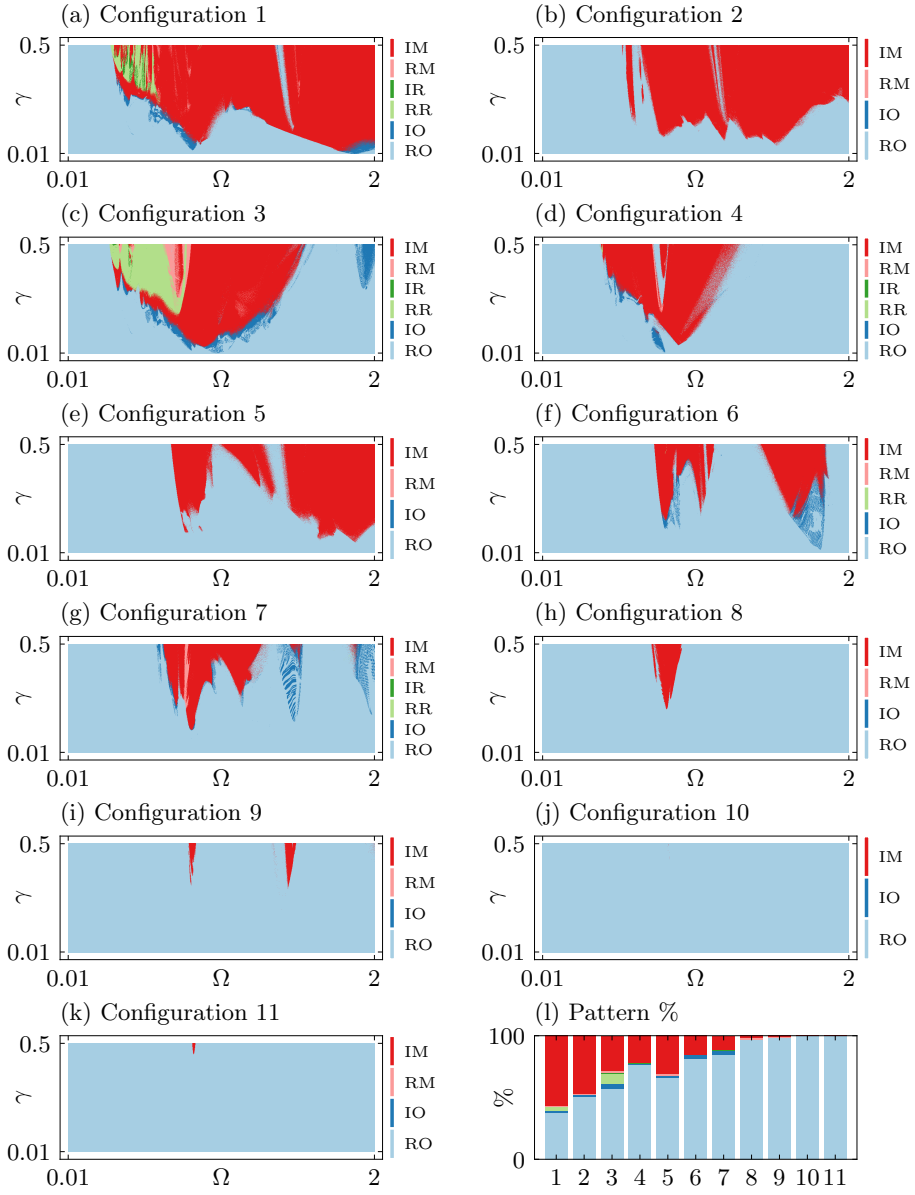

Figure 6.27: Dynamical Patterns Diagrams (DPDs) for the classification of six different types of pendulum dynamical patterns. The DPDs are associated with (a) Configuration 1, (b) Configuration 2, (c) Configuration 3, (d) Configuration 4, (e) Configuration 5, (f) Configuration 6, (g) Configuration 7, (h) Configuration 8, (i) Configuration 9, (j) Configuration 10, (k) Configuration 11. Each diagram is constructed with a grid of 1000×1000 points of the $\gamma \times \Omega$ parameter space. (l) Percentage of occurrence of each type of pattern for each configuration.

2T and MP also appear in smaller quantities. Additionally, the amount of 3T, 4T and 5T attractors is very small compared to the others. When the same analysis is performed, but only accounting for the dynamical responses that are above the threshold of $\bar{P}_{\text{norm}} \geq 0.3$, as done in the OCD analysis, the scenario reverses, as presented in Figure 6.28b. In this case, the predominant attractor becomes the hyperchaotic (HC) with 68.5%, followed by 15.7% of 1T attractors, and by 11.5% of Chaotic (CH) responses. The remaining dynamical responses stay relatively the same. Additionally, the same analysis with the same threshold is performed for each transducer, as indicated in Figures 6.28c and 6.28d. It is observed that the number of hyperchaotic responses increases and the 1T responses decrease even more for the electromagnetic transducer. Conversely, 1T attractors increase and hyperchaotic attractors decrease for the piezoelectric transducer.

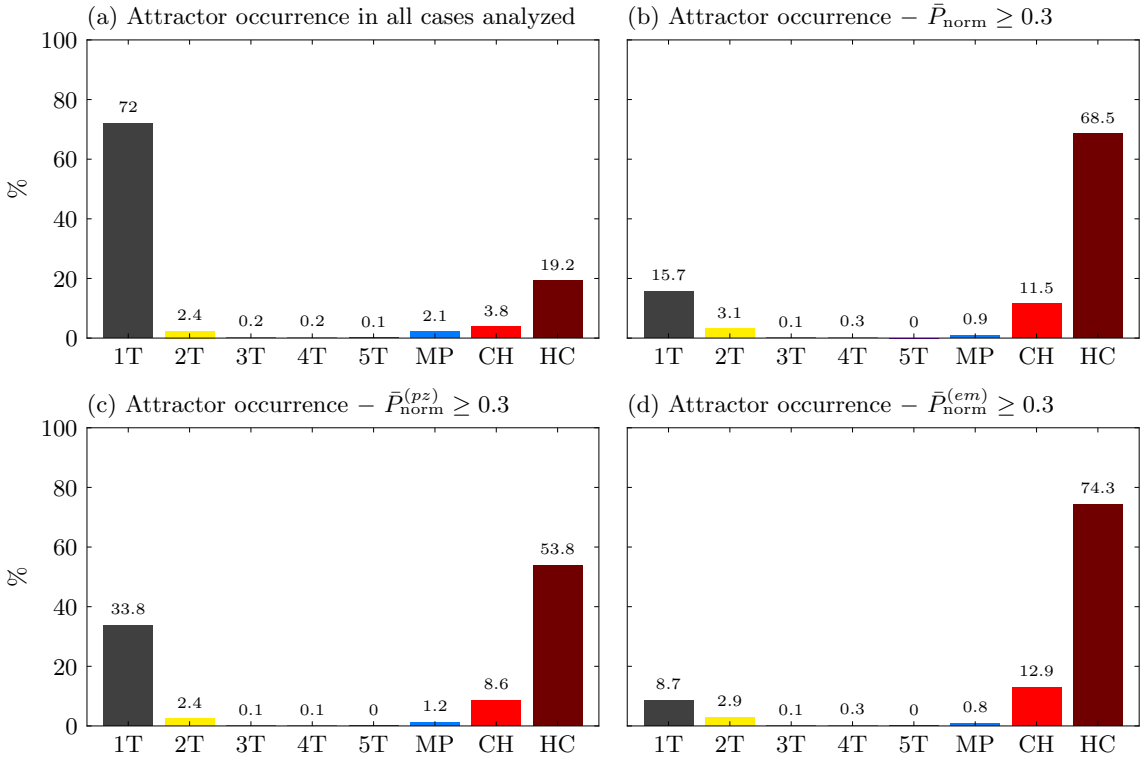

Figure 6.28: Percentage of dynamical responses for the 100 scenarios studied in subsection 6.5.2. (a) Overall percentage with no filter, (b) Percentage of attractors using the filter threshold of $\bar{P}_{\text{norm}} \geq 0.3$ considering the two transducers. (c) Percentage of attractors using the filter threshold of $\bar{P}^{(pz)}_{\text{norm}} \geq 0.3$ considering only the piezoelectric transducer. (d) Percentage of attractors using the filter threshold of $\bar{P}^{(em)}_{\text{norm}} \geq 0.3$ considering only the electromagnetic transducer. Each color represents a distinct dynamical response. Overall, 25×10^6 time series considering unique combinations of 4 key parameters were used in the analysis.

To further investigate the regions of high performance and corroborate the findings presented in Figure 6.28, two configurations from each of Figures 6.23, 6.24

and 6.25 are selected. For each chosen configuration, the overall average maximum output power, $\bar{P}_{\text{avg}}^{(\max)}$, for each value of excitation amplitude, γ, is marked as colorful points in the corresponding configuration OPD, as showed in Figures 6.29, 6.30 and 6.31. Grayscale colors within the OPDs are used to reference the overall lower and higher output powers. Colored points are the points of maximum output power for each distinct value of γ, with the accompanying colorbar indicating their magnitude. The colorbars are truncated within 50% of their maximum value for better representation. The maximum output power magnitudes for each configuration are displayed at the top of the pointing end of the colorbars. Constant values of γ ($\gamma \approx 0.1$, $\gamma \approx 0.2$ and $\gamma \approx 0.3$) are selected, labeled with capital letters, and plotted below the OPDs to display the bandwidths at each selected magnitude of excitation. For each of the three selected values of γ, its respective point of maximum is marked as red circles and labeled with a number from 1 to 3. Their respective phase subspaces and Poincaré maps are built: $\bar{x} \times \dot{\bar{x}}$, representing the x-direction, $\bar{z} \times \dot{\bar{z}}$, representing the z-direction, $\bar{\phi} \times \dot{\bar{\phi}}$, representing the angular subspace of the pendulum, and $\bar{v} \times \bar{I}$ representing the electrical coordinate domain.

Specifically, Figure 6.29 depicts Configurations 1 and 2, where the electromagnetic transducer predominantly contributes to energy conversion. The OPDs for these two cases are represented in Figures 6.29a and 6.29b, demonstrating that the points of maximum are clustered near the resonance regions. Figures 6.29b and 6.29c present the frequency response for each selected fixed γ, more clearly illustrating the wider bandwidth associated with these configurations for distinct discrete magnitudes of excitation. From Figure 6.29e to 6.29j, one can observe the associated phase subspaces and Poincaré maps of each point of maximum marked in Figures 6.29b and 6.29c. These subspaces support the findings associated with Figures 6.27 and 6.28, indicating that the dynamical responses associated with the best performances are the hyperchaotic (HC) and 1T attractors, respectively. Also, these performances must be associated with the triggering of the pendulum's rotation or mixed dynamical pattern, as all the selected points of maximum show this characteristic, as highlighted in the $\bar{\phi} \times \dot{\bar{\phi}}$ phase subspaces.

Figure 6.30 presents the same analysis for Configurations 4 and 6, where the contribution of both transducers is balanced. In this scenario, the points of maximum within the OPDs are more concentrated in a single cluster, resulting in narrower, yet still significant, bandwidths. This is further illustrated by the frequency response for each selected value of γ, as presented in Figures 6.30c and 6.30d. The phase subspaces associated with the selected red points of maximum exhibit a consistent behavior, with more hyperchaotic responses than periodic ones, as displayed from Figures 6.30e to 6.30f. Figure 6.30f is particularly noteworthy as it shows a 2T regular response at a point of maximum, representing 3.1% of the high-performance

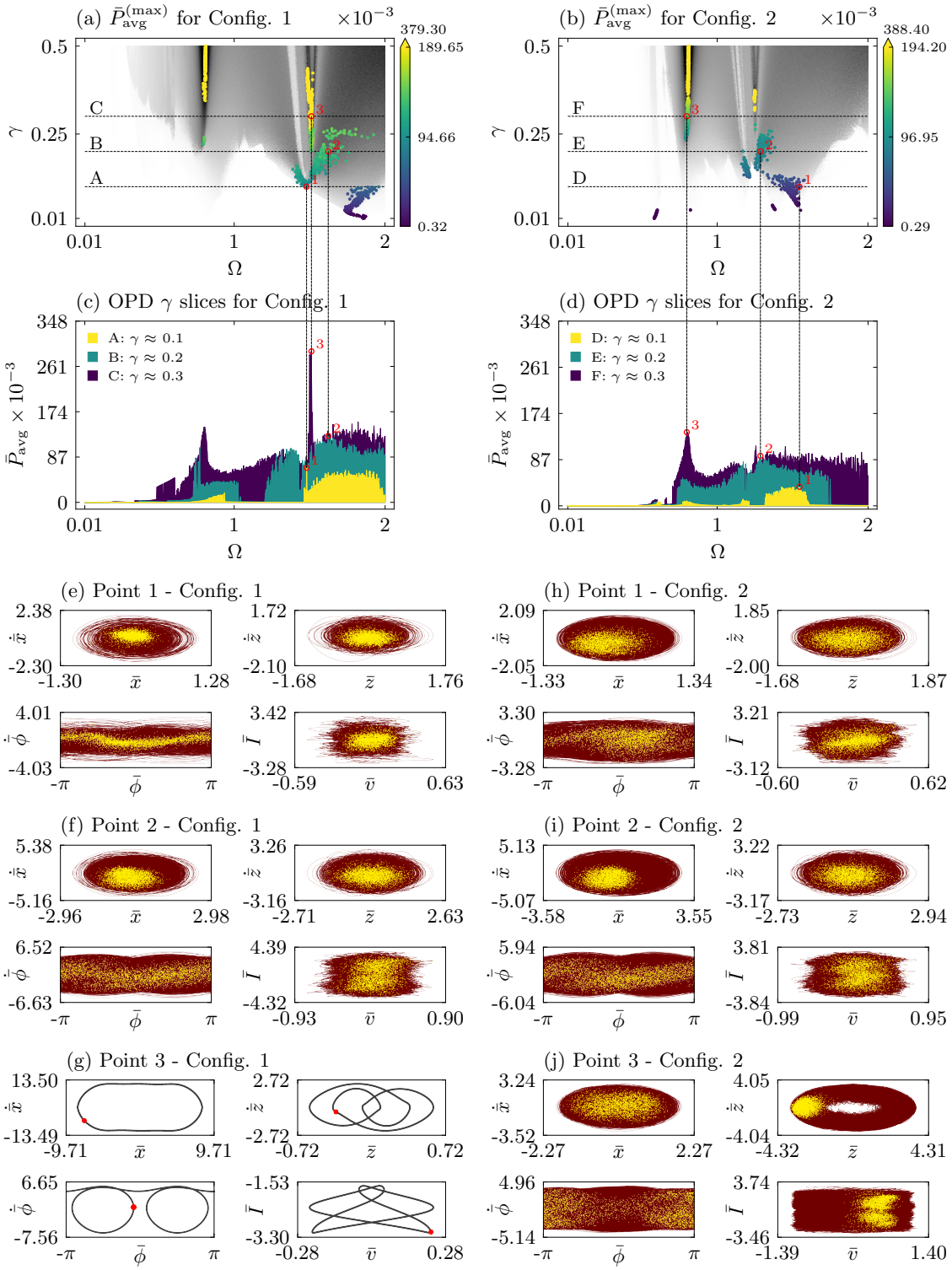

Figure 6.29: Maximum overall average output power, $\bar{P}_{\text{avg}}^{(\max)}$, as a function of γ for Configs (a) 1 and (b) 2. Panels (c) and (d) display the slices A, B, C, and D, E, F of the OPDs, respectively, for 3 values: $\gamma \approx 0.1$, $\gamma \approx 0.2$ and $\gamma \approx 0.3$. Red circles denote the $\bar{P}_{\text{avg}}^{(\max)}$ of each slice. Four phase subspaces ($\bar{x} \times \dot{\bar{x}}$, $\bar{z} \times \dot{\bar{z}}$, $\bar{\phi} \times \dot{\bar{\phi}}$, and $\bar{v} \times \bar{I}$) and their Poincaré maps of the steady-state response are shown representing red points (e) 1, (f) 2, and (g) 3 for Config. 1, and red points (h) 1, (i) 2, and (j) 3 for Config. 2. Non-maximum values within the OPDs are plotted in grayscale.

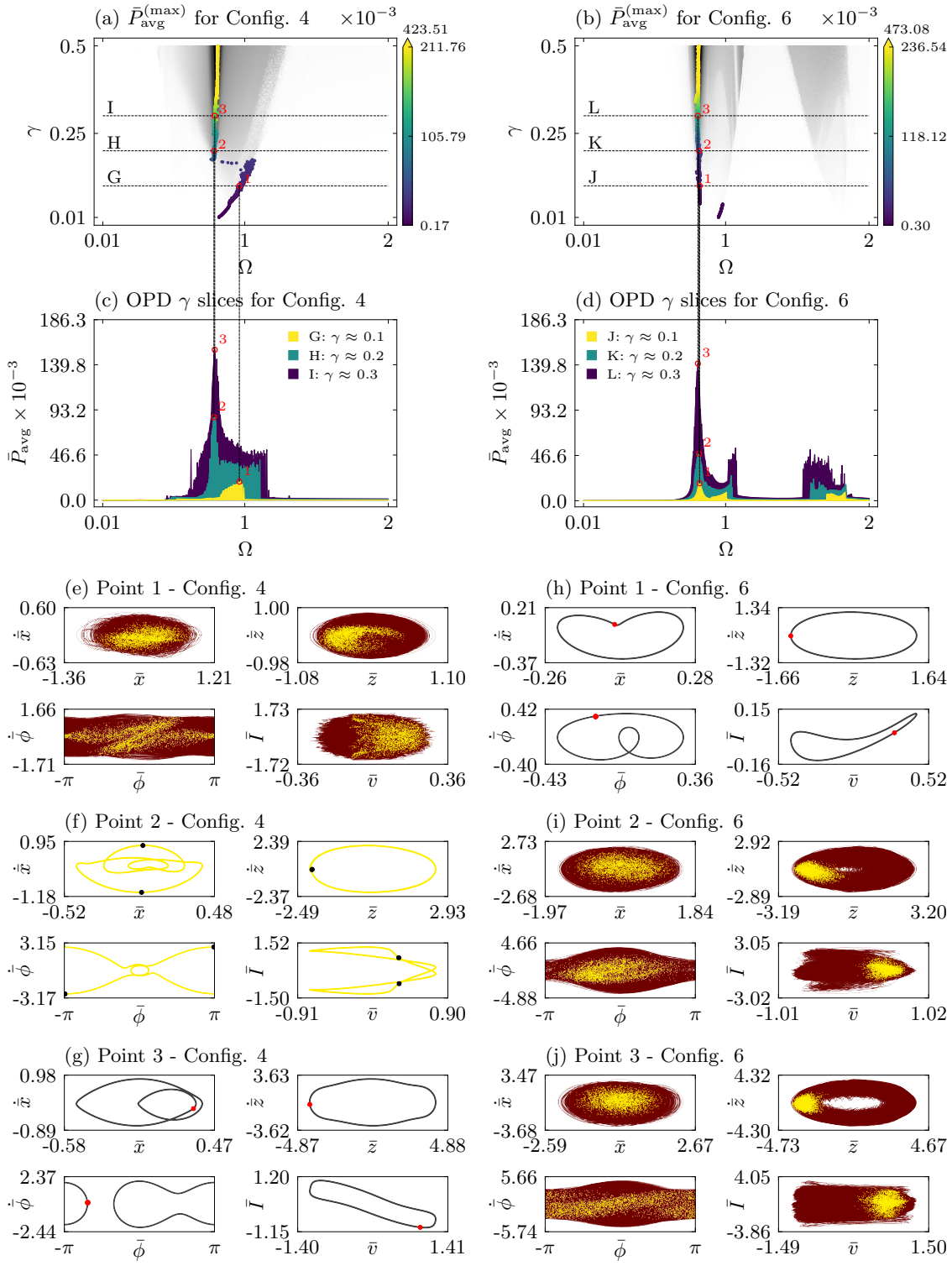

Figure 6.30: Maximum overall average output power, $\bar{P}_{avg}^{(max)}$, as a function of γ for Configs. (a) 4 and (b) 6. Panels (c) and (d) display the slices G, H, I, and J, K, L of the OPDs, respectively, for 3 values: $\gamma \approx 0.1$, $\gamma \approx 0.2$ and $\gamma \approx 0.3$. Red circles denote the $\bar{P}_{avg}^{(max)}$ of each slice. Four phase subspaces ($\bar{x} \times \dot{\bar{x}}$, $\bar{z} \times \dot{\bar{z}}$, $\bar{\phi} \times \dot{\bar{\phi}}$, and $\bar{v} \times \bar{I}$) and their Poincaré maps of the steady-state response are shown representing red points (e) 1, (f) 2, and (g) 3 for Config. 4, and red points (h) 1, (i) 2, and (j) 3 for Confi. 6. Non-maximum values in the OPDs are plotted in grayscale.

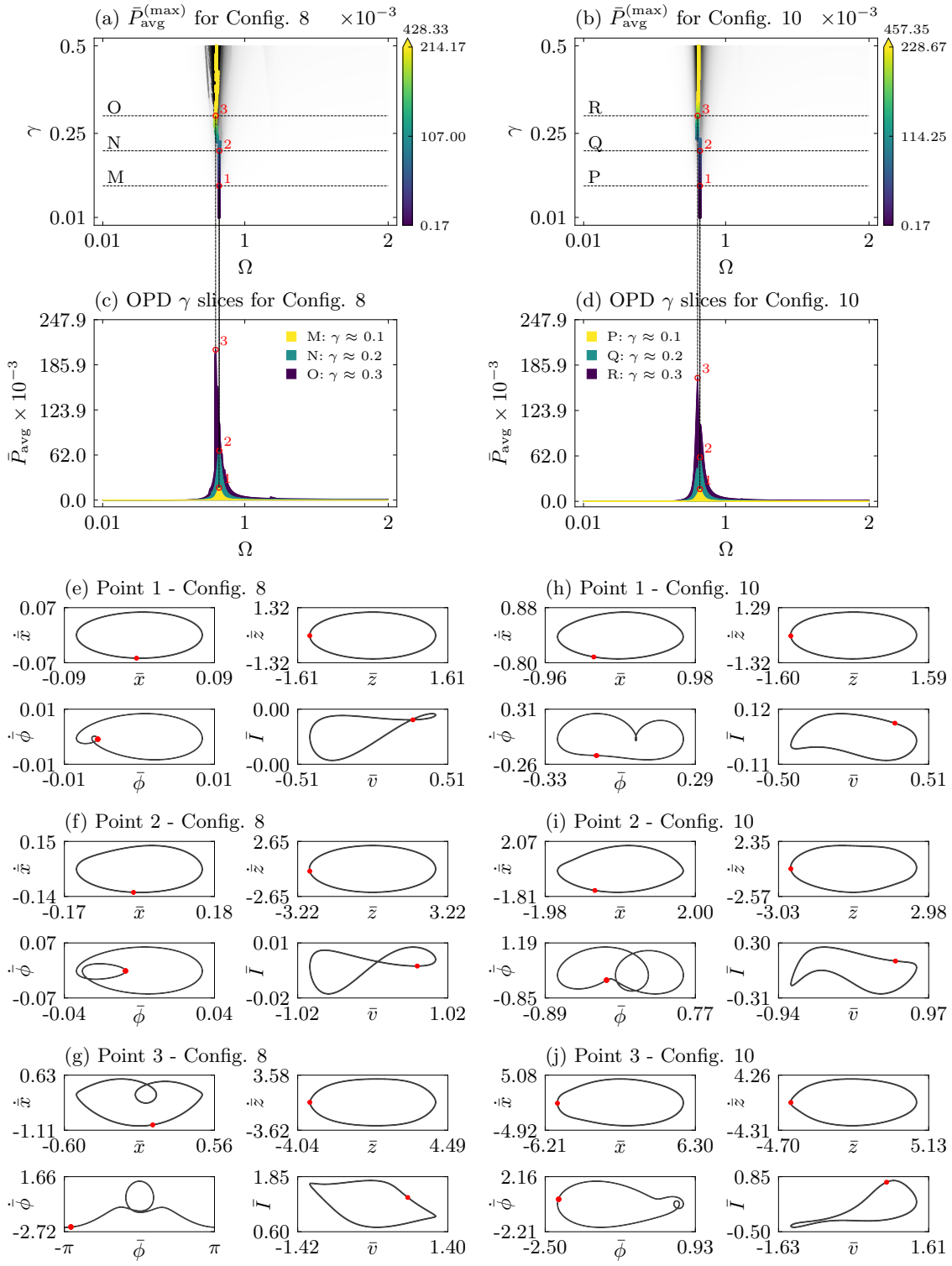

Figure 6.31: Maximum overall average output power, $\bar{P}_{\text{avg}}^{(\max)}$, as a function of γ for Configs. (a) 8 and (b) 10. Panels (c) and (d) display the slices M, N, O, and P, Q, R of the OPDs, respectively, for 3 values: $\gamma \approx 0.1$, $\gamma \approx 0.2$ and $\gamma \approx 0.3$. Red circles denote the $\bar{P}_{\text{avg}}^{(\max)}$ of each slice. Four phase subspaces ($\bar{x} \times \dot{\bar{x}}$, $\bar{z} \times \dot{\bar{z}}$, $\bar{\phi} \times \dot{\bar{\phi}}$, and $\bar{v} \times \bar{I}$) and their Poincaré maps of the steady-state response are shown representing red points (e) 1, (f) 2, and (g) 3 for Config. 8, and red points (h) 1, (i) 2, and (j) 3 for Config. 10. Non-maximum values in the OPDs are plotted in grayscale.

responses above the $\bar{P}_{\text{norm}} \geq 0.3$ threshold. Furthermore, another fact to highlight is that two of the six selected red points of maximum do not show pendulum rotation. The first is depicted in Figure 6.30g, showing a high-amplitude regular oscillatory dynamical pattern (RO), and the second is displayed in Figure 6.30h, showing also RO pattern, but with low amplitude. The latter point corresponds to the point of maximum of the J slice (yellow curve) showing that the high-amplitude pendulum's motion, in this case, commences at higher excitation levels.

Figure 6.31 presents the same analysis for Configurations 8 and 10, where the piezoelectric transducer dominates the energy conversion. These configurations represent the least favorable scenario for the MHEH, characterized by a very narrow bandwidth. This is further illustrated by the red points of maximum that are precisely concentrated at the resonance region of the $\bar{z}$-direction. It also supports the findings of Figure 6.28c, which shows a high occurrence percentage of 1T attractors in the regions of high performance above the $\bar{P}_{\text{norm}} \geq 0.3$ threshold. It is also important to highlight that the pendulum fully rotates around its axis (presents a high-amplitude motion) in only one selected red point of maximum.

Summarizing, this subsection effectively highlights the association of hyperchaotic responses and the full rotation of the pendulum with wider bandwidths and enhanced performance.

6.5.5 Performance Comparison

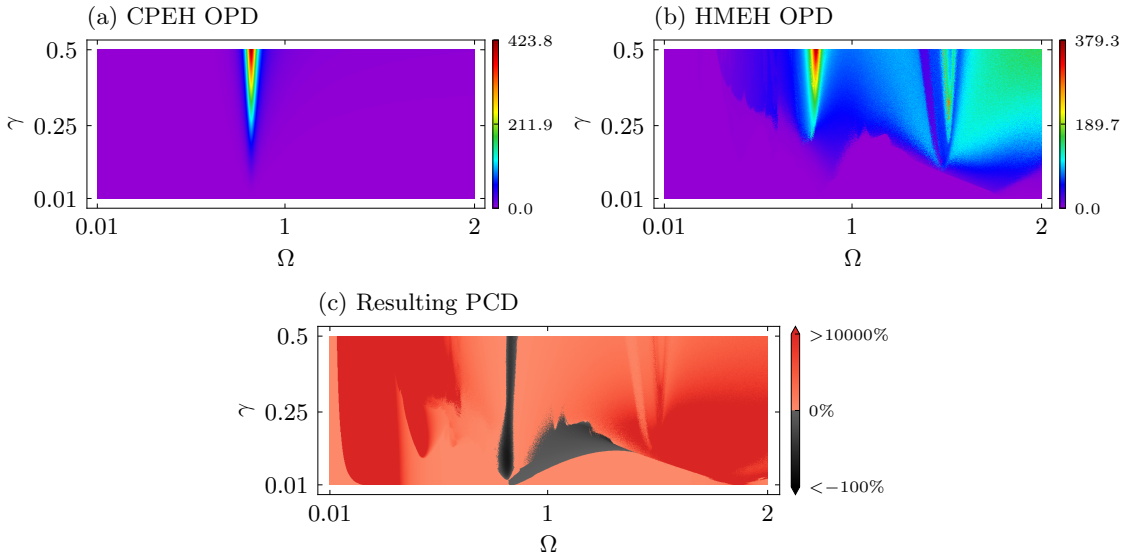

Figure 6.32: Comparison between the CPEH and HMEH performances. (a) OPD for the CPEH, (b) OPD for the HMEH, (c) resulting PCD. Rainbow colors represent $\bar{P}_{\text{avg}}$ of each harvester. Black and red colors represent the $\Delta\bar{P}(\%)$ value.

Finally, a performance comparison is performed between the MHEH best configuration in terms of bandwidth (Configuration 1) and its CPEH counterpart. The comparison is summarized in Figure 6.32, where Figure 6.32a shows the CPEH OPD and Figure 6.32b depicts the HMEH Configuration 1 OPD. By comparing both OPDs using the Performance Comparison Diagram (PCD), as described in Chapter 3, it is revealed that the HMEH indeed performs better than its linear counterpart in all regions of the studied $\gamma \times \Omega$ parameter domain, except for the z direction resonance region, characterized by a black strip around $\Omega = 0.85$, and a small region characterized by poor performance of both harvesters around $\Omega = 1$ and $0.01 \leq \gamma \leq 0.25$. It is important to highlight that the performance enhancement in regions far from $0.7 \leq \Omega \leq 1.3$ can achieve values of $\Delta\bar{P} \geq 10000\%$.

Chapter 7

Conclusions

This work proposes and presents the analysis of two types of mechanical energy harvesting devices. Each device is designed to address a current challenge in the field identified in the existing literature. The first device addresses the application of energy harvesting systems in limited available spaces while maintaining high performance through the exploitation of multistability characteristics. The design of the second device focuses on enabling multidirectional energy harvesting employing pendulum structures. The employment of hybrid transducer schemes to enable optimal performance of this type of structure is also discussed. All the analyses are conducted from a nonlinear dynamics perspective, developed to enhance the characterization of the dynamics and the performance of energy harvesting devices.

Initially, a comprehensive literature review is carried out, revealing the importance of this study by outlining the main devices already developed by other authors, elucidating the most notable nonlinear modulations used to enhance the performance of those devices, and identifying challenges in the field that still need addressing.

In the subsequent Chapter, the description of the methodology of analysis used throughout this thesis is addressed. The methodology is based on a nonlinear dynamics perspective and uses suitable complementary tools to build a robust analysis. These include Poincaré maps, Lyapunov exponents, linear stability theory, and basins of attraction. These tools are synergistically combined to develop a series of diagrams to map certain characteristics such as the type of motion, the occurrence of certain features, the robustness of a solution in a given scenario, and more. Through these diagrams-based analyses, a robust qualitative overview of the performance of these systems is achieved.

A generalization of the modeling of symmetric multistable systems is developed and summarized, which serves as a foundational step in the development of the model of the compact energy harvester presented in Chapter 5.

7.1 Conclusions on the Compact Multistable Energy Harvester

In Chapter 5, a new compact mechanical energy harvester is presented, aiming at applications with limited available spaces, while maintaining optimal performance. A multistable nonlinear structure is designed by incorporating key features of the classical bistable energy harvester and the bistable dual inner-outer beam structure previously described in the existing literature.

The proposed system integrates the compact arrangement of the dual beams, enhanced by magnetic interactions provided by two sets of magnets and transducers. These magnetic interactions provide unprecedented multistable characteristics to the system, and the usage of two transducers enables the advantageous utilization of free useful space within the structure to enhance energy harvesting capacity.

A 2-degrees-of-freedom electromechanical reduced-order model is developed, representing the main qualitative aspects of the proposed energy harvester. Magnetic interactions are modeled by polynomial Duffing-type terms, and the model is normalized to isolate key relationships between system parameters.

Stability analysis reveals that increasing the stiffness ratio and/or the mass ratio between beams can reduce the number of equilibrium points of the system at different rates. Also, by considering different magnetic restitution parameters (α_1, α_2, β_1, β_2), the system can achieve tetrastability (with four stable equilibria), various forms of bistability (with two stable equilibria), and monostability (with one stable equilibrium). Taking into account these differences, eight configurations are selected based on the magnetic setups coupled with different elastic properties for a comprehensive performance analysis.

7.1.1 On the General Overview of the Dynamics and Performance

Initially, the most complex configuration with $(\alpha_1, \alpha_2, \beta_1, \beta_2) = (-2, -1, 1, 1)$ is chosen, and a general overview of its characteristics within the external excitation parameter domain is displayed. For this magnetic setup, two configurations are selected for further dynamical and performance investigations: one with a softer inner beam, which characterizes a multistable state with 4 equilibrium points; and another with the outer and the inner beams with the same stiffness, characterizing a bistable state.

The dynamics of the two configurations are mapped within the external excitation parameter domain, showing rich and complex phenomena characterized by various periodic, chaotic and hyperchaotic orbits. The multistable configuration

predominantly exhibits period-1T, period-3T, and hyperchaotic orbits, while the bistable configuration additionally shows the emergence of chaotic regions. In both cases, period-2T relevant orbits also arise, but in smaller regions. Other types of dynamical responses are also found but not expressively.

The performance analysis revealed that the output electrical response of the first piezoelectric element is proportional to the displacement of the first degree of freedom, while the response of the second piezoelectric element is proportional to the relative displacement between the first and second degrees of freedom. Furthermore, it is observed that the harvester can display high output power when the system's deflection is sufficient to pass through or around all equilibrium points.

By analyzing additional configurations with different stiffness ratios, it is observed that for multistable configurations with 4 stable positions, period-3T orbits are associated with the majority of the points of maximum output power within the excitation parameter domain. In contrast, bistable configurations exhibit a wider range of dynamical responses (primarily period-1T, period-3T, chaotic and hyperchaotic orbits) for the major proportion of points of maximum output power. Additionally, an increase in performance at higher frequencies is observed as the stiffness ratio increases.

Furthermore, the analysis of the basins of attraction for the forced system in the configuration with 4 stable equilibrium positions highlights that operating under high-frequency and high-amplitude excitation conditions can result in the emergence of numerous coexisting solutions. In such scenarios, the predictability of the system's performance is reduced, emphasizing the imperative need to implement a control scheme to ensure good performance in these conditions. We believe that this characteristic holds for all other configurations analyzed in this work due to the system's construction and the similarity in its qualitative performance metrics. Nevertheless, in order to assert with absolute certainty, further detailed analyses of the remaining configurations must be carried out.

7.1.2 On the Performance Considering Different Magnetic Setups

Based on the stability analysis, the total eight key configurations with distinct characteristics were selected to represent all the possible configurations of the system. The analysis involving these configurations is divided into two aspects to evaluate the system's performance under low and high excitation levels.

Results show that for very low excitation levels, monostable configurations yield higher output powers but inferior bandwidths compared with bistable configurations. Conversely, bistable configurations exhibit superior bandwidths but lower

output power. Among the configurations, the tetrastable configuration performs the poorest in this scenario. However, for low to high excitation levels, configurations I (tetrastable) and II (bistable) associated with magnetic parameters (α_1, α_2, β_1, β_2) = (-2, -1, 1, 1) present superior performance in terms of maximum power output and bandwidth when compared to other configurations. The other bistable configurations exhibit similar performance when compared to each other. At very high excitation levels, the performance difference between bistable and tetrastable configurations reduces, as well as between monostable and bistable configurations. Nevertheless, all monostable configurations consistently underperform in scenarios with low to very high excitation levels.

Furthermore, the observed variations in system behavior across these different scenarios are closely tied to the input energy levels. Tetrastable and bistable configurations exhibit potential energy barriers, which under low mechanical excitation levels, cannot be overcome due to insufficient energy, limiting the displacement of these systems and resulting in poor performance. As the system is powered with enough mechanical energy, the multistable characteristics enhance the displacement of the system and its complexity, resulting in enhanced performance. Moreover, at high excitation levels, results indicate that the orbits demonstrating optimal performance consistently manifest as 1T attractors when occurring at intermediary frequency values and as 3T attractors when observed at higher frequency values. These attractors exhibit similar shapes.

7.1.3 Comparison Analysis and Final Considerations

Moreover, regions of interest within the parameter domain are identified based on energy harvesting performance. A comparison between eight different configurations of the proposed harvester and the classical bistable harvester is conducted. The proposed harvester exhibits comparable bandwidth to the classical bistable harvester while surpassing it in terms of output power in almost all operation scenarios of interest. Nevertheless, when considering the output power density, the superiority of the proposed harvester diminishes for specific operational conditions such as moderate performance regions, expressive multiple solution regions, and higher frequencies.

In conclusion, the qualitative analysis presented in this work suggests that the proposed harvester is a promising alternative for applications in closed compact spaces, offering significant advantages over the classical bistable energy harvester. For future works, experimental verification and further model improvements are being pursued to enhance robustness. These next steps can verify and strengthen the findings presented in this study, contributing to the strategies to enhance energy

harvesting capacity.

7.2 Conclusions on the Multidirectional Hybrid Energy Harvester

In Chapter 6, a novel hybrid multidirectional energy harvester is proposed. The new system employs a pendulum structure to achieve multidirectionality and multiple transduction mechanisms to enhance energy conversion. Specifically, a piezoelectric transducer is attached to the cantilever structure, and an electromagnetic transducer is incorporated into the rotational support of the pendulum. Three distinct harvesters of the same class are compared: (1) the classical piezoelectric energy harvester (CPEH), which converts energy in a single direction; (2) the multidirectional energy harvester (MPEH), comprising the same structure as the CPEH combined with a pendulum; and (3) the proposed multidirectional hybrid energy harvester (MHEH), being an evolution of the previous harvester.

A theoretical model is established to describe the main characteristics of the three harvesters and numerical simulations are carried out in order to compare their performances. Results demonstrate that the use of the pendulum structure to achieve efficient multidirectional conversion (utilizing the MPEH), is insufficient since it can work as a dynamical absorber, thereby reducing the system's overall performance when compared to its classic counterpart (CPEH). Alternatively, by employing the proposed MHEH, results show an impressive increase of performance in both maximum output power and bandwidth when compared to the CPEH, demonstrating that the proposed system not only retains the desirable characteristics of the MPEH but can also effectively address its limitations.

7.2.1 On the Role of the Electrical Parameters

The performance of the MHEH system is analyzed by examining the influence of key parameters. Initially, the optimal resistance parameters are identified in order to find the maximum output power regions of both transducers. Using the optimal resistance values, it is demonstrated that the ratio of electromechanical couplings ($\eta = \chi_{em}/\chi_{pz} = \kappa_{em}/\kappa_{pz}$) should be approximately 0.8 for both piezoelectric and electromagnetic transducers to effectively contribute to energy conversion. If this ratio is too low, the piezoelectric element dominates the energy conversion, whereas if η is too high, the electromagnetic transducer converts more energy than the piezoelectric element. Furthermore, it is observed that the electromagnetic transducer predominantly handles the energy conversion at low excitation amplitudes. Alternatively, the piezoelectric transducer takes precedence in energy conversion as the

excitation amplitudes increase. The influence of the natural frequencies of the structure (natural frequencies in each direction of the Cartesian plane) are evaluated and results show that a stiffer horizontal direction (perpendicular to the direction of gravity) enhances the bandwidth of the system.

7.2.2 On the Role of the Mechanical Parameters

Subsequently, a parametric analysis is conducted, focusing on two key structural parameters, Ω_s and Ω_ϕ, and two excitation parameters, γ and Ω. Ω_s represents the ratio between the natural frequencies of the beam structure, while Ω_ϕ represents the ratio between the linearized natural frequency of the pendulum element and the natural frequency in the piezoelectric polarized direction. Greater values of Ω_s represent wider beam widths (a stiffer direction perpendicular to the piezoelectric element), and vice versa, while greater values of Ω_ϕ represent pendulum elements with shorter lengths, and vice versa. γ represents the magnitude of external excitation, while Ω represents the frequency of external excitation.

Initially, system dynamics is assessed considering a specific external source, revealing complex types of periodic, quasi-periodic and aperiodic dynamical responses. Many of these dynamical attractors are characterized by the pendulum rotation, the pendulum oscillation around its equilibrium position, or mixed patterns where both oscillation and rotation occur.

Furthermore, it is demonstrated that a small change in any of the chosen four parameters can result in a complete change in the harvester's performance characteristics. As a result, an extensive array of 25×10^6 time series simulations are performed and compared to determine the best and the worst combination of structural parameters in terms of energy harvesting performance. Results show that configurations with greater values of Ω_s combined with small values of Ω_ϕ results in better performances regarding the operational bandwidth of the MHEH. In other words, configurations using beams with larger widths and wider pendulum lengths perform better than configurations with the opposite characteristics.

7.2.3 On the Comparison of Different Configurations

Afterward, it was observed that configurations with the best performances in terms of bandwidth demonstrated that both transducers contribute significantly to the overall energy conversion, but with the predominance of the electromagnetic transducer. Moreover, configurations that present balanced levels of contributions in energy conversion by both transducers were demonstrated to have shorter bandwidths with greater levels of maximum output power. Alternatively, configurations that show the predominance of the piezoelectric transducer demonstrated tiny band-

widths comparable to those presented by the CPEH in the literature. These configurations represent the worst-case scenario for the MHEH harvester.

A comparison among dynamical responses and patterns is carried out, showing that the majority of dynamical responses related to the overall higher performances are associated with hyperchaotic attractors with 68.5% of occurrence, followed by 1T attractors with 15.7% occurrence, and chaotic with 11.5% occurrence. 2T regular responses present a 3.1% of the total occurrences. Results suggest an association of larger operational bandwidths with the irregular dynamical pattern characterized by both oscillation and rotation of the pendulum (irregular mixed).

Finally, a comparison between the best HMEH configuration (Configuration 1) in terms of performance with its CPEH counterpart reveals a drastic increase in performance in almost all regions of the excitation parameter domain, except for the z direction resonance zone. In some regions, the increase in performance exceeds 10000%.

Overall, this study establishes the hybrid multidirectional energy harvester as a solution that maintains the desirable multidirectional characteristics while mitigating the drawbacks associated with attaching a pendulum without an associated transducer. Also, the analyses presented valuable insight into the structural characteristics of the MHEH to achieve higher performances in operational conditions that require multidirectional capabilities.

7.3 Final Considerations

This work underscores the importance of conducting extensive analysis based on a nonlinear dynamics perspective to map, quantify, and understand key design characteristics of energy harvesting systems. The nonlinear dynamics approach allows for a deeper exploration of the intrinsic complex behaviors and interactions of these systems, leading to more efficient and robust designs. This is particularly relevant in the current in the current decade, where high-performance computing is widely accessible. Furthermore, this type of analysis is recommended not only for numerical investigations but also for experimental studies, as the techniques presented are applicable to practical scenarios.

Moving forward, a high-performance, user-friendly software package is currently being developed. This package will include all the essential tools for analyzing energy harvesters and other dynamical systems using the proposed method. The intention is to release this software as an open-source package for the benefit of the scientific community. At the same time, experimental studies on the proposed energy harvesters are also underway.

References

[1] WU, H., TANG, L., YANG, Y., et al. "A novel two-degrees-of-freedom piezoelectric energy harvester", *Journal of Intelligent Material Systems and Structures*, v. 24, n. 3, pp. 357–368, 2013. doi: 10.1177/1045389X12457254. Available at: <https://doi.org/10.1177/1045389X12457254>.

[2] WU, H., TANG, L., YANG, Y., et al. "Development of a broadband nonlinear two-degree-of-freedom piezoelectric energy harvester", *Journal of Intelligent Material Systems and Structures*, v. 25, n. 14, pp. 1875–1889, 2014. doi: 10.1177/1045389X14541494. Available at: <https://doi.org/10.1177/1045389X14541494>.

[3] COSTA, L. G., DA SILVA MONTEIRO, L. L., SAVI, M. A. "Chaos and Hyperchaos in a Two-Degree of Freedom Duffing Oscillator". In: *Proceedings of the 26th International Congress of Mechanical Engineering*, Virtual Congress, November 2021. doi: 10.26678/ABCM.COBEM2021.COB2021-0402. Available at: <http://abcm.org.br/anais-de-eventos/COB2021/0402>.

[4] MOON, F. C. *Chaotic and fractal dynamics: introduction for applied scientists and engineers*. Federal Republic of Germany, John Wiley & Sons, 1992.

[5] ERTURK, A., INMAN, D. "Broadband piezoelectric power generation on high-energy orbits of the bistable Duffing oscillator with electromechanical coupling", *Journal of Sound and Vibration*, v. 330, n. 10, pp. 2339–2353, 2011. ISSN: 0022-460X. doi: 10.1016/j.jsv.2010.11.018. Available at: <https://www.sciencedirect.com/science/article/pii/S0022460X10007807>. Dynamics of Vibro-Impact Systems.

[6] DE PAULA, A. S., INMAN, D. J., SAVI, M. A. "Energy harvesting in a nonlinear piezomagnetoelastic beam subjected to random excitation", *Mechanical Systems and Signal Processing*, v. 54-55, pp. 405–416, 2015. ISSN: 0888-3270. doi: 10.1016/j.ymssp.2014.08.020. Available at: <https://www.sciencedirect.com/science/article/pii/S0888327014003379>.

[7] BOSE, B. K. "Global Warming: Energy, Environmental Pollution, and the Impact of Power Electronics", *IEEE Industrial Electronics Magazine*, v. 4, n. 1, pp. 6–17, 2010. doi: 10.1109/MIE.2010.935860.

[8] VIOLA, F. M., PAIVA, S. L., SAVI, M. A. "Analysis of the global warming dynamics from temperature time series", *Ecological Modelling*, v. 221, n. 16, pp. 1964–1978, 2010. ISSN: 0304-3800. doi: 10.1016/j.ecolmodel.2010.05.001. Available at: <https://www.sciencedirect.com/science/article/pii/S0304380010002401>.

[9] ZHU, J., LIU, X., SHI, Q., et al. "Development Trends and Perspectives of Future Sensors and MEMS/NEMS", *Micromachines*, v. 11, n. 1, 2020. ISSN: 2072-666X. doi: 10.3390/mi11010007. Available at: <https://www.mdpi.com/2072-666X/11/1/7>.

[10] DAQAQ, M. F., CRESPO, R. S., HA, S. "On the efficacy of charging a battery using a chaotic energy harvester", *Nonlinear Dynamics*, v. 99, n. 2, pp. 1525–1537, Jan 2020. ISSN: 1573-269X. doi: 10.1007/s11071-019-05372-0. Available at: <https://doi.org/10.1007/s11071-019-05372-0>.

[11] TOPRAK, A., TIGLI, O. "Piezoelectric energy harvesting: State-of-the-art and challenges", *Applied Physics Reviews*, v. 1, n. 3, pp. 031104, 2014. doi: 10.1063/1.4896166. Available at: <https://doi.org/10.1063/1.4896166>.

[12] AABID, A., RAHEMAN, M. A., IBRAHIM, Y. E., et al. "A Systematic Review of Piezoelectric Materials and Energy Harvesters for Industrial Applications", *Sensors*, v. 21, n. 12, 2021. ISSN: 1424-8220. doi: 10.3390/s21124145. Available at: <https://www.mdpi.com/1424-8220/21/12/4145>.

[13] WILLIAMS, C., YATES, R. "Analysis Of A Micro-electric Generator For Microsystems". In: *Proceedings of the International Solid-State Sensors and Actuators Conference - TRANSDUCERS '95*, v. 1, pp. 369–372, 1995. doi: 10.1109/SENSOR.1995.717207.

[14] WILLIAMS, C., YATES, R. "Analysis of a micro-electric generator for microsystems", *Sensors and Actuators A: Physical*, v. 52, n. 1, pp. 8–11, 1996. ISSN: 0924-4247. doi: 10.1016/0924-4247(96)80118-X. Available at: <https://www.sciencedirect.com/science/article/pii/092442479680118X>. Proceedings of the 8th International Conference on Solid-State Sensors and Actuators Eurosensors IX.

[15] ERTURK, A. "Piezoelectric energy harvesting for civil infrastructure system applications: Moving loads and surface strain fluctuations", *Journal of Intelligent Material Systems and Structures*, v. 22, n. 17, pp. 1959–1973, 2011. doi: 10.1177/1045389X11420593. Available at: <https://doi.org/10.1177/1045389X11420593>.

[16] ZHANG, Z., XIANG, H., SHI, Z., et al. "Experimental investigation on piezoelectric energy harvesting from vehicle-bridge coupling vibration", *Energy Conversion and Management*, v. 163, pp. 169–179, 2018. ISSN: 0196-8904. doi: 10.1016/j.enconman.2018.02.054. Available at: <https://www.sciencedirect.com/science/article/pii/S019689041830164X>.

[17] JEON, D. H., CHO, J. Y., JHUN, J. P., et al. "A lever-type piezoelectric energy harvester with deformation-guiding mechanism for electric vehicle charging station on smart road", *Energy*, v. 218, pp. 119540, 2021. ISSN: 0360-5442. doi: 10.1016/j.energy.2020.119540. Available at: <https://www.sciencedirect.com/science/article/pii/S0360544220326475>.

[18] WANG, C., SONG, Z., GAO, Z., et al. "Preparation and performance research of stacked piezoelectric energy-harvesting units for pavements", *Energy and Buildings*, v. 183, pp. 581–591, 2019. ISSN: 0378-7788. doi: 10.1016/j.enbuild.2018.11.042. Available at: <https://www.sciencedirect.com/science/article/pii/S0378778818324435>.

[19] XIANG, H. J., WANG, J. J., SHI, Z. F., et al. "Theoretical analysis of piezoelectric energy harvesting from traffic induced deformation of pavements", *Smart Materials and Structures*, v. 22, n. 9, pp. 095024, aug 2013. doi: 10.1088/0964-1726/22/9/095024. Available at: <https://dx.doi.org/10.1088/0964-1726/22/9/095024>.

[20] SOLBAN, M. M., MOUSSA, R. R. "Piezoelectric Tiles Is a Sustainable Approach for Designing Interior Spaces and Creating Self-Sustain Projects." *IOP Conference Series: Earth and Environmental Science*, v. 397, n. 1, pp. 012020, nov 2019. doi: 10.1088/1755-1315/397/1/012020. Available at: <https://dx.doi.org/10.1088/1755-1315/397/1/012020>.

[21] ELHALWAGY, A. M., GHONEEM, M. Y. M., ELHADIDI, M. "Feasibility Study for Using Piezoelectric Energy Harvesting Floor in Buildings' Interior Spaces", *Energy Procedia*, v. 115, pp. 114–126, 2017. ISSN: 1876-6102. doi: 10.1016/j.egypro.2017.05.012. Available at: <https://www.sciencedirect.com/science/article/pii/S1876610217322117>. Inter-

national Conference – Alternative and Renewable Energy Quest, AREQ 2017, 1-3 February 2017, Spain.

[22] DEMARTINO, C., QUARANTA, G., MARUCCIO, C., et al. "Feasibility of energy harvesting from vertical pedestrian-induced vibrations of footbridges for smart monitoring applications", *Computer-Aided Civil and Infrastructure Engineering*, v. 37, n. 8, pp. 1044–1065, 2022. doi: 10.1111/mice.12777. Available at: <https://onlinelibrary.wiley.com/doi/abs/10.1111/mice.12777>.

[23] ABASIAN, A., TABESH, A., NEZHAD, A. Z., et al. "Design Optimization of an Energy Harvesting Platform for Self-Powered Wireless Devices in Monitoring of AC Power Lines", *IEEE Transactions on Power Electronics*, v. 33, n. 12, pp. 10308–10316, 2018. doi: 10.1109/TPEL.2017.2775961.

[24] ABASIAN, A., TABESH, A., REZAEI-HOSSEINABADI, N., et al. "Vacuum-Packaged Piezoelectric Energy Harvester for Powering Smart Grid Monitoring Devices", *IEEE Transactions on Industrial Electronics*, v. 66, n. 6, pp. 4447–4456, 2019. doi: 10.1109/TIE.2018.2860557.

[25] LUO, A., XU, W., SUN, J., et al. "Vibration energy harvester with double frequency-up conversion mechanism for self-powered sensing system in smart city", *Nano Energy*, v. 105, pp. 108030, 2023. ISSN: 2211-2855. doi: 10.1016/j.nanoen.2022.108030. Available at: <https://www.sciencedirect.com/science/article/pii/S2211285522011089>.

[26] LI, F., DENG, C., SUN, M., et al. "A self-powered triboelectric negative ion generator in pipeline", *Nano Energy*, v. 112, pp. 108459, 2023. ISSN: 2211-2855. doi: 10.1016/j.nanoen.2023.108459. Available at: <https://www.sciencedirect.com/science/article/pii/S2211285523002963>.

[27] LI, Z., ZHU, G., YANG, R., et al. "Muscle-Driven In Vivo Nanogenerator", *Advanced Materials*, v. 22, n. 23, pp. 2534–2537, 2010. doi: 10.1002/adma.200904355. Available at: <https://onlinelibrary.wiley.com/doi/abs/10.1002/adma.200904355>.

[28] DAGDEVIREN, C., YANG, B. D., SU, Y., et al. "Conformal piezoelectric energy harvesting and storage from motions of the heart, lung, and diaphragm", *Proceedings of the National Academy of Sciences*, v. 111, n. 5, pp. 1927–1932, 2014. doi: 10.1073/pnas.1317233111. Available at: <https://www.pnas.org/doi/abs/10.1073/pnas.1317233111>.

[29] BANI-HANI, M., KROVI, V., KARAMI, M. A. "Modeling of a beam with a mass in the middle for heart beat vibration energy harvesting". In: *International Design Engineering Technical Conferences and Computers and Information in Engineering Conference*, v. 46414, p. V008T11A092. American Society of Mechanical Engineers, 2014.

[30] KIM, D. H., SHIN, H. J., LEE, H., et al. "In Vivo Self-Powered Wireless Transmission Using Biocompatible Flexible Energy Harvesters", *Advanced Functional Materials*, v. 27, n. 25, pp. 1700341, 2017. doi: 10.1002/adfm.201700341. Available at: <https://onlinelibrary.wiley.com/doi/abs/10.1002/adfm.201700341>.

[31] PARK, D. Y., JOE, D. J., KIM, D. H., et al. "Self-Powered Real-Time Arterial Pulse Monitoring Using Ultrathin Epidermal Piezoelectric Sensors", *Advanced Materials*, v. 29, n. 37, pp. 1702308, 2017. doi: 10.1002/adma.201702308. Available at: <https://onlinelibrary.wiley.com/doi/abs/10.1002/adma.201702308>.

[32] HWANG, G.-T., KIM, Y., LEE, J.-H., et al. "Self-powered deep brain stimulation via a flexible PIMNT energy harvester", *Energy Environ. Sci.*, v. 8, pp. 2677–2684, 2015. doi: 10.1039/C5EE01593F. Available at: <http://dx.doi.org/10.1039/C5EE01593F>.

[33] LI, H., LU, J., MYJAK, M. J., et al. "An implantable biomechanical energy harvester for animal monitoring devices", *Nano Energy*, v. 98, pp. 107290, 2022. ISSN: 2211-2855. doi: 10.1016/j.nanoen.2022.107290. Available at: <https://www.sciencedirect.com/science/article/pii/S221128552200369X>.

[34] SHAFER, M. W., MACCURDY, R., SHIPLEY, J. R., et al. "The case for energy harvesting on wildlife in flight", *Smart Materials and Structures*, v. 24, n. 2, pp. 025031, jan 2015. doi: 10.1088/0964-1726/24/2/025031. Available at: <https://dx.doi.org/10.1088/0964-1726/24/2/025031>.

[35] REISSMAN, T., MACCURDY, R. B., GARCIA, E. "Electrical power generation from insect flight". In: Ghasemi-Nejhad, M. N. (Ed.), *Active and Passive Smart Structures and Integrated Systems 2011*, v. 7977, p. 797702. International Society for Optics and Photonics, SPIE, 2011. doi: 10.1117/12.880702. Available at: <https://doi.org/10.1117/12.880702>.

[36] AKTAKKA, E. E., KIM, H., NAJAFI, K. "Energy scavenging from insect flight", *Journal of Micromechanics and Microengineering*, v. 21, n. 9,

pp. 095016, aug 2011. doi: 10.1088/0960-1317/21/9/095016. Available at: <https://dx.doi.org/10.1088/0960-1317/21/9/095016>.

[37] DELNAVAZ, A., VOIX, J. "Flexible piezoelectric energy harvesting from jaw movements", *Smart Materials and Structures*, v. 23, n. 10, pp. 105020, sep 2014. doi: 10.1088/0964-1726/23/10/105020. Available at: <https://dx.doi.org/10.1088/0964-1726/23/10/105020>.

[38] YANG, Q., WANG, D., ZHANG, M., et al. "Lead-free (Na0.83K0.17)0.5Bi0.5TiO3 nanofibers for wearable piezoelectric nanogenerators", *Journal of Alloys and Compounds*, v. 688, pp. 1066–1071, 2016. ISSN: 0925-8388. doi: 10.1016/j.jallcom.2016.07.131. Available at: <https://www.sciencedirect.com/science/article/pii/S092583881632165X>.

[39] POZZI, M., ZHU, M. "Plucked piezoelectric bimorphs for knee-joint energy harvesting: modelling and experimental validation", *Smart Materials and Structures*, v. 20, n. 5, pp. 055007, apr 2011. doi: 10.1088/0964-1726/20/5/055007. Available at: <https://dx.doi.org/10.1088/0964-1726/20/5/055007>.

[40] MEIER, R., KELLY, N., ALMOG, O., et al. "A piezoelectric energy-harvesting shoe system for podiatric sensing". In: *2014 36th Annual International Conference of the IEEE Engineering in Medicine and Biology Society*, pp. 622–625. IEEE, 2014.

[41] XIAO, Y., NIU, M., YANG, L., et al. "Integrated Triboelectric-Electromagnetic-Piezoelectric Self-Rebounding Energy Harvester for Human Energy Harvesting", *Advanced Materials Technologies*, v. 7, n. 11, pp. 2200340, 2022. doi: 10.1002/admt.202200340. Available at: <https://onlinelibrary.wiley.com/doi/abs/10.1002/admt.202200340>.

[42] HALIM, M., RANTZ, R., ZHANG, Q., et al. "Electromagnetic energy harvesting from swing-arm motion using rotational eccentric mass structure". In: *2017 19th international conference on solid-state sensors, actuators and microsystems (TRANSDUCERS)*, pp. 1863–1866. IEEE, 2017.

[43] CAI, M., LIAO, W.-H. "Design, Modeling, and Experiments of Electromagnetic Energy Harvester Embedded in Smart Watch and Wristband as Power Source", *IEEE/ASME Transactions on Mechatronics*, v. 26, n. 4, pp. 2104–2114, 2021. doi: 10.1109/TMECH.2020.3032536.

[44] LI, X., MENG, J., YANG, C., et al. "A Magnetically Coupled Electromagnetic Energy Harvester with Low Operating Frequency for Human Body Kinetic Energy", *Micromachines*, v. 12, n. 11, 2021. ISSN: 2072-666X. doi: 10.3390/mi12111300. Available at: <https://www.mdpi.com/2072-666X/12/11/1300>.

[45] ZHAO, L.-C., ZOU, H.-X., GAO, Q.-H., et al. "Magnetically modulated orbit for human motion energy harvesting", *Applied Physics Letters*, v. 115, n. 26, pp. 263902, 12 2019. ISSN: 0003-6951. doi: 10.1063/1.5131193. Available at: <https://doi.org/10.1063/1.5131193>.

[46] ZHOU, N., HOU, Z., ZHANG, Y., et al. "Enhanced swing electromagnetic energy harvesting from human motion", *Energy*, v. 228, pp. 120591, 2021. ISSN: 0360-5442. doi: 10.1016/j.energy.2021.120591. Available at: <https://www.sciencedirect.com/science/article/pii/S0360544221008409>.

[47] SHARGHI, H., BILGEN, O. "Energy Harvesting from Human Walking Motion using Pendulum-based Electromagnetic Generators", *Journal of Sound and Vibration*, v. 534, pp. 117036, 2022. ISSN: 0022-460X. doi: 10.1016/j.jsv.2022.117036. Available at: <https://www.sciencedirect.com/science/article/pii/S0022460X22002541>.

[48] TIAN, W., SHI, Y., CUI, H., et al. "Research on piezoelectric energy harvester based on coupled oscillator model for vehicle vibration utilizing a L-shaped cantilever beam", *Smart Materials and Structures*, v. 29, n. 7, pp. 075014, jun 2020. doi: 10.1088/1361-665X/ab87e1. Available at: <https://dx.doi.org/10.1088/1361-665X/ab87e1>.

[49] LIU, H., DONG, W., CHANG, Y., et al. "Working characteristics of a magnetostrictive vibration energy harvester for rotating car wheels", *Review of Scientific Instruments*, v. 93, n. 5, pp. 055001, 05 2022. ISSN: 0034-6748. doi: 10.1063/5.0078131. Available at: <https://doi.org/10.1063/5.0078131>.

[50] YAO, M., WANG, X., WU, Q., et al. "Dynamic analysis and design of power management circuit of the nonlinear electromagnetic energy harvesting device for the automobile suspension", *Mechanical Systems and Signal Processing*, v. 170, pp. 108831, 2022. ISSN: 0888-3270. doi: 10.1016/j.ymssp.2022.108831. Available at: <https://www.sciencedirect.com/science/article/pii/S0888327022000280>.

[51] TAVARES, R., RUDERMAN, M. "Energy harvesting using piezoelectric transducers for suspension systems", *Mechatronics*, v. 65,

pp. 102294, 2020. ISSN: 0957-4158. doi: 10.1016/j.mechatronics.2019.102294. Available at: <https://www.sciencedirect.com/science/article/pii/S0957415819301266>.

[52] LEE, J., CHOI, B. "Development of a piezoelectric energy harvesting system for implementing wireless sensors on the tires", *Energy Conversion and Management*, v. 78, pp. 32–38, 2014. ISSN: 0196-8904. doi: 10.1016/j.enconman.2013.09.054. Available at: <https://www.sciencedirect.com/science/article/pii/S0196890413006158>.

[53] FANG, Z., TAN, X., LIU, G., et al. "A novel vibration energy harvesting system integrated with an inertial pendulum for zero-energy sensor applications in freight trains", *Applied Energy*, v. 318, pp. 119197, 2022. ISSN: 0306-2619. doi: 10.1016/j.apenergy.2022.119197. Available at: <https://www.sciencedirect.com/science/article/pii/S0306261922005657>.

[54] DOTTI, F. E., SOSA, M. D. "Pendulum systems for harvesting vibration energy from railroad tracks and sleepers during the passage of a high-speed train: A feasibility evaluation", *Theoretical and Applied Mechanics Letters*, v. 9, n. 4, pp. 229–235, 2019. ISSN: 2095-0349. doi: 10.1016/j.taml.2019.03.005. Available at: <https://www.sciencedirect.com/science/article/pii/S2095034919300406>.

[55] NABAVI, S. F., FARSHIDIANFAR, A., AFSHARFARD, A. "Novel piezoelectric-based ocean wave energy harvesting from offshore buoys", *Applied Ocean Research*, v. 76, pp. 174–183, 2018. ISSN: 0141-1187. doi: 10.1016/j.apor.2018.05.005. Available at: <https://www.sciencedirect.com/science/article/pii/S0141118717306338>.

[56] WANG, H., ZHU, C., WANG, W., et al. "A Stackable Triboelectric Nanogenerator for Wave-Driven Marine Buoys", *Nanomaterials*, v. 12, n. 4, 2022. ISSN: 2079-4991. doi: 10.3390/nano12040594. Available at: <https://www.mdpi.com/2079-4991/12/4/594>.

[57] ZHAO, L.-C., ZOU, H.-X., XIE, X., et al. "Mechanical intelligent wave energy harvesting and self-powered marine environment monitoring", *Nano Energy*, v. 108, pp. 108222, 2023. ISSN: 2211-2855. doi: 10.1016/j.nanoen.2023.108222. Available at: <https://www.sciencedirect.com/science/article/pii/S2211285523000587>.

[58] TAO, K., YI, H., YANG, Y., et al. "Origami-inspired electret-based triboelectric generator for biomechanical and ocean wave energy harvesting", *Nano Energy*, v. 67, pp. 104197, 2020. ISSN: 2211-2855. doi:

10.1016/j.nanoen.2019.104197. Available at: <https://www.sciencedirect.com/science/article/pii/S2211285519309048>.

[59] SILVA, L. L., MONTEIRO, P., SAVI, M. A., et al. "Piezoelectric Vibration-Based Energy Harvesters for Oil and Gas Applications". In: *International Conference on Offshore Mechanics and Arctic Engineering*, v. 56581, p. V010T11A031. American Society of Mechanical Engineers, 2015.

[60] GHODSI, M., ZIAIEFAR, H., MOHAMMADZAHERI, M., et al. "Development of Magnetostrictive Harvester for Unmanned Aerial Vehicles (UAV)". In: *2019 1st International Conference on Unmanned Vehicle Systems-Oman (UVS)*, pp. 1–6. IEEE, 2019.

[61] PEREZ, M., BILLON, K., GERGES, T., et al. "Vibration energy harvesting on a drone quadcopter based on piezoelectric structures", *Mechanics & Industry*, v. 23, pp. 20, 2022. doi: 10.1051/meca/2022021. Available at: <https://www.mechanics-industry.org/articles/meca/full_html/2022/01/mi220019/mi220019.html>.

[62] LI, D., WU, Y., DA RONCH, A., et al. "Energy harvesting by means of flow-induced vibrations on aerospace vehicles", *Progress in Aerospace Sciences*, v. 86, pp. 28–62, 2016. ISSN: 0376-0421. doi: 10.1016/j.paerosci.2016.08.001. Available at: <https://www.sciencedirect.com/science/article/pii/S0376042116300057>.

[63] XU, T.-B. "Energy harvesting using piezoelectric materials in aerospace structures". In: Yuan, F.-G. (Ed.), *Structural Health Monitoring (SHM) in Aerospace Structures*, Woodhead Publishing, pp. 175–212, Cambridge, United Kingdom, 2016. ISBN: 978-0-08-100148-6. doi: 10.1016/B978-0-08-100148-6.00007-X. Available at: <https://www.sciencedirect.com/science/article/pii/B978008100148600007X>.

[64] TRAN, N., GHAYESH, M. H., ARJOMANDI, M. "Ambient vibration energy harvesters: A review on nonlinear techniques for performance enhancement", *International Journal of Engineering Science*, v. 127, pp. 162–185, 2018. ISSN: 0020-7225. doi: 10.1016/j.ijengsci.2018.02.003. Available at: <https://www.sciencedirect.com/science/article/pii/S0020722517327830>.

[65] COSTA, L. G., DA SILVA MONTEIRO, L. L., PACHECO, P. M. C. L., et al. "A parametric analysis of the nonlinear dynamics of bistable vibration-based piezoelectric energy harvesters", *Journal of Intelligent*

Material Systems and Structures, v. 32, n. 7, pp. 699–723, 2021. doi: 10.1177/1045389X20963188. Available at: <https://doi.org/10.1177/1045389X20963188>.

[66] BOUHEDMA, S., ZHENG, Y., LANGE, F., et al. "Magnetic Frequency Tuning of a Multimodal Vibration Energy Harvester", *Sensors*, v. 19, n. 5, 2019. ISSN: 1424-8220. doi: 10.3390/s19051149. Available at: <https://www.mdpi.com/1424-8220/19/5/1149>.

[67] ZHAO, L., TANG, L., YANG, Y. "Enhanced piezoelectric galloping energy harvesting using 2 degree-of-freedom cut-out cantilever with magnetic interaction", *Japanese Journal of Applied Physics*, v. 53, n. 6, pp. 060302, may 2014. doi: 10.7567/JJAP.53.060302. Available at: <https://dx.doi.org/10.7567/JJAP.53.060302>.

[68] DUTOIT, N. E., WARDLE, B. L., KIM, S.-G. "DESIGN CONSIDERATIONS FOR MEMS-SCALE PIEZOELECTRIC MECHANICAL VIBRATION ENERGY HARVESTERS", *Integrated Ferroelectrics*, v. 71, n. 1, pp. 121–160, 2005. doi: 10.1080/10584580590964574. Available at: <https://doi.org/10.1080/10584580590964574>.

[69] CURIE, P. "Dilatation électrique du quartz", *J. Phys. Theor. Appl.*, v. 8, n. 1, pp. 149–168, 1889.

[70] MASON, W. P. "Piezoelectricity, its history and applications", *The Journal of the Acoustical Society of America*, v. 70, n. 6, pp. 1561–1566, 12 1981. ISSN: 0001-4966. doi: 10.1121/1.387221. Available at: <https://doi.org/10.1121/1.387221>.

[71] CLEMENTI, G., COTTONE, F., DI MICHELE, A., et al. "Review on Innovative Piezoelectric Materials for Mechanical Energy Harvesting", *Energies*, v. 15, n. 17, 2022. ISSN: 1996-1073. doi: 10.3390/en15176227. Available at: <https://www.mdpi.com/1996-1073/15/17/6227>.

[72] LEO, D. *Engineering Analysis of Smart Material Systems*. Wiley InterScience. New Jersey, Wiley, 2007. ISBN: 9780471684770. Available at: <https://books.google.com.br/books?id=jGAvKfLykNsC>.

[73] ANSI/IEEE. "IEEE standard on piezoelectricity". 1987.

[74] FARADAY, M. "V. Experimental researches in electricity", *Philosophical Transactions of the Royal Society of London*, v. 122, pp. 125–162, 1832. doi: 10.1098/rstl.1832.0006. Available at: <https://royalsocietypublishing.org/doi/abs/10.1098/rstl.1832.0006>.

[75] MAXWELL, J. C. "VIII. A dynamical theory of the electromagnetic field", *Philosophical Transactions of the Royal Society of London*, v. 155, pp. 459–512, 1865. doi: 10.1098/rstl.1865.0008. Available at: <https://royalsocietypublishing.org/doi/abs/10.1098/rstl.1865.0008>.

[76] CHUA, L. "Memristor-The missing circuit element", *IEEE Transactions on Circuit Theory*, v. 18, n. 5, pp. 507–519, 1971. doi: 10.1109/TCT.1971.1083337.

[77] LIU, L., GUO, X., LIU, W., et al. "Recent Progress in the Energy Harvesting Technology—From Self-Powered Sensors to Self-Sustained IoT, and New Applications", *Nanomaterials*, v. 11, n. 11, 2021. ISSN: 2079-4991. doi: 10.3390/nano11112975. Available at: <https://www.mdpi.com/2079-4991/11/11/2975>.

[78] ZHENG, Q., SHI, B., LI, Z., et al. "Recent Progress on Piezoelectric and Triboelectric Energy Harvesters in Biomedical Systems", *Advanced Science*, v. 4, n. 7, pp. 1700029, 2017. doi: 10.1002/advs.201700029. Available at: <https://onlinelibrary.wiley.com/doi/abs/10.1002/advs.201700029>.

[79] XU, C., ZI, Y., WANG, A. C., et al. "On the Electron-Transfer Mechanism in the Contact-Electrification Effect", *Advanced Materials*, v. 30, n. 15, pp. 1706790, 2018. doi: 10.1002/adma.201706790. Available at: <https://onlinelibrary.wiley.com/doi/abs/10.1002/adma.201706790>.

[80] TIAN, J., CHEN, X., WANG, Z. L. "Environmental energy harvesting based on triboelectric nanogenerators", *Nanotechnology*, v. 31, n. 24, pp. 242001, mar 2020. doi: 10.1088/1361-6528/ab793e. Available at: <https://dx.doi.org/10.1088/1361-6528/ab793e>.

[81] WANG, Z. L., JIANG, T., XU, L. "Toward the blue energy dream by triboelectric nanogenerator networks", *Nano Energy*, v. 39, pp. 9–23, 2017. ISSN: 2211-2855. doi: 10.1016/j.nanoen.2017.06.035. Available at: <https://www.sciencedirect.com/science/article/pii/S2211285517303890>.

[82] WANG, Z. L., LIN, L., CHEN, J., et al. *Triboelectric Nanogenerators*. Cham, Springer International Publishing, 2016. ISBN: 978-3-319-40039-6. doi: 10.1007/978-3-319-40039-6_3. Available at: <https://doi.org/10.1007/978-3-319-40039-6_3>.

[83] ZOU, Y., RAVEENDRAN, V., CHEN, J. "Wearable triboelectric nanogenerators for biomechanical energy harvesting", *Nano Energy*, v. 77, pp. 105303, 2020. ISSN: 2211-2855. doi: 10.1016/j.nanoen.2020.

105303. Available at: <https://www.sciencedirect.com/science/article/pii/S2211285520308806>.

[84] ZHANG, B., ZHANG, L., DENG, W., et al. "Self-Powered Acceleration Sensor Based on Liquid Metal Triboelectric Nanogenerator for Vibration Monitoring", *ACS Nano*, v. 11, n. 7, pp. 7440–7446, Jul 2017. ISSN: 1936-0851. doi: 10.1021/acsnano.7b03818. Available at: <https://doi.org/10.1021/acsnano.7b03818>.

[85] ESQ., J. J. "XVII. On the effects of magnetism upon the dimensions of iron and steel bars", *The London, Edinburgh, and Dublin Philosophical Magazine and Journal of Science*, v. 30, n. 199, pp. 76–87, 1847. doi: 10.1080/14786444708645656. Available at: <https://doi.org/10.1080/14786444708645656>.

[86] APICELLA, V., CLEMENTE, C. S., DAVINO, D., et al. "Review of Modeling and Control of Magnetostrictive Actuators", *Actuators*, v. 8, n. 2, 2019. ISSN: 2076-0825. doi: 10.3390/act8020045. Available at: <https://www.mdpi.com/2076-0825/8/2/45>.

[87] NARITA, F., FOX, M. "A Review on Piezoelectric, Magnetostrictive, and Magnetoelectric Materials and Device Technologies for Energy Harvesting Applications", *Advanced Engineering Materials*, v. 20, n. 5, pp. 1700743, 2018. doi: 10.1002/adem.201700743. Available at: <https://onlinelibrary.wiley.com/doi/abs/10.1002/adem.201700743>.

[88] IEEE. "IEEE Standard on Magnetostrictive Materials: Piezomagnetic Nomenclature". 1991.

[89] TANG, X., WANG, X., CATTLEY, R., et al. "Energy Harvesting Technologies for Achieving Self-Powered Wireless Sensor Networks in Machine Condition Monitoring: A Review", *Sensors*, v. 18, n. 12, 2018. ISSN: 1424-8220. doi: 10.3390/s18124113. Available at: <https://www.mdpi.com/1424-8220/18/12/4113>.

[90] YANG, Z., ZHOU, S., ZU, J., et al. "High-performance piezoelectric energy harvesters and their applications", *Joule*, v. 2, n. 4, pp. 642–697, 2018.

[91] SAFAEI, M., SODANO, H. A., ANTON, S. R. "A review of energy harvesting using piezoelectric materials: state-of-the-art a decade later (2008–2018)", *Smart Materials and Structures*, v. 28, n. 11, pp. 113001, oct 2019. doi: 10.1088/1361-665X/ab36e4. Available at: <https://dx.doi.org/10.1088/1361-665X/ab36e4>.

[92] ARNOLD, D. P. "Review of Microscale Magnetic Power Generation", *IEEE Transactions on Magnetics*, v. 43, n. 11, pp. 3940–3951, 2007. doi: 10.1109/TMAG.2007.906150.

[93] CEPNIK, C., LAUSECKER, R., WALLRABE, U. "Review on Electrodynamic Energy Harvesters—A Classification Approach", *Micromachines*, v. 4, n. 2, pp. 168–196, 2013. ISSN: 2072-666X. doi: 10.3390/mi4020168. Available at: <https://www.mdpi.com/2072-666X/4/2/168>.

[94] MUSCAT, A., BHATTACHARYA, S., ZHU, Y. "Electromagnetic Vibrational Energy Harvesters: A Review", *Sensors*, v. 22, n. 15, 2022. ISSN: 1424-8220. doi: 10.3390/s22155555. Available at: <https://www.mdpi.com/1424-8220/22/15/5555>.

[95] TAN, Y., DONG, Y., WANG, X. "Review of MEMS Electromagnetic Vibration Energy Harvester", *Journal of Microelectromechanical Systems*, v. 26, n. 1, pp. 1–16, 2017. doi: 10.1109/JMEMS.2016.2611677.

[96] ZHU, G., PENG, B., CHEN, J., et al. "Triboelectric nanogenerators as a new energy technology: From fundamentals, devices, to applications", *Nano Energy*, v. 14, pp. 126–138, 2015. ISSN: 2211-2855. doi: 10.1016/j.nanoen.2014.11.050. Available at: <https://www.sciencedirect.com/science/article/pii/S2211285514002584>. Special issue on the 2nd International Conference on Nanogenerators and Piezotronics (NGPT 2014).

[97] HAN, J., XU, N., LIANG, Y., et al. "Paper-based triboelectric nanogenerators and their applications: a review", *Beilstein Journal of Nanotechnology*, v. 12, pp. 151–171, 2021. ISSN: 2190-4286. doi: 10.3762/bjnano.12.12. Available at: <https://doi.org/10.3762/bjnano.12.12>.

[98] HAROUN, A., TAREK, M., MOSLEH, M., et al. "Recent Progress on Triboelectric Nanogenerators for Vibration Energy Harvesting and Vibration Sensing", *Nanomaterials*, v. 12, n. 17, 2022. ISSN: 2079-4991. doi: 10.3390/nano12172960. Available at: <https://www.mdpi.com/2079-4991/12/17/2960>.

[99] VALLEM, V., SARGOLZAEIAVAL, Y., OZTURK, M., et al. "Energy Harvesting and Storage with Soft and Stretchable Materials", *Advanced Materials*, v. 33, n. 19, pp. 2004832, 2021. doi: 10.1002/adma.202004832. Available at: <https://onlinelibrary.wiley.com/doi/abs/10.1002/adma.202004832>.

[100] DENG, Z., DAPINO, M. J. "Review of magnetostrictive vibration energy harvesters", *Smart Materials and Structures*, v. 26, n. 10, pp. 103001, sep 2017. doi: 10.1088/1361-665X/aa8347. Available at: <https://dx.doi.org/10.1088/1361-665X/aa8347>.

[101] CHUNG, J., SONG, M., CHUNG, S.-H., et al. "Triangulated Cylinder Origami-Based Piezoelectric/Triboelectric Hybrid Generator to Harvest Coupled Axial and Rotational Motion", *Research*, v. 2021, 2021. doi: 10.34133/2021/7248579. Available at: <https://spj.science.org/doi/abs/10.34133/2021/7248579>.

[102] ZHONG, X., YANG, Y., WANG, X., et al. "Rotating-disk-based hybridized electromagnetic-triboelectric nanogenerator for scavenging biomechanical energy as a mobile power source", *Nano Energy*, v. 13, pp. 771–780, 2015. ISSN: 2211-2855. doi: 10.1016/j.nanoen.2015.03.012. Available at: <https://www.sciencedirect.com/science/article/pii/S2211285515001081>.

[103] EGBE, K.-J. I., MATIN NAZAR, A., JIAO, P. "Piezoelectric-triboelectric-electromagnetic Hybrid Rotational Energy Harvesters (H-REH)", *International Journal of Mechanical Sciences*, v. 235, pp. 107722, 2022. ISSN: 0020-7403. doi: 10.1016/j.ijmecsci.2022.107722. Available at: <https://www.sciencedirect.com/science/article/pii/S0020740322006026>.

[104] YANG, T., CAO, Q. "Dynamics and performance evaluation of a novel tristable hybrid energy harvester for ultra-low level vibration resources", *International Journal of Mechanical Sciences*, v. 156, pp. 123–136, 2019. ISSN: 0020-7403. doi: 10.1016/j.ijmecsci.2019.03.034. Available at: <https://www.sciencedirect.com/science/article/pii/S0020740318339080>.

[105] HALIM, M. A., KABIR, M. H., CHO, H., et al. "A Frequency Up-Converted Hybrid Energy Harvester Using Transverse Impact-Driven Piezoelectric Bimorph for Human-Limb Motion", *Micromachines*, v. 10, n. 10, 2019. ISSN: 2072-666X. doi: 10.3390/mi10100701. Available at: <https://www.mdpi.com/2072-666X/10/10/701>.

[106] GAO, L., LU, S., XIE, W., et al. "A self-powered and self-functional tracking system based on triboelectric-electromagnetic hybridized blue energy harvesting module", *Nano Energy*, v. 72, pp. 104684, 2020. ISSN: 2211-2855. doi: 10.1016/j.nanoen.2020.104684. Available at: <https://www.sciencedirect.com/science/article/pii/S221128552030241X>.

[107] XIAO, Y., NIU, M., YANG, L., et al. "Integrated Triboelectric-Electromagnetic-Piezoelectric Self-Rebounding Energy Harvester for Human Energy Harvesting", *Advanced Materials Technologies*, v. 7, n. 11, pp. 2200340, 2022. doi: 10.1002/admt.202200340. Available at: <https://onlinelibrary.wiley.com/doi/abs/10.1002/admt.202200340>.

[108] ERTURK, A., TARAZAGA, P. A., FARMER, J. R., et al. "Effect of Strain Nodes and Electrode Configuration on Piezoelectric Energy Harvesting From Cantilevered Beams", *Journal of Vibration and Acoustics*, v. 131, n. 1, 01 2009. ISSN: 1048-9002. doi: 10.1115/1.2981094. Available at: <https://doi.org/10.1115/1.2981094>. 011010.

[109] ERTURK, A., INMAN, D. J. "An experimentally validated bimorph cantilever model for piezoelectric energy harvesting from base excitations", *Smart Materials and Structures*, v. 18, n. 2, pp. 025009, jan 2009. doi: 10.1088/0964-1726/18/2/025009. Available at: <https://dx.doi.org/10.1088/0964-1726/18/2/025009>.

[110] KIM, M., HOEGEN, M., DUGUNDJI, J., et al. "Modeling and experimental verification of proof mass effects on vibration energy harvester performance", *Smart Materials and Structures*, v. 19, n. 4, pp. 045023, mar 2010. doi: 10.1088/0964-1726/19/4/045023. Available at: <https://dx.doi.org/10.1088/0964-1726/19/4/045023>.

[111] KIM, J. E., KIM, Y. Y. "Analysis of Piezoelectric Energy Harvesters of a Moderate Aspect Ratio With a Distributed Tip Mass", *Journal of Vibration and Acoustics*, v. 133, n. 4, 04 2011. ISSN: 1048-9002. doi: 10.1115/1.4003598. Available at: <https://doi.org/10.1115/1.4003598>. 041010.

[112] ZHANG, H., CORR, L. R., MA, T. "Issues in vibration energy harvesting", *Journal of Sound and Vibration*, v. 421, pp. 79–90, 2018. ISSN: 0022-460X. doi: 10.1016/j.jsv.2018.01.057. Available at: <https://www.sciencedirect.com/science/article/pii/S0022460X18300816>.

[113] OU, Q., CHEN, X., GUTSCHMIDT, S., et al. "An experimentally validated double-mass piezoelectric cantilever model for broadband vibration–based energy harvesting", *Journal of Intelligent Material Systems and Structures*, v. 23, n. 2, pp. 117–126, 2012. doi: 10.1177/1045389X11431746. Available at: <https://doi.org/10.1177/1045389X11431746>.

[114] ZOU, H.-X., ZHAO, L.-C., GAO, Q.-H., et al. "Mechanical modulations for enhancing energy harvesting: Principles, methods and applications", *Ap-*

plied Energy, v. 255, pp. 113871, 2019. ISSN: 0306-2619. doi: 10.1016/j.apenergy.2019.113871. Available at: <https://www.sciencedirect.com/science/article/pii/S0306261919315582>.

[115] WANG, T. "Pendulum-based vibration energy harvesting: Mechanisms, transducer integration, and applications", *Energy Conversion and Management*, v. 276, pp. 116469, 2023. ISSN: 0196-8904. doi: 10.1016/j.enconman.2022.116469. Available at: <https://www.sciencedirect.com/science/article/pii/S019689042201247X>.

[116] STANTON, S. C., MCGEHEE, C. C., MANN, B. P. "Nonlinear dynamics for broadband energy harvesting: Investigation of a bistable piezoelectric inertial generator", *Physica D: Nonlinear Phenomena*, v. 239, n. 10, pp. 640–653, 2010. ISSN: 0167-2789. doi: 10.1016/j.physd.2010.01.019. Available at: <https://www.sciencedirect.com/science/article/pii/S0167278910000394>.

[117] YAN, Y., ZHANG, Q., HAN, J., et al. "Design and investigation of a quad-stable piezoelectric vibration energy harvester by using geometric nonlinearity of springs", *Journal of Sound and Vibration*, v. 547, pp. 117484, 2023. ISSN: 0022-460X. doi: 10.1016/j.jsv.2022.117484. Available at: <https://www.sciencedirect.com/science/article/pii/S0022460X22006678>.

[118] FRISWELL, M. I., ALI, S. F., BILGEN, O., et al. "Non-linear piezoelectric vibration energy harvesting from a vertical cantilever beam with tip mass", *Journal of Intelligent Material Systems and Structures*, v. 23, n. 13, pp. 1505–1521, 2012. doi: 10.1177/1045389X12455722. Available at: <https://doi.org/10.1177/1045389X12455722>.

[119] OSINAGA, S., MACHADO, S., FEBBO, M. "An analytical model of the electromechanical coupling for a piezoelectric stepped buckled beam for energy harvesting applications", *Mechanical Systems and Signal Processing*, v. 179, pp. 109355, 2022. ISSN: 0888-3270. doi: 10.1016/j.ymssp.2022.109355. Available at: <https://www.sciencedirect.com/science/article/pii/S0888327022004885>.

[120] ZHU, Y., ZU, J. W. "Enhanced buckled-beam piezoelectric energy harvesting using midpoint magnetic force", *Applied Physics Letters*, v. 103, n. 4, pp. 041905, 07 2013. ISSN: 0003-6951. doi: 10.1063/1.4816518. Available at: <https://doi.org/10.1063/1.4816518>.

[121] MASANA, R., DAQAQ, M. F. "Electromechanical Modeling and Nonlinear Analysis of Axially Loaded Energy Harvesters", *Journal of Vibration and Acoustics*, v. 133, n. 1, 12 2010. ISSN: 1048-9002. doi: 10.1115/1.4002786. Available at: <https://doi.org/10.1115/1.4002786>. 011007.

[122] KUMAR, K. A., ALI, S. F., AROCKIARAJAN, A. "Piezomagnetoelastic broadband energy harvester: Nonlinear modeling and characterization", *The European Physical Journal Special Topics*, v. 224, n. 14, pp. 2803–2822, 2015. doi: 10.1140/epjst/e2015-02590-8. Available at: <https://doi.org/10.1140/epjst/e2015-02590-8>.

[123] PANYAM, M., DAQAQ, M. F. "Characterizing the effective bandwidth of tri-stable energy harvesters", *Journal of Sound and Vibration*, v. 386, pp. 336–358, 2017. ISSN: 0022-460X. doi: 10.1016/j.jsv.2016.09.022. Available at: <https://www.sciencedirect.com/science/article/pii/S0022460X16304886>.

[124] ZHOU, Z., QIN, W., ZHU, P. "A broadband quad-stable energy harvester and its advantages over bi-stable harvester: Simulation and experiment verification", *Mechanical Systems and Signal Processing*, v. 84, pp. 158–168, 2017. ISSN: 0888-3270. doi: 10.1016/j.ymssp.2016.07.001. Available at: <https://www.sciencedirect.com/science/article/pii/S0888327016302266>.

[125] SUN, S., LENG, Y., HUR, S., et al. "Energy Harvesting Performance of a Novel Nonlinear Quad-Stable Piezoelectric Energy Harvester with Only One External Magnet", *Machines*, v. 10, n. 9, 2022. ISSN: 2075-1702. doi: 10.3390/machines10090803. Available at: <https://www.mdpi.com/2075-1702/10/9/803>.

[126] ZHOU, Z., QIN, W., YANG, Y., et al. "Improving efficiency of energy harvesting by a novel penta-stable configuration", *Sensors and Actuators A: Physical*, v. 265, pp. 297–305, 2017. ISSN: 0924-4247. doi: 10.1016/j.sna.2017.08.039. Available at: <https://www.sciencedirect.com/science/article/pii/S0924424716305817>.

[127] LALLART, M., ZHOU, S., YAN, L., et al. "Tailoring multistable vibrational energy harvesters for enhanced performance: theory and numerical investigation", *Nonlinear Dynamics*, v. 96, n. 2, pp. 1283–1301, Apr 2019. ISSN: 1573-269X. doi: 10.1007/s11071-019-04853-6. Available at: <https://doi.org/10.1007/s11071-019-04853-6>.

[128] KUMAR, A., ALI, S. F., AROCKIARAJAN, A. "Exploring the benefits of an asymmetric monostable potential function in broadband vibration energy harvesting", *Applied Physics Letters*, v. 112, n. 23, pp. 233901, 06 2018. ISSN: 0003-6951. doi: 10.1063/1.5037733. Available at: <https://doi.org/10.1063/1.5037733>.

[129] WANG, W., CAO, J., BOWEN, C. R., et al. "Multiple solutions of asymmetric potential bistable energy harvesters: numerical simulation and experimental validation", *The European Physical Journal B*, v. 91, n. 10, pp. 254, Oct 2018. ISSN: 1434-6036. doi: 10.1140/epjb/e2018-90180-y. Available at: <https://doi.org/10.1140/epjb/e2018-90180-y>.

[130] CAO, J., ZHOU, S., INMAN, D. J., et al. "Nonlinear Dynamic Characteristics of Variable Inclination Magnetically Coupled Piezoelectric Energy Harvesters", *Journal of Vibration and Acoustics*, v. 137, n. 2, pp. 021015, 04 2015. ISSN: 1048-9002. doi: 10.1115/1.4029076. Available at: <https://doi.org/10.1115/1.4029076>.

[131] NORENBERG, J. P., LUO, R., LOPES, V. G., et al. "Nonlinear dynamics of asymmetric bistable energy harvesters", *International Journal of Mechanical Sciences*, v. 257, pp. 108542, 2023. ISSN: 0020-7403. doi: 10.1016/j.ijmecsci.2023.108542. Available at: <https://www.sciencedirect.com/science/article/pii/S0020740323004447>.

[132] AI, R., MONTEIRO, L. L. S., MONTEIRO, P. C. C., et al. "Piezoelectric Vibration-Based Energy Harvesting Enhancement Exploiting Nonsmoothness", *Actuators*, v. 8, n. 1, 2019. ISSN: 2076-0825. doi: 10.3390/act8010025. Available at: <https://www.mdpi.com/2076-0825/8/1/25>.

[133] AHMAD, M. M., KHAN, N. M., KHAN, F. U. "Review of frequency up-conversion vibration energy harvesters using impact and plucking mechanism", *International Journal of Energy Research*, v. 45, n. 11, pp. 15609–15645, 2021. doi: 10.1002/er.6832. Available at: <https://onlinelibrary.wiley.com/doi/abs/10.1002/er.6832>.

[134] AKAYDIN, H. D., ELVIN, N., ANDREOPOULOS, Y. "Wake of a cylinder: a paradigm for energy harvesting with piezoelectric materials", *Experiments in Fluids*, v. 49, n. 1, pp. 291–304, Jul 2010. ISSN: 1432-1114. doi: 10.1007/s00348-010-0871-7. Available at: <https://doi.org/10.1007/s00348-010-0871-7>.

[135] TANDEL, R., SHAH, S., TRIPATHI, S. "A state-of-art review on Bladeless Wind Turbine", *Journal of Physics: Conference Series*, v. 1950, n. 1,

pp. 012058, aug 2021. doi: 10.1088/1742-6596/1950/1/012058. Available at: <https://dx.doi.org/10.1088/1742-6596/1950/1/012058>.

[136] WANG, J., ZHOU, S., ZHANG, Z., et al. "High-performance piezoelectric wind energy harvester with Y-shaped attachments", *Energy Conversion and Management*, v. 181, pp. 645–652, 2019. ISSN: 0196-8904. doi: 10.1016/j.enconman.2018.12.034. Available at: <https://www.sciencedirect.com/science/article/pii/S0196890418313694>.

[137] CAO, D., WANG, J., GUO, X., et al. "Recent advancement of flow-induced piezoelectric vibration energy harvesting techniques: principles, structures, and nonlinear designs", *Applied Mathematics and Mechanics*, v. 43, n. 7, pp. 959–978, Jul 2022.

[138] WANG, J., XIA, B., YURCHENKO, D., et al. "Enhanced performance of piezoelectric energy harvester by two asymmetrical splitter plates", *Ocean Engineering*, v. 270, pp. 113614, 2023. ISSN: 0029-8018. doi: 10.1016/j.oceaneng.2022.113614. Available at: <https://www.sciencedirect.com/science/article/pii/S0029801822028979>.

[139] WANG, J., ZHANG, Y., LIU, M., et al. "Etching metasurfaces on bluff bodies for vortex-induced vibration energy harvesting", *International Journal of Mechanical Sciences*, v. 242, pp. 108016, 2023. ISSN: 0020-7403. doi: 10.1016/j.ijmecsci.2022.108016. Available at: <https://www.sciencedirect.com/science/article/pii/S0020740322008943>.

[140] ZHAO, L. "Synchronization extension using a bistable galloping oscillator for enhanced power generation from concurrent wind and base vibration", *Applied Physics Letters*, v. 116, n. 5, pp. 053904, 02 2020. ISSN: 0003-6951. doi: 10.1063/1.5134948. Available at: <https://doi.org/10.1063/1.5134948>.

[141] ZHOU, Z., QIN, W., ZHU, P., et al. "Scavenging wind energy by a Y-shaped bi-stable energy harvester with curved wings", *Energy*, v. 153, pp. 400–412, 2018. ISSN: 0360-5442. doi: 10.1016/j.energy.2018.04.035. Available at: <https://www.sciencedirect.com/science/article/pii/S036054421830639X>.

[142] WANG, J., GENG, L., ZHOU, S., et al. "Design, modeling and experiments of broadband tristable galloping piezoelectric energy harvester", *Acta Mechanica Sinica*, v. 36, n. 3, pp. 592–605, 2020. doi: 10.1007/s10409-020-00928-5. Available at: <https://doi.org/10.1007/s10409-020-00928-5>.

[143] QIN, W., DENG, W., PAN, J., et al. "Harvesting wind energy with bi-stable snap-through excited by vortex-induced vibration and galloping", *Energy*, v. 189, pp. 116237, 2019. ISSN: 0360-5442. doi: 10.1016/j.energy.2019.116237. Available at: <https://www.sciencedirect.com/science/article/pii/S0360544219319322>.

[144] ZHOU, Z., QIN, W., ZHU, P., et al. "Harvesting more energy from variable-speed wind by a multi-stable configuration with vortex-induced vibration and galloping", *Energy*, v. 237, pp. 121551, 2021. ISSN: 0360-5442. doi: 10.1016/j.energy.2021.121551. Available at: <https://www.sciencedirect.com/science/article/pii/S0360544221017990>.

[145] ADEODATO, A., DUARTE, B. T., MONTEIRO, L. L. S., et al. "Synergistic use of piezoelectric and shape memory alloy elements for vibration-based energy harvesting", *International Journal of Mechanical Sciences*, v. 194, pp. 106206, 2021. ISSN: 0020-7403. doi: 10.1016/j.ijmecsci.2020.106206. Available at: <https://www.sciencedirect.com/science/article/pii/S0020740320343113>.

[146] YUAN, J. H., YANG, Y. Z., ZHANG, Y. H. "A piezoelectric energy harvester with light-activated shape memory polymers", *Ferroelectrics*, v. 550, n. 1, pp. 98–111, 2019. doi: 10.1080/00150193.2019.1652500. Available at: <https://doi.org/10.1080/00150193.2019.1652500>.

[147] MARGIELEWICZ, J., GASKA, D., LITAK, G., et al. "Nonlinear dynamics of a new energy harvesting system with quasi-zero stiffness", *Applied Energy*, v. 307, pp. 118159, 2022. ISSN: 0306-2619. doi: 10.1016/j.apenergy.2021.118159. Available at: <https://www.sciencedirect.com/science/article/pii/S030626192101432X>.

[148] CAETANO, V. J., SAVI, M. A. "Multimodal pizza-shaped piezoelectric vibration-based energy harvesters", *Journal of Intelligent Material Systems and Structures*, v. 32, n. 20, pp. 2505–2528, 2021. doi: 10.1177/1045389X211006910. Available at: <https://doi.org/10.1177/1045389X211006910>.

[149] CAETANO, V. J., SAVI, M. A. "Star-shaped piezoelectric mechanical energy harvesters for multidirectional sources", *International Journal of Mechanical Sciences*, v. 215, pp. 106962, 2022. ISSN: 0020-7403. doi: 10.1016/j.ijmecsci.2021.106962. Available at: <https://www.sciencedirect.com/science/article/pii/S002074032100672X>.

[150] YANG, Z., WANG, Y. Q., ZUO, L., et al. "Introducing arc-shaped piezoelectric elements into energy harvesters", *Energy Conversion and Management*, v. 148, pp. 260–266, 2017. ISSN: 0196-8904. doi: 10.1016/j.enconman.2017.05.073. Available at: <https://www.sciencedirect.com/science/article/pii/S0196890417305319>.

[151] ZHOU, W., WANG, B., LIM, C., et al. "A distributed-parameter electromechanical coupling model for a segmented arc-shaped piezoelectric energy harvester", *Mechanical Systems and Signal Processing*, v. 146, pp. 107005, 2021. ISSN: 0888-3270. doi: 10.1016/j.ymssp.2020.107005. Available at: <https://www.sciencedirect.com/science/article/pii/S0888327020303915>.

[152] CHEN, X., ZHANG, X., WANG, L., et al. "An arch-linear composed beam piezoelectric energy harvester with magnetic coupling: Design, modeling and dynamic analysis", *Journal of Sound and Vibration*, v. 513, pp. 116394, 2021. ISSN: 0022-460X. doi: 10.1016/j.jsv.2021.116394. Available at: <https://www.sciencedirect.com/science/article/pii/S0022460X21004454>.

[153] ZHANG, X., YANG, W., ZUO, M., et al. "An Arc-Shaped Piezoelectric Bistable Vibration Energy Harvester: Modeling and Experiments", *Sensors*, v. 18, n. 12, 2018. ISSN: 1424-8220. doi: 10.3390/s18124472. Available at: <https://www.mdpi.com/1424-8220/18/12/4472>.

[154] ZHANG, X., ZUO, M., YANG, W., et al. "A Tri-Stable Piezoelectric Vibration Energy Harvester for Composite Shape Beam: Nonlinear Modeling and Analysis", *Sensors*, v. 20, n. 5, 2020. ISSN: 1424-8220. doi: 10.3390/s20051370. Available at: <https://www.mdpi.com/1424-8220/20/5/1370>.

[155] CHEN, X., ZHANG, X., CHEN, L., et al. "A Curve-Shaped Beam Bistable Piezoelectric Energy Harvester with Variable Potential Well: Modeling and Numerical Simulation", *Micromachines*, v. 12, n. 8, 2021. ISSN: 2072-666X. doi: 10.3390/mi12080995. Available at: <https://www.mdpi.com/2072-666X/12/8/995>.

[156] FU, H., YEATMAN, E. M. "A methodology for low-speed broadband rotational energy harvesting using piezoelectric transduction and frequency up-conversion", *Energy*, v. 125, pp. 152–161, 2017. ISSN: 0360-5442. doi: 10.1016/j.energy.2017.02.115. Available at: <https://www.sciencedirect.com/science/article/pii/S0360544217302979>.

[157] FU, H., JIANG, J., HU, S., et al. "A multi-stable ultra-low frequency energy harvester using a nonlinear pendulum and piezoelectric transduction for self-powered sensing", *Mechanical Systems and Signal Processing*, v. 189, pp. 110034, 2023. ISSN: 0888-3270. doi: 10.1016/j.ymssp.2022.110034. Available at: <https://www.sciencedirect.com/science/article/pii/S0888327022011025>.

[158] MEI, X., ZHOU, S., YANG, Z., et al. "Enhancing energy harvesting in low-frequency rotational motion by a quad-stable energy harvester with time-varying potential wells", *Mechanical Systems and Signal Processing*, v. 148, pp. 107167, 2021. ISSN: 0888-3270. doi: 10.1016/j.ymssp.2020.107167. Available at: <https://www.sciencedirect.com/science/article/pii/S0888327020305537>.

[159] HU, G., TANG, L., DAS, R. "Internally coupled metamaterial beam for simultaneous vibration suppression and low frequency energy harvesting", *Journal of Applied Physics*, v. 123, n. 5, pp. 055107, 02 2018. ISSN: 0021-8979. doi: 10.1063/1.5011999. Available at: <https://doi.org/10.1063/1.5011999>.

[160] UPADRASHTA, D., YANG, Y. "Finite element modeling of nonlinear piezoelectric energy harvesters with magnetic interaction", *Smart Materials and Structures*, v. 24, n. 4, pp. 045042, mar 2015. doi: 10.1088/0964-1726/24/4/045042. Available at: <https://dx.doi.org/10.1088/0964-1726/24/4/045042>.

[161] KRISHNASAMY, M., UPADRASHTA, D., YANG, Y., et al. "Distributed Parameter Modelling of Cutout 2-DOF Cantilevered Piezo-Magneto-Elastic Energy Harvester", *Journal of Microelectromechanical Systems*, v. 27, n. 6, pp. 1160–1170, 2018. doi: 10.1109/JMEMS.2018.2875788.

[162] WU, Y., QIU, J., ZHOU, S., et al. "A piezoelectric spring pendulum oscillator used for multi-directional and ultra-low frequency vibration energy harvesting", *Applied Energy*, v. 231, pp. 600–614, 2018. ISSN: 0306-2619. doi: 10.1016/j.apenergy.2018.09.082. Available at: <https://www.sciencedirect.com/science/article/pii/S030626191831393X>.

[163] KECIK, K. "Assessment of energy harvesting and vibration mitigation of a pendulum dynamic absorber", *Mechanical Systems and Signal Processing*, v. 106, pp. 198–209, 2018. ISSN: 0888-3270. doi: 10.1016/j.ymssp.2017.12.028. Available at: <https://www.sciencedirect.com/science/article/pii/S0888327017306659>.

[164] KECIK, K. "Simultaneous vibration mitigation and energy harvesting from a pendulum-type absorber", *Communications in Nonlinear Science and Numerical Simulation*, v. 92, pp. 105479, 2021. ISSN: 1007-5704. doi: 10.1016/j.cnsns.2020.105479. Available at: <https://www.sciencedirect.com/science/article/pii/S1007570420303099>.

[165] XU, J., TANG, J. "Modeling and analysis of piezoelectric cantilever-pendulum system for multi-directional energy harvesting", *Journal of Intelligent Material Systems and Structures*, v. 28, n. 3, pp. 323–338, 2017. doi: 10.1177/1045389X16642302. Available at: <https://doi.org/10.1177/1045389X16642302>.

[166] PAN, J., QIN, W., DENG, W., et al. "Harvesting weak vibration energy by integrating piezoelectric inverted beam and pendulum", *Energy*, v. 227, pp. 120374, 2021. ISSN: 0360-5442. doi: 10.1016/j.energy.2021.120374. Available at: <https://www.sciencedirect.com/science/article/pii/S036054422100623X>.

[167] SUN, S., ZHENG, Y., WANG, Y., et al. "Investigation of internal resonance on widening the bandwidth of energy harvester based on a cantilevered double pendulum structure", *AIP Advances*, v. 12, n. 9, pp. 095108, 09 2022. ISSN: 2158-3226. doi: 10.1063/5.0102817. Available at: <https://doi.org/10.1063/5.0102817>.

[168] ZHANG, A., SOROKIN, V., LI, H. "Energy harvesting using a novel autoparametric pendulum absorber-harvester", *Journal of Sound and Vibration*, v. 499, pp. 116014, 2021. ISSN: 0022-460X. doi: 10.1016/j.jsv.2021.116014. Available at: <https://www.sciencedirect.com/science/article/pii/S0022460X21000869>.

[169] BAO, B., ZHOU, S., WANG, Q. "Interplay between internal resonance and nonlinear magnetic interaction for multi-directional energy harvesting", *Energy Conversion and Management*, v. 244, pp. 114465, 2021. ISSN: 0196-8904. doi: 10.1016/j.enconman.2021.114465. Available at: <https://www.sciencedirect.com/science/article/pii/S0196890421006415>.

[170] KUMAR, R., GUPTA, S., ALI, S. F. "Energy harvesting from chaos in base excited double pendulum", *Mechanical Systems and Signal Processing*, v. 124, pp. 49–64, 2019. ISSN: 0888-3270. doi: 10.1016/j.ymssp.2019.01.037. Available at: <https://www.sciencedirect.com/science/article/pii/S0888327019300536>.

[171] SAVI, M. A. *Dinâmica Não-linear e Caos*. Rio de Janeiro, e-papers, 2017. ISBN: 978-85-7650-554-9. Available at: <http://www.e-papers.com.br/produtos.asp?codigo_produto=2929>.

[172] SORIANO, D. C., FAZANARO, F. I., SUYAMA, R., et al. "A method for Lyapunov spectrum estimation using cloned dynamics and its application to the discontinuously-excited FitzHugh–Nagumo model", *Nonlinear Dynamics*, v. 67, n. 1, pp. 413–424, Jan 2012. ISSN: 1573-269X. doi: 10.1007/s11071-011-9989-2. Available at: <https://doi.org/10.1007/s11071-011-9989-2>.

[173] WOLF, A., SWIFT, J. B., SWINNEY, H. L., et al. "Determining Lyapunov exponents from a time series", *Physica D: Nonlinear Phenomena*, v. 16, n. 3, pp. 285 – 317, 1985. ISSN: 0167-2789. doi: 10.1016/0167-2789(85)90011-9. Available at: <https://doi.org/10.1016/0167-2789(85)90011-9>.

[174] OSELEDEC, V. I. "A multiplicative ergodic theorem, Lyapunov characteristic numbers for dynamical systems", *Transactions of the Moscow Mathematical Society*, v. 19, pp. 197–231, 1968.

[175] ECKMANN, J. P., RUELLE, D. "Ergodic theory of chaos and strange attractors", *Rev. Mod. Phys.*, v. 57, pp. 617–656, Jul 1985. doi: 10.1103/RevModPhys.57.617. Available at: <https://link.aps.org/doi/10.1103/RevModPhys.57.617>.

[176] NAYFEH, A. H., BALACHANDRAN, B. *Equilibrium Solutions*. Germany, John Wiley & Sons, Ltd, 1995. ISBN: 9783527617548. doi: 10.1002/9783527617548. Available at: <https://onlinelibrary.wiley.com/doi/abs/10.1002/9783527617548>.

[177] ECKMANN, J. P. "Roads to turbulence in dissipative dynamical systems", *Rev. Mod. Phys.*, v. 53, pp. 643–654, Oct 1981. doi: 10.1103/RevModPhys.53.643. Available at: <https://link.aps.org/doi/10.1103/RevModPhys.53.643>.

[178] YUAN, T.-C., YANG, J., CHEN, L.-Q. "Nonlinear vibration analysis of a circular composite plate harvester via harmonic balance", *Acta Mechanica Sinica*, v. 35, n. 4, pp. 912–925, Aug 2019. ISSN: 1614-3116. doi: 10.1007/s10409-019-00863-0. Available at: <https://doi.org/10.1007/s10409-019-00863-0>.

[179] LI, H., SUN, H., SONG, B., et al. "Nonlinear dynamic response of an L-shaped beam-mass piezoelectric energy harvester", *Journal of Sound and*

Vibration, v. 499, pp. 116004, 2021. ISSN: 0022-460X. doi: 10.1016/j.jsv.2021.116004. Available at: <https://www.sciencedirect.com/science/article/pii/S0022460X21000766>.

[180] LAN, C., TANG, L., HARNE, R. L. "Comparative methods to assess harmonic response of nonlinear piezoelectric energy harvesters interfaced with AC and DC circuits", *Journal of Sound and Vibration*, v. 421, pp. 61–78, 2018. ISSN: 0022-460X. doi: https://doi.org/10.1016/j.jsv.2017.11.019. Available at: <https://www.sciencedirect.com/science/article/pii/S0022460X17307940>.

[181] YAN, B., ZHOU, S., LITAK, G. "Nonlinear Analysis of the Tristable Energy Harvester with a Resonant Circuit for Performance Enhancement", *International Journal of Bifurcation and Chaos*, v. 28, n. 07, pp. 1850092, 2018. doi: 10.1142/S021812741850092X. Available at: <https://doi.org/10.1142/S021812741850092X>.

[182] MURALIDHARAN, A., ALI, S. F. "Broadband power generation using an array of bistable harvesters", *The European Physical Journal Special Topics*, v. 231, n. 8, pp. 1491–1503, Jul 2022. ISSN: 1951-6401. doi: 10.1140/epjs/s11734-022-00507-8. Available at: <https://doi.org/10.1140/epjs/s11734-022-00507-8>.

[183] DENG, H., LI, R., WANG, B., et al. "An annularly-distributed poly-stable array for broadband vibrational energy", *Sensors and Actuators A: Physical*, v. 332, pp. 113106, 2021. ISSN: 0924-4247. doi: 10.1016/j.sna.2021.113106. Available at: <https://www.sciencedirect.com/science/article/pii/S0924424721005719>.

[184] LIAO, Y., LIANG, J. "Unified modeling, analysis and comparison of piezoelectric vibration energy harvesters", *Mechanical Systems and Signal Processing*, v. 123, pp. 403–425, 2019. ISSN: 0888-3270. doi: https://doi.org/10.1016/j.ymssp.2019.01.025. Available at: <https://www.sciencedirect.com/science/article/pii/S0888327019300251>.

[185] LEADENHAM, S., ERTURK, A. "Mechanically and electrically nonlinear non-ideal piezoelectric energy harvesting framework with experimental validations", *Nonlinear Dynamics*, v. 99, n. 1, pp. 625–641, Jan 2020. ISSN: 1573-269X. doi: 10.1007/s11071-019-05091-6. Available at: <https://doi.org/10.1007/s11071-019-05091-6>.

[186] REZAEI, M., TALEBITOOTI, R., LIAO, W.-H. "Exploiting bi-stable magneto-piezoelastic absorber for simultaneous energy harvesting and vi-

bration mitigation", *International Journal of Mechanical Sciences*, v. 207, pp. 106618, 2021. ISSN: 0020-7403. doi: 10.1016/j.ijmecsci.2021.106618. Available at: <https://www.sciencedirect.com/science/article/pii/S0020740321003520>.

[187] SOMMERMANN, P., CARTMELL, M. P. "The dynamics of an omnidirectional pendulum harvester", *Nonlinear Dynamics*, v. 104, n. 3, pp. 1889–1900, May 2021. ISSN: 1573-269X. doi: 10.1007/s11071-021-06479-z. Available at: <https://doi.org/10.1007/s11071-021-06479-z>.

[188] LITAK, G., MARGIELEWICZ, J., GĄSKA, D., et al. "Multiple Solutions of the Tristable Energy Harvester", *Energies*, v. 14, n. 5, 2021. ISSN: 1996-1073. doi: 10.3390/en14051284. Available at: <https://www.mdpi.com/1996-1073/14/5/1284>.

[189] BAE, S., KIM, P. "Load Resistance Optimization of Bi-Stable Electromagnetic Energy Harvester Based on Harmonic Balance", *Sensors*, v. 21, n. 4, 2021. ISSN: 1424-8220. doi: 10.3390/s21041505. Available at: <https://www.mdpi.com/1424-8220/21/4/1505>.

[190] KUMAR, K. A., ALI, S. F., AROCKIARAJAN, A. "Magneto-elastic oscillator: Modeling and analysis with nonlinear magnetic interaction", *Journal of Sound and Vibration*, v. 393, pp. 265–284, 2017. ISSN: 0022-460X. doi: 10.1016/j.jsv.2017.01.007. Available at: <https://www.sciencedirect.com/science/article/pii/S0022460X1730007X>.

[191] PREUMONT, A. *Mechatronics: Dynamics of Electromechanical and Piezoelectric Systems*. Dordrecht, Springer Netherlands, 2006. ISBN: 978-1-4020-4696-4. doi: 10.1007/1-4020-4696-0.

[192] MEIROVITCH, L. *Methods of Analytical Dynamics*. Advanced engineering series. New York, Dover Publications, 2010. ISBN: 9780486432397.

[193] ERTURK, A., HOFFMANN, J., INMAN, D. J. "A piezomagnetoelastic structure for broadband vibration energy harvesting", *Applied Physics Letters*, v. 94, n. 25, pp. 254102, 06 2009. ISSN: 0003-6951. doi: 10.1063/1.3159815. Available at: <https://doi.org/10.1063/1.3159815>.

[194] CELLULAR, A. C., DA SILVA MONTEIRO, L. L., SAVI, M. A. "Numerical investigation of nonlinear mechanical and constitutive effects on piezoelectric vibration-based energy harvesting", *tm - Technisches Messen*, v. 85, n. 9, pp. 565–579, 2018. doi: 10.1515/teme-2017-0070. Available at: <https://doi.org/10.1515/teme-2017-0070>.

[195] NORENBERG, J. P., CUNHA, A., DA SILVA, S., et al. "Probabilistic maps on bistable vibration energy harvesters", *Nonlinear Dynamics*, v. 111, n. 22, pp. 20821–20840, Nov 2023. ISSN: 1573-269X. doi: 10.1007/s11071-023-08864-2. Available at: <https://doi.org/10.1007/s11071-023-08864-2>.

[196] CUNHA, A. "Enhancing the performance of a bistable energy harvesting device via the cross-entropy method", *Nonlinear Dynamics*, v. 103, n. 1, pp. 137–155, Jan 2021. ISSN: 1573-269X. doi: 10.1007/s11071-020-06109-0. Available at: <https://doi.org/10.1007/s11071-020-06109-0>.

[197] NORENBERG, J. P., CUNHA JR, A., WOLSZCZAK, P., et al. "Piezomagnetic vibration energy harvester with an amplifier", *Theoretical and Applied Mechanics Letters*, v. 13, n. 6, pp. 100478, 2023. ISSN: 2095-0349. doi: https://doi.org/10.1016/j.taml.2023.100478. Available at: <https://www.sciencedirect.com/science/article/pii/S2095034923000491>.

[198] CHEN, J., BAO, B., LIU, J., et al. "Pendulum Energy Harvesters: A Review", *Energies*, v. 15, n. 22, 2022. ISSN: 1996-1073. doi: 10.3390/en15228674. Available at: <https://www.mdpi.com/1996-1073/15/22/8674>.

[199] XU, J., TANG, J. "Multi-directional energy harvesting by piezoelectric cantilever-pendulum with internal resonance", *Applied Physics Letters*, v. 107, n. 21, 11 2015. ISSN: 0003-6951. doi: 10.1063/1.4936607. Available at: <https://doi.org/10.1063/1.4936607>. 213902.

[200] PAN, J.-N., QIN, W.-Y., DENG, W.-Z., et al. "Harvesting base vibration energy by a piezoelectric inverted beam with pendulum*", *Chinese Physics B*, v. 28, n. 1, pp. 017701, jan 2019. doi: 10.1088/1674-1056/28/1/017701. Available at: <https://dx.doi.org/10.1088/1674-1056/28/1/017701>.

[201] PAN, J., QIN, W., DENG, W., et al. "Harvesting weak vibration energy by integrating piezoelectric inverted beam and pendulum", *Energy*, v. 227, pp. 120374, 2021. ISSN: 0360-5442. doi: 10.1016/j.energy.2021.120374. Available at: <https://www.sciencedirect.com/science/article/pii/S036054422100623X>.

[202] CARVALHO, P. R., SAVI, M. A. "Synchronization and chimera state in a mechanical system", *Nonlinear Dynamics*, v. 102, n. 2, pp. 907–925, Oct 2020. ISSN: 1573-269X. doi: 10.1007/s11071-019-05441-4. Available at: <https://doi.org/10.1007/s11071-019-05441-4>.

[203] PARKER, T. S., CHUA, L. *Practical numerical algorithms for chaotic systems*. New York, Springer Science & Business Media, 2012.

[204] RAMASUBRAMANIAN, K., SRIRAM, M. "A comparative study of computation of Lyapunov spectra with different algorithms", *Physica D: Nonlinear Phenomena*, v. 139, n. 1, pp. 72–86, 2000. ISSN: 0167-2789. doi: 10.1016/S0167-2789(99)00234-1. Available at: <https://www.sciencedirect.com/science/article/pii/S0167278999002341>.

[205] DAS, S., DOCK, C. B., SAIKI, Y., et al. "Measuring quasiperiodicity", *Europhysics Letters*, v. 114, n. 4, pp. 40005, jun 2016. doi: 10.1209/0295-5075/114/40005. Available at: <https://dx.doi.org/10.1209/0295-5075/114/40005>.

[206] KOLEMEN, E., KASDIN, N. J., GURFIL, P. "Multiple Poincaré sections method for finding the quasiperiodic orbits of the restricted three body problem", *Celestial Mechanics and Dynamical Astronomy*, v. 112, n. 1, pp. 47–74, Jan 2012. ISSN: 1572-9478. doi: 10.1007/s10569-011-9383-x. Available at: <https://doi.org/10.1007/s10569-011-9383-x>.

Appendix A

Elementary Symmetric Polynomials

Symmetric polynomials are mathematical functions that exhibit a particular property: when you interchange the positions of any pair of variables within the polynomial, the function retains its original form. These symmetric polynomials can be elegantly represented using elementary symmetric polynomials. In the context of a polynomial with n variables denoted as $\{\Gamma_1, \Gamma_2, \cdots, \Gamma_n\}$, the corresponding set of elementary symmetric polynomials is defined as $\{e_0, e_1, \cdots, n\}$:

$$\begin{aligned}
e_0 &= 1 \\
e_1 &= \sum_{1\leq j\leq n} \Gamma_j \\
e_2 &= \sum_{1\leq j<k\leq n} \Gamma_j\Gamma_k \\
e_3 &= \sum_{1\leq j<k<l\leq n} \Gamma_j\Gamma_k\Gamma_l \\
&\vdots \\
e_n &= \Gamma_1\Gamma_2\cdots\Gamma_n
\end{aligned}$$

In general, for $0 \leq m \leq n$,

$$e_m = \sum_{1\leq j_1<j_2<\cdots<j_m\leq n} \Gamma_{j_1}\Gamma_{j_2}\cdots\Gamma_{j_m}. \tag{A.1}$$

In the context of monic polynomials of the form $x^n+c_{n-1}x^{n-1}+\cdots+c_2x^2+c_1x+c_0$, with $n \geq 0$, the following identities arise:

$$\prod_{j=1}^{n}(x-\Gamma_j) = x^n - e_1(\Gamma_1,\cdots,\Gamma_n)\,x^{n-1} + e_2(\Gamma_1,\cdots,\Gamma_n)\,x^{n-2} + \cdots$$
$$\cdots + (-1)^n e_n(\Gamma_1,\cdots,\Gamma_n) \tag{A.2}$$
$$= \sum_{j=1}^{n}(-1)^j\, e_j(\Gamma_1,\cdots,\Gamma_n)\,x^{n-j}$$

$$\prod_{j=1}^{n}(x+\Gamma_j) = x^n + e_1(\Gamma_1,\cdots,\Gamma_n)\,x^{n-1} + e_2(\Gamma_1,\cdots,\Gamma_n)\,x^{n-2} + \cdots$$
$$\cdots + e_n(\Gamma_1,\cdots,\Gamma_n) \tag{A.3}$$
$$= \sum_{j=1}^{n} e_j(\Gamma_1,\cdots,\Gamma_n)\,x^{n-j}$$

- **Example**:

For $n=1$:
$$e_0(\Gamma_1) = 1,$$
$$e_1(\Gamma_1) = \Gamma_1.$$
For $n=2$:
$$e_0(\Gamma_1,\Gamma_2) = 1,$$
$$e_1(\Gamma_1,\Gamma_2) = \Gamma_1+\Gamma_2,$$
$$e_2(\Gamma_1,\Gamma_2) = \Gamma_1\Gamma_2.$$
For $n=3$:
$$e_0(\Gamma_1,\Gamma_2,\Gamma_3) = 1,$$
$$e_1(\Gamma_1,\Gamma_2,\Gamma_3) = \Gamma_1+\Gamma_2+\Gamma_3,$$
$$e_2(\Gamma_1,\Gamma_2,\Gamma_3) = \Gamma_1\Gamma_2+\Gamma_1\Gamma_3+\Gamma_2\Gamma_3,$$
$$e_3(\Gamma_1,\Gamma_2,\Gamma_3) = \Gamma_1\Gamma_2\Gamma_3.$$
For $n=4$:
$$e_0(\Gamma_1,\Gamma_2,\Gamma_3,\Gamma_4) = 1,$$
$$e_1(\Gamma_1,\Gamma_2,\Gamma_3,\Gamma_4) = \Gamma_1+\Gamma_2+\Gamma_3+\Gamma_4,$$
$$e_2(\Gamma_1,\Gamma_2,\Gamma_3,\Gamma_4) = \Gamma_1\Gamma_2+\Gamma_1\Gamma_3+\Gamma_1\Gamma_4+\Gamma_2\Gamma_3+\Gamma_2\Gamma_4+\Gamma_3\Gamma_4,$$
$$e_3(\Gamma_1,\Gamma_2,\Gamma_3,\Gamma_4) = \Gamma_1\Gamma_2\Gamma_3+\Gamma_1\Gamma_2\Gamma_4+\Gamma_1\Gamma_3\Gamma_4+\Gamma_2\Gamma_3\Gamma_4,$$
$$e_4(\Gamma_1,\Gamma_2,\Gamma_3,\Gamma_4) = \Gamma_1\Gamma_2\Gamma_3\Gamma_4.$$

Appendix B

Algorithms

This appendix provides illustrative representations of some algorithms used in this work. The algorithms were implemented using C and Python programming languages. Specifically, the C language (C17 standard) was used for the simulation algorithms to solve the models proposed in this thesis, primarily for performance reasons. Python 3.11.8, along with the pandas 2.2.0, NumPy 1.26.3, and Matplotlib 3.8.2 libraries, was used to manipulate and visualize the data produced by the simulations. Particularly, the stability analysis presented in Section 5.2 is performed using Python along the SymPy 1.12 library that allows symbolic mathematical manipulations allied with the visualization framework already established in all the other analyses. Moreover, the derivations of the electromechanical equations through the energetic approach, for both CMEH and MHEH, were performed with the assistance of Wolfram Mathematica 13.3 software.

Finally, the fourth-order Runge-Kutta integrator was employed to solve the nonlinear ODE systems presented in this thesis.

B.1 Poincaré Map Algorithm

In this work, all the analyzed energy harvesting systems are subjected to harmonic external excitations. For this reason, the procedure used to obtain the steady-state Poincaré maps is based on the process depicted in Figure 3.2, where the time coordinate is folded into a toroidal space that repeats itself every period, T. Figure B.1 illustrates the algorithm, where the number of integration steps is divided in terms of harmonic excitation characteristics as $N = N_{\text{per}} \times N_{\text{div}}$. N_{per} is the number of excitation periods, T, employed in the analysis, while N_{div} is the number of time steps per excitation period. With this information, it is possible to compute the final time of integration as $t_f = 2\pi N_{\text{per}}/\omega$, where ω is the excitation frequency. Then, the integration scheme is divided into two nested loops: the first iterating over the number of periods, and the second iterating over the number of divisions per period.

This way, it is possible to insert the Poincaré sections exactly at a division point within a period, as illustrated by the red dashed lines. In these sections, the solution point is obtained and added to the map data.

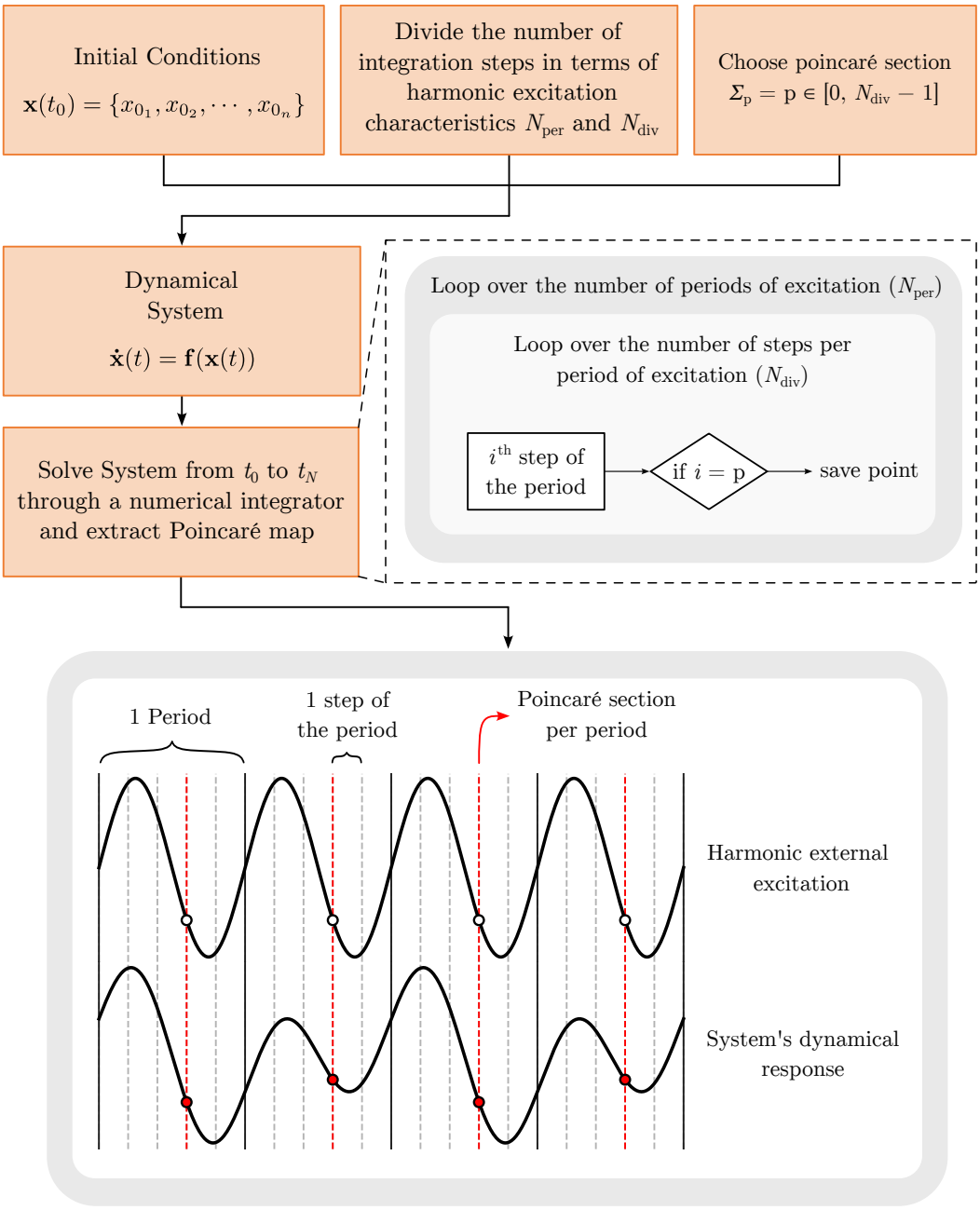

Figure B.1: Procedure to obtain the Poincaré maps.

B.2 Lyapunov Exponents

There are many algorithms to compute Lyapunov exponents available in the literature. The majority of them monitor the perturbed trajectories through linearized versions of the system combined with the usage of Gram-Schmidt reorthonormaliza-

tion or QR decomposition to avoid numerical errors and ill-conditioned terms [203]. For a comparison of classic algorithms, refer to [204]. Notably, in recent years, a new

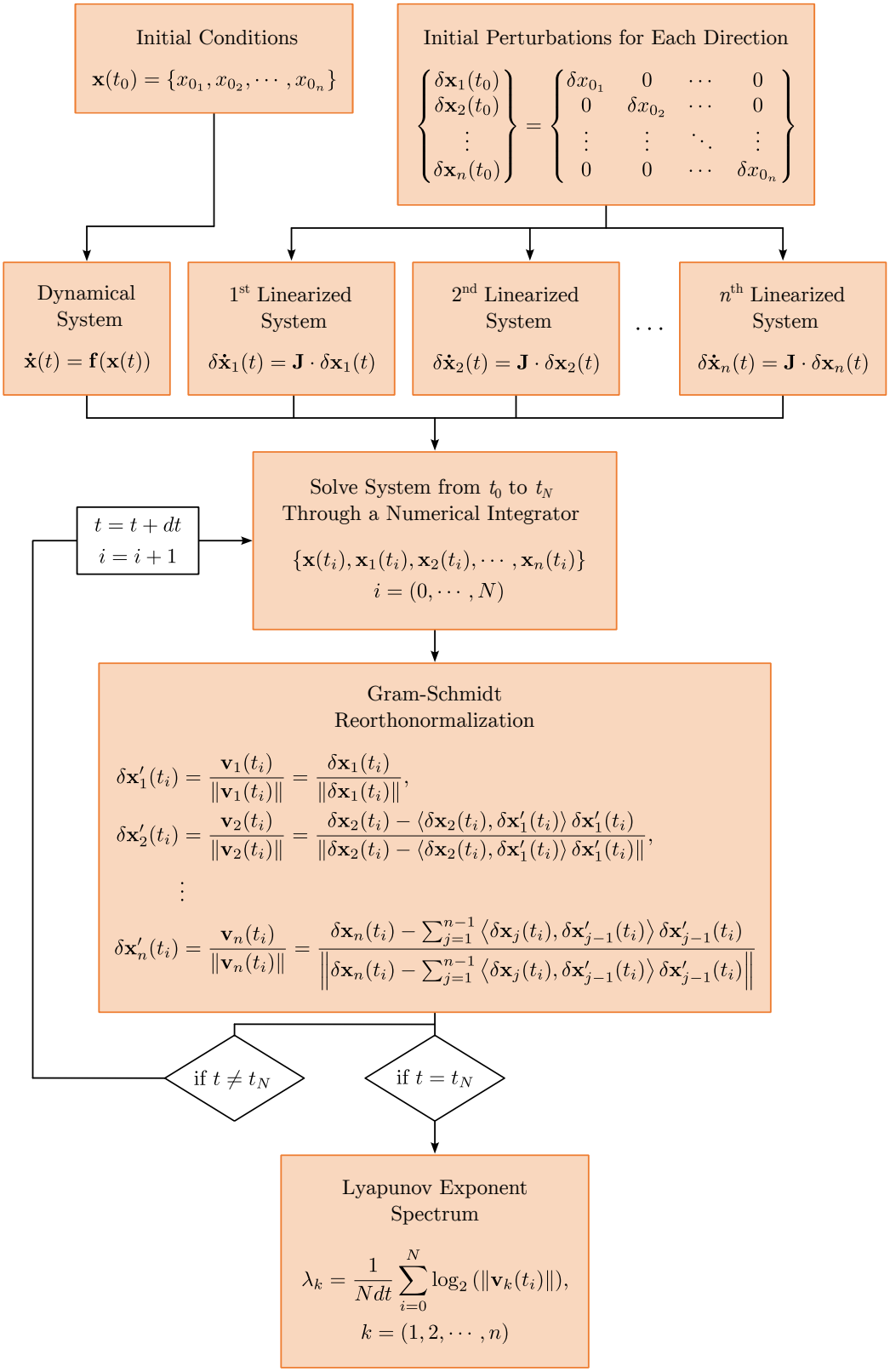

Figure B.2: Procedure to obtain the Lyapunov exponent spectrum, where dt is the time increment, t_0 and $t_N = t_f$ the initial and final time of integration, respectively.

method was proposed by SORIANO *et al.* [172] that does not require the linearization of the system to monitor the perturbed orbits. Instead, they used clones of the actual system to perform the task. In this work, the classical method proposed by WOLF *et al.* [173] is chosen due to the robustness and speed, and the general algorithm is depicted in Figure B.2, where a base $\mathscr{b} = 2$ [bits/s] is used accordingly to [173].

B.3 Parallel Implementation of the Two-Dimensional Diagrams

The procedures to obtain the DRDs, OPDs and LEDs presented in this work are performed utilizing parallel computing techniques. Specifically, due to performance, the codes were developed using C language associated with the OpenMP® API. Figure B.3 provides a schematic representation of the algorithm. The process begins with a mesh composed of $N_x \times N_y$ points. This mesh is then divided into equally distributed chunks of points. Subsequently, each chunk is assigned to a different CPU thread. Each thread executes a `for` loop with distinct points of the mesh. Each iteration of the `for` loop computes a distinct point of the mesh. The OpenMP® API `schedule(static)` command automates this entire process by assigning sets of loop iterations to different threads to execute.

B.4 Limitations of the DRD Algorithm

The combination of Poincaré maps and Lyapunov exponents to construct a robust tool for the automatic classifying dynamical attractors of the system is presented in Chapter 3, however, every tool has its limitations.

The first limitation concerns the algorithm's ability to classify only three of the four possible behaviors outlined in Table 3.1.2. Specifically, it cannot accurately identify quasiperiodic responses. Theoretically, it is conceivable to determine if a system exhibits quasiperiodic behavior using the Lyapunov spectrum. In practice, however, it is almost impossible to make such determinations solely based on evaluating the Lyapunov exponents. This challenge arises from two factors: Firstly, numerical errors are associated with the numerical integrator used to solve the nonlinear dynamical system, as well as numerical errors associated with the procedure to determine the exponents. Secondly, the evaluation of the Lyapunov exponent spectrum is restricted to a finite time range, while Equation 3.9 explicitly states that the correct value of the exponent is assessed as the limit $t \to \infty$. Consequently, the values obtained by all the Lyapunov exponent algorithms are approximations

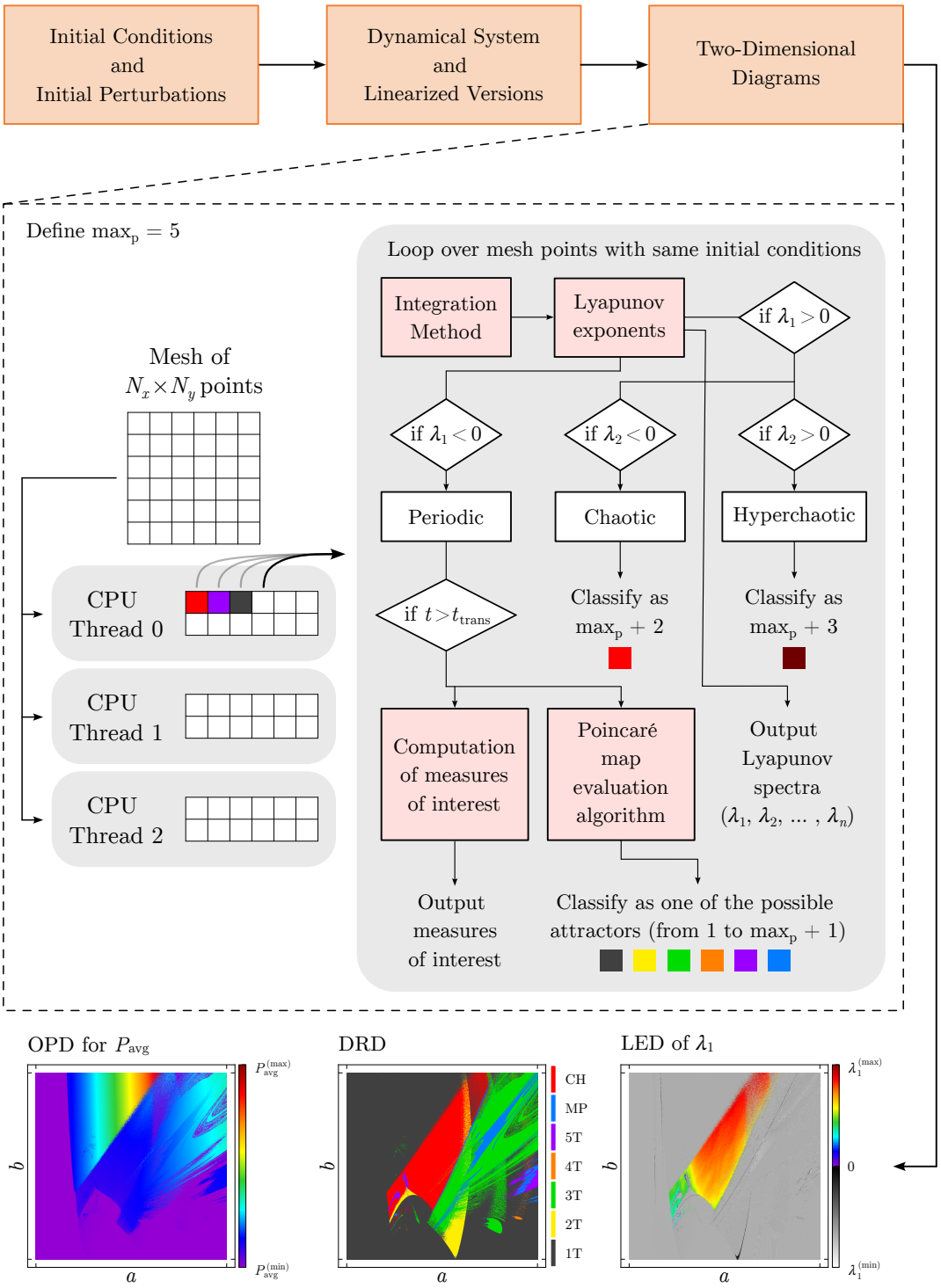

Figure B.3: Schematic illustration of the parallel procedure to obtain the DRDs, OPDs and LEDs for a two-dimensional parameter domain of $N_x \times N_y$ points. In this example, a process utilizing 3 CPU threads is showcased.

of the actual values, with an associated error. While there are existing methods in the literature to identify quasiperiodic behavior, most of them are computationally

intensive [205, 206]. To bypass this issue, the "Many Periods" (MP) classification, illustrated in Figure 3.9, has been incorporated. It includes all high periodic or quasiperiodic attractors that exhibit $\lambda_1 < 0$. This approach is considered a reasonable solution within the scope and objectives of this thesis, however, it is important to notice that attractors that exhibit $\lambda_1 > 0$ and are quasiperiodic can still be erroneously classified.

The second issue also concerns the evaluation of attractors that have the two largest Lyapunov exponents near zero. Due to the same numerical errors, the values and signs of the exponents can be misleading. To mitigate these problems, it is imperative to assess the system over extended time intervals to ensure exponent convergence.

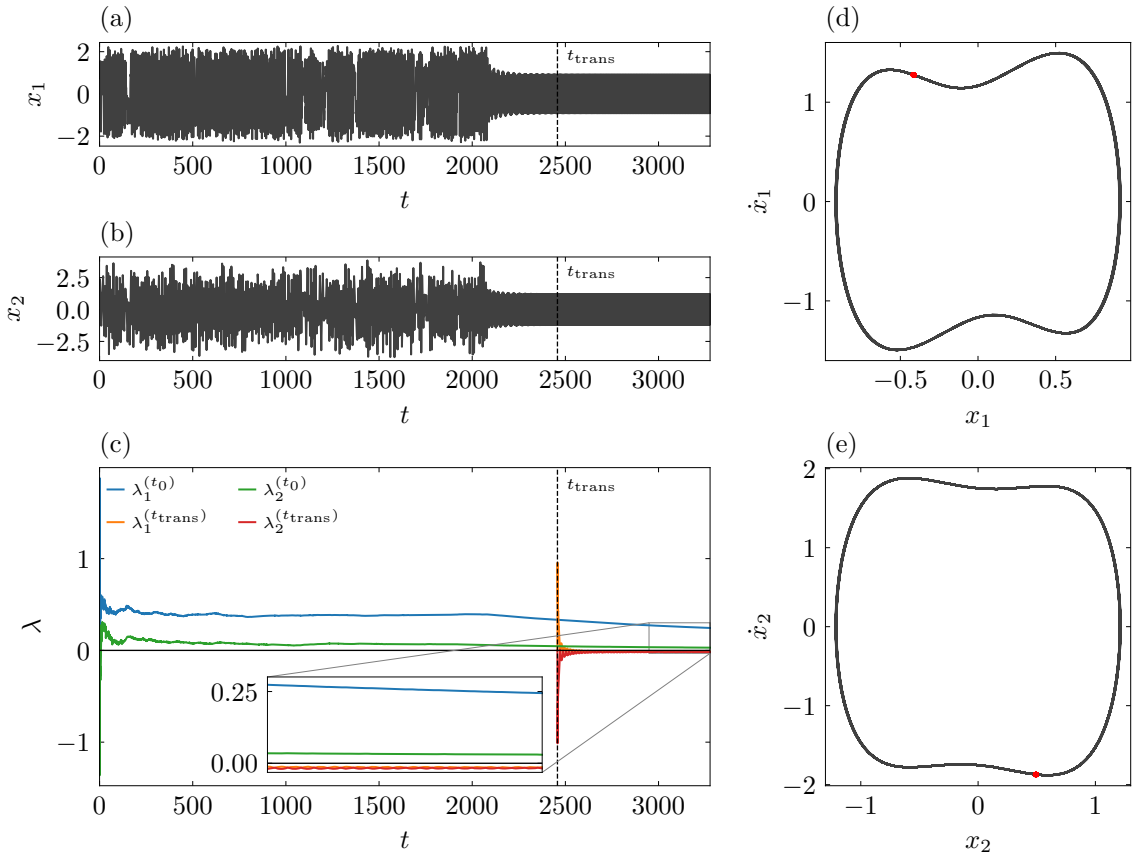

Figure B.4: 1T orbit exhibiting long transient chaos of a 2-DoF Duffing oscillator [3]. Time series of (a) the first and (b) the second DoFs of the system. Steady-state phase space and Poincaré maps of (d) the first and (e) the second DoFs. (c) The convergence of two sets of first and second Lyapunov exponents. $\lambda^{(t_0)}$ set is evaluated starting from $t = t_0$, and $\lambda^{(\text{trans})}$ set is evaluated starting from $t = t_{\text{trans}}$.

The third issue pertains to the numerical convergence of the Lyapunov exponents. As mentioned previously, obtaining an accurate computation of the Lyapunov spectrum necessitates considering a substantial time range to ensure exponent con-

vergence. In certain scenarios, especially when the system exhibits long transient chaotic orbits, the exponents may not converge correctly. To address this challenge, two evaluations with distinct initial times are undertaken:: one with $t = t_0$ and the second starting at $t = t_{\text{trans}}$. This approach yields two spectra that can be compared. If $\lambda_1^{(t_0)} > 0$ and $\lambda_1^{(t_{\text{trans}})} > 0$, $\lambda^{(t_0)}$ spectrum is selected because it has more time to converge, and the behavior is classified as chaotic or hyperchaotic based on the value of the other exponents of the selected spectrum. Alternatively, if $\lambda_1^{(t_0)} > 0$ and $\lambda_1^{(t_{\text{trans}})} < 0$, it indicates that the system is potentially undergoing a long transient chaos orbit. Consequently, $\lambda^{(t_{\text{trans}})}$ spectrum is chosen, as it is not influenced by the transient chaos' effects on the exponent values. In this case, the behavior is classified as periodic. Figure B.4 exemplifies this scenario using a 2-degrees-of-freedom Duffing oscillator, as studied in [3]. This oscillator exhibits a 1T attractor with a long transient chaos phase. When examining Subfigures B.4(a), B.4(b) and B.4(c) one can observe the temporal evolution of some state variables and the convergence behavior of the first two Lyapunov exponents. The dashed lines represent $t_{\text{trans}} = 0.75t_f$. The transient chaos phase concludes just before t_{trans} and subsequent to that, both $\lambda_1^{(t_0)}$ and $\lambda_2^{(t_0)}$ begin to decrease. At t_f it is still decreasing, indicating that the convergence of the $\lambda^{(t_0)}$ exponents does not occur. In contrast, the second set of exponents originating at $t = t_{\text{trans}}$, denoted as $\lambda^{(\text{trans})}$, is not influenced by the transient chaos effects and converges to a negative value at a faster rate than $\lambda^{(t_0)}$. The final values can be observed in the inset zoom in Figure B.4(c). It is important to emphasize that this method is effective primarily when the transient chaos concludes before $t = t_{\text{trans}}$. This underscores the importance of selecting an appropriate t_{trans} value that minimizes the chances of encountering this issue, in addition to ensuring an adequate number of points to evaluate the Poincaré Map correctly.

The last limitation concerns the scenarios in which the system remains in a transient state within the selected simulation time range. In such cases, the classification of attractors can be misleading or erroneous. Using the 2-DoF oscillator studied in [3] as an example, Figure B.5 illustrates a misleading scenario where the system may still be converging to a 1T orbit, as evident from the star-shaped form in the Poincaré map. However, due to the values of the Lyapunov exponents ($\lambda_1 < 0$ and $\lambda_2 < 0$) and the differences in Poincaré map values, the algorithm would classify it as "Many Periods" (MP), which is not incorrect within the given time range, but the system has not reached a steady state yet. Whether this classification is problematic or not depends on the objectives of the analysis. Within the scope of this thesis, such a classification is desired as it characterizes the system within the chosen time range.

Conversely, Figure B.6 illustrates a scenario that combines the misclassification

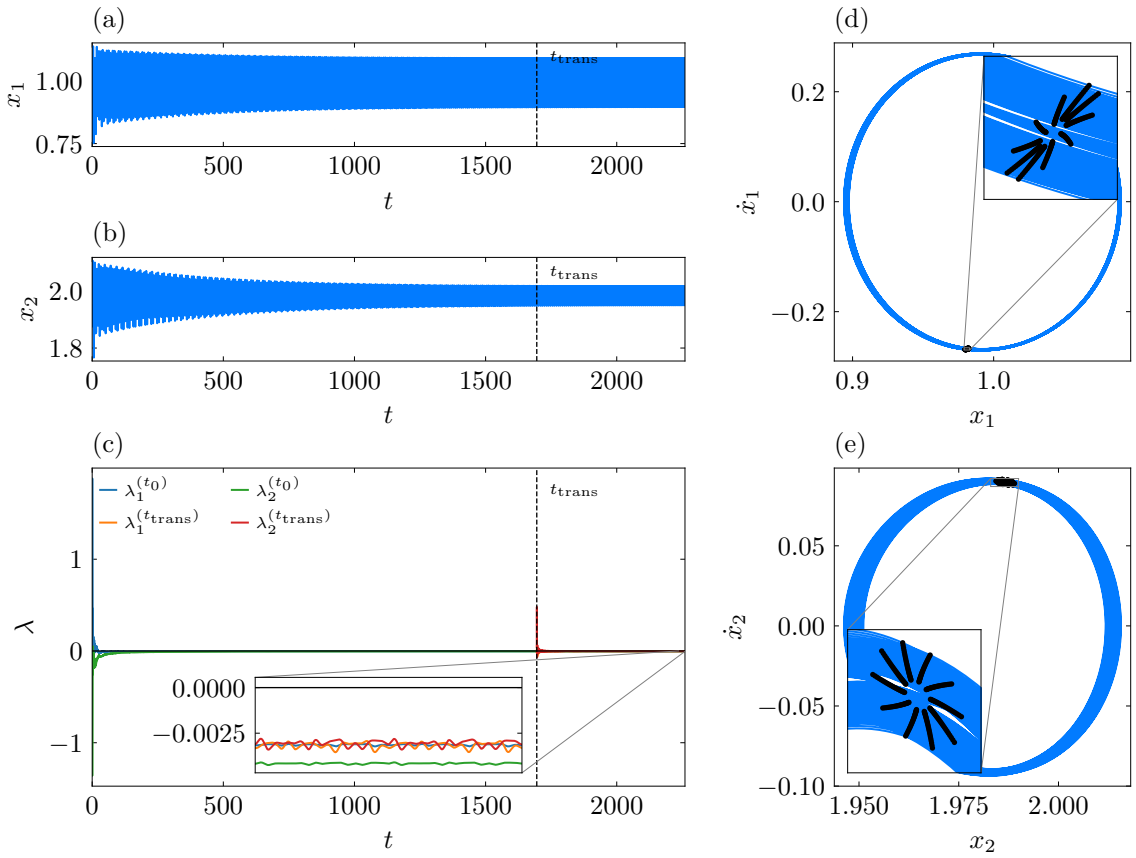

Figure B.5: MP attractor of the 2-DoF oscillator analyzed in [3]. Time series of (a) the first and (b) the second DoFs of the system. Steady-state phase subspace and Poincaré maps of (d) the first and (e) the second DoFs. (c) The convergence of two sets of the first and second Lyapunov exponents. $\lambda^{(t_0)}$ set is evaluated starting from $t = t_0$, and $\lambda^{(\text{trans})}$ set is evaluated starting from $t = t_{\text{trans}}$.

associated with long transients and the first issue concerning quasiperiodic attractors. When examining the Poincaré maps, they suggest a quasiperiodic-like attractor, while the Lyapunov exponents indicate a chaotic response, with $\lambda_1 > 0$. The time series also provides evidence of the system still being in the transient regime. By evaluating only the information available within this time range, it is challenging to classify the attractor accurately. This case exemplifies a classic instance where the classification of the DRD algorithm fails (in this case, it would classify it as chaotic).

Despite the limitations highlighted in this section, all algorithm tests have demonstrated a high degree of effectiveness in mapping the dynamics of nonlinear systems. Through the combination of these approaches, the vast majority of dynamical attractors are properly classified, with the outliers being samples that are still converging to a stable orbit at the final time of integration. In this thesis, the analysis was conducted within the context of these limitations. However,

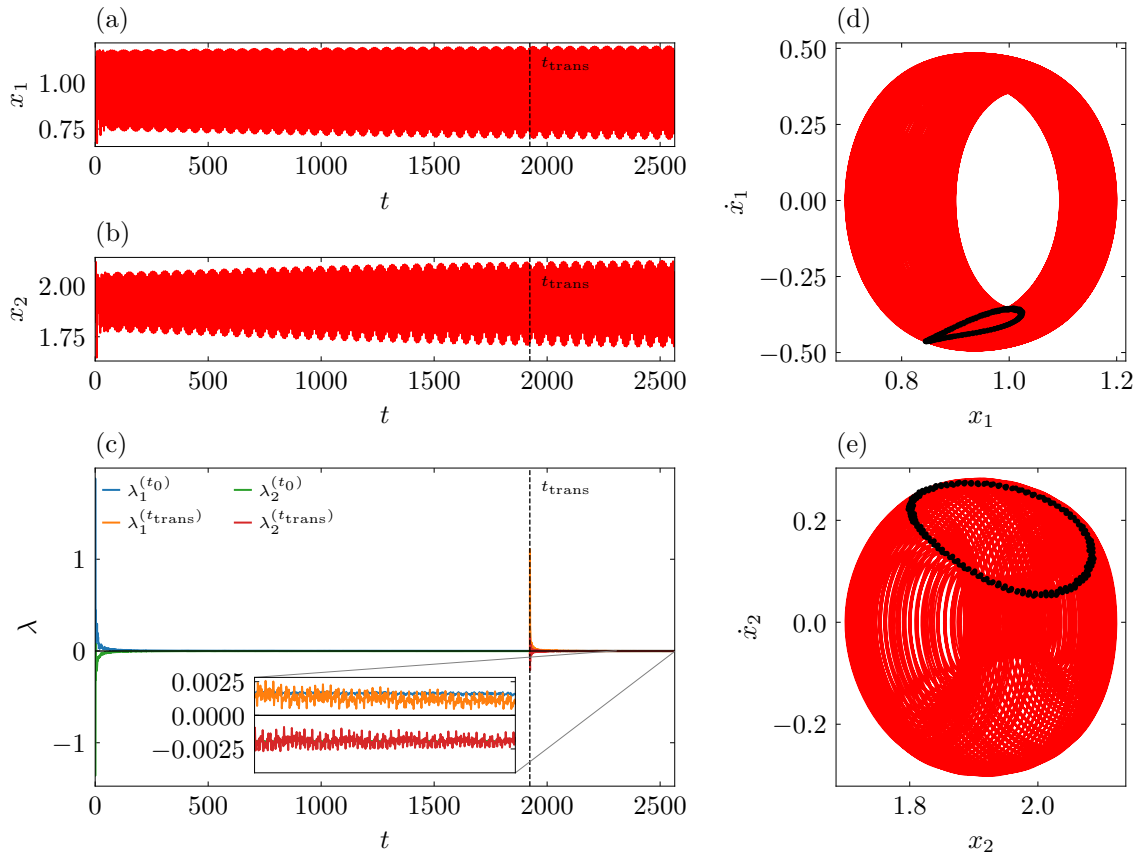

Figure B.6: Wrongly classified quasiperiodic-like attractor of the 2-DoF oscillator analyzed in [3]. Time series (a) the first and (b) the second DoFs of the system. Steady-state phase subspace and Poincaré maps of (d) the first and (e) the second DoFs. (c) The convergence of two sets of the first and second Lyapunov exponents. $\lambda^{(t_0)}$ set is evaluated starting from $t = t_0$, and $\lambda^{(\text{trans})}$ set is evaluated starting from $t = t_{\text{trans}}$

enhancements to the algorithm are planned for future work.

B.5 OCD Algorithm

The procedure to obtain an Occurrence Diagram (OCD) starts by reading the n outputs of any diagram and creating an empty OCD dataset filled with zeros, matching the length of the original datasets. It then iterates over each dataset, evaluating all values of a system characteristic (e.g., output power, attractor). If the values exhibit the relevant feature (RF) of interest, one is added to the corresponding cell position in the OCD dataset.

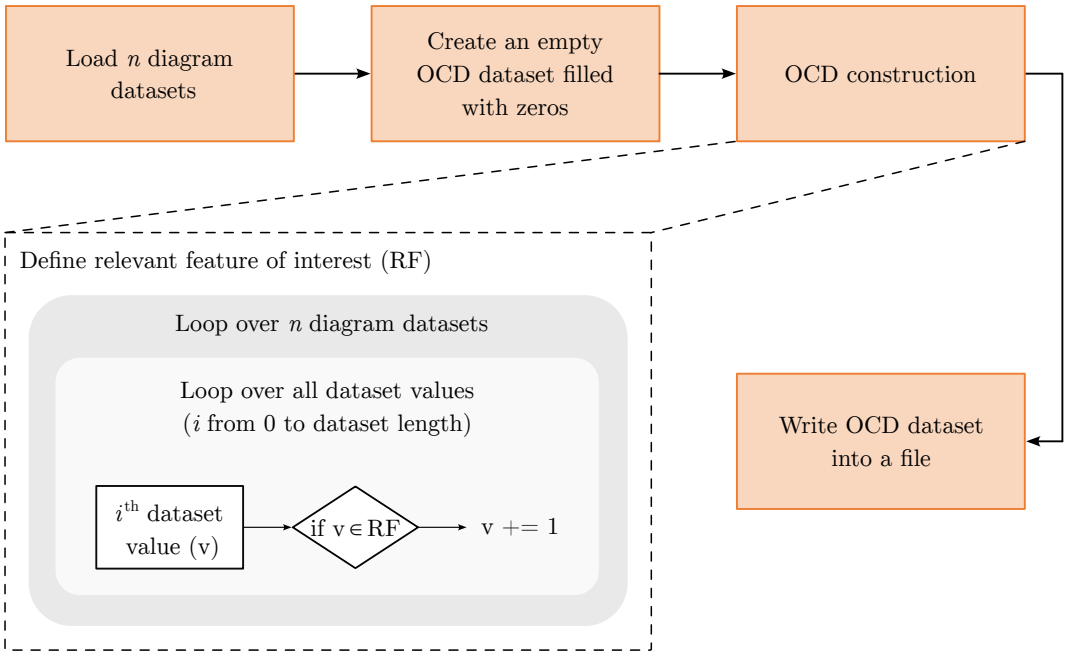

Figure B.7: Schematic illustration of the procedure to obtain the OCDs.

B.6 PCD Algorithm

The procedure to obtain a Performance Comparison Diagram (PCD) starts by reading the OPD datasets from both the reference harvester and the studied harvester. Next, an empty PCD dataset filled with zeros is created, matching the length of the original datasets. The procedure then iterates over the cells of both OPD datasets, retrieves the corresponding values, and applies Equation 3.11 to calculate the result, which is written in the corresponding cell of the PCD dataset.

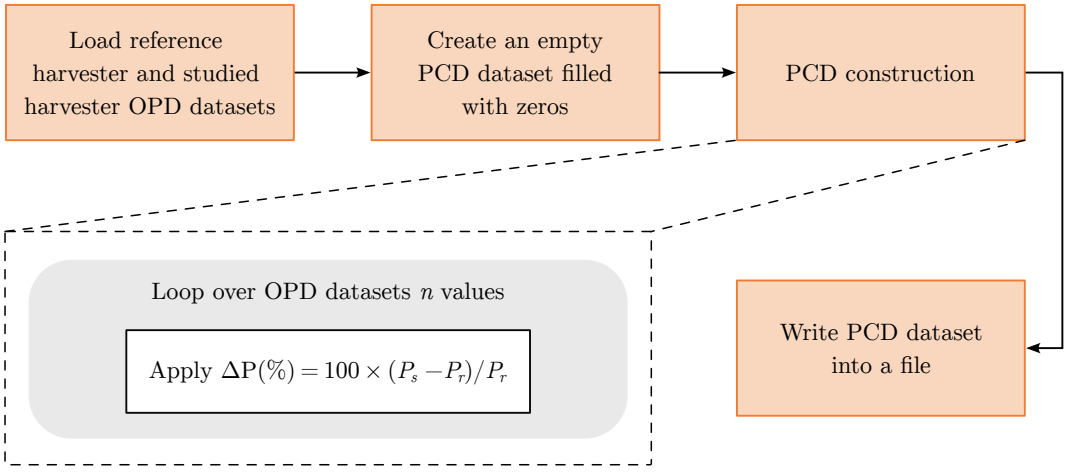

Figure B.8: Schematic illustration of the parallel procedure to obtain the PCDs

B.7 DPD Algorithm for the MHEH

The procedure to obtain a Dynamical Pattern Diagram (DPD) specific for the MHEH starts by reading the full dataset provided by the diagram construction procedure. This dataset contains information such as the attractor classification, the minimum, maximum, and RMS values of all generalized coordinates, and the output power of each transducer, among others. Then, an empty dataset is created,

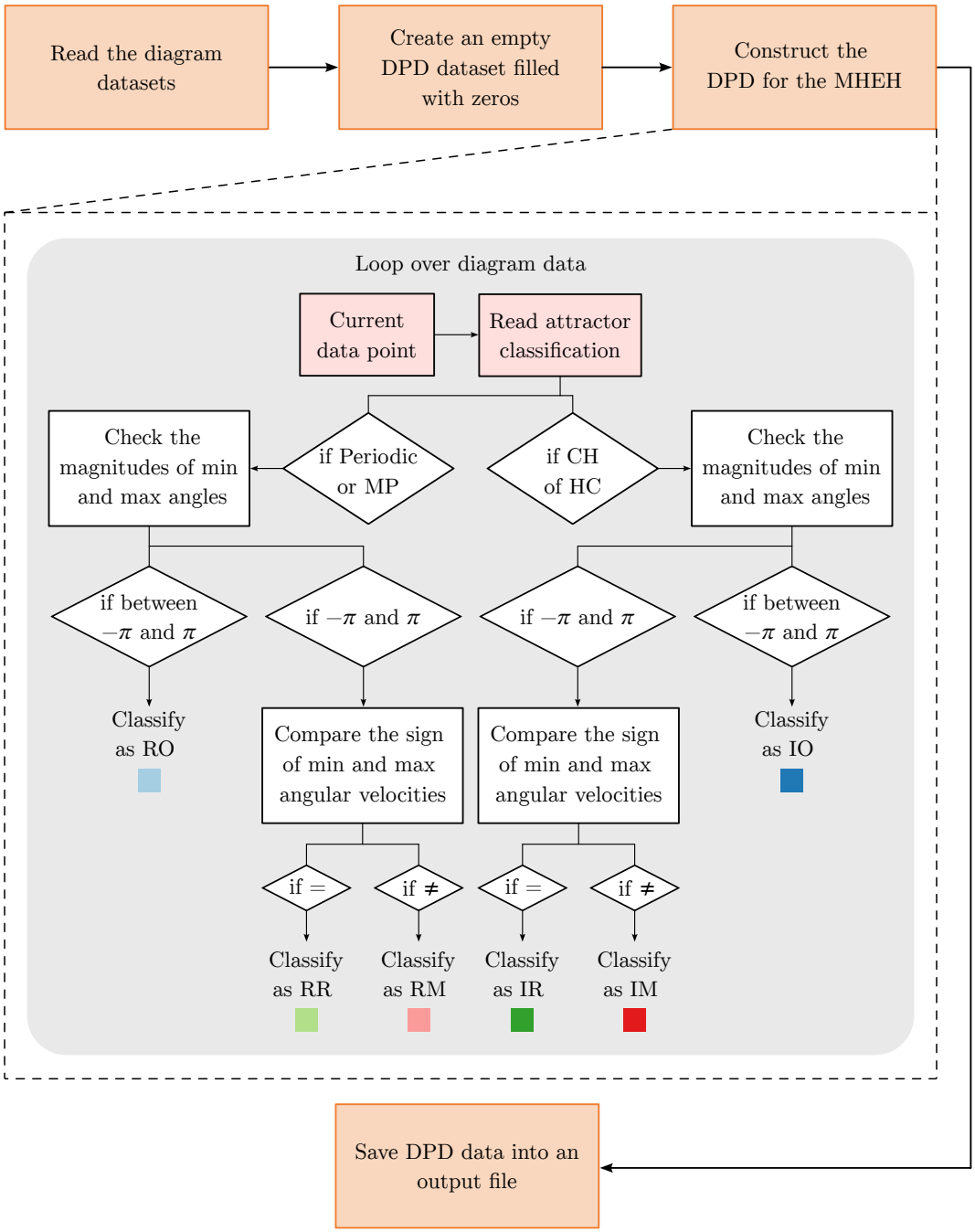

Figure B.9: Schematic illustration of the procedure to obtain the DPDs for the MHEH.

matching the length of the original diagram dataset. The procedure then iterates

over the cells of the original dataset comparing certain features of each point in the analyzed parameter space. Finally, the result is written into an output file containing the updated dataset. The full process is depicted in Figure B.9.

B.8 Stability Analysis Algorithms for the CMEH

The process for determining the stability states of the CMEH is outlined in Figure B.10. Initially, the restitution parameters are chosen. Subsequently, the non-forced system's solution is derived to identify the equilibrium positions. The

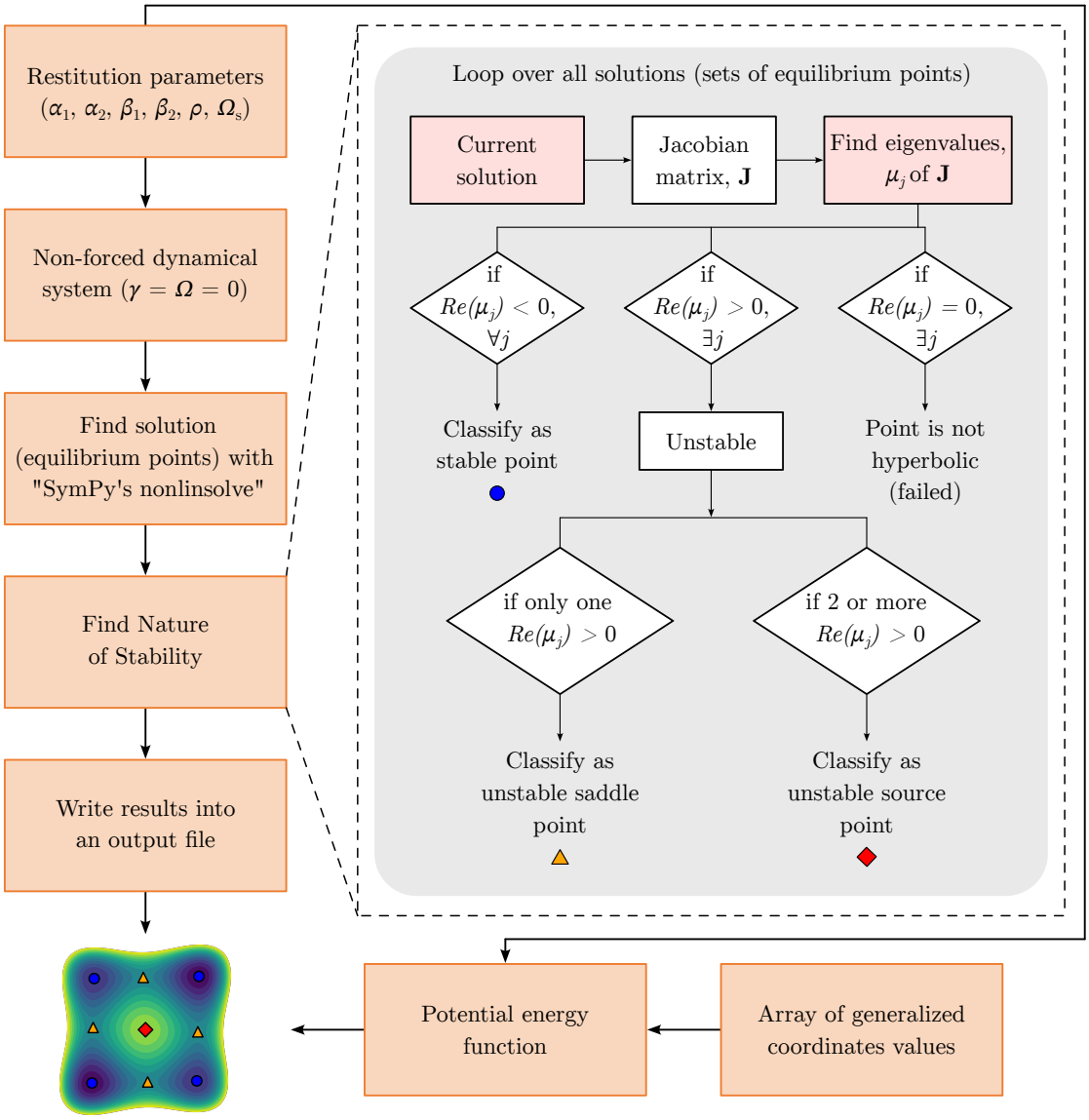

Figure B.10: Schematic illustration of the procedure to obtain the stability states of the CMEH.

characteristics of these equilibrium points are then examined. Each solution of the non-forced system is incorporated into the Jacobian matrix, **J**, from which eigenval-

ues are computed. Utilizing the criteria elucidated in Section 3.1.4, the stability of each equilibrium point is ascertained. Additionally, the system's potential energy is plotted based on a 2D array of position values.

B.9 Basins of Attraction Algorithm

The procedure to obtain the basins of attraction of the fixed points employs a parallel computing scheme using the OpenMP® API, similar to the one used for constructing the diagrams. Figure B.11 details this process. It begins by defining a variable, `npoints`, with an initial value of zero. An empty 2D array, $\mathbf{P}$, is created, where the number of columns corresponds to the number of generalized coordinates of the system, plus an additional column for the label. A mesh of $N_x \times N_y$ distinct initial conditions is then generated.

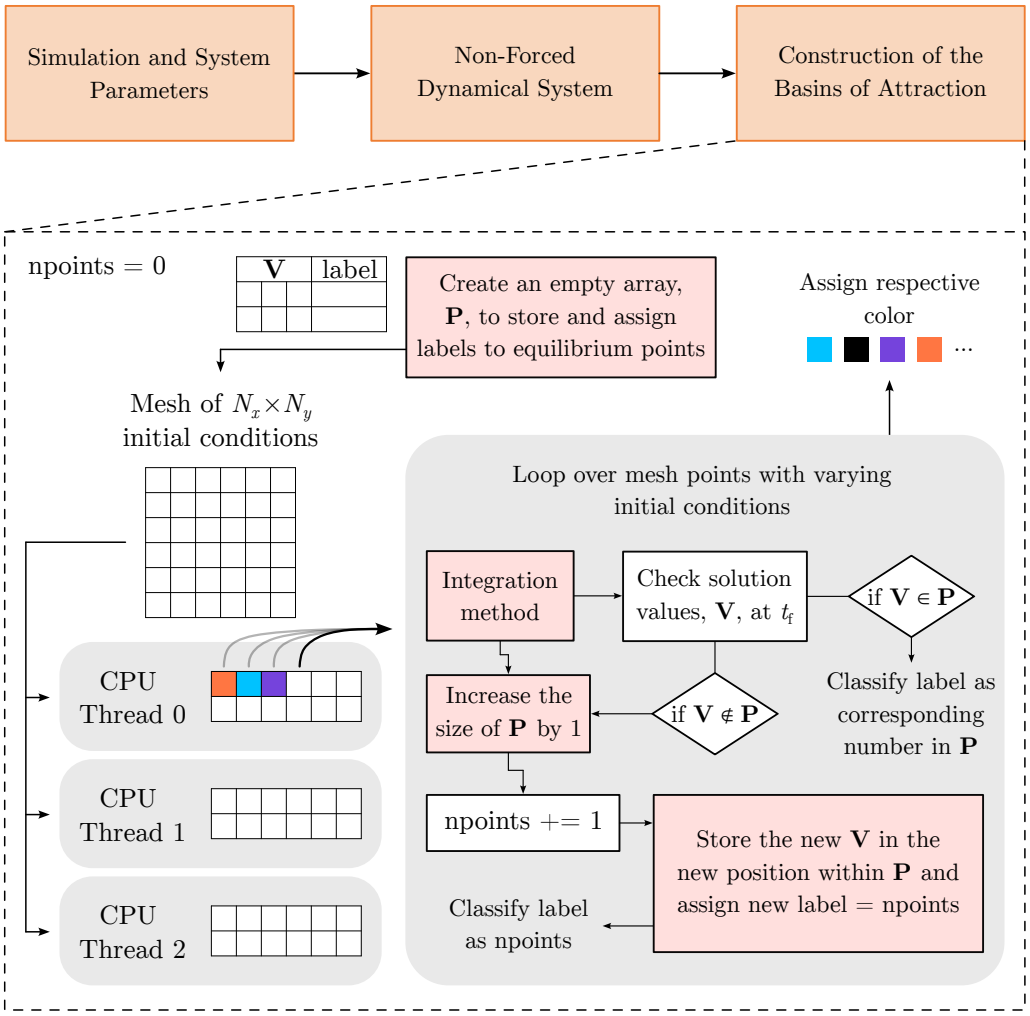

Figure B.11: Schematic illustration of the procedure to obtain the basins of attraction of the fixed points.

A `for` loop iterates over the entire mesh, dividing the iterations into equally

distributed chunks. Each chunk is automatically assigned to a different CPU thread using the `schedule(static)` command of the OpenMP® API. Within each iteration of the loop, the non-forced system's solution is determined using an integration method, and the final solution points, $\mathbf{V}$, at $t = t_f$, are evaluated. Initially, since the array $\mathbf{P}$ is empty, the solution is found, assigned to $\mathbf{V}$, and labeled as 1. In subsequent iterations, the solution is checked against $\mathbf{P}$. If found, it is classified with the corresponding label from $\mathbf{P}$. If $\mathbf{V}$ is not found in $\mathbf{P}$, the number of rows in $\mathbf{P}$ is increased by 1, and the new $\mathbf{V}$ is stored in the new row, and labeled as `npoints + 1`.

In these parallelized tasks, it is crucial to use the `critical` directive of the OpenMP® API before modifying the $\mathbf{P}$ array. The `critical` directive ensures that a section of code is executed by only one thread at a time, preventing race conditions between processors that could lead to incorrect classifications in the algorithm.

Appendix C

Normalization of Electromechanical Equations

The objective of this Chapter is to elucidate the process of normalization of the energy harvesting systems analyzed in this work. The following sections show in detail this process for the compact multistable energy harvester and the hybrid multidirectional energy harvester. In both cases, a dimensionless time, $\tau = \omega_0 t$ is used, where ω_0 is a reference frequency that is unique for each system.

C.1 Normalization of the Compact Multistable Energy Harvester

The four electromechanical equations of the system are written below:

$$\begin{aligned} m_1\ddot{z}_1 + c_1\dot{z}_1 - c_2\left(\dot{z}_2 - \dot{z}_1\right) + \left(k_1 + a_1\right)z_1 + b_1 z_1^3 - k_2\left(z_2 - z_1\right) \\ - \theta_1 v_1 + \theta_2 v_2 = -m_1\ddot{z}_b; \end{aligned} \tag{C.1}$$

$$m_2\ddot{z}_2 + c_2\left(\dot{z}_2 - \dot{z}_1\right) + a_2 z_2 + b_2 z_2^3 + k_2\left(z_2 - z_1\right) - \theta_2 v_2 = -m_2\ddot{z}_b; \tag{C.2}$$

$$C_{p1}\dot{v}_1 + \frac{v_1}{R_1} + \theta_1\dot{z}_1 = 0; \tag{C.3}$$

$$C_{p2}\dot{v}_2 + \frac{v_2}{R_2} + \theta_2\left(\dot{z}_2 - \dot{z}_1\right) = 0. \tag{C.4}$$

Considering the reference frequency of $\omega_0 = \omega_1 = \sqrt{k_1/m_1}$, a reference length, L, and a reference voltage, V, it is possible to write the normalized generalized coordinates of the system as:

$$\bar{x}_i(\tau) = \frac{x_i(t)}{L}, \quad \bar{v}_i(\tau) = \frac{v_i(t)}{V}, \quad (i = 1, 2). \tag{C.5}$$

Using the chain rule, the derivatives of the normalized coordinates are found:

$$\dot{\bar{q}}(\tau) = \frac{d\bar{q}(\tau)}{d\tau} = \frac{d\bar{q}(\tau)}{dt}\frac{dt}{d\tau} = \frac{\dot{q}(t)}{\omega_1 Q}, \tag{C.6}$$

$$\ddot{\bar{q}}(\tau) = \frac{d\dot{\bar{q}}(\tau)}{d\tau} = \frac{d\dot{\bar{q}}(\tau)}{dt}\frac{dt}{d\tau} = \frac{\ddot{q}(t)}{\omega_1^2 Q}, \tag{C.7}$$

where $q = (x_1, x_2, v_1, v_2)$ and $Q = (L, V)$ are dummy symbols representing the generalized coordinates and their respective reference measurements.

The relations shown in Equations C.5, C.6, and C.7 are, then, substituted into the system of electromechanical equations:

$$\begin{aligned} m_1\omega_1^2 L\ddot{\bar{z}}_1 + c_1\omega_1 L\dot{\bar{z}}_1 - c_2\omega_1 L\left(\dot{\bar{z}}_2 - \dot{\bar{z}}_1\right) + \left(k_1 + a_1\right)L\bar{z}_1 + b_1 L^3\bar{z}_1^3 \\ - k_2 L\left(\bar{z}_2 - \bar{z}_1\right) - \theta_1 V\bar{v}_1 + \theta_2 V\bar{v}_2 = -m_1\omega_1^2 L\ddot{\bar{z}}_b; \end{aligned} \tag{C.8}$$

$$\begin{aligned} m_2\omega_1^2 L\ddot{\bar{z}}_2 + c_2\omega_1 L\left(\dot{\bar{z}}_2 - \dot{\bar{z}}_1\right) + a_2 L\bar{z}_2 + b_2 L^3\bar{z}_2^3 + k_2 L\left(\bar{z}_2 - \bar{z}_1\right) \\ - \theta_2 V\bar{v}_2 = -m_2\omega_1^2 L\ddot{\bar{z}}_b; \end{aligned} \tag{C.9}$$

$$C_{p1}\omega_1 V\dot{\bar{v}}_1 + \frac{V}{R_1}\bar{v}_1 + \theta_1\omega_1 L\dot{\bar{z}}_1 = 0; \tag{C.10}$$

$$C_{p2}\omega_1 V\dot{\bar{v}}_2 + \frac{V}{R_2}\bar{v}_2 + \theta_2\omega_1 L\left(\dot{\bar{z}}_2 - \dot{\bar{z}}_1\right) = 0. \tag{C.11}$$

A division process is performed in each side of each equation: Equation C.8 is divided by $m_1\omega_1^2 L$, while Equation C.9 is divided by $m_2\omega_1^2 L$. Equations C.10 and C.11 are divided by $C_{p1}\omega_1 V$ and $C_{p2}\omega_1 V$, respectively, resulting in the following normalized equations:

$$\begin{aligned} \ddot{\bar{z}}_1 + \frac{c_1}{\omega_1 m_1}\dot{\bar{z}}_1 - \frac{c_2}{\omega_1 m_1}\left(\dot{\bar{z}}_2 - \dot{\bar{z}}_1\right) + \left(\frac{k_1 + a_1}{m_1\omega_1^2}\right)\bar{z}_1 + \frac{b_1 L^2}{m_1\omega_1^2}\bar{z}_1^3 \\ - \frac{k_2}{\omega_1^2 m_1}\left(\bar{z}_2 - \bar{z}_1\right) - \frac{\theta_1 V}{m_1\omega_1^2 L}\bar{v}_1 + \frac{\theta_2 V}{m_1\omega_1^2 L}\bar{v}_2 = -\ddot{\bar{z}}_b; \end{aligned} \tag{C.12}$$

$$\begin{aligned} \ddot{\bar{z}}_2 + \frac{c_2}{m_2\omega_1}\left(\dot{\bar{z}}_2 - \dot{\bar{z}}_1\right) + \frac{a_2}{m_2\omega_1^2}\bar{z}_2 + \frac{b_2 L^2}{m_2\omega_1^2}\bar{z}_2^3 + \frac{k_2}{m_2\omega_1^2}\left(\bar{z}_2 - \bar{z}_1\right) \\ - \frac{\theta_2 V}{m_2\omega_1^2 L}\bar{v}_2 = -\ddot{\bar{z}}_b; \end{aligned} \tag{C.13}$$

$$\dot{\bar{v}}_1 + \frac{1}{C_{p1}\omega_1 R_1}\bar{v}_1 + \frac{\theta_1 L}{C_{p1}V}\dot{\bar{z}}_1 = 0; \tag{C.14}$$

$$\dot{\bar{v}}_2 + \frac{1}{C_{p2}\omega_1 R_2}\bar{v}_2 + \frac{\theta_2 L}{C_{p2}V}\left(\dot{\bar{z}}_2 - \dot{\bar{z}}_1\right) = 0. \tag{C.15}$$

By understanding that the linearized natural frequency of each mechanical degree-of-freedom of the system is defined by $\omega_i = \sqrt{k_i/m_i}$, $i = (1, 2)$, it is pos-

sible to write the final version of the electromechanical system of equations as:

$$\begin{aligned}\ddot{\bar{z}}_1 + 2\zeta_1\dot{\bar{z}}_1 - 2\zeta_2\left(\dot{\bar{z}}_2 - \dot{\bar{z}}_1\right) + \left(1+\alpha_1\right)\bar{z}_1 + \beta_1\bar{z}_1^3 - \rho\Omega_s^2\left(\bar{z}_2 - \bar{z}_1\right) \\ - \chi_1\bar{v}_1 + \chi_2\bar{v}_2 = -\ddot{\bar{z}}_b;\end{aligned} \tag{C.16}$$

$$\rho\ddot{\bar{z}}_2 + 2\zeta_2\left(\dot{\bar{z}}_2 - \dot{\bar{z}}_1\right) + \alpha_2\bar{z}_2 + \beta_2\bar{z}_2^3 + \rho\Omega_s^2\left(\bar{z}_2 - \bar{z}_1\right) - \chi_2\bar{v}_2 = -\ddot{\bar{z}}_b; \tag{C.17}$$

$$\dot{\bar{v}}_1 + \varphi_1\bar{v}_1 + \kappa_1\dot{\bar{z}}_1 = 0; \tag{C.18}$$

$$\dot{\bar{v}}_2 + \varphi_2\bar{v}_2 + \kappa_2\left(\dot{\bar{z}}_2 - \dot{\bar{z}}_1\right) = 0. \tag{C.19}$$

where the following new normalized parameters are defined:

$$\begin{aligned}&\rho = \frac{m_2}{m_1}; \quad \Omega_s = \frac{\omega_2}{\omega_1}; \quad \zeta_i = \frac{c_i}{2m_1\omega_1}; \quad \alpha_i = \frac{a_i}{m_1\omega_1^2}; \quad \beta_i = \frac{b_i L^2}{m_1\omega_1^2} \\ &\chi_i = \frac{\theta_i V}{m_1\omega_1^2 L}; \quad \kappa_i = \frac{\theta_i L}{C_{pi}V}; \quad \varphi_i = \frac{1}{C_{pi}R_i\omega_1}; \quad i = (1,2).\end{aligned} \tag{C.20}$$

In Chapter 5, the analyses were conducted considering a harmonic base excitation of the type $z_b(t) = A_b\sin(\omega t)$. By understanding that this type of excitation is a displacement, a similar relation utilized to normalize the generalized coordinates (Eq. C.5) can be used, resulting in the following relation:

$$\omega_1^2 L\ddot{\bar{z}}_b(\tau) = -A_b\omega^2\sin\left(\omega\frac{\tau}{\omega_1}\right). \tag{C.21}$$

Organizing the terms in Equation C.21, the final version of the normalized base excitation term arises:

$$\ddot{\bar{z}}_b(\tau) = -\gamma\Omega^2\sin(\Omega\tau), \tag{C.22}$$

where the new terms, γ and Ω, are defined by the following relations:

$$\gamma = \frac{A_b}{L}; \quad \Omega = \frac{\omega}{\omega_1}. \tag{C.23}$$

Another important point is the normalization of the instantaneous output powers of the system, P_{inst_i}, $i = (1,2)$. To perform the normalization consider the substitution of the relations presented in Equation C.5 in the equations of the instantaneous output power (Eq. 5.18):

$$P_{\text{inst}_i}(\tau) = \frac{V^2}{R_i}\bar{v}_i(\tau)^2, \quad i = (1,2). \tag{C.24}$$

By dividing both sides by $C_{pi}\omega_1 V^2$, $i = (1,2)$, the power dimension [J/s] vanishes, resulting in:

$$\bar{P}_{\text{inst}_i}(\tau) = \varphi_i\bar{v}_i(\tau)^2, \quad i = (1,2). \tag{C.25}$$

where

$$\bar{P}_{\text{inst}_i}(\tau) = \frac{P_{\text{inst}_i}(t)}{C_{pi}\omega_1 V^2}, \quad i = (1, 2). \tag{C.26}$$

C.2 Normalization of the Multidirectional Hybrid Energy Harvester

The five electromechanical equations of the system are written below:

$$(m_s + m_p)\,\ddot{x} + c_x\dot{x} + k_x x + m_p L_p\left[\ddot{\phi}\cos(\phi) - \dot{\phi}^2\sin(\phi)\right] = -(m_s + m_p)\,\ddot{x}_b; \tag{C.27}$$

$$\begin{aligned}(m_s + m_p)\,\ddot{z} + c_z\dot{z} + (k_z + k_{pz})\,z - \theta_{pz}v - m_p L_p\left[\ddot{\phi}\sin(\phi) + \dot{\phi}^2\cos(\phi)\right] = \\ -(m_s + m_p)\,\ddot{z}_b;\end{aligned} \tag{C.28}$$

$$\begin{aligned}m_p L_p^2\ddot{\phi} + (c_{em} + c_p L_p)\dot{\phi} - \theta_{em} I + m_p L_p\left[\ddot{x}\cos(\phi) + (g - \ddot{z})\sin(\phi)\right] = \\ m_p L_p\left[\ddot{z}_b\sin(\phi) - \ddot{x}_b\cos(\phi)\right];\end{aligned} \tag{C.29}$$

$$C_{pz}\dot{v} + \frac{v}{R_{pz}} + \theta_{pz}\dot{z} = 0; \tag{C.30}$$

$$L_{em}\dot{I} + R_{em}I + \theta_{em}\dot{\phi} = 0. \tag{C.31}$$

Considering the reference frequency of $\omega_0 = \omega_z = \sqrt{(k_z + k_{pz})/m_s}$, a reference length, L, a reference voltage V, and a reference current $\mathcal{I}$, it is possible to write the normalized generalized coordinates of the system as:

$$\bar{x}(\tau) = \frac{x(t)}{L}, \quad \bar{z}(\tau) = \frac{z(t)}{L}, \quad \bar{\phi}(\tau) = \phi(t), \quad \bar{v}(\tau) = \frac{v(t)}{V}, \quad \bar{I}(\tau) = \frac{I(t)}{\mathcal{I}}. \tag{C.32}$$

Using the chain rule, as before, the derivatives of the normalized coordinates are found:

$$\dot{\bar{q}}(\tau) = \frac{d\bar{q}(\tau)}{d\tau} = \frac{d\bar{q}(\tau)}{dt}\frac{dt}{d\tau} = \frac{\dot{q}(t)}{\omega_1 Q}, \tag{C.33}$$

$$\ddot{\bar{q}}(\tau) = \frac{d\dot{\bar{q}}(\tau)}{d\tau} = \frac{d\dot{\bar{q}}(\tau)}{dt}\frac{dt}{d\tau} = \frac{\ddot{q}(t)}{\omega_1^2 Q}, \tag{C.34}$$

where $q = (x, z, \phi, v, I)$ and $Q = (L, 1, V, \mathcal{I})$ are dummy symbols representing the generalized coordinates and its respective reference measurements.

The relations shown in Equations C.32, C.33, and C.34 are, then, substituted

into the system of electromechanical equations:

$$\left(m_s+m_p\right)\omega_z^2 L\ddot{\bar{x}}+c_x\omega_z L\dot{\bar{x}}+k_x L\bar{x}+m_p L_p\omega_z^2\left[\ddot{\bar{\phi}}\cos\left(\bar{\phi}\right)-\dot{\bar{\phi}}^2\sin\left(\bar{\phi}\right)\right]= -\left(m_s+m_p\right)\omega_z^2 L\ddot{\bar{x}}_b; \tag{C.35}$$

$$\left(m_s+m_p\right)\omega_z^2 L\ddot{\bar{z}}+c_z\omega_z L\dot{\bar{z}}+\left(k_z+k_{pz}\right)L\bar{z}-\theta_{pz}V\bar{v} - m_p L_p\omega_z^2\left[\ddot{\bar{\phi}}\sin\left(\bar{\phi}\right)+\dot{\bar{\phi}}^2\cos\left(\bar{\phi}\right)\right]=-\left(m_s+m_p\right)\omega_z^2 L\ddot{\bar{z}}_b; \tag{C.36}$$

$$m_p L_p^2\omega_z^2\ddot{\bar{\phi}}+\left(c_{em}+c_p L_p\right)\omega_z\dot{\bar{\phi}}+m_p L_p\omega_z^2 L\left[\ddot{\bar{x}}\cos\left(\bar{\phi}\right)+\left(\frac{g}{\omega_z^2 L}-\ddot{\bar{z}}\right)\sin\left(\bar{\phi}\right)\right] - \theta_{em}\mathcal{G}\bar{I}=m_p L_p\omega_z^2 L\left[\ddot{\bar{z}}_b\sin\left(\bar{\phi}\right)-\ddot{\bar{x}}_b\cos\left(\bar{\phi}\right)\right]; \tag{C.37}$$

$$C_{pz}V\omega_z\dot{\bar{v}}+\frac{V}{R_{pz}}\bar{v}+\theta_{pz}\omega_z L\dot{\bar{z}}=0; \tag{C.38}$$

$$L_{em}\omega_z\mathcal{G}\dot{\bar{I}}+R_{em}\mathcal{G}\bar{I}+\theta_{em}\omega_z\dot{\bar{\phi}}=0; \tag{C.39}$$

A division process is performed in each side of each equation: Both Equations C.35 and C.36 are divided by $m_s\omega_z^2 L$, while Equation C.37 is divided by $m_p L_p^2\omega_z^2$. Equations C.38 and C.39 are divided by $C_{pz}V\omega_z$ and $L_{em}\omega_z\mathcal{G}$, respectively, resulting in the following normalized equations:

$$\left(1+\frac{m_p}{m_s}\right)\ddot{\bar{x}}+\frac{c_x}{m_s\omega_z}\dot{\bar{x}}+\frac{k_x}{m_s\omega_z^2}\bar{x}+\frac{m_p L_p}{m_s L}\left[\ddot{\bar{\phi}}\cos\left(\bar{\phi}\right)-\dot{\bar{\phi}}^2\sin\left(\bar{\phi}\right)\right]= -\left(1+\frac{m_p}{m_s}\right)\ddot{\bar{x}}_b; \tag{C.40}$$

$$\left(1+\frac{m_p}{m_s}\right)\ddot{\bar{z}}+\frac{c_z}{m_s\omega_z}\dot{\bar{z}}+\frac{\left(k_z+k_{pz}\right)}{m_s\omega_z^2}\bar{z}-\frac{\theta_{pz}V}{m_s\omega_z^2 L}\bar{v} - \frac{m_p L_p}{m_s L}\left[\ddot{\bar{\phi}}\sin\left(\bar{\phi}\right)+\dot{\bar{\phi}}^2\cos\left(\bar{\phi}\right)\right]=-\left(1+\frac{m_p}{m_s}\right)\ddot{\bar{z}}_b; \tag{C.41}$$

$$\ddot{\bar{\phi}}+\frac{\left(c_{em}+c_p L_p\right)}{m_p L_p^2\omega_z}\dot{\bar{\phi}}-\frac{\theta_{em}\mathcal{G}}{m_p L_p^2\omega_z^2}\bar{I}+\frac{L}{L_p}\left[\ddot{\bar{x}}\cos\left(\bar{\phi}\right)+\left(\frac{g}{\omega_z^2 L}-\ddot{\bar{z}}\right)\sin\left(\bar{\phi}\right)\right] = \frac{L}{L_p}\left[\ddot{\bar{z}}_b\sin\left(\bar{\phi}\right)-\ddot{\bar{x}}_b\cos\left(\bar{\phi}\right)\right]; \tag{C.42}$$

$$\dot{\bar{v}}+\frac{1}{C_{pz}\omega_z R_{pz}}\bar{v}+\frac{\theta_{pz}L}{C_{pz}V}\dot{\bar{z}}=0; \tag{C.43}$$

$$\dot{\bar{I}}+\frac{R_{em}}{L_{em}\omega_z}\bar{I}+\frac{\theta_{em}}{L_{em}\mathcal{G}}\dot{\bar{\phi}}=0; \tag{C.44}$$

By understanding that the linearized natural frequencies of each mechanical degree-of-freedom are defined by $\omega_z=\sqrt{k_z+k_{pz}/m_s}$, $\omega_x=\sqrt{k_x/m_s}$, and $\omega_\phi=\sqrt{g/L_p}$, it is possible to write the final version of the electromechanical system of

equations as:

$$(1+\rho)\,\ddot{\bar{x}} + 2\zeta_x\dot{\bar{x}} + \Omega_s^2\bar{x} + \rho\ell\left[\ddot{\bar{\phi}}\cos(\bar{\phi}) - \dot{\bar{\phi}}^2\sin(\bar{\phi})\right] = -(1+\rho)\ddot{\bar{x}}_b \tag{C.45}$$

$$(1+\rho)\,\ddot{\bar{z}} + 2\zeta_z\dot{\bar{z}} + \bar{z} - \chi_{pz}\bar{v} - \rho\ell\left[\ddot{\bar{\phi}}\sin(\bar{\phi}) + \dot{\bar{\phi}}^2\cos(\bar{\phi})\right] = -(1+\rho)\ddot{\bar{z}}_b \tag{C.46}$$

$$\ddot{\bar{\phi}} + 2\zeta_\phi\dot{\bar{\phi}} + \Omega_\phi^2\sin(\bar{\phi}) + \frac{1}{\ell}\left[\ddot{\bar{x}}\cos(\bar{\phi}) - \ddot{\bar{z}}\sin(\bar{\phi})\right] - \chi_{em}\bar{I} = \frac{1}{\ell}\left[\ddot{\bar{z}}_b\sin(\bar{\phi}) - \ddot{\bar{x}}_b\cos(\bar{\phi})\right] \tag{C.47}$$

$$\dot{\bar{v}} + \frac{\bar{v}}{\varphi_{pz}} + \kappa_{pz}\dot{\bar{z}} = 0 \tag{C.48}$$

$$\dot{\bar{I}} + \varphi_{em}\bar{I} + \kappa_{em}\dot{\bar{\phi}} = 0 \tag{C.49}$$

where the following new normalized parameters are defined:

$$\begin{aligned}
&\rho = \frac{m_p}{m_s}; \quad \Omega_j = \frac{\omega_j}{\omega_z}; \quad \zeta_i = \frac{c_i}{2m_s\omega_z}; \quad \zeta_\phi = \frac{c_{em}+c_pL_p}{2m_pL_p^2\omega_z}; \quad \ell = \frac{L_p}{L} \\
&\chi_{pz} = \frac{\theta_{pz}V}{m_s\omega_z^2L}; \quad \kappa_{pz} = \frac{\theta_{pz}L}{C_{pz}V}; \quad \varphi_{pz} = C_{pz}R_{pz}\omega_z; \quad i = (x,z); \\
&\chi_{em} = \frac{\theta_{em}\mathcal{J}}{m_pL_p^2\omega_z^2}; \quad \kappa_{em} = \frac{\theta_{em}}{L_{em}\mathcal{J}}; \quad \varphi_{em} = \frac{R_{em}}{L_{em}\omega_z}; \quad j = (x,\phi);
\end{aligned} \tag{C.50}$$

The analyses of the MHEH were conducted considering a harmonic base excitation that has two components, $\mathbf{r_b} = x_b\hat{\mathbf{e}}_x + z_b\hat{\mathbf{e}}_z = -A\sin(\omega t)\left[\sin(\mu)\hat{\mathbf{e}}_x + \cos(\mu)\hat{\mathbf{e}}_z\right]$. By understanding that this type of excitation is a displacement, a similar relation utilized to normalize the generalized coordinates (Eq. C.32) can be used, resulting in the following relation:

$$\omega_z^2L\left(\ddot{x}_b\hat{\mathbf{e}}_x + \ddot{z}_b\hat{\mathbf{e}}_z\right) = -A_b\omega^2\sin\left(\omega\frac{\tau}{\omega_z}\right)\left[\sin(\mu)\hat{\mathbf{e}}_x + \cos(\mu)\hat{\mathbf{e}}_z\right]. \tag{C.51}$$

Organizing the terms in Equation C.51, the final version of the normalized base excitation term arises:

$$\ddot{x}_b\hat{\mathbf{e}}_x + \ddot{z}_b\hat{\mathbf{e}}_z = -\gamma\Omega^2\sin(\Omega\tau)\left[\sin(\bar{\mu})\hat{\mathbf{e}}_x + \cos(\bar{\mu})\hat{\mathbf{e}}_z\right], \tag{C.52}$$

where the new terms, γ, Ω, and $\bar{\mu}$, are defined by the following relations:

$$\gamma = \frac{A_b}{L}; \quad \Omega = \frac{\omega}{\omega_z}; \quad \bar{\mu} = \mu. \tag{C.53}$$

The normalization of the instantaneous output powers of the system, P_{pz} and P_{em}, can be achieved by substituting the relations presented in Equation C.32 in

equation of the instantaneous output power (the two terms in Eq. 6.25, separately).

$$P_{pz}(\tau) = \frac{V^2}{R_{pz}}\bar{v}(\tau)^2, \tag{C.54}$$

$$P_{em}(\tau) = R_{em}\mathcal{G}^2\bar{I}(\tau)^2. \tag{C.55}$$

By dividing both sides of Equation C.54 by $C_{pz}\omega_z V^2$, and both sides of Equation C.55 by $L_{em}\omega_z\mathcal{G}^2$, the power dimensions [J/s] vanish, resulting in:

$$\bar{P}_{pz}(\tau) = \frac{\bar{v}(\tau)^2}{\varphi_{pz}}, \tag{C.56}$$

$$\bar{P}_{em}(\tau) = \varphi_{em}\bar{I}(\tau)^2, \tag{C.57}$$

where

$$\bar{P}_{pz}(\tau) = \frac{P_{pz}(t)}{C_{pz}\omega_z V^2}, \tag{C.58}$$

$$\bar{P}_{em}(\tau) = \frac{P_{em}(t)}{L_{em}\omega_z\mathcal{G}^2}. \tag{C.59}$$